

Probing the role of AGN feedback and galactic mergers in galaxy evolution

Author:
Borislav Nedelchev

Supervised by:
Dr Marc Sarzi
Dr Sugata Kaviraj

Centre for Astrophysics Research
School of Physics, Astronomy and Mathematics
University of Hertfordshire

Submitted to the University of Hertfordshire in partial fulfilment of the requirements of the degree of Doctor of Philosophy.

September 2019

Abstract

In this thesis we aim to probe the role of two of the processes that can dictate the evolution of galaxies – feedback from the central active galactic nucleus (AGN) and mergers. To study the importance of AGN feedback and, in particular, its most direct manifestation as galactic-scale cold-gas winds we assembled two carefully matched large samples of nearby galaxies with and without the presence of optical unobscured Seyfert 2 active galactic nucleus activity. To infer and quantify the presence of such galactic kpc-scale outflows we then studied and compared the properties of the interstellar Na I $\lambda\lambda 5890, 5895$ (NaD) absorption-line doublet, present in some of these systems. We detected excess interstellar NaD absorption in a similar fraction of galaxies in both of our samples. We identified only 53 (or 0.5% of the population) of our Seyfert 2 AGN galaxies potentially harbor outflows. Moreover, in a large fraction of these 53 Seyfert 2s, available ancillary radio and infrared data indicated that star-formation may actually be the principal driver of the outflows. Our results suggest that galactic-scale winds at low redshift are no more frequent in Seyfert 2s than they are in their control-sample counterparts and that optical AGNs are not direct significant contributors to the quenching of star formation in the nearby Universe. On the other hand, to investigate the impact that mergers can have on galaxy evolution we have focused on two galaxies that show signatures of embedded counter-rotating components. Such features are believed to be the fossil records of a past gas acquisition events or a merger. We have successfully separated the contributions of the two distinct kinematic components to the spectra in one of them NGC 448. Drawing on this separation we have shown that the two decoupled stellar components in NGC 448 have similar ages, but different chemical compositions. Our findings indicate that the kinematically distinct component in NGC 448 is truly decoupled, has external origin, and was formed through either the acquisition of gas and a subsequent star-formation episode or from the direct accretion of stars from a companion. Conversely, the presence of a kinematically distinct component in NGC 4365 is not associated to a true kinematic decoupling and is instead most likely due to a projection effect stemming from the triaxial nature of this galaxy. We have also used two samples from a large integral-field spectroscopic survey to verify some of our previous finding and study the demographics of galaxies with embedded counter-rotating components. We have performed some preliminary analysis of this data. The results of this investigation confirm the validity of our method for the detection of cold-gas flows in our Seyfert 2 and control samples. Finally, we have verified some previously known trends in the demographics and properties of galaxies that display stellar counter-rotation as inferred by integral-field observations. On the other hand, our analysis is in contrast with previous studies that have observed that the presence of a counter-rotating stellar component is associated rather frequently with the presence of counter-rotating gas traced by nebular emission.

Declaration

I declare that no part of this work is being submitted concurrently for another award of the University or any other awarding body or institution. This thesis contains a substantial body of work that has not previously been submitted successfully for an award of the University or any other awarding body or institution.

Parts of this submission have been previously published:

1. Parts of the Introduction and Chapter 4 have been published as Nedelchev et al., 2019, *Monthly Notices of the Royal Astronomical Society*, **486**, 1608N.
2. Parts of the Introduction and Chapter 5 have been published as Nedelchev et al., 2019, *Astronomy & Astrophysics*, **623**, 87.

Except where indicated otherwise in the submission, the submission is my own work and has not previously been submitted successfully for any award.

Acknowledgements

First and foremost, I would like to thank my two Jedi masters (supervisors) Dr Marc Sarzi and Dr Lodovico Coccato that taught me the ways of the force (all that I know). I am also forever indebted to all my friends, and in particular Christian Pachnikov and Hristo Vasilev, that were always there when I needed them. Also, I would like to thank Jerly Galeano for her passion and dedication to keep me sound and safe in the last and difficult moments of completing this work. Last but not least, I would like to thank my family for everything that they have done for me.

To my two loving grandmothers Marina and Ruska ...

“Still from the mass the fervent heat outflows,
And on and on the condensation goes,
As slowly all the rallying cores enlist
More portions of the still free floating mist.
Whilst in their vast electrical contents
Are being evolved the chemic elements.”

– Nebula To Man (1905), H. R. Knipe

Contents

Abstract	1
Acknowledgements	3
Contents	4
List of Figures	7
List of Tables	9
List of Abbreviations	10
1 Introduction	1
1.1 A Short Observational Perspective	1
1.1.1 The Notion of a Galaxy	1
1.1.2 Some Observed Galaxy Population Trends	3
1.2 A Brief Overview of Galaxy Formation and Evolution	8
1.2.1 Feedback Processes	10
1.2.1.1 Feedback from Star Formation	11
1.2.1.2 Feedback from Active Galactic Nuclei	14
1.2.1.3 The Role of Galaxy Environment, Mergers, and Gas Accretion	18
1.2.2 Stellar Counter Rotation as a Proxy for Galaxy Assembly	20
1.3 Aims	23
2 Methodology	24
2.1 Galactic Spectra	24
2.2 Fitting Galaxy Spectra	27
2.2.1 Simple Stellar Populations	27
2.2.1.1 The Tremonti et al. Stellar Population Synthesis Models . . .	29
2.2.1.2 The Medium resolution INT Library of Empirical Spectra Stellar Population Synthesis Models	30
2.2.1.3 The Thomas et al. stellar population synthesis models	30
2.2.2 The Penalized Pixel-Fitting Method	31
2.2.3 The Gas and Absorption Line Fitting Algorithm	32
2.2.4 The Emission-line Diagnostic Diagram	33
2.2.5 Stellar Population Properties via Line-strength Fitting	38
2.2.6 The Spectral Decomposition Technique	39

2.2.7	Interstellar Sodium and Absorption-line Profile Fitting	39
3	Data	44
3.1	The Sloan Digital Sky Survey	44
3.1.1	Overview	44
3.1.2	Imaging	44
3.1.3	Fiber Spectroscopy	45
3.1.4	Imaging Catalogues: Galaxy Zoo	45
3.1.5	Spectroscopic Catalogues: OSSY	46
3.1.6	MaNGA: Mapping Nearby Galaxies at APO	46
3.2	MUSE: The Multi-Unit Spectroscopic Explorer	47
4	The Insignificance of Seyfert 2 Activity in Driving Cold-gas Galactic Winds	48
4.1	Overview and Motivation	48
4.2	The SDSS DR 7 Seyfert 2 and Control Samples	51
4.2.1	Seyfert 2 sample	53
4.2.2	Control Sample	54
4.3	Results	56
4.3.1	Control Sample	57
4.3.2	Seyfert 2 sample	63
4.4	Conclusions	68
5	The Kinematically Decoupled Components in NGC 448 and NGC 4365	72
5.1	Overview and Motivation	72
5.2	Observations and Data Reduction	75
5.3	NGC 448 and NGC 4365	76
5.4	Photometric decomposition	76
5.5	Stellar kinematics	79
5.5.1	One-component kinematic fit	79
5.5.2	The kinematic decomposition procedure	82
5.5.3	Two-component fit	83
5.5.3.1	NGC 448	83
5.5.3.2	NGC 4365	87
5.6	Line-strength indices and stellar population properties of NGC 448	89
5.6.1	Line-strength indices	89
5.6.2	Stellar population properties	91
5.7	Discussion and conclusions	95
5.7.1	NGC 448	96
5.7.2	NGC 4365	98
5.7.3	Conclusions	100
6	Further Steps with MaNGA	102
6.1	Overview and Motivation	102
6.2	Samples	104
6.2.1	Seyfert 2 galaxies in MaNGA	104
6.2.2	2-sigma and KDC MaNGA galaxies	104
6.3	Methodology	106
6.4	Preliminary Results	107

6.4.1	The Seyfert 2 galaxy	107
6.4.2	2-sigma MANGA galaxies	108
6.5	Summary and Future Work	117
7	Conclusions and Further Work	118
7.1	Conclusions	118
7.2	Further Work	119
8	Appendix A	121
	Bibliography	124

List of Figures

1.1	The Hubble tuning fork	2
1.2	The color-magnitude star-formation rate (SFR) vs galaxy mass diagrams for the Oh et al. (2011) galaxy sample	4
1.3	Example $(\epsilon, \lambda_{R_c})$ diagrams.	6
1.4	Output from contemporary cosmological simulations and some observed and predicted stellar mass functions	10
1.5	Schematic representation of the “Unified” AGN Model.	15
2.1	Example Sloan Digital Sky Survey galaxy spectra	25
2.2	The basic ingredients in assembling a simple stellar population model	28
2.3	An example <i>GandALF</i> fit to Sloan Digital Sky Survey spectra	32
2.4	BPT diagram for our subsample of the Oh et al. (2011) value-added catalog	34
2.5	Example of the Sato et al. (2006) model for the NaD absorption line spectral profile	40
2.6	Example NaD fits with SDSS color images	41
2.7	S/N_{cont} vs. EW_{NaD} as a function of A/N_{NaD} for our Seyfert 2 and control samples	42
4.1	The result of our control matching procedure	52
4.2	Some SDSS colour images for Seyfert and control galaxies in our study	53
4.3	Kinematics of the NaD absorption component relative to the systemic properties of the galaxy	58
4.4	One-dimensional Gaussian mixture model with two components of the retrieved ISM NaD velocities	60
4.5	Dependence of the AGN bolometric luminosity on the excess NaD line-profile velocity shift	65
4.6	$\Delta\sigma$ vs. ΔV for Seyfert 2 galaxies with interstellar NaD absorption cross-referenced with IR luminosity	66
4.7	$\Delta\sigma$ vs. ΔV for Seyfert 2 galaxies with interstellar NaD absorption cross-referenced with radio data	67
5.1	Photometric decompositions for NGC 448 and NGC 4365	77
5.2	The one-component kinematic maps for NGC 448.	80
5.3	The one-component kinematic maps for NGC 4365.	81
5.4	Example fits to the CaT spectral regions for NGC 448	82
5.5	Spectral flux maps and brightness profile for the kinematic components of NGC 448	84
5.6	Kinematic maps for both components of NGC 448 without the inclusion of a photometric prior	86
5.7	Spectral flux maps of both kinematic components of NGC 448	87

5.8	Kinematic maps for both components of NGC 448 with the inclusion of a photometric prior	88
5.9	Fits to the CaT spectral region of NGC 4365	89
5.10	Equivalent widths of the composite Lick indices for NGC 448	92
5.11	Line-strength index maps and radial profiles for NGC 448.	93
5.12	Single stellar population properties for NGC 448 recovered by fitting the Thomas et al. models.	94
5.13	The metallicity against alpha-element abundance relation for NGC 448	95
5.14	Line-strength index and stellar population properties maps of NGC 4365	100
6.1	The stellar and gaseous kinematics of the Seyfert 2 manga9193-12701 galaxy.	107
6.2	The resolved line-strength indices maps for MaNGA galaxies with distinct kinematic components	109
6.3	The resolved line-strength indices maps for MaNGA galaxies with distinct kinematic components	110
6.4	The resolved line-strength indices maps for MaNGA galaxies with distinct kinematic components	111
6.5	The resolved line-strength indices maps for MaNGA galaxies with distinct kinematic components	112
6.6	The resolved line-strength indices maps for MaNGA galaxies with distinct kinematic components	113
6.7	The resolved line-strength indices maps for MaNGA galaxies with distinct kinematic components	114
8.1	Various measurements on the kinematically distinct galaxies in MaNGA	125
8.2	Same as Fig. A1	126
8.3	Same as Fig. A1	127
8.4	Same as Fig. A1	128
8.5	Same as Fig. A1	129

List of Tables

4.1	Breakdown of our Seyfert 2 and control samples	57
5.1	Photometric components in NGC 448 and NGC 4365.	76
6.1	The DR15 MaNGA galaxies part of our sample of Seyfert 2 DR7 sample. . . .	105

List of Abbreviations

AGN	Active (it) Galactic Nucleus
ALMA	Atacama Large Milimeter/submilimeter Array
SFR	Star-Formation Rate
sSFR	Specific Star-Formation Rate
SDSS	Sloan Digital Sky Survey
ISM	InterStellar Medium
LIRG	Luminous Infrared Galaxy
ULIRG	Ultra Luminous Infrared Galaxy
IFS	Integral Field Spectroscopy
ΛCDM	Lambda Cold Dark Matter
CMB	Cosmic Microwave Background
SMBH	Super Massive Black Hole
BLR	Broad Line Region
IGM	Intra Galactic Medium
CRC	Counter- Rotating Core
KDC	Kinematically Distinct core
IFU	Integral- Field Unit
FWHM	Full- Width-at- Half- Maximum
LINER	Low- Ionization Nuclear Emission- Line Region
IMF	Initial Mass Function
SED	Spectral Energy Distribution
SSP	Simple Stellar Population
LOSVD	Line- Of- Sight- Velocity Distribution

Chapter 1

Introduction

1.1 A Short Observational Perspective

1.1.1 The Notion of a Galaxy

For a long time we did not know the real nature of the so-called “spiral nebulae” and the size of the Universe. Two competing hypotheses had been put forward sparking the “great” debate between Harlow Shapley and Heber D. Curtis (Shapley and Curtis, 1921). On the one hand, the Universe was suggested to be composed of many galaxies like our Milky Way, observed from afar as such “spiral nebulae”. On the other hand, Shapley and others argued these nebulae were just nearby gas clouds and that the Universe had only one galaxy, namely our own. The first steps to resolving this dispute were made by Hubble (1925) who succeeded to measure the distance to two such “spiral nebulae” (M31 and M33). Nowadays, it has been established that galaxies are massive systems one of which is our Galaxy (the Milky Way) that consist of dark matter, stars, and interstellar gas and dust (e.g. Sparke and Gallagher, 2007).

One of the first steps undertaken towards better understanding of the nature of galaxies was their classification on the basis of morphological features (e.g. Hubble, 1922, 1926, 1936). This classification scheme shown in Fig. 1.1 was dubbed as the “tuning fork” because of its distinct shape. On the basis of their appearance the population of galaxies was split into three main classes. Elliptical galaxies (early-type) appear to be quite featureless and smooth with two dimensional light distributions that can be approximated by ellipses. Their brightness peaks in a central region called the “bulge” and then decreases. They devise the stem of the “tuning

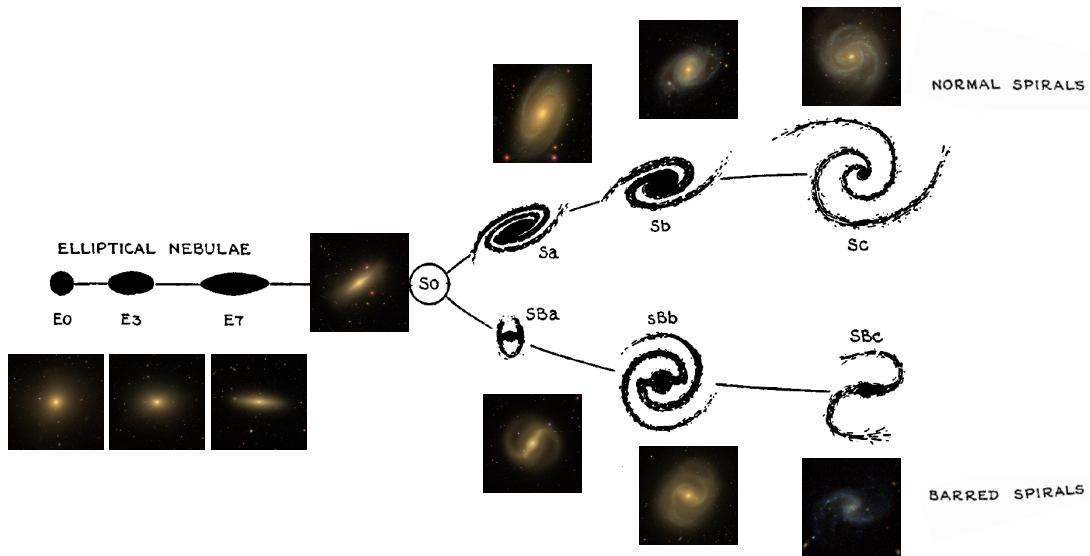


FIGURE 1.1: The original Hubble “tuning fork” taken from Hubble (1926) with example galaxies retrieved from the Sloan Digital Sky Survey.

fork” designated by the letter “E” followed by an integer from zero to seven describing in an increasing order their apparent ellipticity. The two prongs of the “fork” are populated by spiral (also referred to as late-type) galaxies. They also have central bulges, accompanied by a discs and spiral arms. Depending on the prominence of the bulge (decreasing) and openness of the spiral arms (increasing) spirals are sub-classified into further classes designated with the small letters from “a” to “c”. Moreover, the galaxies sitting on the lower prong do additionally show the presence of a “bar”-like structure in their central region indicated by adding the capital letter “B”. The third main class that occupies the intersection of the prongs with the stem consists of early-type galaxies that have morphological properties reminiscent of both elliptical and spiral galaxies called “lenticulars” and nominated as “S0”. This somewhat simple classification was later refined (e.g. de Vaucouleurs, 1959) to include “irregular” galaxies and even more sub-classes.

The following continuous improvement in both the quality of instrumentation and observations has allowed the meticulous quantitative examination of increasingly large, and therefore more representative samples of galaxies covering all Hubble types (e.g. Roberts and Haynes, 1994, for a review). In particular, some early works were focused on extracting the huge amount of information encoded in the light profiles of local galaxies (e.g. Petrosian, 1976; Simien and de Vaucouleurs, 1986). It was thereafter shown that the surface brightness of most galaxies can be well represented with a combination of the functional form proposed by Sérsic (1968). It is

commonly defined as:

$$I(r) = I_e \exp^{-b_n \left(\frac{r}{r_e}\right)^{\frac{1}{n}} - 1}, \quad (1.1)$$

where r_e is a scale (effective) radius encapsulating half of the flux, I_e is the galaxy intensity (flux) at the effective radius, and n is parameter defining the “shape” (i.e. level of concentration) of the profile. The quantity b_n is further defined as a function of the shape parameter (n) to enforce that half of the flux is contained within the scale radius. It can be numerically computed by evaluating the quantile at which the Gamma probability distribution function of a shape parameter of $2n$ integrates to 0.5 (Robotham et al., 2017) or is often approximated as $1.9992n - 0.3271$ for $0.5 < n < 10$ (Capaccioli, 1989). The two other commonly adopted de Vaucouleurs (1948) and exponential profiles can then be shown to be special cases of this Sérsic profile with Sérsic indices of four and one and b_n values of ~ 7.669 and ~ 1.6721 , respectively.

1.1.2 Some Observed Galaxy Population Trends

The advent of even larger sky-wide surveys (e.g. York et al., 2000a; Cole et al., 2001; Scoville et al., 2007, SDSS, 2dFGRS, COSMOS, respectively) spanning a great range of wavelengths and depths combined with unified efforts to gather multi-wavelength data (e.g. Davis et al., 2007, AEGIS) facilitated by the launch of a range of space (e.g. Wright et al., 2010; Milliard et al., 2017, WISE, GALEX, respectively) and radio telescopes such as the Atacama Large Millimeter/submillimeter Array (ALMA) has greatly improved our understanding of the structure, properties, and populations of galaxies.

As a result it was shown that the population of galaxies in the local Universe shows a distinct dichotomy in regards to their colors (e.g. Strateva et al., 2001; Baldry et al., 2004b,a) that also persists at higher redshifts ($z \lesssim 1$) (e.g. Bell et al., 2004) and was noticed as early as the work of de Vaucouleurs (1961). The left panel of Fig. 1.2 shows the difference in the absolute u- and r-band magnitudes (u-r) with respect to the absolute r-band magnitude (M_r) for the Oh et al. (2011) sample of nearby galaxies drawn from the Sloan Digital Sky Survey (York et al., 2000b). Two distinct regions can be discerned there. The most dominant fraction of galaxies sits in the redder (upper) part of the diagram. This so-called “red sequence” consists primarily of early-type galaxies with a smaller fraction of “red” late-type galaxies (Masters et al., 2010a). Contrary to the redder colors of the systems in the red sequence, a sub-population of the galaxies in the local Universe display bluer colors and are of late-type morphology. They occupy the lower section of the color-magnitude diagram (a region labeled as the “blue cloud”) with only a small

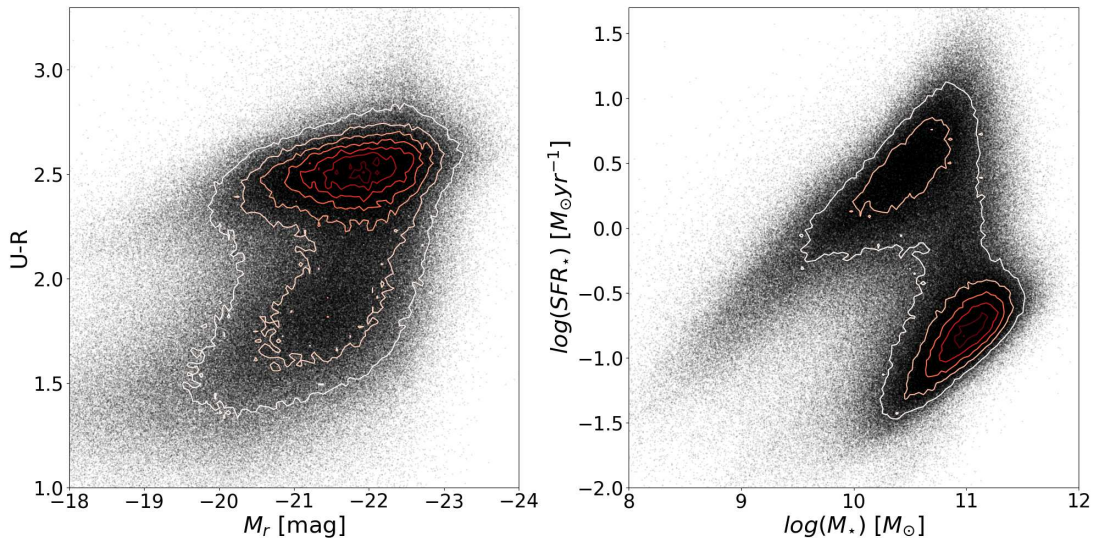


FIGURE 1.2: The u-r color vs M_r magnitude diagram and the star-formation rate (SFR) vs galaxy mass diagram for the Oh et al. (2011) galaxy sample. Left panel: The u-r color against absolute r-band magnitude (M_r) as obtained from the Sloan Digital Sky Survey. Right panel: The total galaxy star-formation rate (SFR) with respect to total galaxy mass. The values have been taken from the value-added catalogues (Kauffmann et al. 2003; Brinchmann et al. 2004; Salim et al. 2007). Contours are placed to reflect the number density of the galaxies in each panel.

presence of early-type blue galaxies (e.g. Schawinski et al., 2009). A smaller number of galaxies lay in-between having somewhat transitional colors and morphology (e.g. Salim, 2014; Coenda et al., 2018) in a region called the “green valley” (e.g. Schawinski et al., 2014).

Similar bimodality also extends to the derived star-formation rates (SFRs) of the population of local (e.g. Brinchmann et al., 2004a; Noeske et al., 2007) and earlier epoch galaxies (e.g. Daddi et al., 2004; Elbaz et al., 2007). The right panel of Fig. 1.2 shows the dependence of the logarithm of the SFRs (as taken from Brinchmann et al. 2004a) on the logarithm of the recovered galaxy mass (from Kauffmann et al. 2003; Salim et al. 2007) for the Oh et al. 2011 SDSS galaxy sample. A large fraction of the actively star-forming galaxies form a tight sequence called the star-forming “main sequence” in analogy to stellar evolution (e.g. Renzini and Peng, 2015). Principally, the gas in these galaxies is converted to stars in lockstep (e.g. Schmidt, 1959; Kennicutt, 1998b, Kennicutt-Schmidt law). At different spatial scales, the SFR surface density has been demonstrated to correlate with the total amount of gas (atomic and molecular) surface density. The efficiency with which the star-formation process occurs also appears to differ depending on the surface density of the total gas and least two distinct regimes have been inferred. Over the lowest gas density regime ($\lesssim 10 M_{\odot} pc^{-2}$) the star-forming capable interstellar medium (ISM) is predominantly in the atomic phase and the star-forming efficiency is notably low. Nevertheless, in the conditions of increasing gas densities ($\gtrsim 10 M_{\odot} pc^{-2}$) the presence

of molecular gas among the star-forming potent gas phase of the ISM also has been shown to increase in conjunction to the efficiency with which this gas is turned into stars. The existence of a third very highly efficient star-formation mode has also been put forward. This so-called starburst or high-density regime ($\gtrsim 100 - 300 M_{\odot} pc^{-2}$) is possibly characterised by even higher star-formation efficiency (e.g. Kennicutt and Evans, 2012, for a review). Furthermore, apart from the main star-forming sequence a sub-population of galaxies have very high SFRs. Within those systems the radiation generated by young stars in an intense central obscured starburst is re-emitted by large amounts of dusty ISM peaking in the infrared (IR) part of the spectrum. This leads to an elevation of the host galaxy infrared luminosity (with some cases when a significant fraction of the host's bolometric luminosity is in the infrared) giving rise to, for example, the class of (ultra) luminous infrared galaxies ((U)LIRGs, e.g. Sanders, 1997; Lonsdale et al., 2006, for reviews). On the other hand, a large fraction of systems in the local Universe display very low SFRs, if any. Most of these galaxies are “quiescent” (“passive”) or “retired” and sit below the star-forming main sequence possess old- to intermediate- age stellar populations (e.g. Robaina et al., 2012; Stasińska et al., 2015) and have significantly lower gas content in comparison to galaxies of similar mass lying on the star-forming sequence (e.g. Saintonge et al., 2011, 2016). In that respect, a big fraction of the star-formation budget in the Universe had already been exhausted in earlier epochs. Drawing on the proliferation of deep large spectral and multi-wavelength surveys, it is now believed that the global instantaneous star-formation rate density of the galaxy population (also referred to as cosmic star-formation) peaked at redshift of ~ 2 . Since then, the global rate at which galaxies form stars has declined to reach the levels observed in the local Universe. At redshifts higher than two, the global instantaneous star-formation rate density is less certain, but has been demonstrated to also decrease (e.g. Madau and Dickinson, 2014, for a review). Moreover, the specific star-formation rates ($sSFR \equiv SFR/M_{\star}$) of the galaxies laying on the main star-forming sequence for redshifts of at least up to two have been demonstrated to correlate with their galaxy masses (e.g. Zheng et al., 2007; Karim et al., 2011). Such an observed mild trend of decrease in the host systems $sSFR$ with respect to their masses implies that the more massive galaxy systems (that are very likely now quiescent) would have concluded most of their star formation earlier in comparison to their low mass counterparts (e.g. Juneau et al., 2005) building a concept also known as “downsizing” (Cowie et al., 1996).

An even fuller and detailed understanding of the structure and properties of galaxies was gained with the advent of advanced instrumentation and techniques such as integral field spectroscopy (IFS). The wealth of information gathered by the first big IFS surveys such as SAURON (Bacon

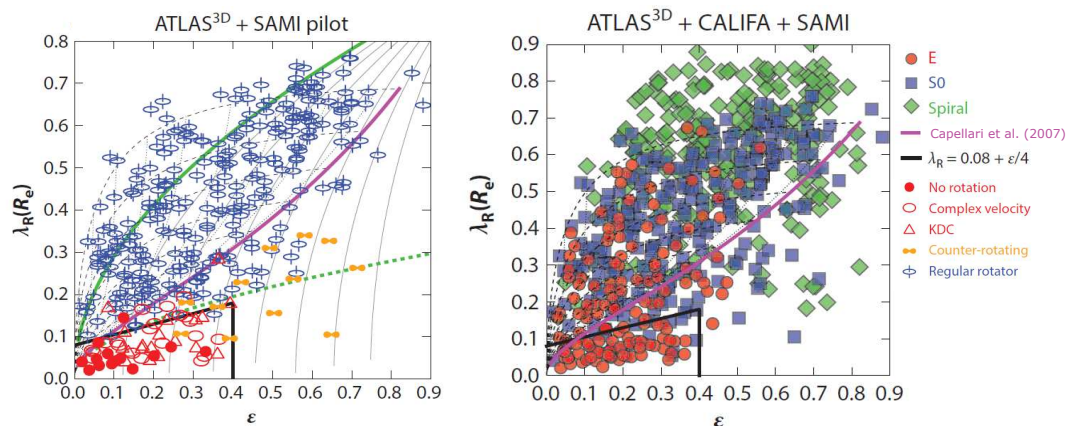


FIGURE 1.3: Example $(\epsilon, \lambda_{R_e})$ diagrams. Left panel: The $(\epsilon, \lambda_{R_e})$ diagram for the galaxies of the ATLAS^{3D} (Cappellari et al., 2011; Emsellem et al., 2011) and SAMI pilot (Fogarty et al., 2015) surveys split on the basis of the characteristics of their velocity fields. The thick solid green line and the thinner black lines designate the theoretical predictions for systems that show different amount of apparent ordered (circular)/non-ordered (complex) orbital rotation (anisotropy) and are viewed edge on (Binney, 2005). The magenta line correspond to the retrieved limiting case of the observed intrinsic galaxy axial ratios for edge-on systems that have at least a small amount of orderly rotating orbits (Cappellari et al., 2007). The dashed lines give the expected positions of such systems when they are viewed from a different vantage point. Nonregular rotators are most commonly found below this magenta line whereas most regular rotators sit above. The green dotted line delimitates an approximate regular/nonregular rotator separation line. The solid black line encompasses the best empirical estimation for the region where slow/nonregular rotators lay. Different symbols designate the velocity field classification. Right panel: The same $(\epsilon, \lambda_{R_e})$ diagram for some of the galaxies of the ATLAS^{3D} (Cappellari et al., 2011; Emsellem et al., 2011), SAMI (Fogarty et al., 2015), and CALIFA (Sánchez et al., 2012) surveys split by their morphology. Figures adopted from Cappellari (2016).

et al., 2001; de Zeeuw et al., 2002) and ATLAS^{3D} (Cappellari et al., 2011) has revolutionized the field of galaxy formation and evolution, for example, showing the complex nature the ionized gas (e.g. Sarzi et al., 2006) or rich structure in the stellar population properties (e.g. Kuntschner et al., 2010) of local galaxies.

From dynamical considerations galaxies can take different intrinsic shapes and configurations of orbits that their stars occupy (e.g Binney and Tremaine, 2008). In particular, the most general case is that of having an intrinsic shape that is described by three axes of different lengths (triaxial). However, somewhat fortunately it has been demonstrated that most galaxies are less complicated symmetric (axisymmetric) systems (e.g. Weijmans et al., 2014). The two-dimensional information that IFS gather have allowed the quantitative separation (Emsellem et al., 2007; Cappellari et al., 2007) of (mainly early-type) galaxies into two distinct categories: slow/non-regular and fast/regular rotators. Such a robust distinction was drawn on the basis of the global apparent (observed) ellipticity of the isophotes (ϵ) with respect to a dimensionless parameter

($\lambda_R = \langle R |V| \rangle / \langle R \sqrt{V^2 + \sigma^2} \rangle$) devised to best quantify the observed projected stellar angular momentum per unit mass. The left panel of Fig. 1.3 shows an example (ϵ , λ_{R_e}) diagram adopted from Cappellari (2016) used to draw such a separation. A number of factors dictate the position of a given galaxy in this diagram. Through modelling Cappellari et al. (2007) had demonstrated that for the fast rotator galaxies within their sample the intrinsic ellipticity of a given galaxy, related to the ratios of the axes that describe its intrinsic shape, is proportional to the amount of ordered (circular)/ non-ordered stellar rotation provided that this is quantified in a way that does not account for the direction of intrinsic rotation. This had allowed the construction of a threshold (magenta line in Fig.1.3) for an edge-on model of a particular intrinsic limiting configuration that is a fast rotator. On the other hand, all slow rotators are expected to be inconsistent with such a model and therefore have been shown to occupy a different part of the diagram (below the magenta line). The inclination of the galaxy with respect to the observer would also change both the projected observed ϵ and λ_{R_e} pairs. This is demonstrated with the dashed black lines. Also drawing on modelling Binney (2005) had demonstrated that the overall amount of apparent ordered (circular)/non-ordered (complex) orbital rotation (anisotropy) is strongly correlated with the observed ellipticity and intrinsic shape defining when viewed edge-on the solid green line and thin black lines in Fig.1.3.

The population of slow rotators have low λ_R ($\lesssim 0.1$) and their velocity fields show limited or no rotation. Generally, they are believed to be brighter, more massive elliptical (weakly) triaxial systems that tend to reside in more dense galaxy environments. The major axes associated to their surface brightness and two-dimensional velocity field do not necessarily coincide. These galaxies were shown to also possess a number of embedded structures such as kinematically decoupled cores or two distinct peaks in their velocity dispersion maps (e.g. Emsellem et al., 2007, 2011; Krajnović et al., 2011; Li et al., 2018). In comparison, fast rotators are usually galaxies that exhibit rather regular two-dimensional stellar velocity fields. Most late-type galaxies have also been demonstrated to be formally classified as fast rotators (right panel of Fig. 1.3) as shown by the kinematics from the CALIFA survey (Sánchez et al., 2012; Falcón-Barroso et al., 2017). Furthermore, the environmental distribution of early-type fast rotators is considered to be similar to that of spirals. The photometric and kinematic major axes in these systems have also been shown to be, to a high degree, coinciding (e.g. Cappellari, 2016, for a review)

1.2 A Brief Overview of Galaxy Formation and Evolution

It is nowadays widely accepted that the Universe began its existence in a very dense high temperature state called *The Hot Big Bang* (e.g. Gamow, 1946). Such an origin for the Universe is supported by a number of independent observations. The first substantial affirmation for the Big Bang is the observed relation between the speed of recession of a galaxy with respect to its distance from us (Lemaître, 1925; Hubble, 1929, the Hubble-Lemaître law). Accounting for such a hot initial phase of the Universe also successfully explains the observed relative proportions of the lightest chemical elements and their isotopes like deuterium, helium and lithium (e.g. Alpher et al., 1948; Weinberg, 1993, for a popular overview). Another verification of the hot beginning of the Universe is the so-called *Cosmic Microwave Background* (CMB) first detected by Penzias and Wilson (1965) and interpreted as the relic imprint of the epoch of recombination by Dicke et al. (1965).

The most successful paradigm capable of explaining this plethora of observations is the so-called Lambda Cold Dark Matter (Λ CDM; concordance) cosmological model (e.g. Narlikar and Padmanabhan, 2001; López-Corredoira, 2017, for critical reviews). Under this framework the Universe is homogeneous and isotropic on large scales, possess no curvature, and its main contents in terms of the critical density are split in: dark matter (~ 0.2715), baryonic matter (~ 0.0495), and dark energy (~ 0.679) as measured by the Planck Collaboration primarily on the basis of the CMB power spectrum (Planck Collaboration et al., 2018). The existence of (cold) dark matter has been first proposed to account for the observed higher than expected velocities of the stars within the solar neighbourhood (Oort, 1932) and individual galaxies within clusters of (Zwicky, 1933; Andernach and Zwicky, 2017, for a translation). These observations have been later extended to show that such dark matter must also be present in galaxies both through theoretical arguments aided by numerical simulations (e.g. Ostriker and Peebles, 1973) and by measuring galaxy rotation curves (e.g. Rubin and Ford, 1970; Rubin et al., 1985). It has been shown it is not baryonic in origin and exerts gravitational force, but signatures for any other interaction have not been conclusive and the search for any possible carrier fundamental particles is still ongoing (e.g. Peter, 2012; Boveia and Doglioni, 2018, for reviews). Similarly, prompted by observations of Type Ia supernovae, that can be calibrated as candles and used as distance indicators, dark energy was introduced as the theoretical means by which to explain the measured accelerated rate of expansion and curvature of the Universe (e.g. Schmidt et al., 1998; Riess et al., 1998; Perlmutter et al., 1999). Its nature is not yet clear and the physical

mechanisms that led to its existence are under debate (e.g. Peebles and Ratra, 2003; Huterer and Shafer, 2018, for a reviews).

Under the concordance cosmological model the observed structure of the Universe at different scales is believed to have formed hierarchically. Small density perturbations left from the very early times after the Big Bang grew progressively larger and got amplified via gravitational instabilities as the Universe expanded and cooled down. Slightly over dense regions gained even higher densities and, conversely, under dense ones lost further density. Owing to its collisionless nature dark matter relaxed first and collapses quicker to form a population of dark matter halos. Such dark matter clumps subsequently grew further either through the accretion of both dark and baryonic matter or mergers (e.g. White and Rees, 1978). During the collapse the baryon gas embedded within dark matter halos experiences strong shock heating. Through radiative cooling the then hot gas loses thermal energy and either accretes (e.g. White and Frenk, 1991; Birnboim and Dekel, 2003) or collapses to form a protogalaxy at the bottom of the gravitational well, dominated by dark matter. As the gas moved towards the central region of the dark matter halo it gained angular momentum until a balance was achieved. During this process the gas had sank to the center of the dark matter halo to very likely form a rotating disk. Once there, the gas cooled further and became self-gravitating (as opposed to being predominantly influenced by the gravity of the dark matter halo). At the places where cooling dominates over heating from the contraction, some dense cores would inevitably reach the uttermost densities at which nuclear fusion takes place, giving birth to the first stars (e.g. Mo et al., 2010; Somerville and Davé, 2015, for a review).

State-of-the-art individual galaxy and large-scale structure simulations (e.g. Fig. 1.4, left panel) based on this paradigm, incorporating ever more complex physics, have been incredibly successful in explaining the discerned trends and characteristics of both the nearby and higher-redshift galaxy population collected through contemporary big surveys of ever increasing observational quality. However, they have only limited prognostic power and more specifically require further refined treatment and calibration of the various physical processes that regulate the amount of baryons that end up as the stellar component of galaxies (e.g. Naab and Ostriker, 2017, for a review). One observed discrepancy between the predictions of large-scale structure formation without additional sub-grid feedback processes and observations concerns the inferred galaxy stellar mass function (Fig. 1.4, right panel). The customary functional form to describe the shape of either the galaxy stellar mass or luminosity function is that of Schechter (1976). It expresses the number of galaxies per unit mass or luminosity (Φ). A characteristic “knee” is present at

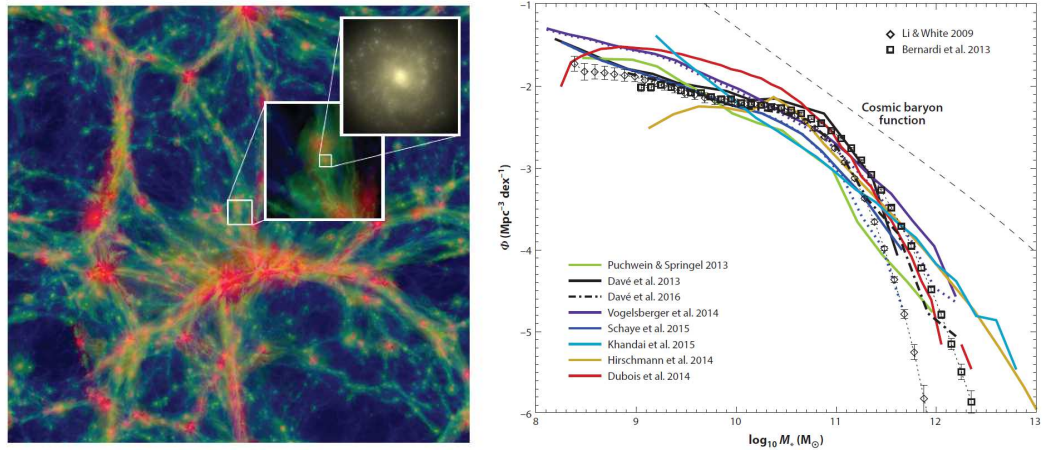


FIGURE 1.4: Left panel: A cosmological volume slice from the EAGLE set of simulations adopted from Schaye et al. (2015). The different colors portray the density of the present gas of different temperature where lower temperatures are shown in blue and higher in red. The zoom-in panels focus on the filamentary nature of the gas and an individual galaxy “observed” using the SDSS filter set with the added expected dust extinction. Right panel: Collated observed and predicted stellar mass functions from a number of simulations (Davé et al., 2013; Puchwein and Springel, 2013; Vogelsberger et al., 2014; Dubois et al., 2014; Hirschmann et al., 2014; Khandai et al., 2015; Schaye et al., 2015; Davé et al., 2016) and surveys (Li and White, 2009; Bernardi et al., 2013). The dashed line designates the galaxy mass function with the cosmic baryon fraction. Figure taken from Naab and Ostriker (2017).

the galaxy stellar mass or luminosity where the function changes from being a power law to exponential. This knee separates the Schechter distribution into a faint or low-mass section and brighter higher-mass end.

1.2.1 Feedback Processes

At least two distinct in nature (feedback) processes have been demonstrated to have the ability to shape the galaxy mass and luminosity function and further account for the observed bi-modality in the star-formation rates and colors of the galaxy population (e.g. Peng et al., 2010). One of those processes that drives the evolution of galaxies within the model used in their work is strongly correlated with the stellar mass of a given galaxy (“mass quenching”). An example of such mass process can be the direct expulsion of gas in the form of galaxy-wide winds either driven by the presence of an active galactic nucleus (AGN) or an intense burst of star formation (e.g. Veilleux et al., 2005, for a review). On the other hand, the other process is strongly linked to the environment a galaxy resides in (“environment quenching”) with a the potential addition of the influence of mergers (“merger-quenching”).

1.2.1.1 Feedback from Star Formation

The cumulative energy and momentum of multiple supernovae explosions (SNe) and the winds and radiation output associated with massive stars during an episode of vigorous star formation can impact the process of star-formation itself serving as a means of self-regulation (the so-called star-formation feedback). Much progress has been made in understanding how such a feedback process works from numerical point of view at different scales from individual stars to cosmological volumes (e.g. Dale, 2015, for a review). In particular, the star-forming regions within galaxies have been shown to be capable of actively expelling a non-negligible fraction of their hosts' ISM in the form of galactic-scale winds or outflows with the aid of multi-wavelength observations (e.g. Rupke, 2018, for a review).

From a modelling perspective, much effort has been put in trying to discern the exact physical processes that drive each particular ISM phase entrained in the large-scale outflow. It is believed that the dominant energy and momentum sources are the timely explosions of core-collapse SNe. The different phases of the out-flowing gas are advected by and propelled through ram pressure by the hotter wind component or the cooler phase of the outflow is simply the result of some thermal instabilities within the expanding hot ISM. (e.g. Zhang, 2018, for a review). On the basis of whether or not some cooling process (e.g. radiative cooling) is capable of dissipating a non-negligible amount of energy in a wind generating hot shocked gas medium over times shorter than its flow time two distinct regimes of outflows have been usually assumed: “energy-driven” or “momentum-driven”. Owing to the conservation of energy, in the case of an energy-driven wind, both the mass-outflow rate and terminal velocity of the wind are dictated by the rate at which energy is injected. On the other hand, in a momentum-driven outflow the conservation of momentum puts those two quantities to be proportional to the rate at which momentum is instead deposited. A core-collapse Type II supernova explosion, ending the life of a massive young star, can release on average $\sim 10^{51}$ erg of kinetic energy carried out by $\sim 2 - 10 M_{\odot}$ expanding stellar ejecta material (e.g. Hartmann, 1999). The momentum and energy carried out by the explosion then impart the surrounding ISM and drive a shock to form a supernova remnant. The resulting remnant undergoes a few distinct evolutionary phases: free expansion, Sedov-Taylor, pressure-driven snowplow, and momentum-conserving (e.g. Ostriker and McKee, 1988, for a review). The free expansion last as long as the mass of ambient ISM, being swept by the shock, is smaller than the ejecta mass. Expansion continues through a Sedov-Taylor phase where the propagation of the shock is dictated primarily by the ambient medium density and the

initial supernova energy until radiative cooling starts to be important. When the inner medium temperature lowers enough and the shock front slows down such that the material behind is cooled down efficiently because its cooling time is smaller than the flow time, the remnant transitions to a pressure-driven “snowplow” phase. Over this stage the thermal energy trapped inside the shock is still substantial and therefore the expansion of the remnant is mostly driven by the thermal pressure exerted by the its interior and the edge of expansion is characterised by a thin and dense shell (the “snowplow”). Once most of the thermal energy is radiated away the expansion of the supernova remnant slowly fades away conserving momentum (momentum-conserving snowplow).

With what efficiency is then momentum and thermal energy transferred into the surrounding ambient ISM depends on the complexities of the interaction vary with different investigations, but the total injected momentum has been shown not to be too sensitive to either environmental factors (e.g. inhomogeneities) (e.g. Kim and Ostriker, 2015; Walch and Naab, 2015; Martizzi et al., 2015, however see). The efficacy with which the cumulative feedback from SNe then feedback on larger scales to possibly produce a “superbubble” is also debated and can depend on a the geometry in which the SNe explode and the timelapse between explosions and some of the underlying galactic host (e.g. Creasey et al., 2013; Gentry et al., 2017; Fielding et al., 2018). Furthermore, the winds associated with the progenitors of core-collapse supernovae and later asymptotic giant branch stars can also deposit energy and form hot gas bubbles that can facilitate the formation of larger-scale galactic winds (e.g. Hopkins et al., 2012). In some starburst galaxies the energy injection provided by supernovae and winds from massive stars can be also comparable (e.g. Leitherer et al., 1999).

Generally, driving of the flow of gas can be achieved through forces arising from either radiation or thermal pressure (e.g. Zhang, 2018, for a review). In the particular case of actively star-forming galaxies the transport and coupling of cosmic rays, generated and accelerated in the explosions of SNe, through any magnetized interstellar medium can also give rise to a viable driving force (e.g. Wiener et al., 2017; Farber et al., 2018).

First backbone models of the evolution of large-scale winds were developed assuming energy-conservation (negligible radiation cooling), spherical symmetry and the injection of thermal energy and mass by an episode of centralized star formation and the corresponding release of thermal energy from SNe. These rates of energy and mass input are canonically expressed through the net energy rate provided by SNe and the star-formation rate through two coupling

constants deemed the thermalization efficiency and mass-loading rate. The net energy rate provided by the SNe explosions, in turn, is usually also expressed through the star-formation rate assuming an underlying number of SNe explosions per unit mass of stars formed and the energy generated by an individual SN. Moreover, the number of SNe explosions can be set to be a function of the initial mass function (e.g. Chevalier and Clegg, 1985). Such models result in asymptotic wind velocity at large radii that are only a function of the thermalization efficiency and mass-loading rate. This type of outflow is said to be “adiabatic” as the expansion of the wind fluid happens without heat transfer. In the general case of adiabatic energy-driven outflows the rate at which energy is injected in the ambient gas and transformed into bulk motion is proportional to the mass loss rate that also depend on the square of the terminal wind velocity as the energy is somewhat efficiently converted to kinetic one. This naturally leads to mass outflow rates that are proportional to the star-formation rate and inversely proportional to the square of the wind terminal velocity (e.g. Murray et al., 2005).

In galaxies with sufficiently high star-formation densities the UV radiation stemming from (young) massive stars can also perhaps directly exert non-negligible pressure on any present gas and dust clouds (e.g. Fall et al., 2010; Murray et al., 2011). Generally, the momentum carried by the photons of a source with a given luminosity is that luminosity divided by the speed of light. Nevertheless, the pressure exerted by radiation is not only dependent on this momentum, but also how much of it is coupled to the gas or dust material in consideration with a few distinct regimes of wind dynamics on the basis of this coupling strength (e.g. Murray et al., 2005; Andrews and Thompson, 2011).

Models incorporating both SN and radiation feedback complimented with realistic cooling have shown that both mechanisms need to act in order to reproduce some of the basic observational properties of large-scale galactic winds. In galaxies rich in gas and undergoing starburst (e.g. ULIRGs) the wind driving by the force stemming from radiation pressure on the gas would be significant. Conversely, the outflows observed in galaxies with lower star-formation rates and lower ISM densities the thermal energy injection from supernovae and stellar winds would more likely dominate as a flow-driving mechanism (e.g. Andrews and Thompson, 2011; Hopkins et al., 2012). In the central starburst region of a wind, whether radiation- or thermal-pressure driven, is likely energy-conserving and expands adiabatically until its volume is large enough such that cooling processes start to dissipate non-negligible amount of energy. Further outwards, the wind switches to a regime in which momentum is conserved instead and swept up material can routinely possess velocities of up to $\sim 1 - 2 \times 10^3 \text{ km s}^{-1}$ (e.g. Thompson et al., 2015a,b).

Observationally, such winds have been shown to be multiphase in nature (e.g. Leroy et al., 2015; Martín-Fernández et al., 2016) and have been found to be ubiquitous among both local (e.g. Cicone et al., 2016) and intermediate (e.g. Rubin et al., 2014) or higher redshift galaxies (e.g. Weiner et al., 2009; Sell et al., 2014; Jones et al., 2018).

The different ISM phases entrained in the outflow are routinely traced with a number of different probes. Signatures of out-flowing material have been found in many different ranges of the electromagnetic spectrum. These include various absorption lines in the rest-frame ultraviolet (e.g. Zhu et al., 2015, Fe II and Mg II) and absorption and emission complexes in the optical (e.g. Concas et al. 2017, 2019, interstellar Na I $\lambda\lambda 5890, 5895$ absorption-line doublet and [O III]) as well as infrared to millimeter wavelengths (e.g. Spilker et al., 2018; Fluetsch et al., 2019, OH and CO). Wind velocities measured using these different proxies depend on the observer line of sight and morphology of the outflow and can vary from $\sim 100 \text{ km s}^{-1}$ (e.g. Cazzoli et al., 2016) to $\sim 1000 \text{ km s}^{-1}$ for the lower-mass most powerful starburst galaxies (e.g. Martin, 1999). Different amount of material depending on the ISM phase is being pushed by and with these outflows. The mass outflow rates reported in some galaxies surpass the rate of star-formation and are therefore expected to stifle the star-formation process that empowers them. Large amounts of dust produced in and around the outflow-instigating SNe and massive stars are usually also entrained in these galactic winds, however carried outwards at much lower velocities (e.g. Heckman and Thompson, 2017, for a review). In the more broad cosmological context, galaxy-scale winds driven by star-formation are believed to be to a large part responsible for the enrichment of the interstellar and intergalactic medium with metals. They are also a vital ingredient in explaining the observed metallicity scaling relations within the galaxy population (e.g. Tumlinson et al., 2017; Maiolino and Mannucci, 2019, for reviews).

1.2.1.2 Feedback from Active Galactic Nuclei

Supermassive black holes (SMBHs) are ubiquitously found in the centres of most if not all galaxies (e.g. Magorrian et al., 1998; Marleau et al., 2013). They often show their presence by the release of copious amounts of gravitational potential energy as a consequence of the active infall of material from a surrounding accretion disk. When undergoing such an active phase the SMBHs manifest as an “Active Galactic Nuclei”. A standard “Unified” model for AGN (Fig. 1.5) was put forward to explain the multiple different phenomenological features attributed to the accretion onto the central SMBH (Antonucci, 1993). In it, the line of sight an observer has

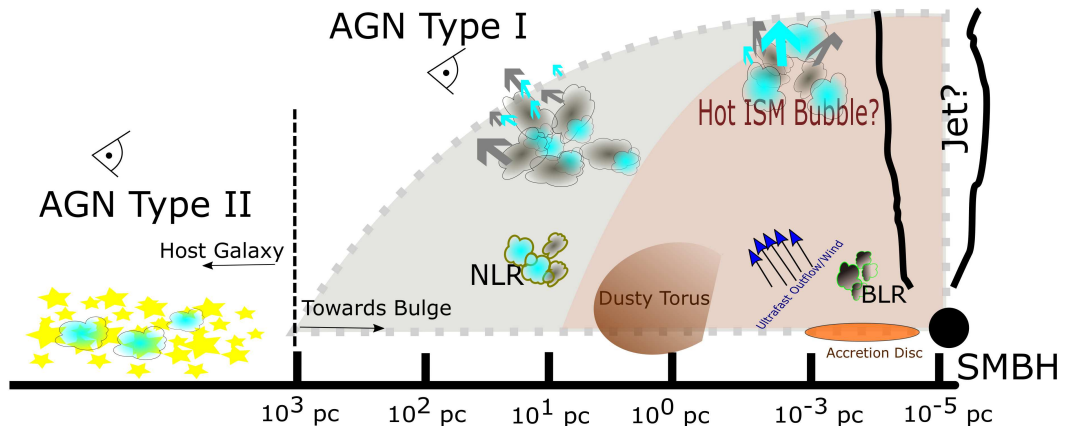


FIGURE 1.5: Schematic representation of the “Unified” AGN Model. In addition to the usual AGN structural elements we also show some of the hypothesised ingredients that can give rise to larger-scale AGN-driven galactic winds not in scale. The scale for the main AGN model components is adopted from Blandford et al. (1990).

towards the very central energy generating engine and the rate at which material accrete onto the SMBH dictate which characteristic observational signatures an AGN host galaxy exhibits.

Radiation emitted by the accretion disc illuminates high velocity clouds of gas present at parsec scales in the immediate surroundings of the SMBH, photoionizing them and, therefore, giving rise to a multitude of characteristic spectral emission lines. Gravitationally influenced by the SMBH these clouds possess very high velocities explaining, for example, the broad Balmer lines observed in the spectra of Type I AGN galaxies. The region surrounding the galactic center linked to the origin of such broad nebular emission is dubbed the *broad-line region* (BLR). This system is lodged in a more optically and possibly somewhat geometrically thick dusty torus spanning a few parsecs in size. It acts to block the direct view towards the central SMBH and its associated accretion disk along certain lines of sight. However, some escaping radiation can still reach the more dynamically relaxed gas present further than the BLR and excite it producing the notable narrower emission line complexes detected in the spectra of Type II AGN galaxies. The region giving rise to such emission lines is called the *narrow line region* (NLR) (e.g. Blandford, 1990; Netzer, 2013). This picture is further complicated by the commonly established existence of small pc-scale fast winds and outflows traced through X-ray and UV spectroscopy stemming from the vicinity of the accretion disk in some of the more powerful AGNs. These outflows were first detected through a blue-shifted absorption lines in the X-ray and labelled as ultrafast outflows (UFOs) and have velocities that can reach 0.3 of the speed of light (e.g. Tombesi et al., 2011). Such black hole winds can be understood to be arising as a consequence of the radiation pressure exerted by the continuum emission of the accretion disk of a SMBH accreting at rates for which the black hole radiates with power compatible to the Eddington luminosity, the

Eddington luminosity is defined as the maximum luminosity at which the force of radiation can act to oppose the gravitational force). They, therefore, can carry great amounts of momentum and energy that can be passed to the host galaxies ISM (e.g. King and Pounds, 2003). At the zone of interaction the ISM such UFOs can get abruptly slowed down and should form a hot shocks. Two distinct regimes of further outflow growth can be distinguished on the basis of whether or not cooling processes occur efficiently (i.e. momentum- or energy- conservation, respectively). On the one hand, in the energy-conserving regime a UFO impacts the ambient ISM to produce large propagating hot shocks that efficiently maintain thermal energy. The result could be a large bubble that expands adiabatically and sweeps up the host galaxy ISM in a “snowplow” to produce fast large-scale outflows in a scenario deemed “blast-wave”. This scenario is somewhat similar to directly coupling a fraction of the SMBH Eddington luminosity to launch an energy-conserving wind (Silk and Rees, 1998). On the other hand, as these flows evolve they would more likely naturally reach a scale at which radiative losses would become important and they would transition into a momentum conserving stage. Cooling could occur moderately fast and leads to substantial compression of the shocked gas resulting in a relatively geometrically narrow post-shocked region. Owing to the conservation of momentum and that any thermalised energy input being radiated away, the post-shocked gas would be able to impart only a smaller amount of its energy to the host ISM though ram pressure and the now larger-scale wind would maintain a terminal velocity that would be a function of the original UFO momentum injection rate (e.g. Zubovas and King, 2012; King and Pounds, 2015a, for a review).

As previously discussed the majority of the photons in an AGN are emitted at higher frequencies deeming it unviable that such radiation could directly efficiently couple to the ubiquitously existing population of electrons in the central galaxy regions. However, the dust grains embedded in the gas and coupled to it via electromagnetic forces could instead have large enough radiation cross sections, particularly in the IR, and, therefore, experience non-negligible radiation pressure (Fabian, 2012). The magnitude of this pressure has been shown to be strongly dependent on the luminosity of the driving source and the optical depths of the medium for ultraviolet and infrared radiation and under favourable conditions such a force has been shown to be capable of driving large-scale outflows powered by the AGN (e.g. Ishibashi and Fabian, 2015).

From a numerical point of view, at least two palpable “modes” of feedback from the AGN have been adopted in contemporary cosmological simulations. One is the so-called “quasar” or “radiative” mode when the rate of accretion onto the SMBH is high (close to the Eddington limit). It is expected that the (cold) gas contents of the host galaxy should be most impacted

when experiencing such a phase (e.g. Silk and Rees, 1998). The other is dubbed as mechanical (or also “radio”, “maintenance”, or radio jet) mode. Such feedback is switched on whenever accretion happens at much lower rate. It is associated with the presence of a hot galactic halo and large-scale jets that form as a consequence can carve very large scale bubbles filled with very hot gas into the surrounding inter-galactic medium (IGM) (e.g. Sijacki et al., 2007; Blandford et al., 2019).

In somewhat massive systems, the energy released when their supermassive black holes accrete matter can exceed the gravitational binding energy of their host galaxies by several orders of magnitude. Thus, from a theoretical point of view, energetic feedback from AGN is thought capable of disrupting the progress of star formation in such systems, through the heating and ejection of the galaxy’s gas reservoir (e.g. Fabian, 2012). As such, energetic feedback from active galactic nuclei is often invoked as a key mechanism for suppressing star formation in massive galaxies, where stellar winds and supernovae explosions are not sufficiently energetic to efficiently expel gas from their deep gravitational potential wells (e.g. Silk and Rees, 1998). Such (negative) AGN feedback is frequently incorporated in models of galaxy formation, to prevent the overprediction of over-massive systems in the models and bring their predicted properties, like colours, in line with observations (e.g. Croton et al., 2006; Scannapieco et al., 2012; Kaviraj et al., 2017). From an empirical perspective, the AGN hypothesis is qualitatively supported by the observed correlations between SMBH masses and various global physical properties of their host galaxies (e.g. velocity dispersion), which suggest that the host galaxy and its SMBH may grow in lockstep with each other (see King and Pounds, 2015b, for a review). In particular, energy-driven AGN winds where the energy injection rate scales with the black hole mass naturally lead to relation that is very close to the observed one (e.g. Murray et al., 2005). Nevertheless, the detailed processes behind this possible coevolution (Kormendy and Ho, 2013) remain unclear, and gaining insight into the impact that SMBHs can have on the evolution of their hosts in large statistical samples of galaxies is essential (Schawinski, 2012).

The clearest examples of host-AGN interaction are arguably found in nearby brightest cluster galaxies. The AGN in these systems have been shown to deposit vast amounts of energy into the surrounding intracluster medium via heating and (mega-parsec scale) jets both observationally and by means of modelling (e.g. Binney, 2004; Scannapieco et al., 2005; English et al., 2016; Gitti et al., 2012, for a review), which maintain the hot-gas reservoirs in these systems, prevent cooling flows and thus suppress star formation (e.g. Binney and Tabor, 1995; Li et al.,

2015). In lower-density environments (where the majority of galaxies live), the empirical picture is much less clear. Direct observational evidence for AGN feedback on galactic scales in such environments remains sparse. More specifically, while outflows have been observationally detected in a number of instances around AGN in various gas phases, most of these detections have been made in ultra-luminous infrared galaxies or some of the closest quasar-host galaxies (e.g. Nyland et al., 2013; Rupke et al., 2005b; Harrison et al., 2014), with only a few examples where the AGN have been shown to couple with kpc-scale outflows that are capable of impacting star-formation on galactic scales (Cicone et al., 2014; Harrison, 2017, for a review). Thus, it is still unclear to what extent the general AGN population could drive kpc-scale galactic outflows capable of possibly limiting or quenching star-formation in the local Universe.

Indeed, recent observational work has cast doubt on the ability of AGN to directly regulate star formation in the nearby Universe. For example, Schawinski et al. (2014) found that black hole accretion occurs preferentially in quenched galaxies that experience a rapid decay of their star-formation rates. Amongst the population of galaxies the time delay between the peak of star formation and the onset of AGN activity has been reported to be of at least several dynamical timescales (e.g. Kaviraj et al., 2015b; Shabala et al., 2017, for radio and e.g. Schawinski et al., 2007; Kaviraj, 2009; Wild et al., 2010 for optical). Consequently, at least radio AGN, couple mainly to residual gas, at a point where star formation has already declined and the original gas reservoir is already significantly depleted (e.g. Sarzi et al., 2016). Similarly, AGN in general may not play a significant direct role in regulating their associated star formation episodes and not couple directly to the cold-gas reservoir (Kaviraj et al., 2011). A fuller understanding of the role of AGN in regulating star formation, therefore, demands a direct study of whether outflows of neutral material (which could be ultimately responsible for quenching star formation) are more likely launched in AGN hosts. Most importantly, a quantitative statement about the putative role of AGN in influencing the evolution of their host galaxy requires a study that employs a complete sample of such AGN in the local Universe.

1.2.1.3 The Role of Galaxy Environment, Mergers, and Gas Accretion

Most generally, galaxies assemble their stellar mass through either star-formation that exhaust any existing cold-gas reservoir, mergers, or by some accretion of gas accompanied by a subsequent episode of star formation.

Such gas can be acquired either directly from cosmological filaments or reaccreted from material already expelled in a galactic-scale wind (e.g. Kacprzak, 2017, for an overview). From a modelling perspective, gas accretion is expected to dominate the mass assembly budget of galaxies (e.g. L’Huillier et al., 2012). Observationally, the imprint of gas accretion from cosmological filaments have been successfully inferred using the kinematics of individual planetary nebulae and globular clusters in some galaxies (e.g. Coccato et al., 2013). Moreover, the misalignment of the ionized-gas component with respect to the stellar body of some galaxies is indicative of past gas accretion events and is not rare (e.g. Sarzi et al., 2006; Davis et al., 2011).

For galaxies residing in higher density environments, ram pressure stripping (e.g. Gunn and Gott, 1972; Brown et al., 2017; Bellhouse et al., 2017) and strangulation (e.g. Peng et al., 2015; Maier et al., 2016) can act to remove cold gas and have been associated with the termination of the process of star formation. Such removal of gas has been directly demonstrated in a class of “jellyfish” galaxies (e.g. Smith et al., 2010; Ebeling et al., 2014) that show long tails of gas that is being stripped due to its interaction with the (hot) intracluster medium. A great deal of recent progress in understanding the details of how these two processes impact galaxies infalling towards the centres of either galaxy clusters or groups has been made by the GASP survey (Poggianti et al., 2017). The removal of the cold- or molecular- gas “fuel” for star formation has been seen to usually happen outside-in leading to truncation or asymmetry in the distribution of the observed ionized-gas ISM (e.g. Bellhouse et al., 2017; Gullieuszik et al., 2017; Moretti et al., 2018) primarily through ram pressure stripping. However, both ram pressure and strangulation in conjunction to galaxy harassment have been shown to also act simultaneously in a number of cases (e.g. Fritz et al., 2017). Moreover, it has also been shown that gas in-flows (e.g. Vulcani et al., 2018b) can occur in such high density environments possibly also triggering the AGN and its capability of driving outflows (e.g. Radovich et al., 2019) and star-formation outside of the main galactic body in a process labeled as a “cosmic web enhancement” (e.g. Vulcani et al., 2018a, 2019).

Supplementary to this picture of higher density environments, galaxies could experience growth and change in morphology due to mergers (e.g. Conselice, 2014, for a review). The dichotomy between fast and slow rotators in the local universe has been suggested to stem to a high extent from the different merger and star-formation episodes suffered by their progenitors (e.g. Penoyre et al., 2017; Cappellari, 2016, for a review). In the framework of hierarchical Λ CDM models mergers between gas-rich fast-rotator disk galaxies were put forwards as a means by which slow-rotator ellipticals can naturally form and in addition explain the observed faint “tails” and

“bridges” that have been reported to surround early-type systems (e.g. Toomre and Toomre, 1972; Toomre, 1977; Naab and Burkert, 2003). More recently, a two-phase formation scheme for the assembly of (early-type) galaxies (Oser et al., 2010, 2012) had been proposed in which an initial “in-situ” collapse of cooled gas in dark matter halos builds up some of the initial stellar contents of massive systems in a process resembling earlier proposed formation scenarios (“monolithic” and/or “dissipative” collapse) (e.g. Eggen et al., 1962; Searle et al., 1973; Larson, 1975; Carlberg, 1984; Kormendy, 1989). Then, the growth of more massive systems is largely driven by a phase of mergers. Recent simulation (e.g. De Lucia et al., 2012; Kaviraj et al., 2015a; Martin et al., 2017) and observational (e.g. Williams et al., 2014; Lofthouse et al., 2017) work have shown that minor-to-intermediate mergers and even more strongly major mergers may not be the dominant mechanism of galaxy stellar growth. Major mergers have also been demonstrated to be capable of shutting down the star-formation process in local galaxies, albeit not playing a major part in bringing the population of blue star-forming galaxies into redder quiescent systems (e.g. Weigel et al., 2017).

1.2.2 Stellar Counter Rotation as a Proxy for Galaxy Assembly

The kinematic and stellar population properties of local galaxies carry the imprint of their formation and evolution histories. Within the local Universe, most galaxies display rather regular kinematic appearance (Krajnović et al., 2008; Cappellari, 2016). However, a fraction of the local galaxies show some peculiarities in their stellar (e.g. Krajnović et al., 2011) or gas (e.g. Sarzi et al., 2006) kinematics or both. Often these peculiarities imply underlying rotation around more than one axis (or anti-parallel spin), characterising a class of galaxies labelled as “multi-spin galaxies” (Rubin, 1994). The observed multiple-spin axes could arise from a number of morphologically different structures. These range from polar ring or disc structures (e.g. NGC 4650A, Iodice et al., 2015) and large-scale counter-rotating discs (e.g. NGC 4550, Coccato et al., 2013), to kinematically distinct or counter-rotating cores (e.g. NGC 5813, Krajnović et al., 2015). The latter population of galaxies with a kinematically distinct core (KDC) displays an abrupt change in the direction of the velocity field accompanied by a large change in the kinematic position angle. In some of these special cases the velocity of the KDC switches sign (i.e. the two kinematic components show opposite rotation to one another) to differentiate a subclass of KDC whose members are specifically defined as having counter-rotating cores (CRC). Another signature of a counter-rotating component is the presence of two symmetric velocity dispersion peaks along the main rotation axis in a subclass of multi-spin galaxies labelled as

“ 2σ ” (Krajnović et al., 2011). “Intrinsic” counter rotation is observed when the rotation occurs around the same rotation axis, but involves different kinematic components rotating in opposite directions. Conversely, if the (decoupled) components have different misaligned rotation axes and their angular momentum vectors simply project anti-parallel onto the sky plane, the counter-rotation is deemed to be “apparent” (Corsini, 2014).

Observationally, a number of disc galaxies (i.e. some lenticulars and spirals) have been demonstrated to possess a truly decoupled kinematic structure that counter-rotates with respect to the main stellar body and often has a disc-like morphology (e.g. Coccato et al., 2011, 2013, 2015; Katkov et al., 2013; Morelli et al., 2017). Either using long-slit or integral-field unit (IFU) spectroscopic observations, in conjunction with a spectroscopic decomposition technique (Coccato et al., 2011), has revealed that the distinct cores of such galaxies are more extended embedded components, comprise of younger stellar populations, and are always accompanied by a substantial gas reservoir traced by ionized gas emission (Johnston et al., 2013; Pizzella et al., 2014a; Mitzkus et al., 2017a). Owing to their peculiar nature, galaxies with counter-rotating components have been investigated with the aid of numerical simulations. Several different formation scenarios have been proposed and modelled to explain their existence. The most favoured formation channel for such kinematically distinct components in lenticulars and spirals is the external acquisition of gas as a consequence of a gas-rich major or minor merger and a subsequent period of in situ star formation (Pizzella et al., 2004). Detailed numerical modelling has indeed shown that both gaseous and stellar counter rotation can result from a minor-merger scenario, provided that initially the two progenitors have opposite spins and that the gas content of one of the progenitors is substantially higher than that of the other such that the gas accreted on retrograde orbits is not dissipated and swept up by any pre-existing gas (e.g. Bassett et al., 2017). Another channel for the formation of disc-like counter-rotating distinct kinematic components is proposed in Algorry et al. (2014). The consequential gas accretion from two distinct large-scale cosmological filaments under a very specific spatial configuration in their zoom-in cosmological simulation naturally forms a population of counter-rotating stars implanted within the host galaxy. Evans and Collett (1994) also suggested that counter-rotating stellar discs can form through the internal separatrix crossing mechanism. The change from elliptical to circular disc (e.g. through the disbandment of a bar structure in a triaxial halo) shifts some stars, initially moving on box orbits across the separatrix to tube orbits, shaping two co-rotating and counter-rotating stellar populations. Another mechanism that was put forward to explain the formation of two counter-rotating discs is the (near) coplanar major merger of two opposite spin spirals

(e.g. Puerari and Pfenniger, 2001; Crocker et al., 2009). In such a merger the resultant prograde rotating stellar disc becomes “heated” more than the retrograde one to naturally explain the kinematic structure of galaxies similar to NGC 4550 (Crocker et al., 2009). The situation is even more complicated with regards to ellipticals. Kinematically distinct cores have long been known to occur frequently in the centres of elliptical galaxies (e.g. Bender, 1988). Generally, distinct kinematic features can be the tell-tale signs for either intrinsically more centrally concentrated embedded small components, or just “tip-of-the-iceberg” indication of more extended kinematic structures. Nevertheless, McDermid et al. (2006) reported a dichotomy in the KDCs found within massive ellipticals. The elliptical slow rotators mainly host more extended KDCs (on kiloparsec scales) with stellar populations with ages comparable to that of the stars within the main galaxy body. Conversely, the more centrally concentrated KDCs (of a few hundred parsecs) usually have noticeably younger stellar populations and are predominantly found in fast-rotating galaxies. The KDCs in massive ellipticals could also be a mere projection effect. The (weak) triaxial nature of some of these galaxies (Cappellari et al., 2007) allows them to support multiple types of different orbit families (e.g. de Zeeuw and Franx, 1991) and therefore viewed from a different vantage point these can appear to possess a KDC, nicely illustrated in Statler (1991).

A lot of effort from a simulation standpoint has also been focused towards understanding the nature of the kinematically distinct components within more massive ellipticals. Ever since their first detection these KDCs have been suggested to be the signature of a past merger (e.g. Kormendy, 1984; Balcells and Quinn, 1990). Indeed, Hoffman et al. (2010) proposed that a merger event involving progenitors harbouring a non-negligible gas reservoir ($\sim 20\%$) can frequently result in elliptical galaxies that exhibit a KDC whose properties resemble that of a faster- (counter-) rotating embedded disc. Bois et al. (2011) performed another comprehensive set of high-resolution merger simulations with various initial progenitor mass ratios. Their results showed that the remnants of a merger between two spiral galaxies with opposite spin would resemble slow rotators. Furthermore, the remnants would often harbour a central KDC, although these simulations did not manage to reproduce all the observed morphological and kinematic properties of the massive elliptical galaxies part of the ATLAS^{3D} survey (Cappellari et al., 2011). Moreover, KDCs need not be just a consequence of a merger of opposite spin galaxies. The reactive force stemming from the substantial mass loss in the merger process can act to naturally place gas or stars, or both, on retrograde orbits and conspire to form a KDC embedded in the remnant elliptical galaxy (Tsatsi et al., 2015). Most recently, Schulze et al.

(2017) followed the formation and evolution of a small-scale (and almost certainly therefore younger) KDC in a high-resolution equal-mass-merger simulation with specific emphasis on the KDC stability. Perhaps surprisingly, they discovered that such structures could be semi-stable for about 3 Gyr and highly dynamic, undergoing global gyroscopic precession, before being gradually dissolved and dispersed within a few gigayears.

1.3 Aims

This thesis aims to probe the importance of AGN feedback and mergers in the context of galaxy evolution. It comprises of three works outlined in three parts:

In Chap. 4 of this thesis we study the interstellar Na I $\lambda\lambda 5890, 5895$ absorption-line doublet in a large sample of ~ 9900 nearby Seyfert 2 galaxies. We aim to quantify the significance of optical, unobscured AGN activity in driving kpc-scale outflows that can quench star formation. To that extent, we have devised a carefully matched sample of $\sim 44,000$ control objects that match our Seyfert 2 galaxies in a number of galaxy properties, including morphology and color.

Chapter 5 focuses on two specific cases of early-type slow-rotator galaxies with kinematically distinct components NGC 448 and NGC 4365. Guided by integral-field spectroscopic observations we would show that these objects are very different in their structure and formation. We have measured the brightness profiles, kinematics, and stellar population properties of the peculiar kinematic structures in these galaxies and shed light on their true nature and formation mechanism.

Chapter 6 provides a follow-up investigation on our ability to trace cold gas using the interstellar Na I $\lambda\lambda 5890, 5895$ absorption-line doublet and also focuses on some of the properties of galaxies with kinematically distinct components in two samples drawn from a large integral-field spectroscopic survey.

Chapter 2

Methodology

2.1 Galactic Spectra

The optical spectra of most galaxies is predominately due to the combination of an underlying stellar continuum with a multitude of absorption and, in some cases, emission lines, tracing the presence of ionized gas, possibly further and altogether modulated by the dust reddening along the observer line of sight. Additionally, we sometimes observe the ionised-gas emission and non-thermal continuum associated to the presence of an accreting central supermassive black hole. Finally, interstellar material could also lead to additional absorption features. Each of these constituents provides complimentary information for the physical properties of the host galaxy and, therefore, successfully decoupling their contribution to the spectra is vital for our study of galaxies.

Figure 2.1 shows a selection of galactic spectra drawn from the Sloan Digital Sky Survey, which offers a panoramic view of the nearby galaxy population within a redshift of $z < 0.2$. Most of the galaxies in the nearby Universe show either extremely weak or no emission lines in their optical spectra (e.g. Brinchmann et al., 2004b; Oh et al., 2011). Therefore, they were labelled as either *passive* or *quiescent*. Their spectra (bottom in black of Fig. 2.1) is primarily characterized by the some well-known strong absorption lines (e.g. Ca II H and K, Mg *b*, and NaD), originating mostly within the stellar atmospheres of their constituent stars with highest contribution credited to older stars (mainly, cooler K and F main sequence stars) (e.g. Hamilton, 1985; Rose, 1985). The cumulative effect of some strong ionized metal absorption lines displayed by the

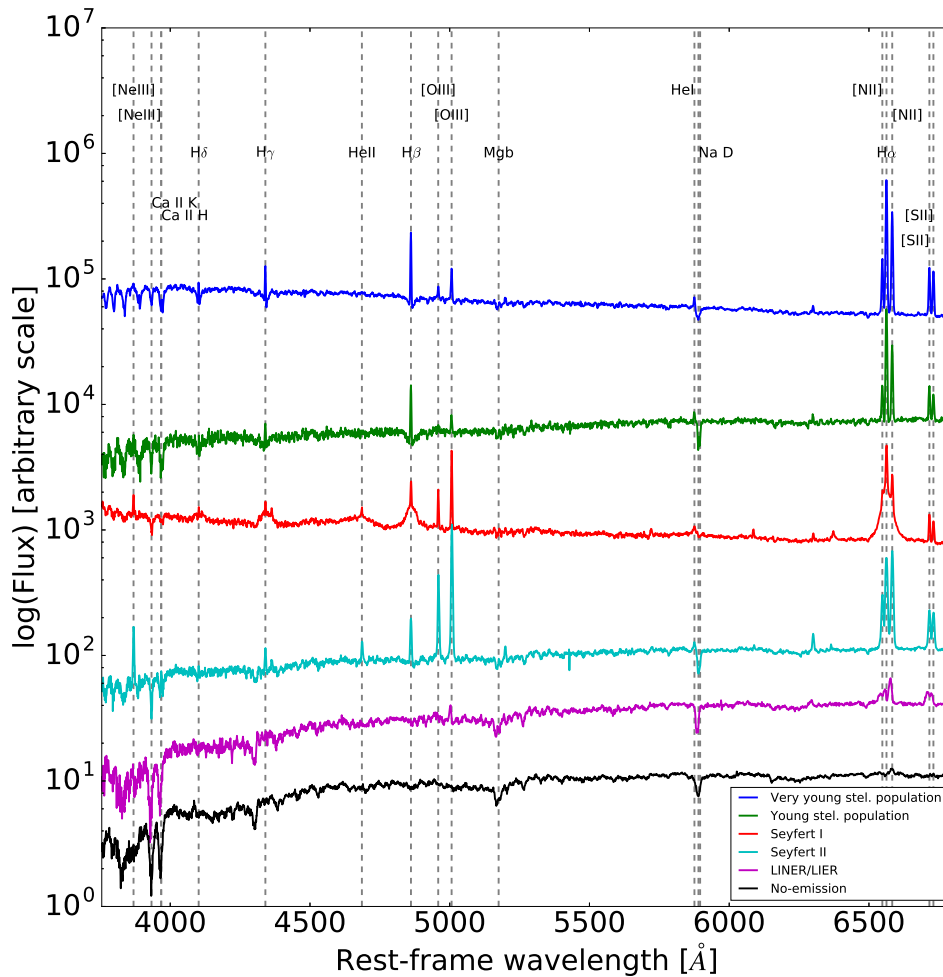


FIGURE 2.1: Example Sloan Digital Sky Survey galaxy spectra. From top to bottom: Typical spectrum of a galaxy with very young stellar population (dominated by O- and B-type stars) in dark blue. Representative spectra (in green) of a young stellar population (A-type stars). Note the strong Balmer emission lines present in the spectra of both of these star-forming galaxies. Shown in red is an archetypal spectra of a broad-line Seyfert 1 galaxy. Emphasis should be put on the presence of nonthermal continuum in the blue part of the spectra and the pronounced very high full-width-at-half-maximum ($\text{FWHM} > 800 \text{ km s}^{-1}$) of the $\text{H}\alpha$ line. Exemplary Seyfert 2 spectra (light blue). Attention should be paid to the notably strong $[\text{O III}]$ nebular lines. Illustrative low-ionization nuclear region or diffuse ionized gas (LIER) spectra (in magenta) with older stellar population. Quintessential spectra (in black) of an old-age quiescent galaxy. Vertical lines delineate the positions of some pronounced absorption and emission spectral lines.

old stars accumulated through the star-formation history of such systems dominates the spectral region around 4000 Å to form a break in the spectral continuum (e.g. Balogh et al., 1999, D4000). The larger fraction of light these galaxies emit is in the redder part of the spectrum. The remaining population of galaxies show the presence of significant interstellar medium in the form of ionized gas.

A small fraction of galaxies possess strong ionized-gas emission where the forbidden [O III] λ 5007 and [N II] λ 6583 lines are much stronger than the Balmer H β and H α respectively (Fig. 2.1 shown in light blue and red) which is a clear sign that the ISM in these systems is ionized from the presence of an AGN. So-called type I AGNs also display a second set of broad-line Balmer series emission-line components with distinctly high full-width-at-half-maximum (FWHM $> 800 \text{ km s}^{-1}$). Within these systems the broad-line emission is also accompanied by a featureless blue continuum, observed both in the optical and UV and therefore giving rise to the peculiar steep gradient from the blue to the red part of the spectrum, that arises from the emission of the accretion disk (i.e. optically thick accreting matter) around the supermassive blackhole powering the central active galaxy engine (e.g. Hubeny et al., 2001). In Fig. 2.1 we show examples of Seyfert type 2 and 1 AGNs which are generally the brightest, albeit rarest manifestation of AGN activity.

On the other hand, most systems with nebular emission have stronger H α and H β emission with respect to [N II] λ 6583 and [O III] λ 5007 (in green and dark blue in Fig. 2.1) and also display strong Balmer absorption lines and generally blue overall colors. Such features are indicative of the presence of ongoing star formation and nebular emission originating in H II regions surrounding the youngest and most massive stars ($< 20 \text{ Myr}$ Kennicutt, 1998a). If star formation is not sustained the spectra of such galaxies is expected to undergo passive evolution with massive stars and their associated H II regions quickly disappearing (e.g. Smith et al., 2002b; Sánchez et al., 2012).

A further subclass of emission-line galaxies show weaker nebular emission with abundant forbidden lines (in purple in Fig. 2.1). Large fraction of these galaxies have nebular emission falling in the so-called category of low ionization nuclear regions (Heckman, 1980, LINER), and occur generally in objects dominated by old- and intermediate-age stellar population as signalled for instance by the absence of strong Balmer absorption lines (e.g. Cid Fernandes et al., 2004). The origin of the LINER emission could be due to a number of sources (low-luminosity AGN, hot evolved stars, shocks) and is not fully understood (e.g. Ho, 2008, for a review).

Finally, not shown in Fig. 2.1 there exists another category of galaxy spectra (called transition or composite) where the nebular emission is due to a combination of either AGN activity and H II regions. Because of to the limited spatial resolution of our observations sometimes we can happen to observe both the central active regions of a galaxies and circum-nuclear star-forming regions.

2.2 Fitting Galaxy Spectra

For the purpose of this thesis we are interested in determining both the stellar population content (Chap. 5) and the presence of interstellar-gas absorption in our target galaxies (Chap. 4) on the one hand looking, in particular, for evidence of distinct stellar population with different kinematics and stellar properties (e.g. age and metallicity), and on the other hand, for the presence of in-flowing and out-flowing gas. Furthermore, we would need to place these results in the context of the type of nebular activity present in our target galaxies (e.g. finding evidence for outflows driven by AGN activity). To achieve these goals we will avail ourselves of dedicated tools allowing to fit the observed spectra and robustly separate their nebular and stellar components while also extracting the stellar and gas kinematics (pPXF, *GandALF*, or kinematic decomposition sections). For the purpose of fitting the stellar continuum we will need to use physically motivated models and specifically various sets of single-age stellar population models. On the other hand, nebular emission will be simply characterised by a series of Gaussian functions and, through the use of a diagnostic diagram (see, Sect. 2.2.4), the relative strength of the various emission lines will lead to classification of the observed nebular activity and to link it to the most likely source of ionization (e.g. AGN vs. star formation). Subtracting the nebular emission from the galaxy spectra will then allow to correctly interpret the strength of various stellar absorption lines and therefore infer the mean stellar population properties (see, Sect. 5.6). Finally, our fit to the stellar and nebular components could reveal the presence of additional interstellar absorption lines (e.g. due to neutral Sodium discussed in Sect. 2.2.7).

2.2.1 Simple Stellar Populations

The ability to conduct accurate inference on the properties of unresolved extra-galactic stellar population through integrated spectra is conditional on the accuracy of any adopted stellar or simple synthetic stellar population models. Most often, these models are constructed assuming

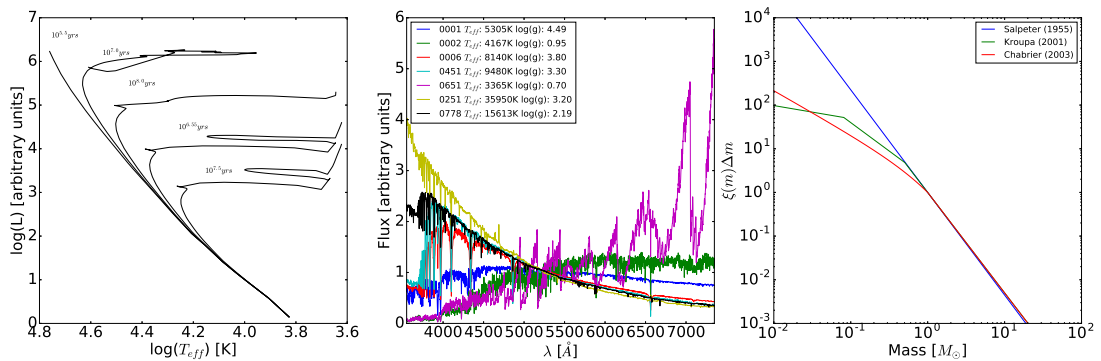


FIGURE 2.2: The basic ingredients in assembling a simple stellar population model. Left panel: Isochrones at a few different ages taken from Girardi et al. (2000). Middle panel: Example spectra from the Sánchez-Blázquez et al. (2006, MILES) empirical stellar library. Right panel: The most commonly used formulations of the initial mass function of Salpeter (1955), Kroupa (2001), and Chabrier (2003)

an underlying initial mass function (IMF), a set of stellar evolution tracks (isochrones), and a library of stellar spectra (e.g. Walcher et al., 2011; Conroy, 2013, for a reviews). Such techniques have been labeled as *isochrone synthesis* modelling.

First, a choice is made on the birth mass distribution of a stellar population. The IMF has been originally introduced by Salpeter (1955) as means by which one can describe the relative number of stars with respect to their mass. In its simplest most canonical form it is a power law with a given index (logarithmic slope, $\Gamma \sim 1.35$ for the case of a Salpeter (1955) IMF). However, prompted by some observations within our Galaxy some other forms have also been put forward (e.g. Kroupa, 2001; Chabrier, 2003). In particular, these later works report a deficiency in the number of stars with masses lesser than $1 M_{\odot}$ in the Solar neighbourhood in comparison to Salpeter IMF (right panel of Fig. 2.2). Even though, the universality and exact shape of the IMF have been recently questioned (e.g. Lyubenova et al., 2016; Sarzi et al., 2018b; Martín-Navarro et al., 2019) no strong clear observational evidence for a large systematic variation exists (Bastian et al., 2010, for a review).

Having selected a set of appropriate masses with which the population is generated the subsequent evolution of these stars is then taken into account. The life-cycle of stars is primarily dictated by their initial masses and to a lesser degree their underlying chemical composition. Stars of different masses can undergo through a variety of evolutionary phases (e.g. main sequence, thermally pulsating asymptotic giant branch, red giant branch, or helium burning). Contemporary stellar evolution theory allows for the adequate computation of evolutionary models (e.g. Hidalgo et al., 2018) that include all stellar evolutionary stages and major advances have been made in generating tables of theoretical stellar evolutionary tracks and isochrones (e.g. left panel

of Fig. 2.2) encompassing a wide range of masses and chemical compositions (e.g. Yi et al., 2001; Bressan et al., 2012; Choi et al., 2016).

Lastly, the stellar evolution output (e.g. T_{eff} , surface gravity, metallicity) needs to be converted to an observable spectral energy distribution (SED). This conversion is performed by drawing spectra from a stellar spectral library. Most generally, such libraries are based either on theoretical models of stellar atmospheres or have been compiled using a set of observed standard stars (empirical libraries). Theoretical spectral libraries (e.g. Westera et al., 2002; Munari et al., 2005, BaSeL and SYNTHE libraries, respectively) have the advantage of covering much larger ranges of stellar parameters and possess broad wavelength coverage. On the other hand, empirical libraries (e.g. Sánchez-Blázquez et al., 2006; Prugniel and Soubiran, 2001, MILES and ELODIE, respectively) are more limited in their coverage, but are not dependent on the intricate physics needed to perform the theoretical calculations.

With such complexity in the construction of simple single stellar population (SSP) models at hand perhaps it is surprising to find that most of the popular stellar population models achieve excellent spectral fit in the optical part of the spectra among most representative galaxies types. Furthermore, in most cases the subtleties in regards to the choice of stellar evolution tracks seem to not have a very pronounced effect on the ability of SSP models to represent real galaxy spectra (e.g. Chen et al. 2010a; Ge et al. 2019; however, also see Han and Han 2019).

In particular, in this thesis we would adopt three sets of stellar model “templates” in our analysis. In our Chapter 4 we have made extensive use of the Tremonti et al. (2004) models. To derive the properties of the stellar population in Chapter 5 we have taken advantage of the Thomas et al. (2011) models and to extract the kinematics and spectra we have used the the Medium resolution INT Library of Empirical Spectra (MILES) models.

2.2.1.1 The Tremonti et al. Stellar Population Synthesis Models

Tremonti et al. (2004) devised a set of stellar population templates covering the wavelength range between 3200 Å and 9300 Å with a resolution (FWHM of ~ 3 Å) specifically tailored to fitting spectra from the Sloan Digital Sky survey. The group adopted the Bruzual and Charlot (2003) simple stellar population models and refined them to capture more complicated multi-starburst star-formation history for ten different stellar populations of ages 0.005, 0.025, 0.1, 0.2, 0.6, 0.9, 1.4, 2.5, 5, and 10 Gyr) at three metallicities ($1/5$, 1, and $2.5 Z_{\odot}$).

2.2.1.2 The Medium resolution INT Library of Empirical Spectra Stellar Population Synthesis Models

The Medium resolution INT Library of Empirical Spectra (MILES) models Vazdekis et al. (2010); Falcón-Barroso et al. (2011); Vazdekis et al. (2012, 2015); Röck et al. (2016); Vazdekis et al. (2016) are a set of SSP models based on an assembly of empirical stellar libraries. At their most broad wavelength coverage the models span the wavelength range $\lambda\lambda 1680 - 50000$ Å and cover metallicities in between $-1.79 \leq [M/H] \leq +0.26$ with ages starting at 30 Myr. In the ultraviolet range some of these models utilise the Next Generation Spectral Library (Gregg et al., 2006). The optical part of the spectra is based on the core MILES observations with some extension by the Indo-U.S. stellar library (Valdes et al., 2004). Towards redder wavelengths and in particular in the CaT region these models draw on the CaT library spectra (Cenarro et al., 2001) with the further infrared extent making use of the Infrared Telescope Facility (IRTF) stellar library (Cushing et al., 2005; Rayner et al., 2009). Another advantage of these models stem from the inclusion of varying alpha-element-to-iron abundance ratio ($[\alpha/Fe]$) and the multiple different IMF they have been constructed with.

2.2.1.3 The Thomas et al. stellar population synthesis models

The simple stellar population models of Thomas et al. (2011) are based on a re-calibration of the MILES stellar library. The basis for their synthesis is the Maraston (2005) code. They cover an extended range of α - elemental abundance ($[\alpha/Fe] = -0.3, 0.0, 0.3, \text{ and } 0.5$ dex) and a multitude of further single elemental abundance for C, N, Na, Mg, Si, Ca, and Ti. A big novelty of these models is that they also provide the error estimates on all widely expected line-strength indices for each set of models and stellar parameters. For these models the Lick absorption-line strengths were estimated through an empirical calibration procedure involving the change of index strengths with respect to the corresponding provided stellar parameters (i.e. T_{eff} , $logg$, and $[Fe/H]$). The construction of such relations involves fitting a model (e.g. polynomial) and is therefore they are labelled “fitting functions”. Such functions allow for some interpolation into regions of the parameter space of stellar properties that might not be so well represented in the empirical stellar library. As an intrinsic advantage, a fitting function is assigned to each absorption-line index and, therefore, can be more easily utilised as an input for stellar synthesis codes. Moreover, by performing a set of Monte Carlo simulations where both the line-strength indices and stellar parameters are perturbed (according to the errors on the stellar parameters

as of the empirical library) the fitting functions can be re-evaluated and folded back into the stellar population synthesis code to put a constraint on the statistical errors on the population Lick absorption-line strengths. Then, by assuming the resultant population line-strength indices, ages, metallicities, and $[\alpha/Fe]$ ratios should be normally distributed and the associated spreads (standard deviations) in the obtained values are assumed to be informative of any accompanying formal statistical errors.

2.2.2 The Penalized Pixel-Fitting Method

Historically, Slipher (1914) first noticed that the line profiles of the pronounced absorption lines in Virgo Nebula (NGC 4594) imply the presence of some rotation. Later, drawing on technological developments more advanced techniques were proposed to quantify and measure the extent of such rotation (e.g. Simkin, 1974). Many different methods have been developed to extract the line-of-sight velocity distribution (LOSVD) of the stellar content of galaxies from an observed spectra (e.g. Tonry and Davis, 1979, 1981; Rix and White, 1992a) with some of these methods also developing the ability to simultaneously extract the stellar population content of the target galaxies.

Throughout this work we have used the Cappellari and Emsellem (2004); Cappellari (2017) Penalized Pixel-Fitting (pPXF) to match the galaxy stellar continuum and estimate the LOSVD, where the latter is described in terms of a velocity, velocity dispersion, and the higher “moment” h_3 and h_4 coefficients (i.e. the Gauss-Hermite parametrization van der Marel and Franx (1993)). This method draws on the comparison in pixel space of a linearly combined set of selected “templates” that are subsequently convolved with the model LOSVD to best match the observed galaxy spectrum. The linear combination of the “templates” is built through the Bounded-Variables Least Squares (BVLS) algorithm (Lawson and Hanson, 1974) and the rest of the non-linear parameters are inferred by the widely utilized *MPFIT* library (Markwardt, 2009a). To combat any potential imperfections in either the sky subtraction or spectral calibration pPXF allows for the addition of multiplicative Legendre polynomials of a selected order. Even though existing state-of-the-art spectral stellar libraries and population synthesis models provide a satisfactory basis to facilitate undergoing investigations into the properties of galaxies they are not devoid of all flaws (e.g. Ge et al., 2019; Conroy, 2013, see for a review). To that extent, pPXF also allows for the insertion of additive Legendre polynomials of a given order. These act to change the strength of individual absorption lines within the constructed model spectrum

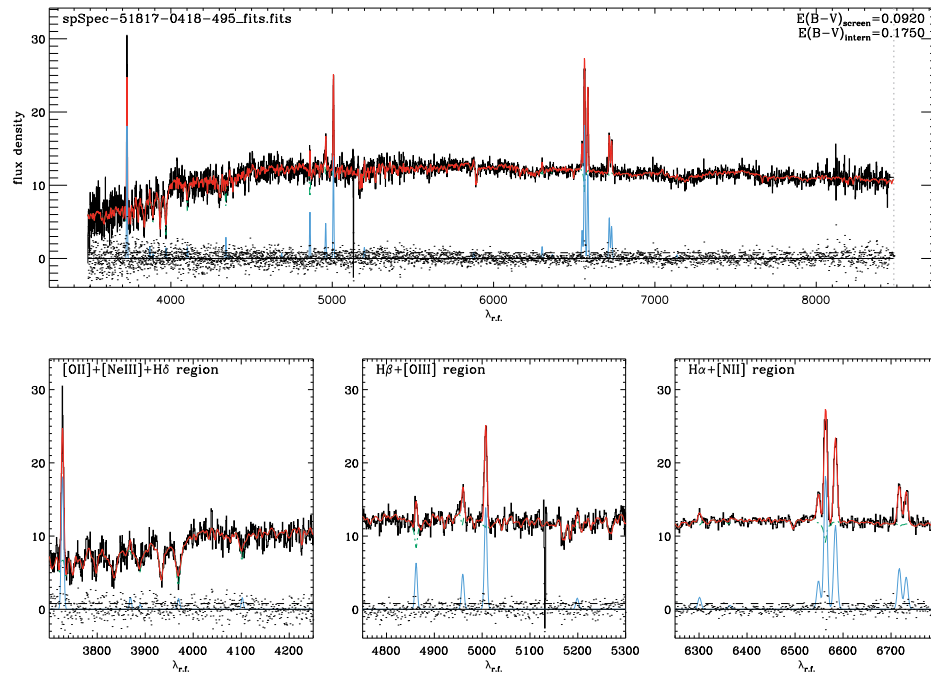


FIGURE 2.3: An example *GandALF* fit to Sloan Digital Sky Survey spectra. Top panel: The SDSS spectrum in black with the best-fitting model including emission lines in red and to the stellar continuum in dash-dotted green. Residuals are shown as black points. All fitted emission lines are displayed in blue. The horizontal dashed line designates the one sigma level of the residual. Bottom panels: Zoom-in sections of the spectra around regions of interest around the stronger emission lines.

and, therefore, limit the potential mismatch (“template mismatch”) between the selected set of “templates” and the observed spectra.

Even though pPXF allows for multiple component LOSVD assigned to different stellar population mix for the purpose of separating counter-rotating stellar populations in Chapter 5 a more dedicated routine was adopted (see section 5.5.2).

2.2.3 The Gas and Absorption Line Fitting Algorithm

To adequately account for any emission lines present in the spectra we have used the Gas AND emission Line Fitting (*GandALF*) Sarzi et al. (2006) method. Figure 2.3 shows an example *GandALF* fit to a spectra. The procedure adopts the LOSVD extracted by pPXF, but also constructs a further set of Gaussian emission-line “templates” in addition to the stellar “templates”. Single Gaussian is used in the case of single emission lines (e.g. [HeI] $\lambda 5875.60$). For more complicated emission-line species (i.e. doublets or the entire Balmer series) a set of Gaussians is constructed to reflect the intrinsic relative strength of the lines constrained by atomic physics.

Next, similar to pPXF the stellar “templates” are broadened by a prior extracted LOSVD and linearly combined utilizing BVLS to simultaneously find the best combination of emission-line and stellar, convolved with the given LOSVD, “templates” while iteratively (non-linearly using *MPFIT*) seeking to infer the gaseous kinematics (i.e. the velocities and velocity dispersions of the Gaussian line profiles) that best match the observed spectra. With such a robust methodology, provided satisfactory spectral calibration, quality of the fit, and knowledge of the foreground Galactic extinction, *GandALF* can also successfully recover the extent by which both the stellar continuum and gaseous emission are modulated by the host galaxy dust content (Oh et al., 2011). *GandALF* includes a model for two simple dust screen components, reflecting the host galaxy reddening. The Calzetti et al. (2000) dust model is adopted for both components with one of them affecting the entirety of the spectrum, while the other only the nebular emission. Corresponding best-fitting $E(B - V)$ values are non-linearly solved for simultaneously with the emission-line kinematics. Such a process, in comparison to simply masking the emission lines, improves the overall quality of the fit. Having a model for each emission line allows us to safely place our spectra on the BPT diagnostic diagram and last, but not least, is informative of any interstellar dust contents.

2.2.4 The Emission-line Diagnostic Diagram

Some galaxies display a myriad of emission lines. These nebular lines originate from the transitions of excited ions and atoms within the interstellar medium. They encode valuable information for the physical conditions (e.g. temperature, pressure, ion abundances) of their gas source. The most relevant sources of gas excitation in the context of galactic ISM includes the ionization ultra-violet radiation released by young massive stars born in a recent star-forming episode, active galactic nuclei, and shocks (Osterbrock and Ferland, 2006, for a detailed treatment).

Stars are born from interstellar matter in cloud complexes that undergo gravitational collapse in a process that involves the interplay of complex macro- and micro- physics. A non-negligible fraction of these stars possess high masses ($\gtrsim 17M_{\odot}$), have very high surface temperatures ($> 25 \times 10^4 K$) and, therefore, produce copious amounts of ultraviolet photons (for a review see McKee and Ostriker, 2007). These photons transfer energy to the surrounding ISM and conspire to create a region, where different atomic processes lead to the generation of ionized-gas emission, deemed as a nebula. Within such regions ubiquitous in Hydrogen (H) the photons

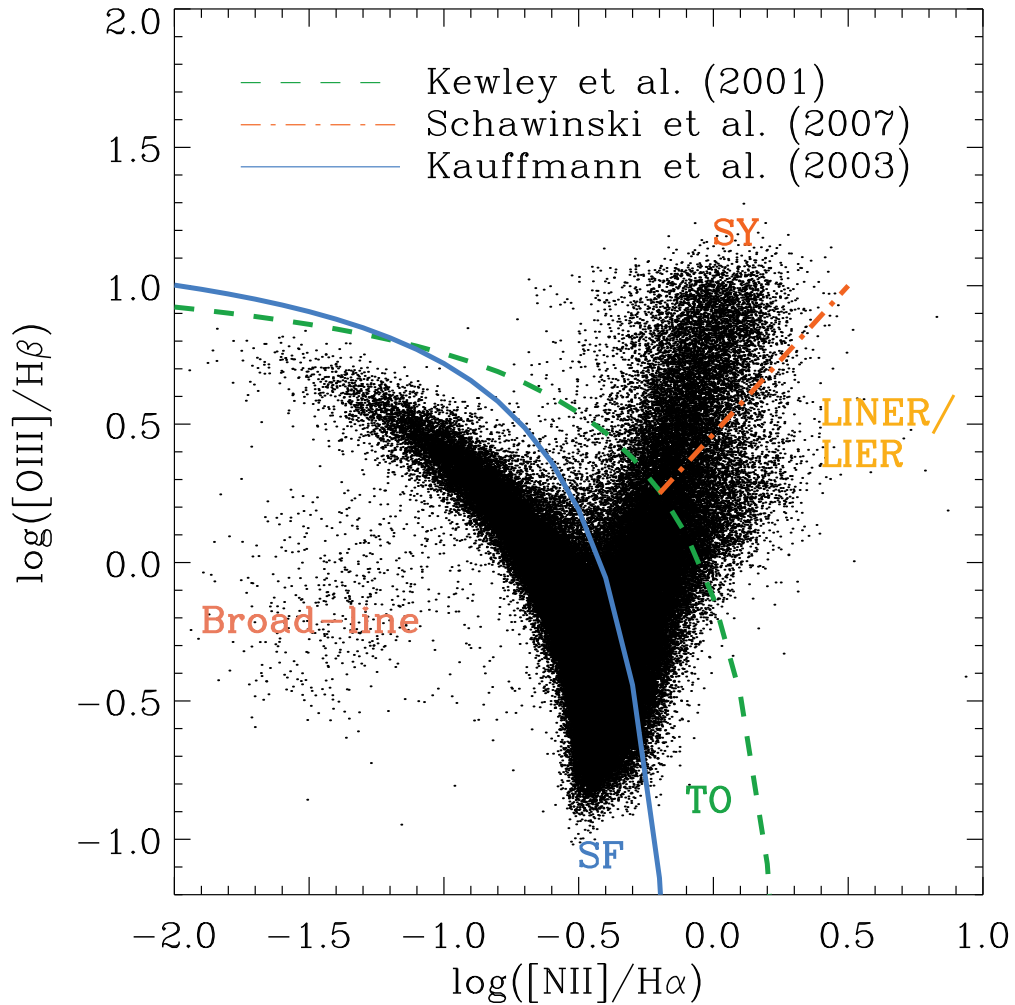


FIGURE 2.4: The most commonly adopted $[\text{N II}]\lambda 6583/\text{H}\alpha$ versus $[\text{O III}]\lambda 5007/\text{H}\beta$ optical (BPT) diagnostic diagram for the Sloan Digital Sky Survey galaxies with detected nebular emission (i.e. with $A/N > 3$ in all four lines) analysed as part of the Oh et al. (2011) value-added catalog. The dashed green, solid blue, and dash-dotted orange lines show the boundaries between objects with star-forming (SF), composite(transit, TO), Seyfert, and LINER/LIER emission from Kewley et al. (2001), Kauffmann et al. (2003), and Schawinski et al. (2007), respectively. Notice a cloud of points rightwards of the star-forming abundance sequence. These objects were properly treated in Oh et al. (2015) where they were refit including a broad-line component to the Balmer emission lines.

of energies exceeding the H ionization potential (13.6 eV) get absorbed with all residual energy passed to the freshly unbound photoelectron. Through electron-electron or electron-ion collisions the nebula strives to redistribute the newly acquired energy and retain a Maxwellian velocity distribution with a particular equilibrium temperature. These collisions are in the root of some of the nebula's most prominent emission lines. Historically, most of these lines of gaseous nebulae were labeled as “forbidden” (i.e. they occur even despite the parity selection rule). They are emitted by collisionally excited ions (e.g. O^+ , O^{++} , and N^+) that may not be highly abundant, but have low energy levels that are quite close to the ground one (i.e. low-lying energy

levels). Similarly, photoionization and electron recapture compete to balance. The number of high energy photons, capable of photoionization, is proportional to the temperature and dependent on the shape (hardness) of the spectral energy distribution given by the excitation source. The process of recapturing an electron can result in an excited state. These excited states then subsequently decay to lower and lower energy levels eventually reaching ground state in a process called recombination. Each electron jump from a higher level to a lower one involves the emission of a photon with a specific energy leading to the production of the well-known H I Balmer and Paschen emission line series. In the case of optically thin medium (low density limit, Case B recombination) the intensities of these lines can be directly computed from atomic physics assuming an electron density and temperatures (Osterbrock and Ferland, 2006). Massive (or hot) stars or regions of star formation are not the only possible genesis of ionization in regards to extra-galactic objects. Another means by which the gas reservoir could gain energy and get excited is the presence of an active galactic nucleus. Ongoing accretion onto the SMBH should result in the emission of copious amounts of very high energy photons extending from the UV to X-rays surpassing the energy budget available in star-forming regions and other gaseous nebulae. Even though the exact spectral shape of the ionizing source or the geometry of the system of emitters in that particular case is still under debate observations (e.g. Kraemer and Crenshaw, 2000; Kraemer et al., 2009) and theoretical modelling (e.g. Kallman and Bautista, 2001) have demonstrated that in the vicinity of an AGN, collisionally excited forbidden emission lines need be boosted as the high energy output would keep very high electron temperature with abundance of ionization photons (e.g. Koratkar, 1999; Groves, 2007, for reviews). Moreover, either slow (Allen et al., 2008) or fast shocks (Dopita et al., 2018) could also serve as excitation for the ISM resulting in the emission of a multitude of nebular lines. The Baldwin–Phillips–Terlevich (BPT) (Baldwin et al., 1981) diagrams are one of the most widely adopted excitation diagnostic diagrams. One particular variation is based on the ratios of the strong ([O III] λ 5007, H β , H α , and [N II] λ 6583) emission lines. These were chosen such that their wavelengths are in the optical spectral domain for the nearby Universe and the lines that define the ratios [O III] λ 5007 and H β against [N II] λ 6583 and H α are close enough in wavelength such that no correction due to reddening need be applied. Generally, these ionization lines of different species trace particular zones of an underlying nebula, owing to their different ionization potentials. In particular, for a nebula of given elemental abundance arising from either an assembly of hot stars or a star-forming region the number of photons capable of ionizing Oxygen depends on ratio of the local ionizing photon flux and the local hydrogen density (i.e. ionization parameter) and the effective temperature of the ionizing source as to a first-order approximation the spectral

energy distribution of most stars is that of a blackbody. Therefore, the fraction of single ionized Oxygen ions is expected to decrease with decreasing ionization factor and source temperature. Consequently, the size of the zone where double ionized Oxygen ions (O^{++}) could exist would also shrink yielding lower total [O III] $\lambda 5007$ emission.

On the other hand, for a source with identical effective temperature, a decrease in the ionization factor would lead to the formation of a progressively larger zone where singly ionized species such as N^+ would be ubiquitously found, until it completely overlaps with the already present ionized H^+ zone. Furthermore, naturally, an increase in the effective temperature of the ionization source would raise the fraction of available higher-energy photons and would act to enlarge the size of the partially ionized zone (Veilleux and Osterbrock, 1987). It has also been argued extensively that the effective temperature of the ionizing source of a nebulae originating from regions of star-formation does not vary significantly, but instead there exists an observed anti-correlation between the ionization parameter and stellar metallicity of an underlying ionization stellar population. The stellar atmospheres of stars of lower metallicities would show less pronounced line absorption in conjunction to having higher ionization parameter. Therefore, an increase in ultraviolet photons would lead to the formation of a larger O^{++} zone and a smaller N^+ one. Such a change in the ionizing structure of the nebula would occur at high ionization factor values and, therefore, lower than solar stellar atmospheric metallicities pushing the ratio of [O III] $\lambda 5007/H\beta$ to increase and, on the contrary, [N II] $\lambda 6583/H\alpha$ to decrease. At low ionization factors these line ratios change the opposite way (Evans and Dopita, 1985; Dopita and Evans, 1986).

In contrast to nebulae from hot young stars within star-forming galaxies, nebulae originating from an ionizing source with more ubiquitous X-ray photons (e.g. “harder” sources like AGN) possess a very high ionization area in proximity to the source and a much larger zone of partial ionization, as highly energetic photons can penetrate somewhat deep into any nearby medium. Within this partially ionized area the ionization status of different atoms and ions can vary. Such regions would generally also hold a fraction of single ionized N (i.e. N^+), but is not the dominant Nitrogen state, and a portion of hot free electrons. Overall, with decreasing ionization factor a high-ionization line such as [O III] $\lambda 5007$ would decrease in strength, whereas a lower-ionization line (e.g. [N II] $\lambda 6583$) increases in strength.

The intensities of the [N II] $\lambda 6583$ lines within partially ionized regions, however, are expected to be larger with respect to $H\alpha$ in the case of AGNs in comparison to star-forming galaxies as

collisional excitation in the presence of such hot free electrons boosts [N II] $\lambda 6583$ emission in nebulae, where such extended partly ionized zones are present. Furthermore, enhancement in the strength of the [N II] $\lambda 6583$ line strength has also been traced to abnormally high Nitrogen elemental abundances within the central regions of galaxies with an AGN (e.g. Hamann and Ferland, 1999, for a review). On the other hand, double ionized O^{++} ions are produced in the presence of high energy UV photons and are expected to be substantially present predominantly in the very inner regions of the nebulae close to the ionization source. There, the relatively larger numbers of photons of the “hard” ionization source that can double ionize Oxygen would also generally conspire to bring the [O III] $\lambda 5007/H\beta$ ratio in the case of AGN comparable to the one of highly excited star-forming regions (i.e. either with higher ionization factors or higher effective source temperature or both) (Veilleux and Osterbrock, 1987).

Therefore, within the BPT diagram the [O III] $\lambda 5007/H\beta$ ratio is a good indicator for the mean level of ionization and the temperature within the emitting medium, whereas [N II] $\lambda 6583/H\alpha$ is also quite sensitive to its metallicity. As previously noted, the fact that most local galaxies with an AGN with only some very small exceptions appear to show solar-to-supersolar ISM central metallicities (e.g. Groves et al., 2006) further enhances the separation between star-forming and other (like AGN) ionization mechanisms (Kewley et al., 2019, for a review). An example of such a BPT diagram for all of the Oh et al. (2011) value-added catalogue of SDSS galaxies is shown in Fig. 2.4. Using empirical and theoretical considerations the diagram can be shown to contain at least four separate regions.

On the basis of a large sample of SDSS spectra Kauffmann et al. (2003) derived an empirical relation (blue line in Fig. 2.4) that isolate galaxies where the ionization of the ISM gas reservoir originates purely from star-formation. Within this demarcation the galaxies form a tight sequence (dubbed the *star-forming abundance sequence*, SF). Its position and extent (Kewley et al., 2013) on the BPT diagram is primarily dictated by the expected gradients and spread in metallicity of the ISM contents of the host galaxies (e.g. Belfiore et al., 2017; D’Eugenio et al., 2018). The region bounded by the Kauffmann et al. (2003) and the theoretically derived *maximum starburst line* of Kewley et al. (2001) (green dashed line in Fig. 2.4) is commonly referred to as the *composite* (CO) or *transition* region (TO). It sits on the root of the other “wing” of this BPT diagram dubbed the *mixing sequence*. The section demarcated by the Kewley et al. (2001) and Schawinski et al. (2007) (orange dashed-dotted line in Fig. 2.4) lines hosts galaxies with LINER or its non-AGN equivalent (LIER). Most commonly such emission is ascribed to either a low ionization nuclear region associated to low-luminosity AGN (e.g. Hernández-García et al.,

2016; Ho, 2008, for a review), the substantial residence of hot evolved stars (e.g. Sarzi et al., 2010; Singh et al., 2013; Belfiore et al., 2016, LIER), or shocks (Rich et al., 2014, 2015; Alatalo et al., 2016). All systems laying above the Schawinski et al. (2007) and Kewley et al. (2001) distinction lines are most likely Seyfert galaxies (SY). We would also like to note the disconnected cloud of points sitting to the left of the star-forming sequence. These systems show anomalous emission line ratios due to an over-imposed broad-line region (Oh et al., 2015) a signature for an underlying AGN.

2.2.5 Stellar Population Properties via Line-strength Fitting

Obtaining the stellar population properties on the basis of integrated galaxy spectra has been a long-lasting endeavour in extra-galactic astrophysics. Many different methods have been developed to recover a given host galaxy stellar population star-formation history (e.g. equivalent simple stellar population age) and chemical properties (e.g. metallicity and alpha-elemental abundance). Many different methods have been developed for this purpose ranging from those that aim to estimate a mass or luminosity-weighted stellar age, metallicity or other chemical properties (e.g. the abundance of alpha elements) to those that attempt to reconstruct star-formation or chemical evolution history. These techniques could draw, either from the fit to the entire spectrum (e.g. Ocvirk et al., 2006; Cappellari, 2017; Wilkinson et al., 2017), by interpreting the strength of a selected set of absorption lines (e.g. Worthey et al., 1994), or fitting only broadband data (e.g. Leja et al., 2017).

The spectral decomposition (see Sect. 2.2.6) we have adopted in modelling the individual contribution of each kinematic component of our galaxies with counter-rotation allows also to obtain for each component a model consisting of the best linear combination of SSP templates. In this case, the most robust way to estimate the properties of the two counter-rotating stellar populations is to draw from the observed line strengths of these best-fitting templates in order to obtain luminosity weighted average age, metallicity ($[Z/H]$) and alpha-element abundance ($[\alpha/Fe]$). More specifically we have applied the methodology of Morelli et al. (2008) further improved in Coccato et al. (2011) where the observed line strengths are matched to the ones obtained by extrapolation of a fine grid of SSP models. This permits us to infer the age, metallicity, and alpha-element abundance. The method itself is based on Mehlert et al. (2003) where the best-fitting combination of stellar population parameters is searched for iteratively on a grid. This

grid is further refined by linearly interpolating between the prior points of the stellar population parameters and the corresponding model line strengths until the model line strength values match the observed ones within the measurement errors.

2.2.6 The Spectral Decomposition Technique

The spectral decomposition technique (Cocato et al., 2011) allows for the robust separation of any spectrum consisting of two pronouncedly distinct (e.g. counter-rotating) kinematic components. This method disentangles the contribution of each component to the spectra by taking advantage of the characteristic spectral imprint (e.g., asymmetric or double trough line profiles) such a spectrum displays. This decomposition technique is based on pPXF, but instead of using the Gauss-Hermite parametrization for the LOSVD it uses two separate Gaussian line-of-sight velocity distribution functions for both stellar components. Naturally, it also separately constructs two unique sets of linearly (using BVLS) combined stellar “templates” that get convolved with their corresponding Gaussian LOSVDs. Their parameters (velocity and velocity dispersion) and the light fraction contributed by each of the components are also non-linearly optimized for using the standard *MPFIT* library. Because of the complexity of this fitting approach, it is common practice to normalize both the galaxy spectra and templates to unity to obtain the fractional contribution to the flux within a given wavelength range of both components in terms of a single parameter instead of assigning two separate light fraction contribution parameters. Identical to pPXF, multiplicative Legendre polynomials of a pre-selected order account for any potential imperfections in the calibration of the spectra and its modulation by the presence of dust. Although such a fitting procedure is robust enough, it is still necessary to test the impact of varying the initial guesses for both kinematic components (i.e. their velocities, velocity dispersions and light fraction contributions) to ensure the procedure has converged to a global minimum as opposed to a local one.

2.2.7 Interstellar Sodium and Absorption-line Profile Fitting

Optical absorption-line spectroscopy can be used as an effective means by which to probe the various phases of the interstellar medium (ISM). In particular, the Na I $\lambda\lambda 5890, 5895$ Sodium absorption doublet in the optical (NaD) has been shown to trace its warm neutral component (e.g. Heckman et al., 2000) in external galaxies. It stems from Na in neutral state and because

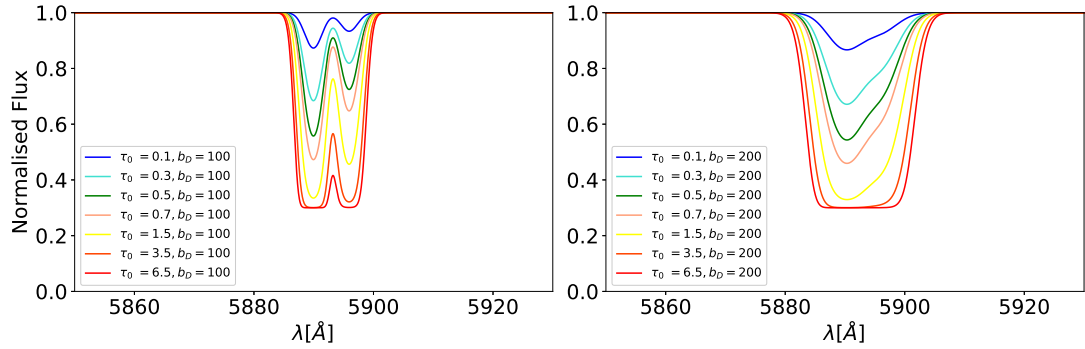


FIGURE 2.5: The changes in the shape of the Sato et al. (2006) model for the NaD absorption line spectral profile used in our analysis with respect to the given input parameters.

Sodium has a relatively low ionization potential (5.13908 eV) the presence of the NaD absorption feature indicates that cold to warm gas resides in the line-of-sight between an illuminating source and the observer. Historically, within our Galaxy Heger (1919) first observed an extra set of NaD lines towards two stars and proposed that they could originate in the ISM. Drawing from atomic physics, this feature arises from the an electron transitioning from either the $P_{1/2}^2$ or $P_{3/2}^2$ states to the $S_{1/2}^2$ state. Furthermore, the ratios of the optical depths for both transitions, measured by the centroids of the lines, has been theoretically shown to be 1 : 2 for the the blue-er and red-er line in the doublet respectively (Arav et al., 1999; Morton, 2003).

Most generally, absorption excess in comparison to the best-fitting stellar continuum model in the NaD absorption feature of external galaxies would capture a multitude of overlapping clouds absorbing light from the extended stellar background light source. The line profile of such an excess NaD absorption feature would be a function of various different factors (e.g. the geometry of the cloud complex, its line-of-sight velocity distribution, or the thermodynamic state of the gas). To simplify the very complex nature of the problem of fitting such excess absorption we work under the assumption that these individual clouds are thermalised (i.e. both their constituents and as an assembly obey the Maxwellian velocity distribution), that the fraction they effectively cumulatively cover the extended background light source (i.e. the covering fraction) is itself independent of the clouds' velocities, and that the individual NaD absorption lines generated by each of the clouds are not saturated. In such a case the excess NaD absorption profile (Fig. 2.5) after normalization by the best-fitting model stellar continuum is given by Sato et al. (2009):

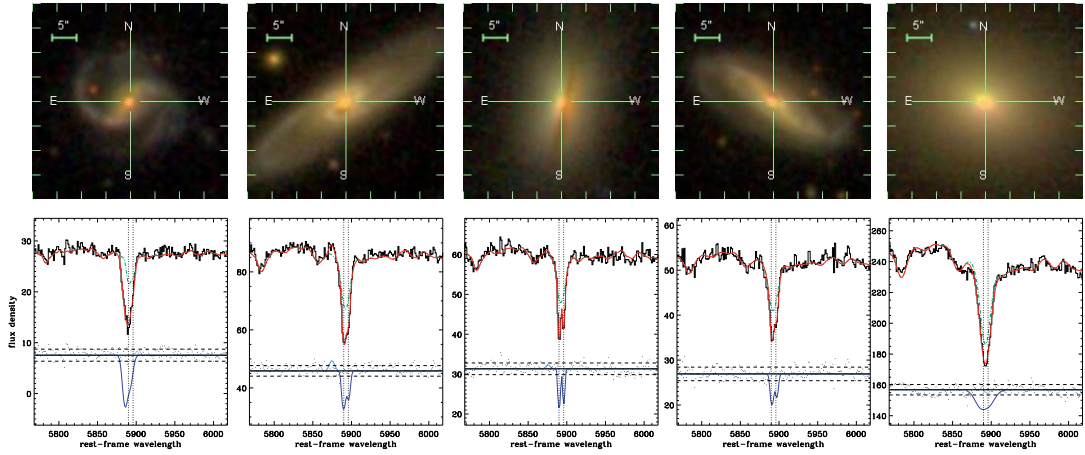


FIGURE 2.6: SDSS colour images (top row) and example fits for the NaD region (bottom row) for five of our galaxies. Lower panel: The best-fitting model is represented in red. The contribution of the best-fitting stellar continuum and nebular emission is shown in green dashed-dotted and continuous, correspondingly. The black dots represent the residual of the fit and the horizontal dashed lines its associated standard deviation. The vertical dotted lines mark the rest-frame position of the NaD lines and the best-fitting excess NaD profile is displayed in blue. Adopted from Sarzi et al. (2016).

$$I(\lambda) = 1 - C_f \left\{ 1 - \exp \left[- 2\tau_0 e^{-(\lambda - \lambda_{\text{blue}})^2 / (\lambda_{\text{blue}} b/c)^2} - \tau_0 e^{-(\lambda - \lambda_{\text{red}})^2 / (\lambda_{\text{red}} b/c)^2} \right] \right\} \quad (2.1)$$

where C_f is the covering factor of the absorbing cloud complex, τ_0 is the optical depth at the centre of the red NaD line, λ_{blue} , λ_{red} are the red- or blue- shifted wavelengths of the two NaD lines, and $b_D = \sqrt{2}\sigma_{\text{NaD}}$ is the Doppler parameter. The red- or blue- shifted central-line values and b_D yield the quantity of interest here, namely the velocity V_{NaD} and the width σ_{NaD} of the NaD lines. Figure 2.5 shows the line profile resulting from the change of both optical depth and covering fraction for a fixed V_{NaD} and width σ_{NaD} .

Within this framework neutral interstellar material (as traced by the excess NaD profile) that is been entrained within an outflow, observed against the stellar background of the host galaxy as part of a multiphase galactic wind (e.g. Rupke and Veilleux, 2013; Cazzoli et al., 2016) would display negative velocity with respect to the host galaxy systemic one (e.g. Rupke et al., 2005a; Chen et al., 2010b). Conversely, red-shifted excess NaD profile would be indicative of inflowing material (e.g. Rubin, 2017). As outlined before we assume a single velocity distribution for the absorbing gas clouds along the line of sight. However, this may not necessarily correctly reflect galaxies where both a significant ‘‘systemic’’ population of absorbers, settled in the galaxy plane, and a population of outflowing clouds coexist. In particular, this can be most problematic when looking at objects from an intermediate inclination angle (Chen et al., 2010b). While such an approach would tend to underestimate the outflow velocity in galaxies that are viewed from

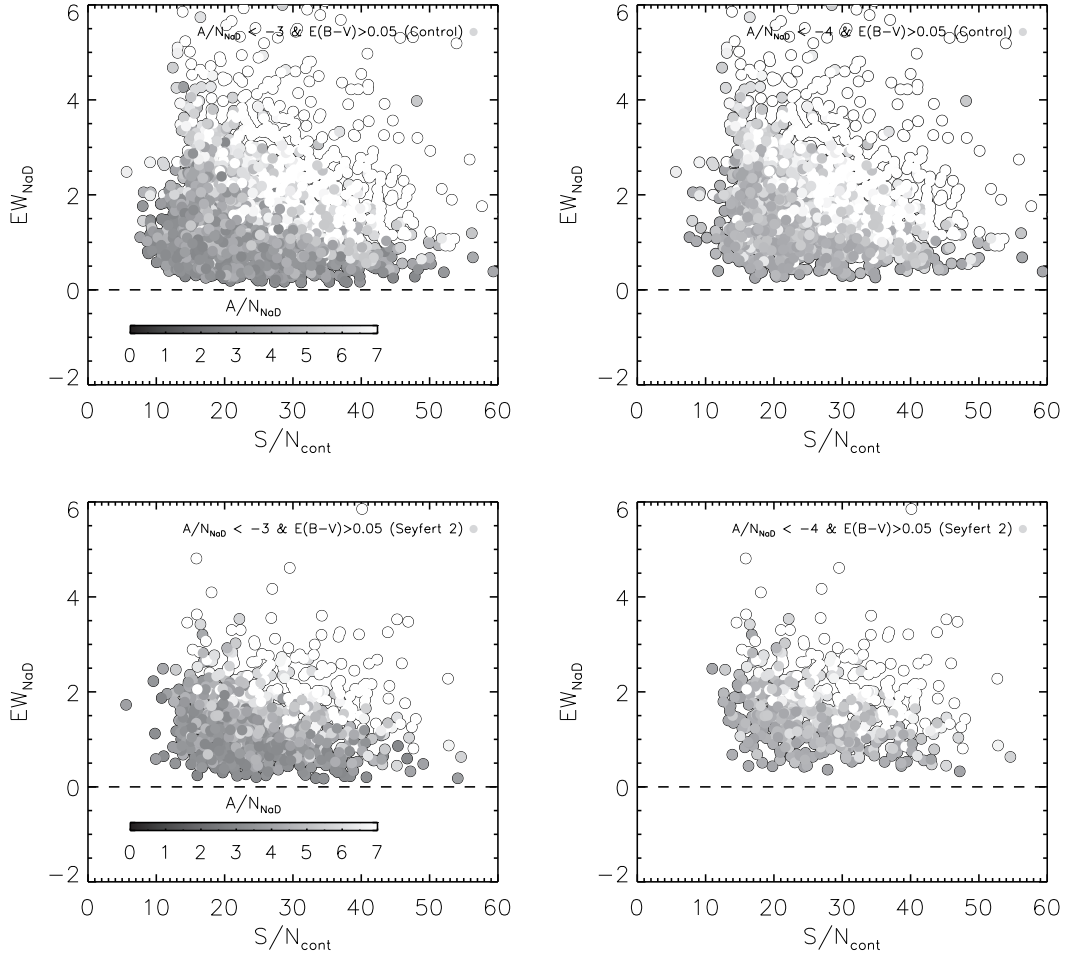


FIGURE 2.7: The signal-to-statistical-noise (S/SN) in the stellar continuum (S/N_{cont}) against equivalent width of the Sodium NaD lines (EW_{NaD}) gray-coded by the amplitude-to-noise of the Sodium lines (A/N_{NaD}) for our SDSS samples (see Chap. 4). Top left panel: with imposed A/N_{NaD} threshold limit of $A/N_{NaD} > 3$ and $E(B-V) > 0.05$ for the control sample. Top right panel: with imposed A/N_{NaD} threshold limit of $A/N_{NaD} > 4$ and $E(B-V) > 0.05$ as of our reported analysis for the control sample (see Chap. 4.2.2). Bottom left panel: with imposed A/N_{NaD} threshold limit of $-A/N_{NaD} > 3$ and $E(B-V) > 0.05$ for the Seyfert 2 sample (see Chap. 4.2.1). Bottom right panel: with imposed A/N_{NaD} threshold limit of $A/N_{NaD} > 4$ and $E(B-V) > 0.05$ as of our reported analysis for the Seyfert sample.

intermediate inclination angles, using a single NaD velocity profile will suffice to capture the kinematic behavior of the cold gas across a large sample of galaxies and should be robust enough to estimate and compare the fractions of objects that could display gas outflows in this work.

To define a detection threshold for an NaD absorption excess, we have run our NaD fitting procedure through a large number of simulated spectra, obtained by adding random noise and an artificial NaD absorption profile to the best-fitting stellar population model. By exploring how well the input NaD parameters and, in particular, V_{NaD} and σ_{NaD} , are recovered as a function of the observed amplitude-to-noise (A/N), A/N_{NaD} ratio between the peak amplitude of the NaD

profile and the input noise level, we have concluded that at least $A/N_{\text{NaD}} > 4$ values are required to secure unbiased V_{NaD} and σ_{NaD} measurements. Still in keeping with the emission-line results of Sarzi et al. (2006), we note that our $A/N_{\text{NaD}} > 4$ threshold translates into a lower detection limit for the equivalent width (EW) of the NaD lines at any given signal-to-residual-noise ratio in the stellar continuum of the SDSS spectra used in Chapter 4 (S/rN, where residuals are taken from our *GandALF* fits). For our sample, the mean signal-to-residual noise (S/rN) is ~ 26 , so that the median EW of the detected NaD interstellar lines is $\sim 1.8 \text{ \AA}$ with a scatter of $\sim 0.8 \text{ \AA}$ (Fig. 2.7). For an illustration of the typical quality of our fits to the NaD line profile we refer the reader to Fig. 2.6, which shows SDSS spectra of a quality that is also typical of the sample objects of this study.

Chapter 3

Data

3.1 The Sloan Digital Sky Survey

3.1.1 Overview

The Sloan Digital Sky Survey (York et al., 2000b) is a consortia of large surveys carried out with a dedicated 2.5 m telescope at the Apache Point Observatory (APO) in New Mexico (Gunn et al., 2006). It provides both imaging and spectroscopy. Its data products are made available in multiple phases and delivered in a self-consistent sequence of data releases. The most current data release (Aguado et al., 2019, DR15) has cataloged and identified more than 200,000,000 unique galaxy sources.

3.1.2 Imaging

Since its beginning the survey has covered more than 14,000 square degrees¹ in five bands (*ugriz*) (Fukugita et al., 1996; Smith et al., 2002a). As part of the survey images are taken with the Sloan Digital Sky Survey Photometric Camera (Gunn et al., 1998) and reduced and calibrated using an automated dedicated pipeline (Lupton et al., 2001; Pier et al., 2003; Padmanabhan et al., 2008) that also detect objects and extract their photometric properties. The measurements undergo quality assessments (e.g. Ivezić et al., 2004) and are released as science-ready data products. Most relevant for our work is the image cutout service (Nieto-Santisteban et al., 2004) that we have utilized to recover the color-composite images presented afterwards.

¹<https://www.sdss.org/dr15/scope/>

3.1.3 Fiber Spectroscopy

The Sloan Digital Sky Survey telescope is equipped with two multi-object fiber-fed spectrographs. Each fiber is attached to a specially prepared plug plate where the holes correspond to the expected sky position of a pre-selected object. As part of the Legacy spectral survey they obtained more than 1.5 million spectra of pre-selected on the basis of imaging galaxies as part of: magnitude-limited sample of galaxies (Strauss et al., 2002, Main Legacy SDSS sample), near-volume-limited sample of galaxies (Eisenstein et al., 2001, Luminous Red Galaxies), and a magnitude-limited sample of quasars (Richards et al., 2002, Quasar). After Data Release 9 the galaxy component of the spectroscopy survey was also expanded to higher redshifts with a sample of galaxies observed through the (e)BOSS survey (Dawson et al., 2013, 2016). The spectra of the Legacy survey was fed to the spectrograph through 640 fibers. Each fiber had a diameter of $3''$ that subsequently gets split into two channels by a beamsplitter ($\lambda < 6000 \text{ \AA}$ and $\lambda > 6000 \text{ \AA}$, red and blue, respectively) and gets converted by a grism to a spectra that consequently is reconstructed to span from 3800 \AA to 9200 \AA sampled with a fixed step of 69 km s^{-1} and with instrumental resolution ranging from 1850 to 2200 from the red to the blue end. For the following (e)BOSS survey the spectrographs were improved with a new set of grisms and cameras and fed through 1000 fibers with smaller diameter of $2''$. There the recovered spectra wavelength range was also larger ($3650\text{-}10,400 \text{ \AA}$) with resolution of 1560-2270 in the blue channel and 1850-2650 in the red channel (Smee et al., 2013). The spectra for Data Release 7 was re-reduced, re-calibrated, and re-measured with re-run with the *spectro2d* and *spectro1d* pipelines (Stoughton et al., 2002). The spectra for the (e)BOSS survey were re-reduced and re-calibrated again adopting *spectro2d*, but all the classification and emission- and absorption-line measurements were done using the methods outlined in Bolton et al. (2012).

3.1.4 Imaging Catalogues: Galaxy Zoo

Galaxy Zoo (Lintott et al., 2008) was a large “citizen science” project that tasked the general public to morphologically classify SDSS objects flagged as galaxies. The final science data product of the project is a catalog containing nearly 900,000 galaxies split into early-type, late-type, or unknown (Lintott et al., 2011). The objects to classify were pre-selected by the photometric pipeline (Lupton et al., 2001) and processed into red-green-blue images (Lupton et al., 2004) with the SDSS g, r, and i filters as a basis that provides wide dynamic range and facilitate the identification of faint galaxy features. The volunteers were prompted to morphologically

asses the galaxies into elliptical, clockwise/Z-wise spiral, anticlockwise/S-wise spiral, other spiral galaxy (e.g. edge-on), merger, or star/artefact/don't know. Their votes were then weighted and corrected for some known classification biases (e.g. Bamford et al., 2009) and assembled in a final catalog of SDSS object IDs, sky coordinates, number of votes placed, debiased type likelihoods for each classification, and three tags (spiral, elliptical, and uncertain) that were placed to reflect an agreement of the vote fraction greater than 0.8. Throughout this work we have adopted these tags as a proxy for the morphological type of our SDSS sample galaxies.

3.1.5 Spectroscopic Catalogues: OSSY

The Oh et al. (2011) value-added SDSS catalogue (hereafter OSSY) analyzed in detail the spectra of 664,187 galaxies spanning $0.0 < z < 0.2$ from the Data Release 7 of the Sloan Digital Sky Survey (Strauss et al., 2002; Abazajian et al., 2009) to provide key quantities such as the value of the stellar velocity dispersion and the strength of nebular emission lines. As a first step the stellar kinematics were extracted using pPXF, adopting the templates of Tremonti et al. (2004) in conjunction with the MILES stellar templates masking the regions potentially occupied by ionized-gas emission. Subsequently, the group ran (*GandALF*) to extract the nebular emission and clean the spectra from ionized-gas emission lines and derive the line strengths of a multitude of stellar absorption lines. The group performed stringent quality control for each step of the analysis to eliminate bad data, safeguard against misfitting, and secure the robustness of the adopted analysis approach.

3.1.6 MaNGA: Mapping Nearby Galaxies at APO

The most current data release (Aguado et al., 2019, DR15) of SDSS has made available 4824 integral-field cubes as part of the Mapping Nearby Galaxies at APO (Bundy et al., 2015, hereafter MaNGA). MaNGA is an optical fiber-bundle integral-field unit (IFU) spectroscopic survey that aims to deliver nearly 10000 galaxy observation with a set of 17 independent IFUs, each fed through a tightly-packed array of optical fibers. These individual IFUs are hexagonal and vary in size with the largest one accepting 127 fibers (32'' in diameter) and the smallest one having as an input only 19 fibers (12'' in diameter). For each plate there are two 12'', four 17'', four 22'', two 27'', and five 32'' diameter hexagonal optical bundles that provide the feed to the spectrographs (Yan et al., 2016). The sample of galaxies, selected for observation, and the IFU setup were chosen so that a spatial coverage between 1.5 to 2.5 effective radii with a typical

sampling of 1-2 kpc is expected (Drory et al., 2015). The data reduction from the raw output of the spectrographs to the final data product cubes is carried out with the MaNGA Data reduction pipeline (Law et al., 2016). Each data product cube covers $\sim 3600\text{--}10300 \text{ \AA}$. The effective spatial resolution in the reconstructed MaNGA cubes varies around a full-width-at-half-maximum of $2.54''$ with a spectral resolution that is a function of both wavelength and spatial position with a median value of 72 km s^{-1} .

3.2 MUSE: The Multi-Unit Spectroscopic Explorer

The Multi-Unit Spectroscopic Explorer (MUSE) is an integral field spectrograph currently mounted on the Unit Telescope 4 (Yepun, UT4) part of the Very Large Telescope (VLT). The Multi Unit Spectroscopic Explorer (MUSE) is a second-generation wide-field optical integral field spectrograph operating in the visible wavelength range with superb spatial resolution. It is an assembly of 24 identical modules composing of an advanced slicer, spectrograph, and a high pixel density (4k) detector. These modules are individually fed by a sequence of optical systems responsible for derotating and splitting the field of view (FOV) into 24 sub-fields. MUSE operates in two modes: narrow and wide field. The narrow one spans $7.5 \times 7.5 \text{ arcsec}^2$ with spatial sampling of 0.025 arcsec . The wide-field mode is with a larger field of view ($1 \times 1'$), but with worse spaxel size of $0.2''$ by $0.2''$. The large number of spaxels adjudges MUSE as a very efficient “light bucket”, therefore, empowering a variety of scientific inquiries that could benefit from such an instrument (Bacon et al., 2006, 2010).

Chapter 4

The Insignificance of Seyfert 2 Activity in Driving Cold-gas Galactic Winds

4.1 Overview and Motivation

Large-scale galactic outflows have been proposed as a viable mechanism to “quench” the process of star formation in a short timescale and explain the transition of galaxies from the blue cloud to the red sequence and the bimodality in the SFR of the population of local galaxies (e.g. Schawinski et al., 2014, for a review). Furthermore, winds energized by an AGN or a circumnuclear starburst have been used as a mechanism to establish and maintain the strong correlation between the mass of the central SMBH and the bulge of the host galaxies (e.g. Gebhardt et al., 2000; King and Pounds, 2003; Murray et al., 2005). Generally, it is now understood the gaseous contents of a galaxy could undergo a sort of a duty cycle of as the triggering of different star-formation bursts or AGN can lead to the gas being pushed away in outflow and subsequent cooling and gravity could bring back the previously expelled material back in an episode of an inflow (e.g. Kim and Ostriker, 2018). Furthermore, expulsion of gas out into the circumgalactic medium could not, nevertheless, be enough to stifle its star-formation. Star formation can be rejuvenated as gas can be acquired from multiple different sources including the intergalactic medium, satellite gas and feedback material (e.g. Putman, 2017, for a review).

One efficient way to identify galaxies that are going through an outflow phase is to look for the presence of interstellar Na I $\lambda\lambda 5890, 5895$ absorption that is blue-shifted with respect to the systemic velocity of the galaxy. Indeed, the low-ionisation potential of Sodium makes the

detection of blue-shifted NaD lines an unambiguous signature of neutral interstellar material and also neutral hydrogen. The ISM traced by NaD must be somewhat shielded from non-ionizing radiation as excess in regards to the galactic stellar continuum NaD absorption is often associated with high extinction by dust (Veilleux et al., 2005). Blue-shifted NaD absorption features could stem from ISM that is entrained within an outflow (e.g. Rupke et al., 2005a). NaD has also been observed as part of a multiphase winds with the aid of integral-field unit observations (e.g. Rupke and Veilleux, 2013). Furthermore, in conjunction with red-shifted NaD and modelling techniques the line (i.e. P-Cygni) and surface brightness profiles of those lines can provide a way to assess the morphologies and sizes of such galactic-scale winds (Prochaska et al., 2011; Scarlata and Panagia, 2015).

Studying the NaD absorption feature has been routinely used as a probe of outflowing gas in galaxies with various properties using either long-slit, fiber or integral-field spectroscopy. Heckman et al. (2000) focused on a small sample of infrared-bright starburst galaxies. There the NaD lines were found to be both blue- and red- shifted. The outflowing material traced in absorption was found to span kpc-scales in these galaxies where the outflow is likely driven by intense star-formation that can be associated with a merger. Such studies were further extended (Rupke et al., 2002) to show that outflows are ubiquitous among such galaxies and that a non-negligible fraction of the gas could be ejected into the intergalactic medium. In larger sample Rupke et al. (2005a,b) detected cool winds in almost all of their infrared-luminous galaxies. Drawing on the size of their sample the group was able to confirm some of the theoretically expected wind and host galaxy properties (e.g. increase in velocity with increasing host SFR). Similarly, Martin (2005, 2006) focused on a sample of IR-bright galaxies that showed widespread winds traced by NaD absorption to highlight that the cool winds in there galaxies were likely momentum conserving and driven by ram pressure possibly exerted by the hotter wind phase and found some hints that radiation pressure could also play a role in propelling the wind. The NaD absorption feature has also been used to probe winds amongst the more general galaxy population. Chen et al. (2010b) used stacked spectra to trace outflows within nearby star-forming galaxies. They reported that NaD absorption due to ISM was predominantly found in galaxies with large dust extinction, higher star-formation rates and mass. However, perhaps surprisingly, for the galaxy stacks with blue-shifted out-flowing NaD no distinct correlation was reported between the line centroids and the host star-formation rate unlike in the cases of individual objects. Instead, a strong correlation was reported with respect to the width of the blue-shifted NaD lines. Using data from the SDSS, Concas et al. (2019) further confirmed these observations complementing

that outflows in face-on galaxies have expected P-Cygni profiles and that excess NaD absorption is found to have similar characteristics irrespective of the BPT classification. However, no clear evidence of ionized-gas outflows was present amongst their purely star-forming galaxies and signatures of multiphase winds were found only in systems with an AGN. Bae and Woo (2018) performed a similar comparison but on an object-by-object basis. No significant difference with respect to ionized-gas emission-line classification was reported in the kinematics of the interstellar NaD. Moreover, no link between the kinematics of the ionized-gas and neutral outflow components was found pointing out that within most of those galaxies the primary driving mechanism at least for the cold wind component is star-formation and not the AGN. Roberts-Borsani and Saintonge (2019) again on the basis of a stacking analysis further strengthened previous conclusions and added that the cool outflows in the general galaxy population have somewhat low mass outflow rates in comparison to other gas phases and that the mass-loading factor for the winds has a nearly constant value of 0.1 for normal nearby star-forming galaxies.

Individual systems that exhibit large-scale winds, traced by the NaD absorption feature, have also been studied extensively with the aid of integral-field observations. Davis et al. (2012) showed that the strong cold-gas outflow component of the AGN-driven wind of NGC 1266 can extend out to ~ 400 pc. The geometry and extent derived for the outflow from both NaD absorption and CO observations (Alatalo et al., 2011) have been shown to agree well. The cool NaD and CO traced wind was found to be embedded into a more extended (~ 1.5 kpc) ionized-gas ISM phase with higher velocity. A sample of six ULIRGs with signatures of mergers was studied by Rupke and Veilleux (2013) with the aid of IFU observations. They report that the outflows in such systems are multiphase with bipolar morphology and extent up to a few kpc. The presence of an AGN within these galaxies was shown to lead to higher outflow velocities. The velocities of the wind ionized gas phase were correlated with the ones observed in the neutral one. Complimentary study was conducted by Cazzoli et al. (2016) using spatially resolved observations of nearby IR luminous galaxies verified some previous conclusions. Namely, NaD outflows are widely found to be conical in morphology and are more often found among galaxies at higher inclinations. The velocities of the winds scale with the level of star formation and that the cold component is likely entrained and accelerated by interaction with the hotter component. Moreover, the winds in these galaxies carry a significant amount of mass and some non-negligible portion of it is expected to escape the gravitational potential and provide negative feedback to the star-forming process. Most recently, Rupke et al. (2017) reported few kpc-scale winds in all of his sample consisting of 10 galaxies with powerful AGN. Their galaxies were

shown to exhibit mass a large range of outflow rates and wind velocities and can suppress the host galaxy star formation.

However, such AGN-driven winds are not as well understood (e.g. Harrison et al., 2018) as their multiphase large-scale galactic counterparts present amongst the population of star-forming galaxies have been routinely studied (e.g. Rupke, 2018, for a review). Even despite this huge effort, the dominant driving mechanism (whether AGN or starbursts) behind the formation of the winds that can quench the star-formation process it is still not clear (Wylezalek et al., 2018).

In this chapter we measure the incidence and kinematics of interstellar NaD absorption in one of the largest samples of nearby Seyfert 2 galaxies drawn from the Sloan Digital Sky Survey Abazajian et al. (2009), and compare these results with similar measurements obtained in a carefully selected control sample designed to match our Seyfert 2 galaxies in redshift, luminosity, size, light concentration, apparent flattening, colour and, when available, morphological classification into early or late type objects. We use this comparison to quantify whether the frequency of kpc-scale cold-gas outflows increases in Seyfert 2's, with a view to understanding the impact that the central engines of Seyfert 2 galaxies have on their hosts.

4.2 The SDSS DR 7 Seyfert 2 and Control Samples

Both of our Seyfert 2 and Control samples are based on SDSS DR7. For our measurements of NaD line strength and position, we re-analysed the SDSS spectra that were used for the construction of the OSSY value-added catalogue. The relative intensity of emission lines, as measured in OSSY, was also used to select our core Seyfert 2 sample and classify the nebular emission of our control objects by means of standard BPT diagnostic diagrams (Baldwin et al., 1981).

For measuring total luminosities and colours we obtain absolute, de-reddened, K-corrected magnitudes from the SDSS DR7 in the u- and r-band, that are based on the best-fitting de Vaucouleurs or exponential model magnitudes (*ModelMag*). The K-corrections are taken from the *kcrr* value for the u- and r-band listed in the SDSS *Photoz* table (O'Mill et al., 2011), whereas for computing absolute magnitudes we use the luminosity distance returned by the *fCosmoDl* functions in the SDSS *CfunBASE* library (Taghizadeh-Popp, 2010) and the SDSS redshift listed in the *SpecObjAll* table. All necessary isophotal measurements for measuring the radial extent, flattening and concentration of the SDSS galaxies are taken from the SDSS *PhotoObjAll* table,

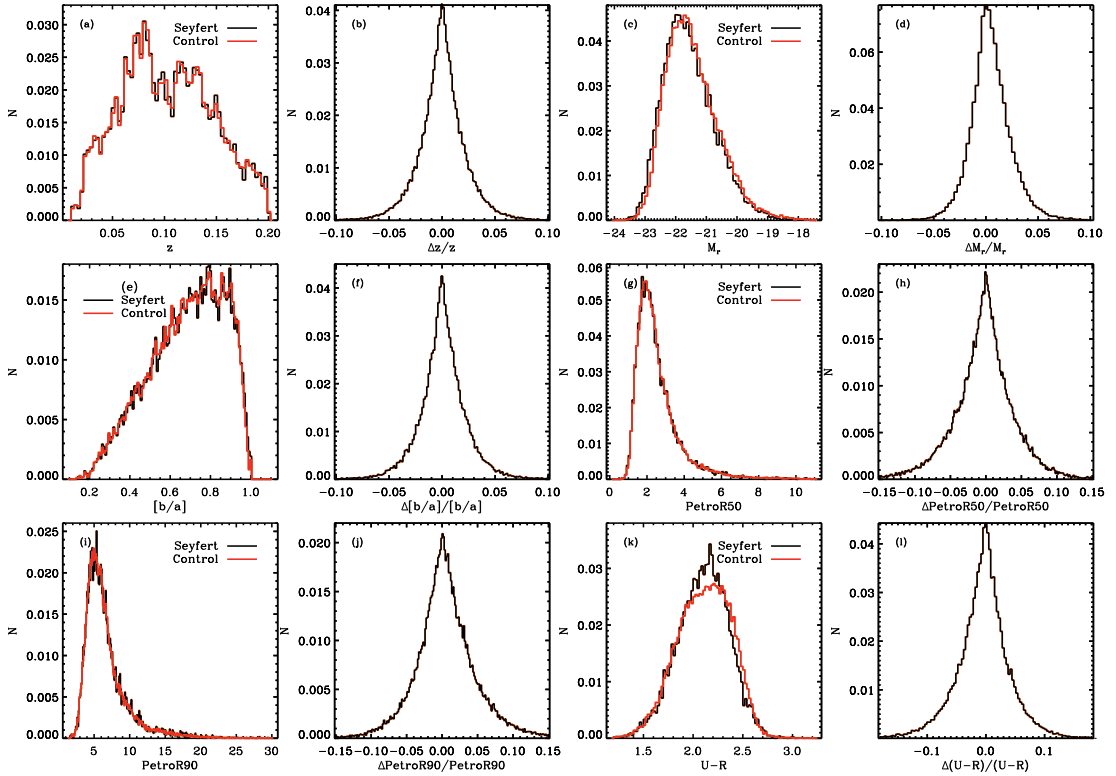


FIGURE 4.1: The result of our control matching procedure. Panels (a), (c), (e), (g), (i), (k) show the distribution of our Seyfert 2 and control samples in all parameters used in the matching process - redshift (z), absolute r-band magnitude (M_r), isophotal semi- minor and major ratio ($[b/a]$), Petrosian radius containing 50% of the light ($PetroR50$), Petrosian radius containing 90% of the light ($PetroR90$), and the difference in the absolute magnitude in the u- and r- bands ($U - R$). The remaining panels (b), (d), (f), (h), (j), (l) present the fractional difference between the aforementioned parameters for the galaxies in the control sample and the Seyfert 2 galaxy they match, normalised by the value of the corresponding parameter for the Seyfert 2. We achieve a good overall matching between the Seyfert 2 and control galaxy distribution, with the slight exception of $U - R$ where our matching procedure produces slight differences near the peak of the colour distribution.

in particular, the r-band values for the $isoA$ and $isoB$ measurements of the major- and minor-axis radii and the $petroR90$ and $petroR50$ entries for the Petrosian radii enclosing 90% and 50% of the Petrosian flux.

Finally, in this work, we consider only the OSSY catalogue objects that were visually inspected by the Galaxy Zoo citizen-science project (Lintott et al., 2011). Since around 94% of the OSSY catalogue objects were covered by Galaxy Zoo, the requirement of a visually-classified morphology does not significantly reduce the final sample of 625,607 objects from which we select the Seyfert 2 and control samples that underpin this study.



FIGURE 4.2: Some SDSS colour images for Seyfert and control galaxies in our study. The image in the first column is the Seyfert 2 galaxy in question, while the next five columns in the corresponding row are the five closest-matched control galaxies. The top two rows show morphologically matched early- and late-type objects, respectively. All other rows show the results of our matching procedure when morphological criteria cannot be used due to an “uncertain” classification in Galaxy Zoo for the Seyfert in question.

4.2.1 Seyfert 2 sample

As a starting point for selecting a sample of Seyfert 2 host galaxies, we look for objects in the OSSY catalogue which had emission-line amplitude-to-noise ratios greater than 3, for both the $[\text{O III}]\lambda 5007$ and $[\text{N II}]\lambda 6584$ forbidden emission lines and for the $\text{H}\alpha$ and $\text{H}\beta$ recombination lines. Such a detection threshold allows us to safely place them on the so-called BPT (Baldwin et al., 1981) emission-line diagnostic diagrams and, more specifically, on the one introduced by Veilleux and Osterbrock (1987) that combines the $[\text{N II}]/\text{H}\alpha$ and $[\text{O III}]/\text{H}\beta$ line ratios. We adopt the empirical demarcation of Kauffmann et al. (2003) to separate these galaxies into ones where the gas ionization is driven by star-formation (SF) activity and ones potentially driven by AGN. Furthermore, by applying the Kewley et al. (2001) maximum theoretical star-burst division line, we differentiate a class of galaxies with a superposition of AGN and star-formation

activity (TO for “transition”). Finally, the rest of the emission-line galaxies with plausible AGN emission were divided on the basis of the empirical criterion developed in Schawinski et al. (2007). This allows us to isolate Seyfert galaxies (Sy) from galaxies with central low-ionisation nuclear regions (LI). We make such a distinction because quite rarely in SDSS galaxies such a central low-ionisation emission can be ascribed to truly nuclear emission powered by AGN activity, and instead is more often due to extended low-ionisation emission (Sarzi et al., 2010; Cid Fernandes et al., 2010, 2011; Yan and Blanton, 2012; Singh et al., 2013; Belfiore et al., 2016).

As a result of this selection process we arrive at an initial sample of 10,983 Seyfert galaxies. Since many of these Seyfert objects could potentially display broad-line regions (BLR) and a featureless AGN continuum that would considerably complicate our NaD measurements (Cardoso et al., 2017), we further restrict ourselves solely to *narrow-line* Seyfert 2 galaxies, by excluding the Type 1 Seyferts identified by Oh et al. (2015). This leaves us with a final sample of 9859 Seyfert galaxies.

4.2.2 Control Sample

In order to ascertain the importance of AGN in driving outflows, we will compare our NaD analysis of the Seyfert 2 sample, to an identical analysis on a carefully selected sample of control galaxies. Following a procedure similar to Westoby et al. (2007), we proceed by finding, for each Seyfert 2 object in our sample, five control galaxies that are closest to the Seyfert in question in the following quantities:

1. Redshift, z , from the SDSS DR7 pipeline.
2. Absolute r-band magnitude, M_r , K-corrected and de-reddened for the Galactic extinction, as described above. This is done to match galaxies as closely as possible in their total stellar luminosity.
3. Apparent flattening, b/a , using the r-band isophotal minor- to major-axis ratio. For spiral galaxies, this quantity provides a useful measure of inclination.
4. The radius containing 90% of the Petrosian flux, $PetroR90$, which, when combined with our z matching, enables us to match galaxies in their intrinsic size. This also ensures that

the SDSS spectroscopic measurements encompass roughly the same fraction of galaxy light in our Seyfert 2 and control galaxies.

5. The radius containing 50% of the Petrosian flux, $PetroR50$, which, when combined with our $PetroR90$ matching, allows us to match galaxies in their degree of light concentration. In the absence of a robust visual classification, this, to some extent, provides a proxy for the galaxy morphology (Shimasaku et al., 2001; Strateva et al., 2001).
6. $u - r$ colour, based on their M_u and M_r absolute magnitudes. Combined with our M_r matching, this allows us to pick objects with comparable positions in the M_r vs. $u - r$ colour-magnitude diagram, therefore selecting galaxies with similar star-formation rates and star formation histories.

To find the best control objects for each of our Seyfert 2 galaxies we decided against minimising the sum of the absolute differences in each matching parameter (e.g. Δz) as done for instance in Westoby et al. (2007) and opted instead to consider such differences in relative terms (i.e. $\Delta z/z$) and weighting them as follows:

$$\Delta C = \frac{|\Delta z/z|}{0.05} + \frac{|\Delta M_r/M_r|}{0.1} + \frac{|\Delta[b/a]/[b/a]|}{0.05} + \frac{|\Delta_{petroR90}/petroR90|}{0.1} + \frac{|\Delta_{petroR50}/petroR50|}{0.05} + \frac{|\Delta(M_u - M_r)/(M_u - M_r)|}{0.1} \quad (4.1)$$

This allows us to find matching control objects more precisely at the higher- and lower- end of the Seyfert 2 distribution for each of the previous parameters, and to assign a relative-error meaning to our adopted weights. The weights themselves are chosen following an iterative process. Very broad initial constraints (i.e. asking all parameters to be not so precisely matched) were initially imposed and further tightened, guided by the specific number of available control galaxies for every Seyfert, in our parameters of interest, until our matching procedure achieved the relative best match across all six adopted parameters.

For each of our Seyfert 2 objects, we compute ΔC for all OSSY galaxies, and then pick the five objects with the lowest ΔC as control counterparts for the Seyfert in question. During this process, if a Seyfert 2 object had a robust ‘‘super-clean’’ Galaxy Zoo classification and was classified either as a spiral or an elliptical, we proceeded to find the best five control galaxies as

done above, but while considering only OSSY objects that were also robustly classified to be of the same morphological type. This selection process results in 44,123 unique control galaxies, because not using the whole set of possible controls and discarding the ones already adopted could introduce systematic errors in the matching process, resulting in a biased control sample. Fig. 4.1 shows how our matching process returns control galaxies, with parameter distributions that closely match the corresponding distributions for our Seyfert 2 sample (panels a, c, e, g, i, and k). Fig. 4.1 also shows how the values for these parameters for the five best control galaxies are generally within 5 to 10% of the ones of their parent Seyfert 2 objects (panels b, d, f, h, j, and l), broadly consistent with the weighting applied in Eq. (1). The only exception in this respect concerns our colour matching, since the $u - r$ distributions for our Seyfert 2 and control sample differ slightly near their peaks and red tails.

Fig. 4.2 further illustrates the quality of our control sample selection, by presenting SDSS colour composite images for 5 randomly selected Seyfert 2 galaxies (left column) and their respective five best controls (columns to the right). In Fig. 4.2 the top two rows are Seyfert 2 galaxies that are classified by Galaxy Zoo as an elliptical and spiral respectively. Conversely, the last three rows show how our matching process returns control galaxies that look similar to our Seyfert 2 objects even when the morphology of the latter was classified as “uncertain” by Galaxy Zoo.

To conclude the description of our control sample, we emphasize that while it includes objects that are similar to our Seyfert sample galaxies in all respect except for the central nebular activity, this does not mean that different manifestations of AGN activity do not occur in our control sample objects. Whether AGN are present and could launch outflows in our control sample will not affect our analysis, however, since our prime goal is to ascertain whether cold-gas outflows are launched more efficiently in objects with unobscured, optical AGN activity (e.g. Seyfert-host galaxies) than in similar object with other kinds of central activity (including passive systems).

4.3 Results

We begin by discussing the incidence and kinematics of NaD interstellar absorption in our control sample, while also defining the NaD blue-shift threshold that identifies outflowing systems (§ 4.3.1). We then compare these results with what is observed in our Seyfert 2 sample (§ 4.3.2). However, before conclusions can be drawn from such a comparison, it is important to first consider the incidence of interstellar NaD absorption in both the control and Seyfert 2

Emission class	all	with NaD	NaD outflows
Seyfert 2	9859	561 (5.7 ^{+0.3%} _{-0.2%})	53 (9.5 ^{+1.5%} _{-1.3%})
control-total	44123	2174 (4.9 ^{+0.1%} _{-0.1%})	352 (16.2 ^{+0.9%} _{-0.9%})
control-SF	6710	587 (8.7 ^{+0.4%} _{-0.4%})	92 (15.7 ^{+1.8%} _{-1.6%})
control-TO	5895	567 (9.6 ^{+0.4%} _{-0.4%})	147 (25.9 ^{+2.3%} _{-2.1%})
control-LINER	859	105 (12.2 ^{+1.3%} _{-1.2%})	27 (25.7 ^{+5.0%} _{-4.5%})
control-NE	30659	915 (2.9 ^{+0.1%} _{-0.1%})	87 (9.5 ^{+1.1%} _{-1.0%})

TABLE 4.1: Breakdown of our Seyfert 2 and control samples, according to whether or not interstellar NaD absorption was detected (third column, for objects with $A/N_{\text{NaD}} > 4$ and $E(B - V) > 0.05$, see § 2.2.7) and furthermore if it likely traces outflows (fourth column, for objects also with $\Delta V = V_{\text{NaD}} - V_{\star} < -100 \text{ km s}^{-1}$, see § 4.3.1). Control galaxies are further subdivided according to their emission-line classification either as star-forming regions (SF), composite AGN/star-forming activity (TO), low-ionisation - possibly truly nuclear - emission regions (LINER), or displaying little to no emission (NE). Percentages in the third column refer to the fraction of objects with interstellar NaD absorption out of the number of objects in each of our subsamples (second column) and percentages in the fourth column refer to the fraction of NaD-outflowing objects with respect to the number of objects with detected NaD interstellar absorption (third column). The confidence intervals on the percentage fractions are calculated following Gehrels (1986) using Poisson error, except in the cases of small number statistics ($N < 300$) where we adopted the bimodal distribution ones.

samples. Tab. 4.1 shows that the fraction of Seyfert 2 objects where NaD interstellar absorption is detected (5.7^{+0.3%}_{-0.2%}) is similar to that of control galaxies (4.9^{+0.1%}_{-0.1%}).

Such a remarkable similarity, combined with our careful control sample construction, allows us to directly compare the NaD kinematics in our two samples and to reflect on the importance of AGN feedback. In particular, this finding goes against the argument that the AGN in Seyfert 2 galaxies would substantially ionise its surroundings. Such ionising action of the AGN would reduce the incidence of NaD interstellar absorption among our Seyfert 2s and thus limit the usefulness of the NaD lines as a tracer of cold-gas large-scale outflows only to objects with a faint AGN, which may not be able to provide much energetic feedback, as reported for instance by Villar Martín et al. (2014) for their sample of bright type 2 quasars. Instead, such similarity is in fact not surprising having in mind that, in general, the host galaxies of Seyfert activity are not outstandingly different in their total amount of molecular gas reservoirs than the general galaxy population (e.g. Maiolino et al. 1997; Saintonge et al. 2012; Rosario et al. 2018; however, also see Vito et al. 2014).

4.3.1 Control Sample

Tab. 4.1 shows that the majority (69%, or 30,659 out of 44,123 objects) of our control galaxies exhibit no or very weak nebular emission, with most remaining objects being almost evenly

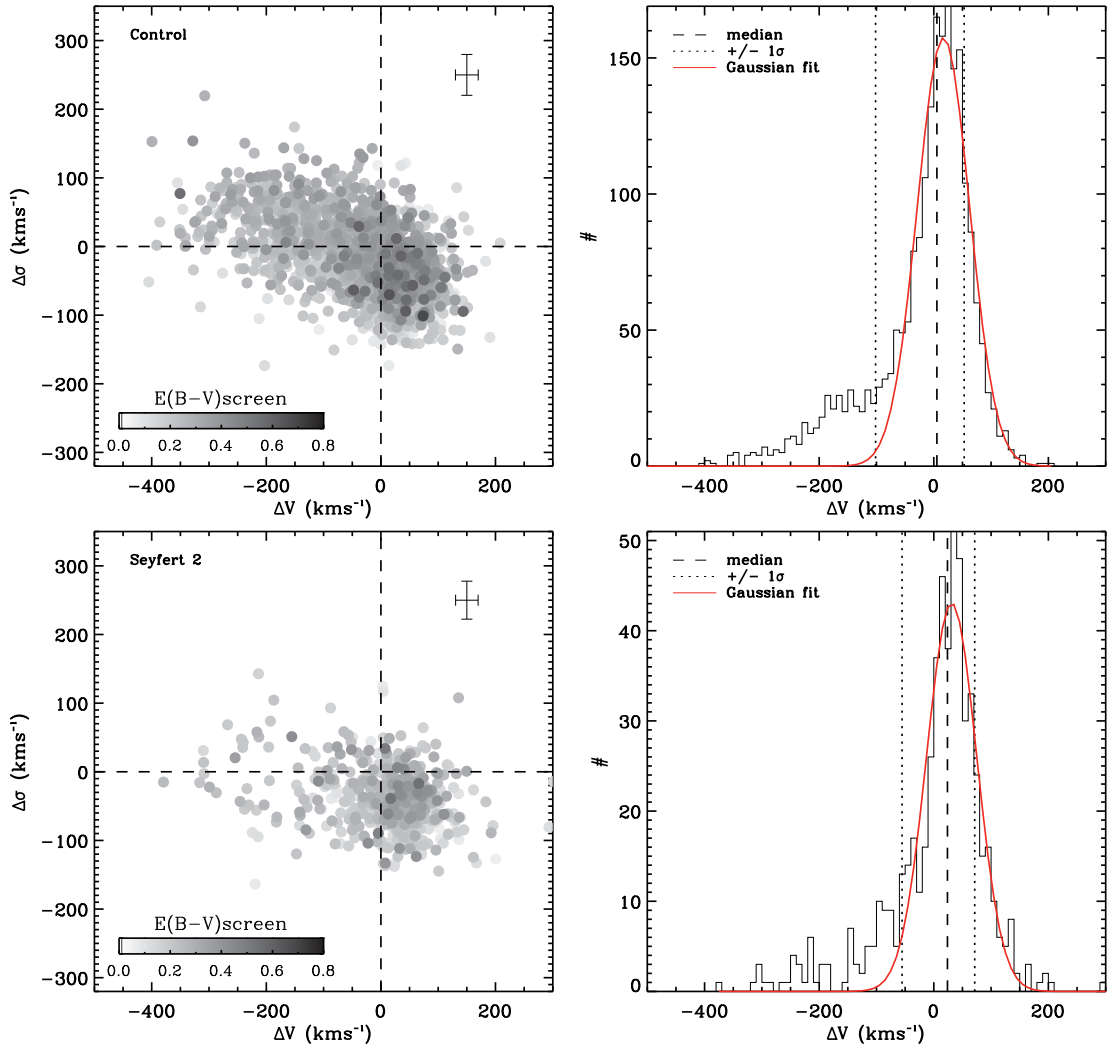


FIGURE 4.3: Kinematics of the NaD absorption component relative to the systemic properties of the galaxy, for our control and Seyfert 2 sample, where the observed NaD excess can be safely attributed to interstellar absorption. Top left: $\sigma_{\text{NaD}} - \sigma_{\star}$ ($\Delta\sigma$) versus $V_{\text{NaD}} - V_{\star}$ (ΔV) for our control sample, colour-coded by the dust reddening $E(B-V)$. Only galaxies with $A/N > 4$ for the NaD absorption and with $E(B-V) > 0.05$ are shown (see text for more details). Top right: Histogram showing the distribution of the velocity offsets $\Delta V = V_{\text{NaD}} - V_{\star}$ for all the control galaxies shown in the top-left panel. The dashed line indicates the median of the distribution, and the dotted lines correspond to the $\pm 1\sigma$ levels containing 68% of the ΔV distribution. The red line shows the best-fitting Gaussian to the underlying distribution and emphasises the pronounced tail of galaxies with a $\Delta V < -100$. Bottom left: An identical $\Delta\sigma$ vs. ΔV diagram as in the top-left panels, but now for our Seyfert 2 sample. Bottom right: An identical ΔV distributions as in the top-right panels, but now for our Seyfert 2 sample. The mean errors on the left panels are given in their top right corners.

split between star-forming (13%) and composite (13%) nebular emission, plus a minority (3%) of galaxies displaying LINER-like emission. Tab. 4.1 also shows that the incidence of interstellar NaD absorption is around 9-12% for control galaxies with detected ionized-gas emission, dropping to just 3% among quiescent objects, which is consistent with the weak or absent nebular emission in these systems.

To understand the kinematics of interstellar NaD absorption in our control sample, we start by considering the top left panel of Fig. 4.3, where the velocity V_{NaD} and velocity dispersion σ_{NaD} of the NaD absorption is compared to the galaxy's systemic velocity and central velocity dispersion (V_{\star} and σ_{\star} respectively). The colour-coding indicates the reddening by dust, $E(B - V)$. In this $\sigma_{\text{NaD}} - \sigma_{\star}$ versus $V_{\text{NaD}} - V_{\star}$ diagram, we observe the same trend as that observed in Sarzi et al. (2016), in that a majority of objects with nearly zero (or even slightly positive) $V_{\text{NaD}} - V_{\star}$ (ΔV) and negative $\sigma_{\text{NaD}} - \sigma_{\star}$ ($\Delta\sigma$) values is followed by a long tail of galaxies with increasingly blue-shifted and broad NaD profiles, i.e. with progressively negative ΔV and increasing $\Delta\sigma$ values.

The bulk of the objects with $\Delta V \sim 0$ consists of control galaxies where the NaD profile traces material that is likely settled in a dusty disk which is dynamically colder than the stellar bulge (thus corresponding to $\Delta\sigma < 0$ values), or of highly-inclined systems where it would be hard to detect possible outflows. Conversely, detecting outflows and increasingly blue-shifted NaD lines is facilitated by looking at more face-on galaxies, where broad NaD profiles are also expected since the line of sight intersects a multitude of cold-gas clouds moving at different velocities within large-scale bi-conical galactic winds (Fujita et al., 2009; Krumholz et al., 2017). Visual inspection of our control galaxies combined with using the inclination values derived from the axis ratio of late-type galaxies (51% of our control sample) confirms that the observed $\Delta\sigma$ vs ΔV anticorrelation is mainly driven by galaxy inclination. This trend is supported by the systematically higher $E(B - V)$ values among low- ΔV objects, as would be expected for nearly edge-on dusty systems (Unterborn and Ryden, 2008; Masters et al., 2010b). We proceed to address when NaD outflows are likely to occur in our control galaxies, by studying the distribution of values for their NaD velocity offset (ΔV), as shown in the top right panel of Fig. 4.3. The ΔV distribution is skewed toward negative values (with a statistical skewness value of ~ -1.42) and has a pronounced tail of objects with blue-shifted NaD interstellar absorption profiles. Yet, as stated before, the bulk of the control objects in Fig. 4.3 shows $\Delta V \sim 0$ values, so that a Gaussian fit to the entire ΔV distribution captures well the distribution of the majority of these galaxies and allows us to isolate the tail of control objects that have NaD outflows. Observing that the control

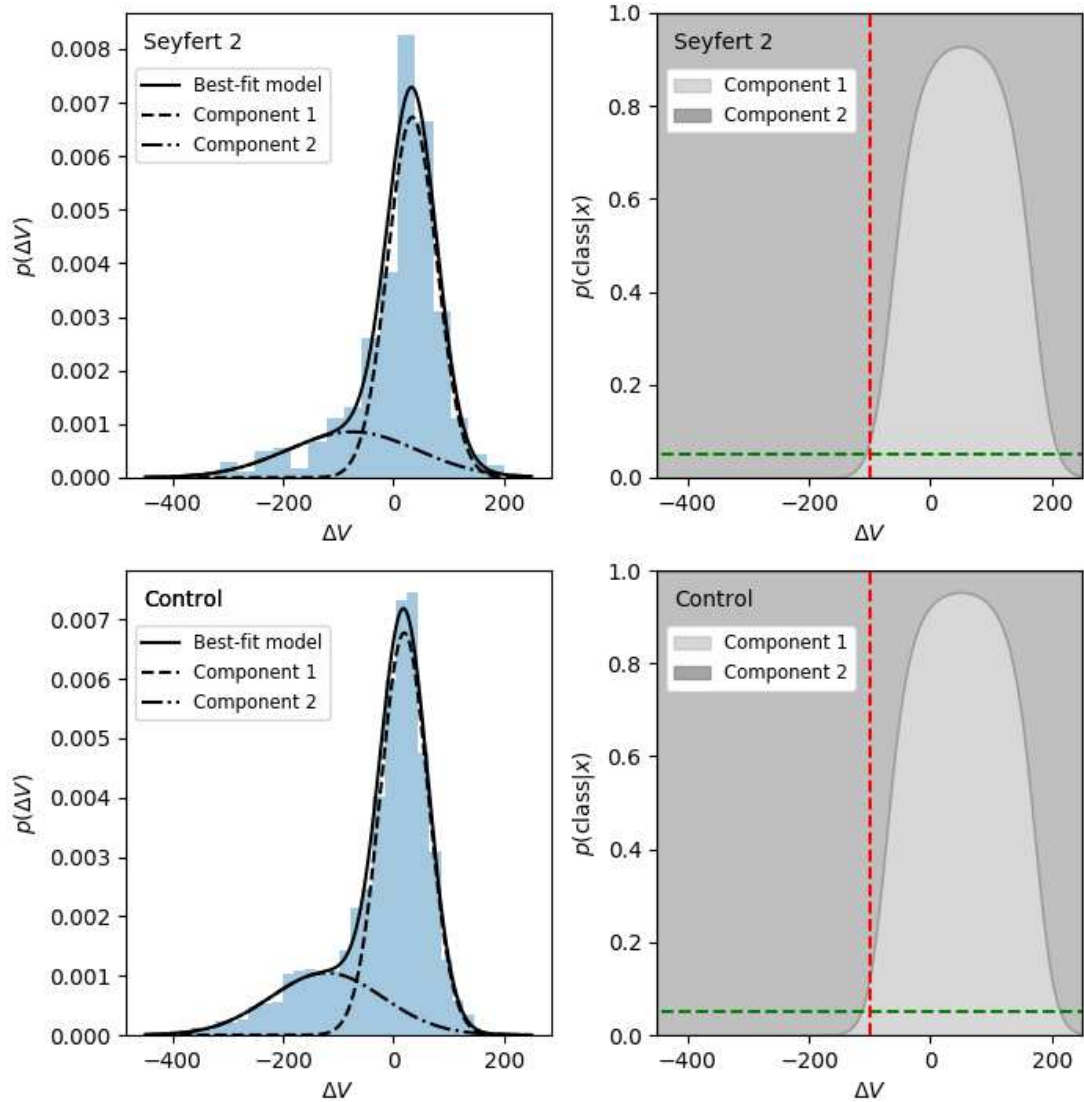


FIGURE 4.4: One-dimensional Gaussian mixture model with two components of the retrieved ascribed to ISM NaD velocities for both the Seyfert 2 and control samples. Top left: $V_{\text{NaD}} - V_{\star}$ (ΔV) histogram along with the best-fit Gaussian mixture model. Dashed and dotted-dashed lines show the first (“bulk”) and second (“tail”) components respectively. Top right: The probability that a given ΔV is drawn from each Gaussian component as function of ΔV itself. Note that in order to be confident that a ΔV is drawn with a probability greater than 95% (marked by the horizontal dashed green line) from the second Gaussian (here loosely referred to as the “tail”) ΔV has to be lower than -100 km s^{-1} (vertical dashed red line). Bottom left: An identical to the top-left panel histogram along with the best-fit Gaussian mixture model, but now for our control sample. Bottom right: An identical to the top-right panel probability distributions, but now for our control sample. Note that the required 95% credibility criteria gives a very close ΔV separation threshold to the one adopted for our Seyfert 2 sample.

galaxies with $\Delta V < -100 \text{ km s}^{-1}$ (the $\sim 16^{\text{th}}$ percentile of the overall ΔV distribution) already lie outside the region occupied by 90% of the objects enclosed by the fitted Gaussian (which has a standard deviation of 45 km s^{-1}), we consider this ΔV threshold to be a conservative estimate for the start of the tail of blue-shifted NaD control objects. Furthermore, we performed a simple Gaussian mixture modeling to probabilistically assign our retrieved ISM NaD velocity distributions for both the Seyfert 2 and control samples utilizing the `Scikit-learn` Python package (Pedregosa et al., 2011) following (Ivezić et al., 2014, see their Chap. 4.4.3) to two Gaussian components (the first of which is loosely referred to as “bulk” and a second one as a “tail”, respectively). In this Gaussian mixture model the data is assumed to be comprised of two Gaussians, each one characterised by a mean, covariance, and normalization factor. Therefore, the probability of having a given velocity drawn from a Gaussian mixture model given a set of those Gaussian parameters can be expressed as the sum over the number of all components of the multiple of the normalization factors of each Gaussian with the given mean and covariance. Each velocity should belong to a component so the sum of the normalization factors for all constituent Gaussians should add to unity. However, the probability of having a given velocity drawn from a Gaussian mixture model given a set of those Gaussian parameters can be interpreted using a concept deemed “hidden” variables. The Gaussian components are then interpreted as different “classes”, to designate that each velocity intrinsically belongs to only one of the specific individual Gaussian components. Under this interpretation the Gaussian to which each velocity belongs can be labeled (“class label”) with such a hidden variable that is involved in its generation by the data. Generally, the class labels to which each velocity belongs are not known, however the probability that for each velocity is generated by one of the classes (“responsibility”) can be obtained using Bayes’s theorem. This expression naturally incorporates the fact that it is less likely for a velocity that is further away from the mean of the Gaussian component to be associated with that particular component. To seek the set of best-fitting parameters (including the best set of label classes) instead of a maximum likelihood estimation the package draws on an expectation-maximization algorithm (Dempster et al., 1977) in order to avoid directly estimating the intrinsically complex objective function that is associated with our Gaussian mixture model. The algorithm works under the assumption that the responsibility for each velocity is known and fixed in each of its iteration. The algorithm starts with a set of assumed responsibilities. The approach of evaluating new responsibilities at each step can greatly reduce the complexity of evaluating the necessary likelihood function and the values for the Gaussian mixture parameters can be estimated in a simplified way. This executes a “maximization” step the aim of which is to drive the minimization of the fit likelihood function towards a local minimum. It is followed

by an “expectation” step, where the initial responsibilities are again updated knowing that they represent the probability of each each velocity being generated by a given label. The process is repeated until convergence is established.

Prompting for a high degree of credibility (95%), we can confirm that all objects with $\Delta V < -100 \text{ km s}^{-1}$ (our threshold for “outflowing” objects, derived by simply fitting single Gaussians to the overall Seyfert 2 and control sample ISM NaD velocity distributions) could be assigned to a second component, deemed to be, in our case, the “tails” of the sample NaD ΔV distributions. This is illustrated in Fig 4.4 where we show the best-fitting model and its separate best-fit Gaussian components for each of our samples. We note that this process returned best-fit Gaussians to the “bulk” of both Seyfert 2 sample and our control one nearly identical to the ones obtained by simply fitting a single Gaussian to the overall ISM NaD velocity distributions as outlined in the text. Consequently, we deem galaxies with $\Delta V < -100 \text{ km s}^{-1}$ as being likely to host cold-gas outflows, which are expected to be on kpc-scales given that at the mean redshift of our sample ($z \sim 0.1$) the 3'' SDSS fibers subtend a region 5.5 kpc across. Previous specially resolved observations of such galactic winds do, indeed, confirm that most often their spatial extent is at kpc-scales (e.g. Martin, 2005; Rupke et al., 2002, 2005b; Rupke and Veilleux, 2011; Cazzoli et al., 2014; Rupke and Veilleux, 2015; Liu et al., 2015).

Among the control galaxies with detected NaD interstellar absorption, around $\sim 16.2\%$ (Table 4.1) display NaD profiles blue-shifted by more than 100 km s^{-1} , which amounts to $\sim 0.8\%$ of the control sample and is consistent with the overall outflow detection rate found in Sato et al. (2009). Interestingly, we find that NaD outflows are not found most commonly in the star-forming objects (which host 16% of outflowing objects). Instead, outflows seem to be produced more efficiently in galaxies with either central composite AGN/star-forming or LINER-like emission (in 25% of the cases). Outflows are also traced in quiescent control objects with NaD interstellar absorption (10% of the cases) that generally display weak emission and where reddening prevented, in particular, the detection of [O III]. As such, the upper-limits on the [O III]/H β line ratio indicates the presence of star formation or composite AGN/star-formation activity in most of these quiescent objects.

To study the role of star formation in driving outflows and further ascertain when it most likely powers them, it is instructive to look into the infrared (IR) luminosity of our control sample. For instance, it is well established that more than 50% of all luminous infrared galaxies or ultraluminous infrared galaxies have blue-shifted NaD profiles indicative of outflowing gas (Heckman

et al., 2000; Rupke et al., 2002, 2005a,b; Martin, 2005; Cazzoli et al., 2016) and that in turn, the average contribution of the AGN to the observed total bolometric IR luminosity amounts on average to 25% (with the exception of Seyfert 1 emission-line galaxies (Nardini et al., 2010; Kilerci Eser et al., 2014).

To estimate the IR luminosities (L_{IR}) of our control galaxies with NaD interstellar absorption, we employ the Ellison et al. (2016) catalog of predicted infrared luminosities for galaxies in the SDSS DR7, selecting only objects where the expected error in their infrared luminosity estimate is less than 0.1 dex. Among our control objects with interstellar NaD detection, 1519 (70%) have L_{IR} values from Ellison et al., and around 30% (461) of these have $L_{IR} > 10^{11} L_{\odot}$ that would identify them as LIRGs or even ULIRGs. The fraction of objects with $L_{IR} > 10^{11} L_{\odot}$ is substantially higher for objects with NaD outflows, being around 55% (148 objects out of 268), whereas for the bulk of our control objects that have $\Delta V \sim 0 \text{ km s}^{-1}$ the fraction of objects with $L_{IR} > 10^{11} L_{\odot}$ drops to 25% (313 out of 1251).

A higher incidence of U/LIRGs amongst our NaD-outflowing control objects is consistent with many of them being powered by star-formation, even though only 36 out of these 148 NaD-outflowing and IR-bright control objects display central nebular emission dominated by HII regions (i.e. star-forming). This may suggest either that circum-nuclear star formation is driving the outflow or that shocks in the outflow lead to a more complex emission-line spectrum, which could be recognised as LINER-like or composite AGN/star-forming emission, as found in 56% of our NaD-outflowing and IR-bright objects (e.g. Rich et al., 2014, 2015; Ho et al., 2014, for ULIRGs and normal galaxies, respectively). In fact, shocks may also help explain why, more generally and not in just U/LIRGs, NaD outflows are often associated with composite or LINER-like emission in our control galaxies, which can also be observed in the NaD kinematic analysis of the Jeong et al. (2013) sample by Park et al. (2015, see their Fig. 4) and some of the MaNGA survey galaxies (Wylezalek et al., 2018).

4.3.2 Seyfert 2 sample

As noted above, the fractions of Seyfert and Control objects with interstellar NaD absorption are very similar, which is important, as this allows us to compare the cold-gas kinematics and, in particular, the incidence of NaD outflows in our two samples.

We proceed by studying the kinematics of the interstellar NaD lines in our Seyfert sample. The bottom left panel of Fig. 4.3, which shows the same $\Delta\sigma$ vs. ΔV diagram that we previously discussed for our control galaxies, indicates that among our Seyfert sample there is also a population of galaxies with blue-shifted NaD interstellar lines (e.g. with $\Delta V < 0$) that are likely tracing outflowing material. The ΔV distribution for our Seyfert 2 sample (bottom right panel of Fig. 4.3) shows a skewed distribution (with a statistical skewness ~ -1.22), similar to that observed in the control sample, with a tail of objects with $\Delta V < -100 \text{ km s}^{-1}$ extending away from the bulk of the systems that have nearly zero or slightly positive ΔV values. Compared to the control sample, however, the tail of objects with blue-shifted NaD profiles is less pronounced, as it contains 9.4% of all Seyfert 2 galaxies with interstellar NaD absorption (compared to 16.2% for the control galaxies), corresponding to 0.53% of the overall Seyfert 2 sample (i.e. those with and without NaD absorption).

Given that the overall incidence of NaD-outflowing systems is similar to that found in our control sample, it is important to recall that our sample of 9859 Seyfert 2 galaxies offers a representative view of the Seyfert 2 population within the footprint of the SDSS survey. Finding only 53 of such objects with kpc-scale cold-gas outflows already suggests that optical AGN activity cannot be important in driving galactic winds that may lead to subsequent quenching of star-formation in the nearby Universe, even accounting for the fact that some more NaD-outflowing systems may have remained undetected in inclined Seyfert 2 galaxies. In fact, the role of AGN feedback may be even smaller considering how well connected Seyfert 2 and star-formation activity are (e.g. Kauffmann et al., 2003), so that circumnuclear star formation may also play a part in driving the NaD outflows that we observe in our Seyfert 2 sample.

To further quantify the importance of AGN feedback we check if the radiative power output of the AGN, i.e. its bolometric luminosity as traced by the extinction-corrected luminosity of the [O III] emission line (Lamastra et al., 2009), correlates with the velocity offset ΔV of the interstellar NaD absorption. This is shown in Fig. 4.5, where we find a modest tendency for galaxies with higher values of [O III] luminosity ($\log L_{[\text{O III}]}$) to display blue-shifted interstellar NaD profiles (indicative of an outflow) more often. The fraction of NaD-detected Seyfert 2 galaxies where $\Delta V < -100 \text{ km s}^{-1}$ indeed increases from $\sim 3_{-3}^{+10}\%$ or $\sim 9_{-4}^{+5}\%$, for objects with low to intermediate [O III] luminosities, to $\sim 19_{-11}^{+16}\%$ for the most luminous (top 16% percentile) Seyfert 2 nuclei. Outflows are not predominantly found in such bright AGN (where we find $\sim 32\%$ of the outflows), however, and inclination biases can also be excluded as we do not find -

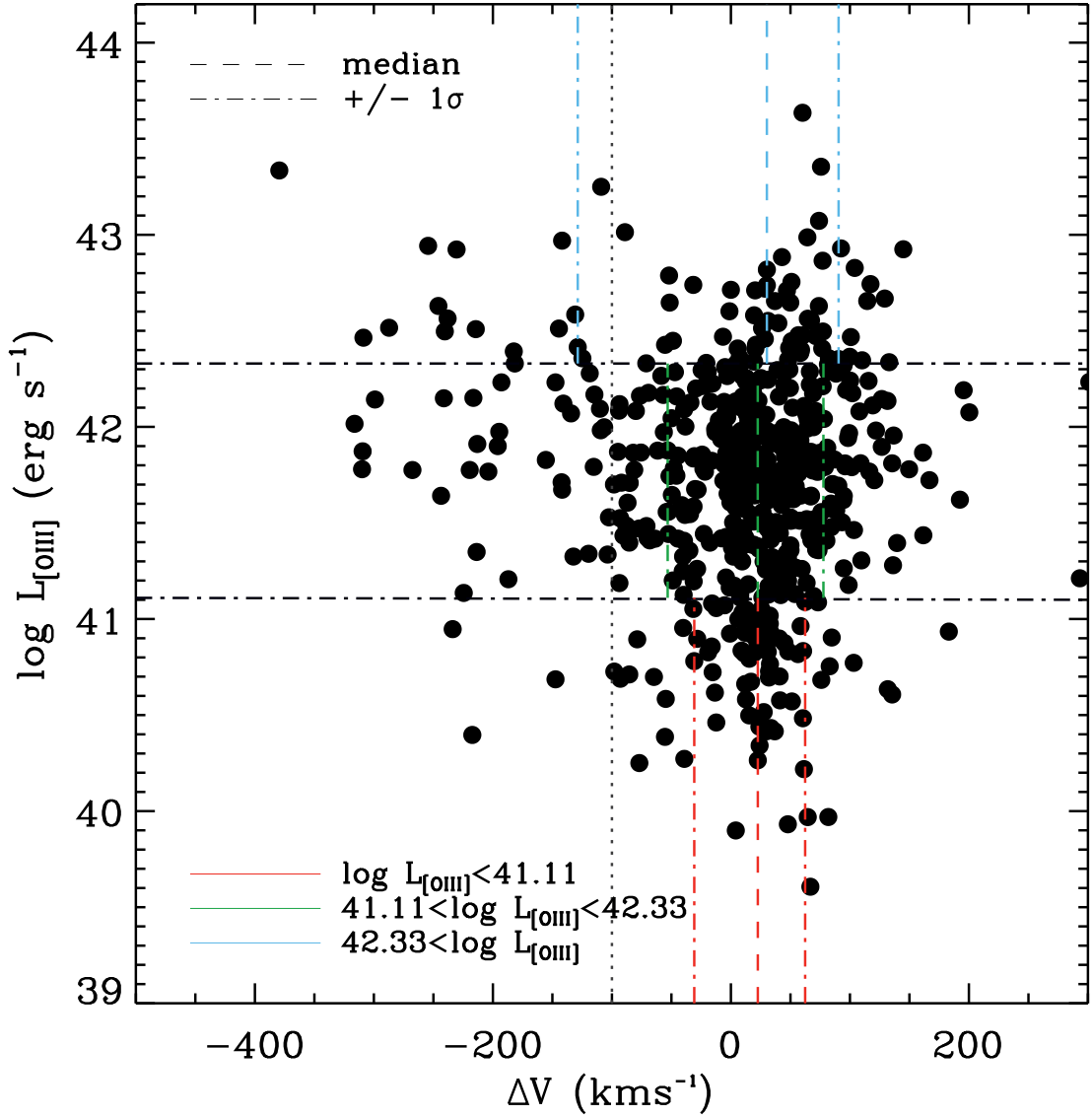


FIGURE 4.5: Dependence of the AGN bolometric luminosity, as traced by $\log L_{[\text{O III}]}$ calculated using the extinction-corrected $[\text{O III}]$ flux provided by the OSSY catalogue, on the velocity shift $\Delta V = V_{\text{NaD}} - V_{\star}$. The horizontal dashed-dotted lines indicate the ($\pm 1\sigma$) 16% and 84% percentiles of the $\log L_{[\text{O III}]}$ distribution. In each of the three $\log L_{[\text{O III}]}$ regions defined by these $\pm 1\sigma$ $\log L_{[\text{O III}]}$ limits, the vertical dashed and dashed-dotted lines show the median and the $\pm 1\sigma$ values for the velocity shifts ΔV , respectively. Finally, the gray vertical dotted lines indicate our $\Delta V = -100 \text{ km s}^{-1}$ threshold for identifying NaD outflows, as derived from our control sample (see text in § 4.3.1). Only at the highest $\log L_{[\text{O III}]}$ end does the ΔV distribution becomes more skewed, with a tail of outflowing objects. These objects comprise the most luminous $\sim 20\%$ of Seyfert 2 galaxies, and 32% of all NaD-outflowing Seyfert 2 objects.

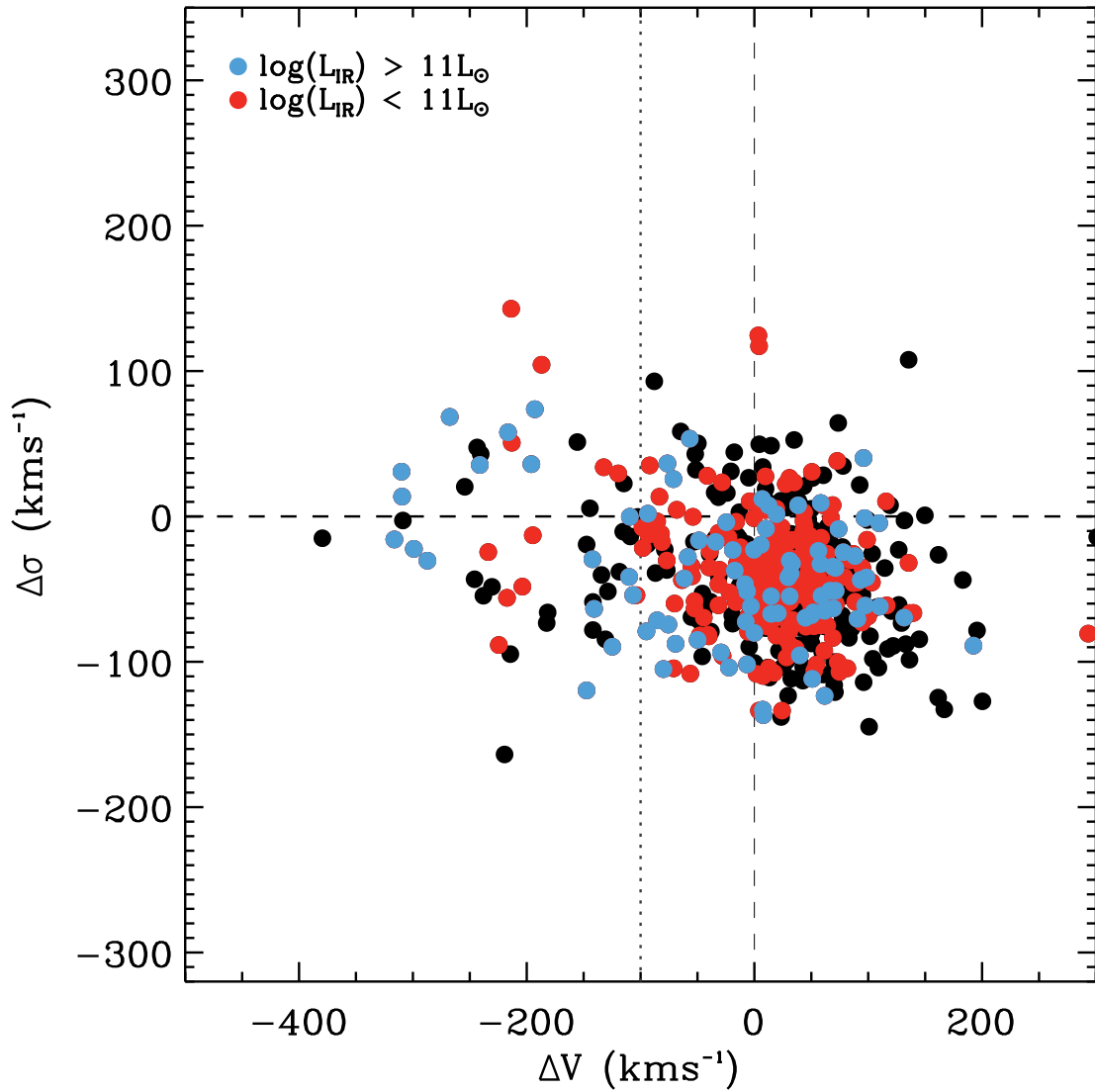


FIGURE 4.6: $\Delta\sigma$ vs. ΔV for Seyfert 2 galaxies with interstellar NaD absorption, similar to the one in Fig. 4.3 but now showing the objects colour-coded with IR luminosity estimates from the catalogue of Ellison et al. (2016). Blue and red points indicate galaxies with IR luminosities above and below the $L_{IR} = 10^{11}L_{\odot}$ threshold i.e. LIRGs and ULIRGs respectively. Among the outflowing Seyfert 2 galaxies (i.e. those to the left of the grey vertical dotted line that marks our $\Delta V = -100$ threshold for identifying NaD outflows, see § 4.3.1) 60% would be classified as LIRGs or ULIRGs.

at least for Seyfert 2 in late-type galaxies (which are 38% of the Seyfert 2 hosts) - a correlation between axis ratio and [O III] luminosity.

If the weak trend shown by Fig. 4.5 could still be interpreted as evidence for AGN feedback in our NaD-detected Seyfert 2, one also has to keep in mind that the luminosity of the [O III] line in AGN is found to correlate with the star-formation rate of the host galaxy (LaMassa et al., 2013).

To check whether star-formation is possibly also driving the NaD outflows observed in our

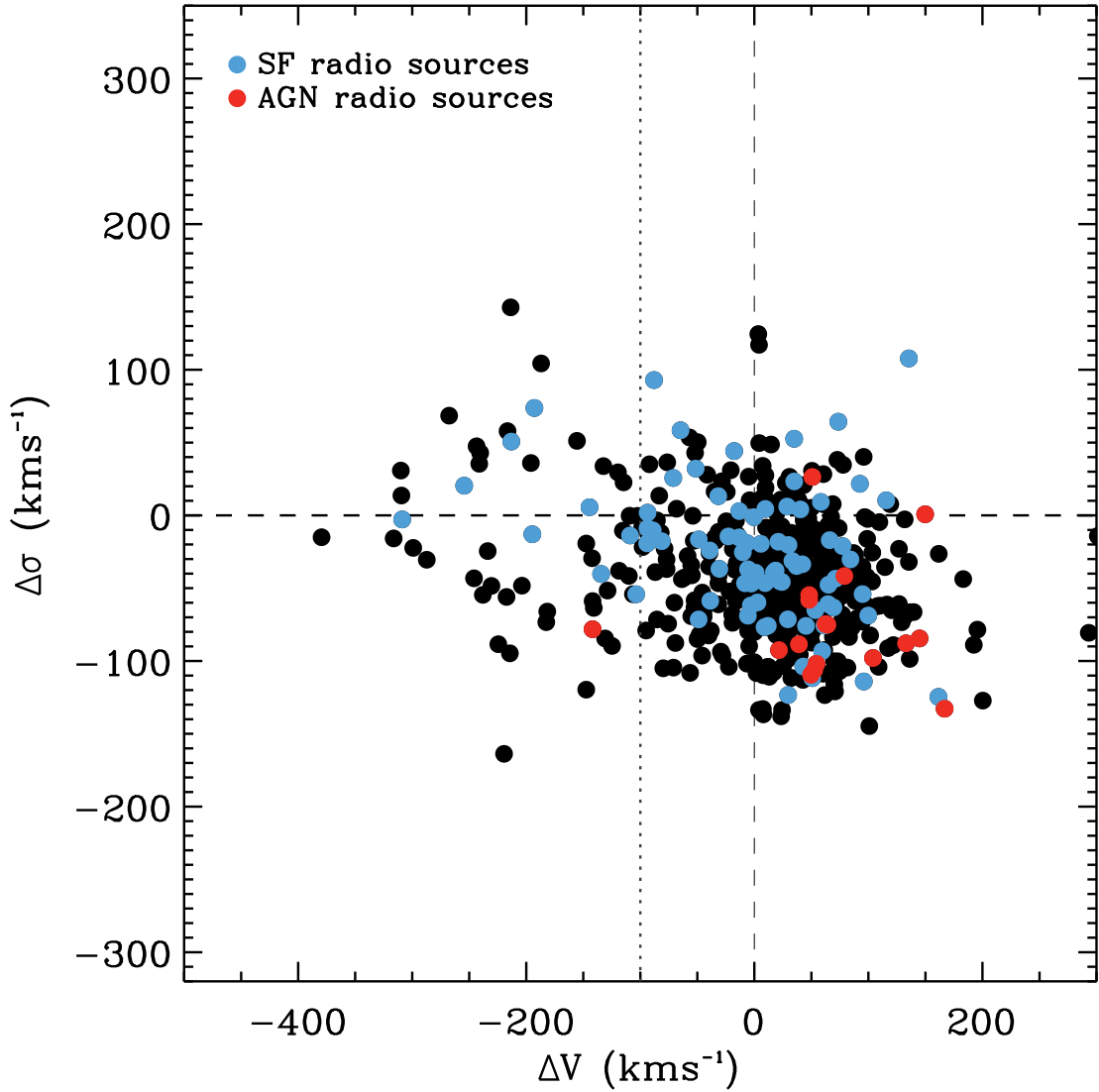


FIGURE 4.7: $\Delta\sigma$ vs. ΔV for Seyfert 2 galaxies with interstellar NaD absorption, similar to the one Fig. 4.3 and Fig. 4.6, but now showing radio sources that Best and Heckman (2012) associate with either AGN activity (red points) or star formation (blue points). Among the ten outflowing Seyfert 2 galaxies whose radio emission was classified in this way by Best and Heckman, only one is considered by these authors as being powered by a central AGN.

Seyfert 2 sample, we draw again from the work of Ellison et al. (2016) and look for the incidence of LIRGs or ULIRGs among our Seyfert 2 galaxies. This is illustrated by Fig. 4.6, where we present the same $\Delta\sigma$ vs. ΔV diagram for the NaD-detected Seyfert 2s as in Fig. 4.3, but now highlighting objects with L_{IR} above and below $L_{IR} = 10^{11} L_{\odot}$, which is the LIRG threshold. The Ellison et al. catalogue provides L_{IR} estimates for 308 (55%) of our Seyferts with NaD interstellar absorption, and of these, around 28% (88) are sufficiently IR-bright to be classified as LIRGs or ULIRGs. Among objects with L_{IR} estimates, the fraction of NaD-outflowing Seyferts (i.e. with $\Delta V < -100 \text{ km s}^{-1}$) with $L_{IR} > 10^{11} L_{\odot}$ is substantially higher than for Seyferts that show little or no evidence of cold-gas outflows (i.e. with $\Delta V > -100 \text{ km s}^{-1}$), with these fractions being

60% (17 out of 28) and 25% (71 out of 280), respectively. The incidence of LIRGs or ULIRGs among NaD-outflowing Seyfert 2s is thus nearly twice as that of bright AGNs (32%), suggesting that circumnuclear star formation could indeed be driving many of the outflows observed among our Seyfert 2 galaxies. In fact, this possibility appears even more likely when considering that the fraction of IR-bright NaD-outflowing Seyfert 2s is also remarkably consistent with the corresponding value for the NaD-outflowing control objects (55%, § 4.3.1).

To further probe the relative role of AGN and star-formation in driving NaD outflows, we appeal to ancillary radio data for our galaxies. In particular, we employ the Best and Heckman (2012) radio catalogue of SDSS galaxies, where the presence of radio emission in each galaxy is linked to either star-formation activity or a radio-AGN, using their stellar-population properties, the ratio of the radio-to-optical-emission luminosity and standard BPT diagnostic diagrams. Fig. 4.7 again shows the $\Delta\sigma$ vs. ΔV diagram for our NaD-detected Seyfert 2 galaxies, where the coloured points now indicate whether the radio emission is dominated by star-formation or AGN activity. The Best and Heckman catalogue includes 97 (19%) of our Seyfert 2 sample with interstellar NaD absorption and, out of these objects, the radio emission is ascribed to a radio AGN only in 17 objects (18%). Most importantly Fig. 4.7 shows that, among the ten radio-detected Seyfert 2 that also exhibit an NaD-outflow, only one is classified as a radio AGN by Best and Heckman. Radio-AGN Seyfert 2 galaxies, in fact, generally show nearly zero or even slightly positive ΔV values, consistent with the results of Sarzi et al. (2016), and also with what we find when cross-correlating the Best and Heckman catalogue with our control sample.

In summary, only a few dozen Seyfert 2 galaxies show kpc-scale cold-gas outflows among the large sample of almost 10,000 SDSS galaxies that we have analysed. Furthermore, although nearly a third of these outflowing systems feature some of the most luminous of our Seyfert 2 nuclei, both the IR luminosity and the nature of the radio emission in our Seyfert 2 galaxies indicates that star-formation may be powering an even higher fraction of the NaD-outflows observed in the Seyfert 2 population.

4.4 Conclusions

Using SDSS DR7 data and the value-added catalogues of Oh et al. (2011, 2015), we have selected a nearly complete sample of $\sim 10,000$ nearby ($z < 0.2$) Seyfert 2 galaxies, and investigated the kinematics of their cold-gas medium at kpc-scales, as traced by interstellar NaD absorption

lines. In order to set a detection threshold for possible cold-gas outflows and draw conclusions on the incidence of AGN-driven outflows in the nearby Universe, we have also measured the properties of the interstellar NaD absorption in a carefully-selected sample of $\sim 44,000$ control galaxies that match our Seyferts in redshift, luminosity, size, light concentration, apparent flattening, colour and morphological classification. Our main results are as follows:

- The incidence of detected NaD absorption across our Seyfert 2 and control samples are similar, being 5.7% and 4.9% in the two populations respectively. This is particularly important, as it allows for a direct comparison between the cold-gas kinematics found across these two galaxy populations.
- Out of 9859 Seyfert 2 galaxies, only 53 show evidence of kpc-scale cold-gas outflows. Even accounting for inclination biases against the detection of NaD-outflowing systems, this result strongly suggests that optical AGN activity cannot be important in driving galactic winds capable of possibly quenching star-formation in the nearby Universe.
- The overall cold-gas kinematic behavior traced by the NaD interstellar absorption in Seyfert 2 and control galaxies (as shown in the $\sigma_{\text{NaD}} - \sigma_{\star}$ versus $V_{\text{NaD}} - V_{\star}$ diagrams) is rather similar, and the presence of an optical AGN does not boost the fraction of NaD outflows compared to the control sample, where such outflows are likely driven by star-formation. In fact, the incidence of NaD outflows among Seyfert 2s is actually lower, being $9.5^{+1.5}_{-1.3}\%$ of NaD-detected objects, compared to $16.2^{+0.9}_{-0.9}\%$ for the control sample.
- Consistent with previous studies, many NaD-outflowing Seyfert 2 galaxies are some of the brightest AGN ($\log L_{[\text{O III}]}$ $> 42.3 \text{ erg s}^{-1}$). However, this only accounts for 32% of the outflows detected in Seyfert 2s.
- On the other hand, ancillary radio and IR data of our Seyferts (available for 19% and 55% of the objects with interstellar NaD absorption) suggests that star-formation is likely to be the bigger contributor to the observed NaD-outflows. Among the NaD-outflowing systems with radio or IR measurements, around 90% show radio emission consistent with being powered by star formation rather than AGN activity, and 55% show IR luminosity consistent with a LIRG or ULIRG classification. That a similar behavior is observed across our control sample further indicates that star formation is the principal driver of many of the outflows observed in our Seyfert 2 galaxies.

The negligible fraction of Seyferts found to host outflows in this work reinforces the conclusions of recent studies (e.g. Kaviraj et al., 2015b; Sarzi et al., 2016), which have suggested that the long time delay between the onset of star formation and the triggering of the AGN hinders the ability of the AGN to strongly regulate star formation activity. In essence, the gas reservoir is greatly depleted before the AGN is triggered, so that the AGN acts largely to mop up residual gas in the system, rather than influencing the bulk of the star formation episode. It is worth noting again that, since these papers have studied galaxies outside clusters, this scenario operates in low-density environments (which, nevertheless, host the vast majority of galaxies) at low redshift. Since performing similar NaD analyses at high redshift is complicated by the low signal-to-statistical noise in the stellar continuum, drawing similar conclusions at higher redshift is currently infeasible.

While our results, combined with the recent literature, suggests that optical AGN activity may not play a dominant role in quenching star formation in the nearby Universe, future integral-field observations, possibly assisted by adaptive optics, may shed further light on the relative role of AGN and star formation in powering the kpc-scale cold-gas outflows found in Seyfert 2 galaxies. It is worth noting, in this context, that the [O III] luminosity distribution of our Seyfert 2 sample extends to the more typical values observed in Seyfert 1 systems. Hence, even though the measurement of NaD outflows in these objects is generally hampered, either by the presence of a non-thermal continuum, or by a real absence of neutral Sodium along the line of sight, it appears unlikely that Seyfert 1s could power many more kpc-scale cold-gas outflows, just on the basis that their engines could possibly be more powerful than the AGN probed in this study. On the other hand, it also remains to be established how frequently the ionised-gas outflows often found in nearby Type 1 AGN (e.g. Perna et al., 2017) really extend to kpc scales, again, for instance, through the use of integral-field spectroscopy (e.g. Cresci et al., 2015).

Integral-field observations may also clarify the impact of shocks on the nebular emission that is observed in most of the NaD-outflowing galaxies in our control sample, which very often shows composite AGN/star-forming activity and LINER-like emission. Indeed, if shocks do not always contribute to the observed nebular spectrum (as is the case in the study of Ho et al., 2014), this may leave some room for AGN, possibly during a very obscured phase (Perna et al., 2017; Harrison, 2017), to contribute to the outflows observed in our control sample and also in the more general galaxy population.

A further avenue of exploration is the role of mergers in driving inflows and outflows of cold

gas. Deep surveys like the Stripe 82 and, in particular, new datasets that are both wide and deep (e.g. DECaLS and those further downstream like LSST (Ivezic et al., 2008; Abell et al., 2009; Schlegel et al., 2015; Blum et al., 2016)) are capable of revealing faint tidal features due to recent interactions (e.g. Kaviraj, 2014b,a). Such data can be combined with the NaD analysis presented here to elucidate the role of merging in triggering galactic-scale outflows in the nearby Universe.

Nevertheless, to conclude, the results from this study suggest that galactic-scale outflows at low redshift are no more frequent in Seyferts than they are in similar non-active galaxies, that such optical AGN are likely not direct dominant contributors to the quenching of star formation in the nearby Universe and that star formation may be the principal driver of outflows even in systems that host an AGN.

Chapter 5

The Kinematically Decoupled Components in NGC 448 and NGC 4365

5.1 Overview and Motivation

Two distinct sub-classes of galaxies with signatures for centralized counter-rotation have been extensively studied before. On the one hand, “counter-rotating” population of stars can be found within some massive slow-rotator early-type galaxies (ETGs), where most often a KDC is usually present (e.g. Efstathiou et al., 1980, 1982; Franx and Illingworth, 1988; Jedrzejewski and Schechter, 1988; Franx et al., 1989). They are found to be rare amongst the early-type galaxy population ($\sim 7\%$), however such features seem to be abundant within $\sim 42\%$ of slow rotator systems (Krajnović et al., 2011) and even more rare ($\sim 2\%$), in particular, amongst just the fast rotator population (Emsellem et al., 2011). The stellar populations of galaxies with larger-scale KDCs are of old ages and have mainly negative metallicity gradients (e.g. Mehlert et al., 1998; Davies et al., 2001; Emsellem et al., 2004; Kuntschner et al., 2010; McDermid et al., 2015) in conjunction to the higher mass elliptical galaxy population. Furthermore, these KDCs seem to be of comparable age to the host galaxy as suggested by the absence of evidence for substantial stellar population age gradients (e.g. McDermid et al., 2006; Kuntschner et al., 2010; McDermid et al., 2015; Krajnović et al., 2015). Generally, the light profiles of KDC host galaxies are thought to be similar to the ones of the overall slow-rotators population of similar stellar

mass (e.g. Carollo et al., 1997a,b). However, the light profiles of galaxies with noticeable KDCs found in some slow rotators can also show the presence of additional photometric exponential or low Sérsic indices photometric subcomponents. This can stem from the more complex orbital families that can be present in non-axisymmetric galaxy potential systems often also displaying kinematically distinct cores (Krajnović et al., 2013). Even, despite continuous effort the origin of the KDCs observed such systems is still poorly understood. The nature of apparent angular momentum vector of KDCs with respect to their host galaxy can be argued to be an indication for an external formation mechanism. Earlier studies (e.g. Efstathiou et al., 1980; Kormendy, 1984), noting on the fact that the light profile of NGC 5813 can be well represented by two photometric sub-components, prompted investigation as to whether KDCs are not embedded remnants of smaller galaxies. This “core-within-a-core” formation scenario (e.g. Franx and Illingworth, 1988), however, contradicts the observation that galaxies with KDCs have negative metallicity gradients and compatible stellar population properties as the core should be more metal-poor than the rest of the galaxy if externally acquired. More scenarios for the formation of KDCs include the disruption of a satellite galaxy during a minor merger (e.g. Franx et al., 1989). In such an encounter, the distinct angular momentum of the KDC arises because of the specifics of the merger encounter (orbital configuration) and, in particular, because of the orbital angular momentum of the satellite. The merger of spiral galaxies (e.g. Bois et al., 2011) can also produce slow rotators with KDCs. Furthermore, KDCs can, in general, originate from acquired gas that settles at the bottom of the gravitational potential and subsequently form stars (e.g. Bender and Surma, 1992). The picture that KDCs are the remnants of past mergers is challenged by the observation that did not find any deep photometric evidence (e.g. shells) of a past merger event provided such features are long lived (e.g. Jedrzejewski, 1987). More likely, the KDCs could have formed at earlier epoch, as supported by the old stellar population associated with them, by a hierarchical merging of small systems, possibly involving gas (e.g. Bender and Surma, 1992). Such larger-scale KDC systems are intrinsically different from the ones with smaller scale (few hundred pc) KDCs. Such small-scale size KDCs are associated with younger stellar population ages and some interstellar medium. They are thought to form due to recent accretion of gas followed by a period of star-formation. Their presence is expected to be visible only for a limited time period, when the integrated light of the galaxy is out-shined by their newly formed young stellar population to dominate any measurement made on the spectra (McDermid et al., 2006). Finally, KDCs may not even be physically distinct embedded structures, but actually an observational effect from the observed in projection mass imbalance of the prograde and retrograde smooth population of stars in short-axis tube orbits within a triaxial galaxy (e.g. de Zeeuw

and Franx, 1991; Statler, 1991). Support for this hypothesis has been gained by some recent dynamical modelling effort (e.g. van den Bosch et al., 2008; Krajnović et al., 2015).

On the other hand, a small fraction $\sim 4\%$ (Krajnović et al., 2011) of galaxies can also host embedded counter-rotating discs (e.g. Rubin et al., 1992; Rix et al., 1992). Such 2σ systems are typically found within lower mass galaxies (Cappellari et al., 2013) than their early-type counterparts with KDCs. The multiple kinematic components in these galaxies have been revealed through the complex line-of-sight velocity distributions of their stellar content, often clearly exhibiting two peaks (e.g. Pizzella et al., 2014b). Evidence that such embedded discs with high angular momenta are present also comes from dynamical modelling (e.g. Cappellari et al., 2007; Mitzkus et al., 2017b). The relative masses, sizes, shapes, and stellar population properties of the two counter-rotating stellar discs would generally dictate the appearance of the velocity field (i.e. positions and amplitudes of the velocity dispersion peaks) of their host galaxy. One case of equal mass discs is NGC 4550 as confirmed by such modelling (Cappellari et al., 2007) and observations (Coccatto et al., 2013). Again using modelling, the mass was found to be approximately split 30 to 70% in between the two counter-rotating discs in NGC 4473 (Cappellari et al., 2007). Most often, the two components are associated with stellar populations of different properties and a large amount of ISM as traced by ionized gas emission (Coccatto et al., 2011, 2013; Johnston et al., 2013; Coccatto et al., 2015; Pizzella et al., 2014a; Mitzkus et al., 2017a). Galaxies with counter-rotating components do not appear to live in different environments (considering both satellites and companions of similar size) as demonstrated by Bettoni et al. (2001).

In this chapter we would explore the properties of two galaxies NGC 448 and NGC 4365 known to be hosting 2σ stellar velocity dispersion structure and a KDC, respectively, and attempt to use the counter-rotating stellar features in these galaxy as a proxy for their assembly. Katkov et al. (2016) independently studied NGC 448 and extracted a long-slit spectrum along the galaxy major axis to perform a thorough investigation of the properties of the two kinematically decoupled components. Our second galaxy NGC 4365 was also extensively observed with the SAURON integral-field spectrograph (Davies et al., 2001) and comprehensive dynamical modelling by means of the Schwarzschild (1979) orbit superposition method has shown that the KDC is not necessarily a true kinematically decoupled structure, but instead appears to be an artefact due to the triaxial nature of NGC 4365 (van den Bosch et al., 2008).

5.2 Observations and Data Reduction

The spectroscopic observations were carried out with the MUSE integral field spectrograph. Observations were taken in November and December, 2014 (NGC 448), and on 12 February, 2015 (NGC 4365), in service mode during grey time and photometric conditions. The seeing was about $1''$, as measured from the ESO meteo monitor. MUSE was configured in wide-field mode, without adaptive optics, and in nominal-wavelength mode; this setup ensured a field of view of $1' \times 1'$, a spatial sampling of $0.''2 \times 0.''2$ per pixel, a spectral coverage of 4800-9300 Å, and a spectral sampling of $1.25 \text{ \AA pixel}^{-1}$.

The observations were organised in several exposures of 1260 s intervals with offset sky exposures of 270 s in between. Scientific exposures were dithered by $\sim 1''$ and rotated by 90° with respect to each other to minimise the instrumental signature of the different spectrograph on the combined data cubes. The total exposure times are 42 m and 2.9 h for NGC 4365 and NGC 448, respectively.

The basic data reduction (bias subtraction, flat fielding, and wavelength calibration) was carried out using the MUSE ESO pipeline version 1.6.2 (Weilbacher et al., 2012). We also utilised the Zurich Atmosphere Purge (ZAP) sky subtraction procedure (Soto et al., 2016) to remove any residual sky features left over by the main MUSE ESO data-reduction pipeline. The ZAP code implements a sky-subtraction method based on a principal component analysis complemented with data filtering and segmentation that allows robust flux preservation with negligible or no impact on any astronomical source line profiles. These two procedures were executed through their ESO Reflex environment (Freudling et al., 2013) implementations. In the case of NGC 448, the ZAP cleaning was done by directly evaluating the sky on the object cube itself. For NGC 4365, we used the dedicated sky exposures as the galaxy occupied the whole field of view, therefore leaving no spaxels dominated purely by the sky signal. As a subsequent step we ran the Cappellari and Copin (2003) Voronoi binning algorithm aiming to achieve a signal-to-noise ratio (S/N) of 90, evaluated considering the whole MUSE spectral wavelength range. We consider the mean of the spectrum as the signal, and the noise as the square root of the mean of the variance returned by the MUSE ESO pipeline. Furthermore, to suppress any of the low-signal levels in the outer parts of the observed field of NGC 448 we chose to apply a further elliptical mask aligned to the galaxy position angle (PA) with a semi-major to semi-minor axis ratio of 1.5 on the MUSE reconstructed white-light image with a semi-major axis of 190 spaxels,

TABLE 5.1: Photometric components in NGC 448 and NGC 4365. The first column gives the description of the fitted photometric component. Second column is the integrated magnitude of the photometric component returned by `galfit` (see Sect. 3). The third column provides the estimated effective radius in arcseconds. The fourth column outlines the best-fitting Sèrsic index. The fifth column is the semi-minor to semi-major axial ratio of the best-fitting model. The last column is the position angle of the best-fitting Sèrsic profile.

Name	mag	R_e	n	b/a	PA
KDC (NGC 448)	19.32	1.04	1.16	0.89	-52.9
KDC (NGC 448)	17.25	6.50	1.03	0.28	-61.0
Main (NGC 448)	16.11	22.40	1.89	0.89	-65.0
KDC (NGC 4365)	6.70	27.72	1.46	0.77	44.3
Main (NGC 4365)	9.10	3.90	0.98	0.75	42.7

thereby minimising the effect of the outer regions with very low S/N on the size of the bins in sections of higher S/N. No additional masking was used in the case of NGC 4365.

5.3 NGC 448 and NGC 4365

5.4 Photometric decomposition

In this section we exploit the exquisite imaging capabilities of MUSE by analysing the galaxy images obtained by collapsing the datacubes along wavelength. The purpose is to identify the presence of photometrically distinct components and compare their properties with those of the structural components that we would identify via the spectroscopic decomposition (see

§ 5.5.3). In this way it is possible to i) establish a direct association between photometric and kinematic components; and ii) to use the photometric information as priors in the spectroscopic decomposition to constrain the flux of the components. The use of photometric priors in the spectroscopic decomposition to improve the accuracy of the kinematics and stellar population measurements has been successfully applied in several cases (e.g. Coccato et al., 2014, 2015; Sarzi et al., 2016; Tabor et al., 2017).

The photometric decomposition is performed using the two-dimensional (2D) fitting algorithm `galfit` (Peng et al., 2002). We use the reconstructed images rather than independent archive images in order to have the same conditions (e.g. seeing, sky background contamination) as the spectroscopic data. Indeed, the purpose is not to retrieve accurate parameters of the structural components (e.g. seeing-corrected scale radii), but to obtain good fitting surface brightness

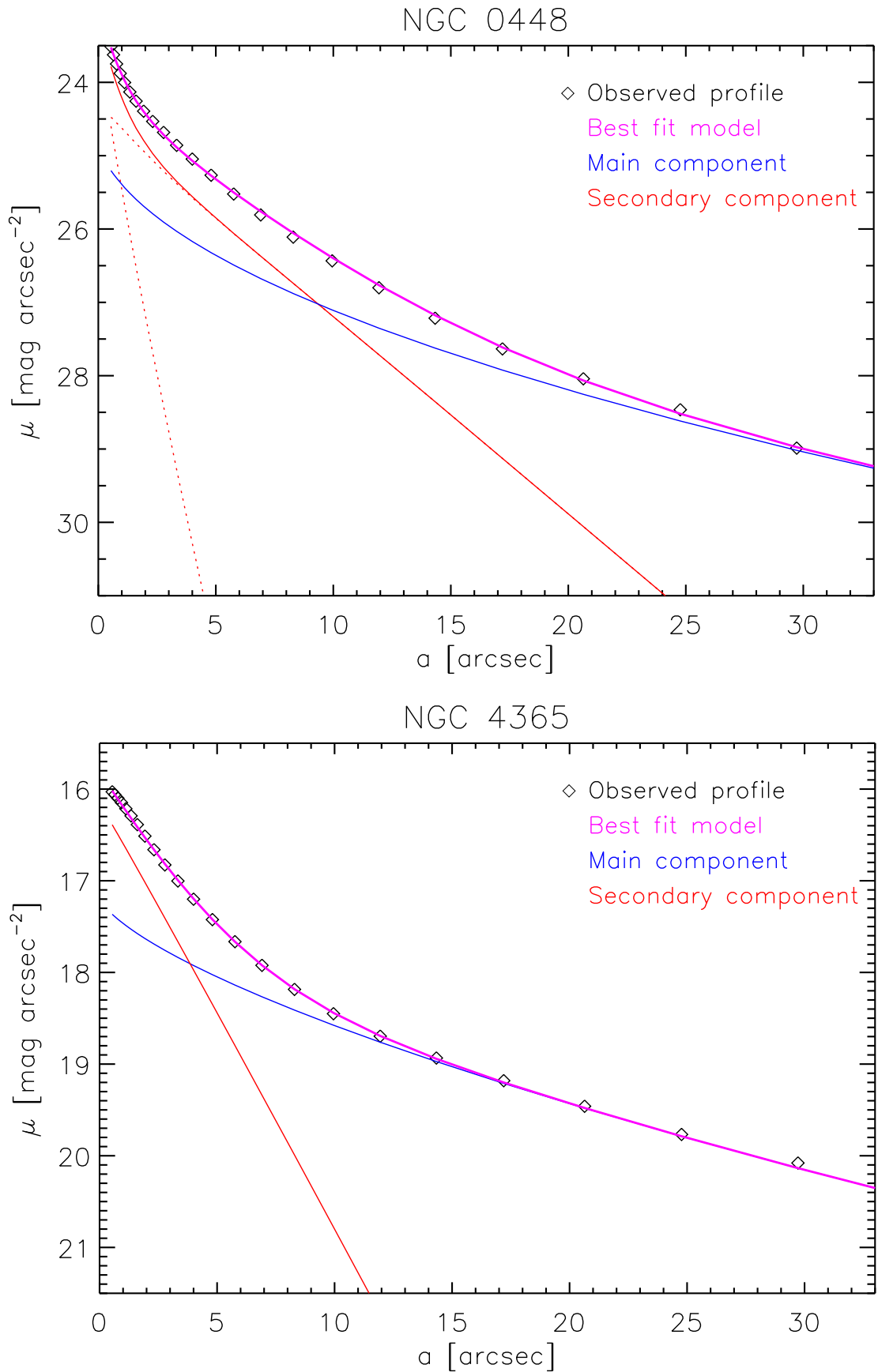


FIGURE 5.1: Photometric decompositions for NGC 448 (upper panel) and NGC 4365 (lower panel). Each plot shows: the surface brightness profile measured from the reconstructed images (diamonds), the best fit model (magenta) as obtained from the combination of the structural components that are associated to the main galaxy (blue) and to the kinematically distinct core (KDC, labelled as “secondary component”, in red). In the case of NGC 448, the KDC is assumed to include two subcomponents (dashed red lines).

profiles that contain the same observational effects as the spectra, in order to eventually use them as constraints in the spectral decomposition.

In our decomposition, all components are parametrised with Sersic profiles, which allows for the behaviour of both disk and spheroidal structures to be encapsulated. Our fits include only the minimum number of components required to reach a good fit, rejecting additional components that would contribute only a relatively small fraction of the stellar light (e.g. less than the 5% freedom that we already allow in our spectroscopic decomposition when adopting photometric priors, § 5.1). For NGC 448, we identified three Sersic components and for NGC 4365 we identified two. We also note that fits based on one Sersic component never lead to satisfactory models for the observed surface-brightness distribution, in particular in the regions where we observe a KDC signature. Table 5.1 summarises the properties of our identified components, whereas in Fig. 5.1 we compare their surface brightness radial profiles with those measured on the reconstructed images using the *iraf* task *ellipse* (Jedrzejewski, 1987).

As regards NGC 448, we would like already report here that the sum of the first two photometric components in NGC 448 is likely associated with the kinematic counter-rotating component, whereas the third photometric component is in fact ascribed to the main galactic stellar kinematic component. We also note that within the MUSE field of view, our photometric model agrees well with what was predicted by Katkov et al. (2016) on the basis of their innermost first three components, consisting of a Sersic and two exponential profiles. Indeed, even though their fourth and most extended Sersic component is responsible for 17% of the total light of NGC 448, this halo component does not contribute much light within the MUSE field of view, dropping already to less than a 6% fractional contribution at a radius of $20''$.

As for NGC 4365, we note that although a single core-Sersic profile can match well the light profile in the KDC region of this galaxy (Ferrarese et al., 2006), here we performed a two-component decomposition for the purpose of testing whether these would then match the results of a spectral decomposition. As discussed below, we find no evidence for two structurally different stellar components in NGC 4365.

5.5 Stellar kinematics

5.5.1 One-component kinematic fit

As a first step in extracting the individual properties of our two distinct stellar structural components in these galaxies we used the Penalized Pixel-Fitting (Cappellari and Emsellem, 2004) and the Gas AND emission Line Fitting (Sarzi et al., 2006) methods to recover the velocity, velocity dispersion, and the h_3 and h_4 coefficients of the Gauss-Hermite parametrisation van der Marel and Franx (1993) of the line-of-sight (stellar) velocity distribution and any potential ionized-gas emission line properties in each Voronoi bin. The pPXF procedure uses a model that is parametrised in terms of Gauss-Hermite functions for the LOSVD, and a set of linearly combined template spectra to best match the observed galaxy spectrum in pixel space. An important requirement for the extraction of an accurate LOSVD is that the spectral resolution of the templates provided to build the observed galaxy spectrum matches the instrumental one. The spectral resolution was measured by fitting a high-resolution solar spectrum template to the twilight spectra, after having combined them following the same sequence of the science observations, similar to (Sarzi et al., 2018a). The measured instrumental FWHM is 2.8 \AA , its variation across the field of view and the wavelength range is $\sim 0.1 \text{ \AA}$. The adopted method ensures the measurement of the effective instrumental spectral resolution, which includes both the instrument properties and data reduction steps. With these considerations in mind we adopted as template spectra the Vazdekis et al. (2012, MIUSCAT) stellar population synthesis models, spanning the broad $3465\text{-}9469 \text{ \AA}$ wavelength range based on the Girardi et al. (2000) stellar isochrones with $-0.71 < [Z/H] < +0.22$, $0.06 < t < 18 \text{ Gyr}$, and with a unimodal initial-mass function with a power-law slope coefficient of 1.3 (Salpeter, 1955). This stellar population synthesis model template library with a constant FWHM resolution of 2.8 \AA was retrieved through the on-line portal¹. Prior to performing both pPXF and *GandALF* fits, the spectra of both our template library and observations were logarithmically re-binned to a common velocity step of 55.17 km s^{-1} . Due to the higher spectral resolution and relatively high S/N of the CaT absorption lines we extracted the kinematics of NGC 448 within the $8350\text{-}8900 \text{ \AA}$ spectral region. A first degree additive polynomial and a third-degree multiplicative polynomial were used to account for template mismatch, any imperfections in the sky subtraction procedure, and potential inaccuracies stemming from the spectral calibration process. For NGC 4365, we instead opted to extract the kinematics by creating an optimal template to match the summed up spectrum within

¹<http://www.iac.es/proyecto/miles/pages/webtools/tune-ssp-models.php>

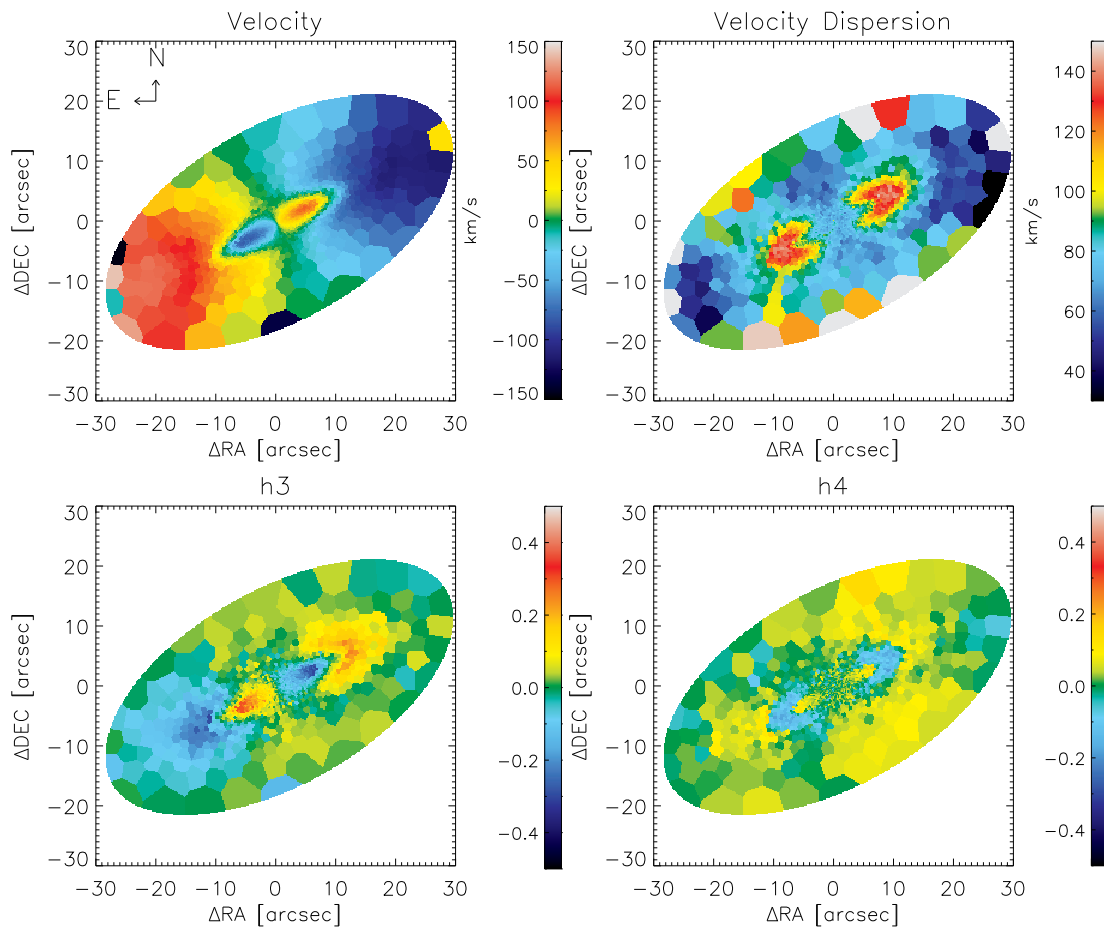


FIGURE 5.2: The one-component kinematic maps for NGC 448. Top Left: The retrieved velocity field. Top Right: The velocity dispersion field. Bottom Left: The map of the h3 Gauss-Hermite coefficient in the parametrisation of the LOSVD. Bottom Right: The map of the h4 Gauss-Hermite coefficient in the parametrisation of the LOSVD.

a central circular aperture by performing an initial pPXF fit. This template and a high-order additive and multiplicative polynomial (15th and 15th degree, respectively) were later adopted to similarly extract the one-kinematic-component maps through pPXF and *GandALF* within each Voronoi bin.

Figure 5.2 presents the 2D kinematic maps for NGC 448 extracted by performing the procedure described above. We observe abrupt changes in the direction of the velocity field (upper-left panel) with a maximum rotation amplitude of $\sim 140 \text{ km s}^{-1}$. There is a pronounced anti-correlation between the velocity and h3 coefficient in the outer regions of the galaxy, plausibly due to the presence of an extended disk component that rotates in a noticeably different manner to that of the main stellar body. Moreover, within the inner central part, this anti-correlation persists even after the velocity field switches direction. We confirm the classification of NGC 448 as a “ 2σ ” galaxy (top-right panel), because of the two pronounced symmetric off-centre peaks

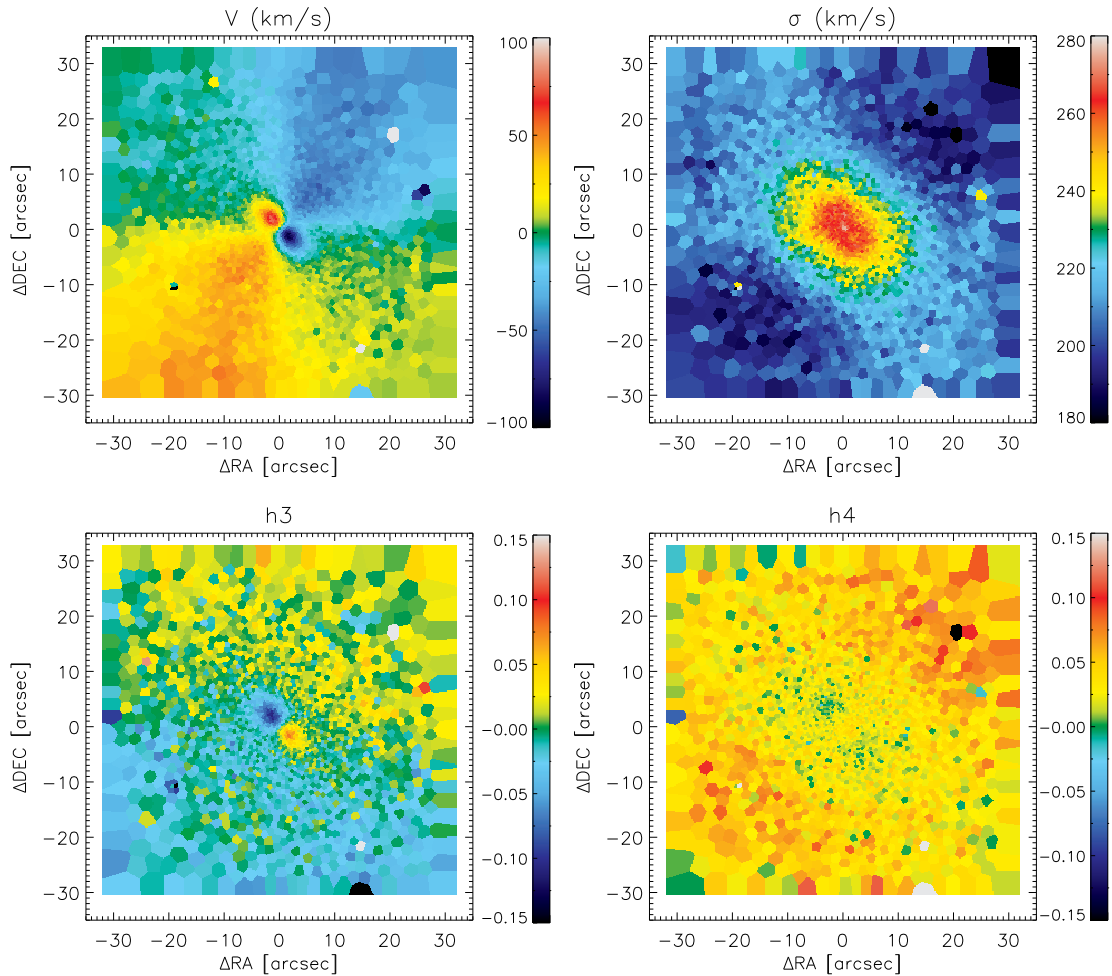


FIGURE 5.3: The one-component kinematic maps for NGC 4365. Top Left: The retrieved velocity field. Top Right: The velocity dispersion field. Bottom Left: The map of the h3 Gauss-Hermite coefficient in the parametrisation of the LOSVD. Bottom Right: The map of the h4 Gauss-Hermite coefficient in the parametrisation of the LOSVD.

of $\sim 230 \text{ km s}^{-1}$ in the velocity dispersion map. The behaviour of the h4 Gauss-Hermite coefficient used to capture symmetric departures from purely Gaussian LOSVD profile indicates that at the positions where the velocity dispersion is at its highest values the LOSVD has pronounced, extended “wings”. Taken together, such kinematic behaviour in NGC 448 is found to be symptomatic of the presence of an embedded central intrinsically counter-rotating disk (Rubin et al., 1992; Rix and White, 1992a; Bertola et al., 1996; Cappellari et al., 2007; Vergani et al., 2007) that from these maps appears to span at least $\sim 13''$ in its radial extent.

In Figure 5.3 we show the 2D kinematic maps for NGC4365. The velocity field (upper left panel) displays a clear “four-part counter-rotating” morphology because it possesses four maxima at different amplitudes and positions and the velocity field has a distinctive “S-shape” twist (Statler, 1991). The central velocity extrema have an amplitude of $\sim 80 \text{ km s}^{-1}$, whereas in

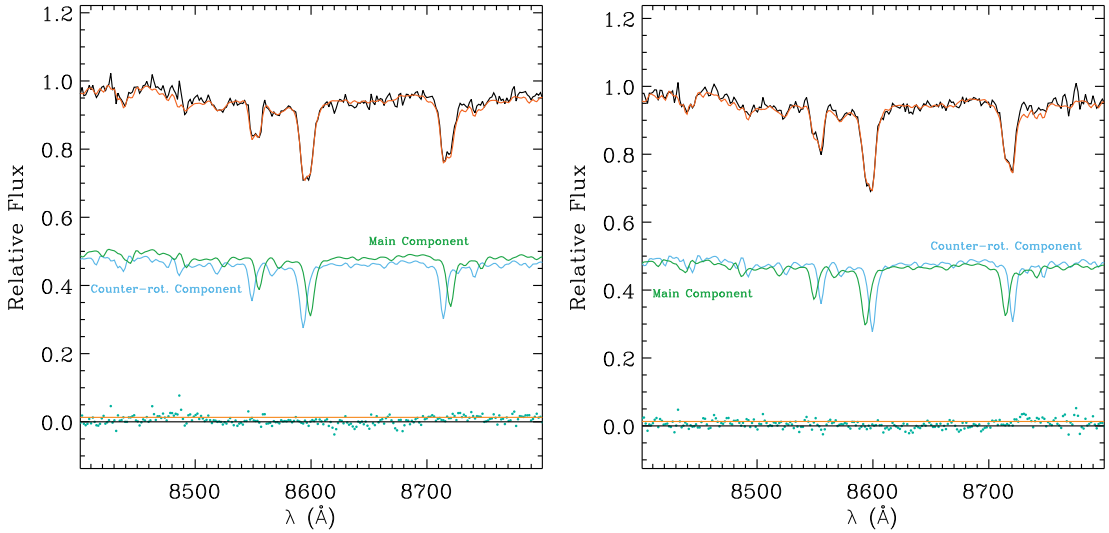


FIGURE 5.4: Fits to the CaT spectral regions for bins of approximately 9 arcsec roughly along the major axis of the centre of the NGC 448 field where the two distinct kinematic components have an absolute velocity difference of $\sim 212 \text{ km s}^{-1}$. The best-fitting models are in green. The contributions of the counter-rotating and main galaxy components are shown in blue and red, respectively. The green points signify the residual from our fitting and the orange line is set at the level of the resistant dispersion of the residual.

the outer regions the velocity amplitude at the extrema is smaller ($\sim 55 \text{ km s}^{-1}$). The velocity dispersion (upper-right panel) is centrally peaked with a maximum value of $\sim 270 \text{ km s}^{-1}$. The h_3 coefficient (bottom-left panel) strongly correlates with the observed velocity pattern where we also observe a kinematically distinct behaviour for the velocity field. Such correlation is less pronounced in the outer parts.

5.5.2 The kinematic decomposition procedure

To derive the individual properties of the two different structural components, we followed a procedure identical to that of Coccato et al. (2011). This so-called kinematic decomposition method takes advantage of the characteristic spectral imprint (e.g. asymmetric or double trough line profiles) of a spectrum, which constitutes two overlapping stellar populations of different kinematics. The method builds on pPXF in that it aims to model the observed spectra and therefore to also achieve a separation of two possible stellar kinematic structural components in every spatial bin, by constructing a unique set of linearly combined templates for each component convolving it with a separate Gaussian line-of-sight velocity distribution function. To account for any potential inaccuracies in the spectral calibration and the effects induced by the reddening from dust on the spectra similarly to pPXF, our procedure adopts multiplicative Legendre polynomials of a pre-selected order assumed to be identical for both components. We avoid the use of

additive Legendre polynomials, because they could profoundly bias our line-strength measurements (Cappellari, 2017). Given the complexity of this fitting approach, a useful simplification is achieved through the normalisation of both the galaxy spectra and templates to unity. In this way we are able to obtain the fractional contribution to the flux within a given wavelength range of both components in terms of a single parameter instead of assigning two separate light fraction contribution parameters. Due to the surprisingly good calibration in both our chosen set of templates and MUSE spectra, we found that such an arbitrary choice of normalising wavelength range does not influence any of the forthcoming conclusions and chose for simplicity to normalise all templates and MUSE spectra with respect to their mean levels. The main workhorse minimisation procedure within both pPXF and our kinematic decomposition method is the interactive data language (IDL) implementation (Markwardt, 2009b) of the Levenberg-Marquardt least-squares curve-fitting algorithm that is sometimes found to converge, not necessarily towards a global minimum. We experimented with switching it with the slower, but potentially more sturdy, downhill simplex (AMOEBA) method (Nelder and Mead, 1965) with little to no success in line with the Cappellari (2017) finding that the minimisation algorithm does not noticeably influence the inferred pPXF results. Even though our fitting procedure is robust enough, it is not necessarily immune to completely unreasonable sets of initial guesses for the velocities of the two kinematic components. Therefore, we tested the impact of varying the initial guesses for both kinematic components (i.e. their velocities and velocity dispersions) in our decomposition model until we were convinced of the general validity of the results obtained.

5.5.3 Two-component fit

As described above, such a kinematic decomposition procedure allows us to simultaneously and independently retrieve the properties of the kinematic components, namely their velocity, velocity dispersion, fractional contribution to the flux (light fraction), and best-fitting stellar population template. Here, we focus on the individual photometric and kinematic properties of the observed distinct components of our galaxies.

5.5.3.1 NGC 448

Figure 5.4 shows an example spectrum in the CaT region for NGC 448 near the position of maximum velocity difference, where both components contribute almost the same fraction to the overall light (at $\sim 9''$). In the case of NGC 448, the line profiles are clearly double peaked,

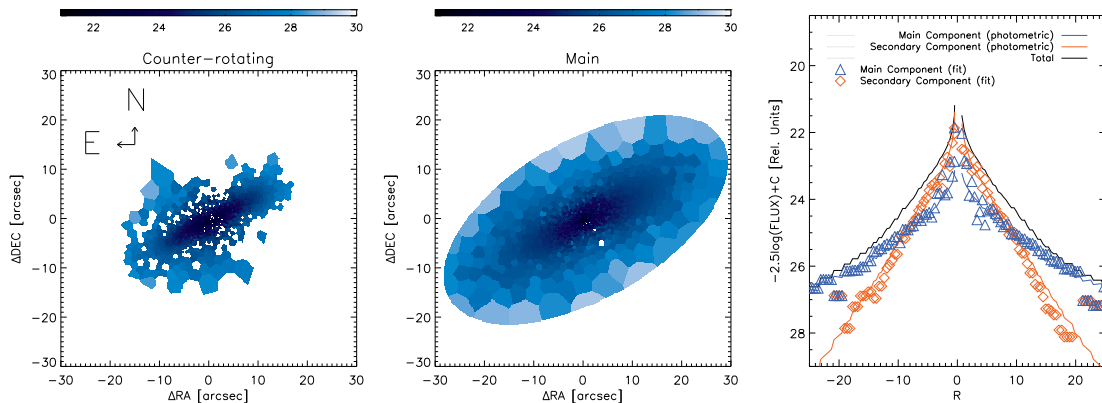


FIGURE 5.5: Spectral flux maps and profile averaged over the number of spaxels for NGC 448. Left panel: Reconstructed surface-brightness map of the counter-rotating component. Middle panel: Reconstructed surface brightness map of the main component. Right panel: Radial profile for both kinematic components, taken through a pseudo slit approximately aligned with the semi-major axis. The black, orange, and blue solid lines illustrate the photometrically derived total, the counter-rotating, and the main component flux contributions, respectively. The blue triangles and the orange diamonds show the flux contribution derived for the counter-rotating and main components, respectively, as derived through our fitting procedure without imposing any constraints.

highlighting the complex nature of the underlying stellar LOSVD. Figure 5.5 shows the reconstructed brightness maps averaged over the number of spaxels of both kinematic components. The light profiles taken along the photometric major axis show that our kinematic and photometric decompositions agree remarkably well with each other (right panel of Fig. 5.5), so that the more (primary) and less (secondary) extended photometric components can be confidently attributed to the main and counter-rotating kinematic components, respectively. In this respect, we presently assume that the innermost photometric component belongs to the counter-rotating structure, consistent also with the conclusions of (Katkov et al., 2016), although our data do not allow us to rule out that more central light could be assigned also to the main component. This limitation, however, does not affect our main conclusions. Further adaptive-optics-assisted MUSE observations may help in understanding the kinematics of NGC 448 in the very central few arcseconds.

We chose to discard all bins where either the fitting routine did not converge or the fractional light contribution of the counter-rotating component was less than 15%. This somewhat arbitrary choice is motivated by the observation that the light of the less-extended kinematic component experiences a sharp rise at a radius of $\sim 19''$ along the pseudo-slit extracted from the IFU data, where its contribution to the total flux indeed drops below 0.15. Furthermore, we retrieved the amplitude of the strongest CaT line and compared it to the level of the residual noise evaluated by computing the robust standard deviation of the residual (Beers et al., 1990, their Eq. 9).

The turn-off where the amplitude of the line drops below three times the residual noise level coincides roughly with our adopted light fraction threshold.

Nevertheless, because we did not impose any prior on the spatial extent of both of our kinematic components, the decomposition within the regions of small or zero velocity difference in between them erroneously detected a higher light fraction in one of the components. Figure 5.6 shows the two-dimensional (2D) kinematic maps for NGC 448. The upper-left panel gives the retrieved velocity for the counter-rotating kinematic component. Both kinematic components rotate with comparable velocities and a maximum velocity amplitude for the counter-rotating component of $\sim 120 \text{ km s}^{-1}$ at a distance of $\sim 11''$ from the centre of the galaxy. Its velocity dispersion is significantly lower (mean σ_* of $\sim 40 \text{ km s}^{-1}$) in comparison to that of the main stellar body ($\sim 60 \text{ km s}^{-1}$), strengthening the idea that the counter-rotating component is indeed a disk. Driven by the excellent correspondence between the light profiles of the photometric components determined in Section 5.4 and those of the kinematic components, we decided also to impose the light contribution we obtained from photometry into our kinematic spectral model allowing only a small adjustment of at most 5%. In Fig. 5.7 we show again the reconstructed surface brightness maps of both components and correspondingly their major-axis profiles. We consider again, as for our previous estimate, that we can reliably detect the counter-rotating component when its contribution to the total flux is higher than 0.15. In the bins where this condition was met (left panel of Fig. 5.7) the mean absolute difference between the fixed photometric fractional contribution and the one retrieved by our previous analysis is $\sim 7.5\%$. This difference is higher predominantly within the very central region, where the velocity difference between both kinematic components is rather small and thereby most likely did not originally allow a very robust kinematic decomposition. Even though fixing the photometric contributions is not strictly necessary, because of the complex nature of our kinematic decomposition method it relieves some of the parameter degeneracies. This, in turn, results in a more consistent parameter estimation. Moreover, in doing so we need not impose somewhat fiducial criteria to separate the Voronoi bins which contain both kinematic components from the ones where just a single one is present. Instead, as such a criteria, we simply adopted the light fraction above which we deem the detection of the counter-rotating component reliable.

We now describe the kinematics obtained by imposing the photometric decomposition, which we adopt in the remainder of our further analysis. Figure 5.8 shows the velocity and velocity dispersion maps for our two kinematically distinct components. We have replaced all bins where we recovered the fractional contribution of the counter-rotating component to be less than 15%

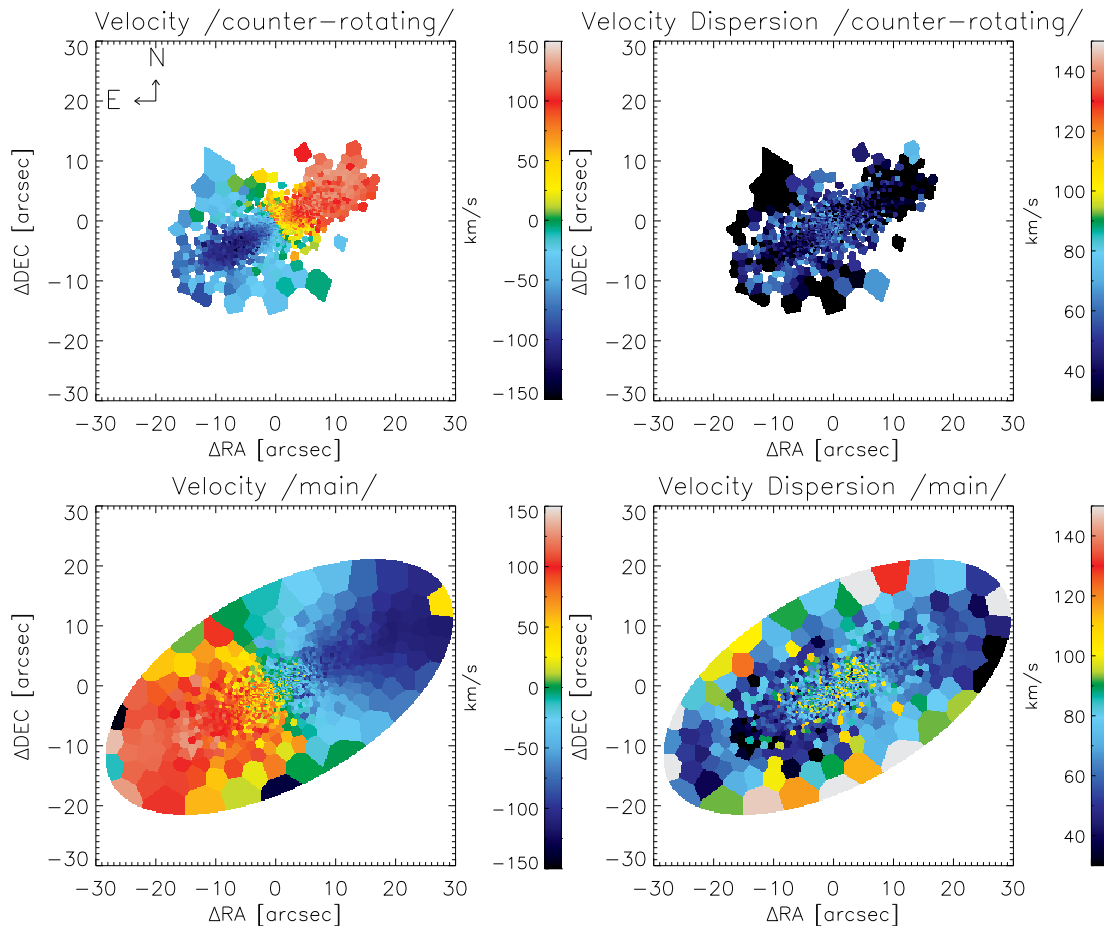


FIGURE 5.6: The extracted kinematic maps without imposing any priors on the fractional light contribution for NGC 448. The bins are selected such that the fractional contribution of the counter-rotating component is greater than 15%. Top-left panel: The velocity field of the counter-rotating kinematic component. Top-right panel: The velocity dispersion map for the counter-rotating component. Bottom-left panel: The velocity field of the main kinematic component. Bottom-right panel: The velocity dispersion map for the main component.

within the main stellar one with our previous single kinematic-component fit. The results that we obtained folding the photometric decomposition information back into our kinematic decomposition also agree to a high degree with the ones where it was left as a free parameter. The mean absolute differences between the kinematics extracted with and without incorporating the photometric decomposition are $\sim 11 \text{ km s}^{-1}$ in velocity and $\sim 12 \text{ km s}^{-1}$ in velocity dispersion. The velocity amplitudes for both components are again comparable with the counter-rotating component reaching a maximum of $\sim 125 \text{ km s}^{-1}$ at a distance of $\sim 12''$. The main component has a maximum velocity amplitude of $\sim 135 \text{ km s}^{-1}$ in the outskirts of the field along roughly the major photometric axis. The counter-rotating disk component has a lower velocity dispersion and a mean value of $\sim 46 \text{ km s}^{-1}$ with a maximum of $\sim 75 \text{ km s}^{-1}$ in the very centre and a minimum of $\sim 30 \text{ km s}^{-1}$. The main component has higher velocity dispersion with a mean value of $\sim 86 \text{ km s}^{-1}$.

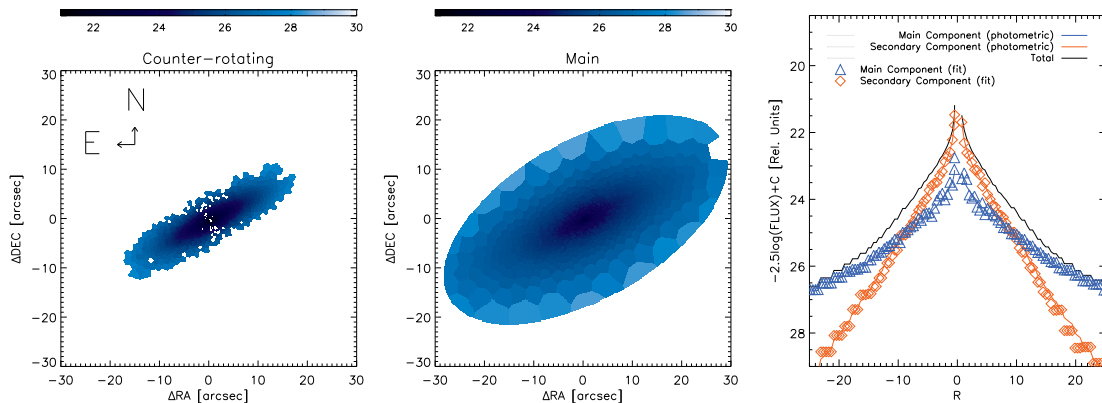


FIGURE 5.7: Spectral flux maps averaged over the number of spaxels and profile fixed to the one recovered by the photometric decomposition for NGC 448. Left panel: Reconstructed surface brightness map of the counter-rotating component. Middle panel: Reconstructed surface brightness map of the main component. Right panel: Radial profile for both kinematic components, taken through a pseudo slit approximately aligned to the semi-major axis. The black, orange, and blue solid lines illustrate the photometrically derived total, counter-rotating, and main component, respectively, flux contribution. The blue triangles and the orange diamonds show the flux contribution derived of the counter-rotating and main components as derived through our fitting procedure without imposing any constraints.

We report an absence of ionized-gas emission in NGC 448. Although the [O III], $H\beta$, [N II], and $H\alpha$ emission lines should normally reside in the 4700-6715 Å wavelength range, none of them had a sufficient amplitude-to-noise retrieved through our *GandALF* fit to surpass the detection threshold of > 3 . Furthermore, neither the Katkov et al. (2016) long-slit spectrum, nor the McDermid et al. (2015) ATLAS^{3D} observations with SAURON showed the presence of such emission lines. The lack of gas is further enforced by the limits put on the H_2 mass ($\log M(H_2) < 7.74 [M_\odot]$) of Young et al. (2011) based on IRAM CO J = 1–0 and J = 2–1 emission observations. In addition, the galaxy is not detected in the FIRST 1.4 GHz survey, excluding the presence of strong-enough star formation, that could serve as an ionizing source (Nyland et al., 2017).

5.5.3.2 NGC 4365

We also applied the kinematic decomposition technique to NGC 4365. Figure 5.9 shows a spectrum of NGC 4365 as an example of our attempt at performing such a decomposition in the CaT region. Unlike the case for NGC 448, our kinematic and photometric decompositions did not return light fractions consistent with one another. Moreover, the retrieved kinematics were found to be very highly dependent on the choice of the set of initial guesses. Furthermore, the derived fractional light contribution did not display any consistent profile when left free to vary. Our photometric decomposition shows an excess of light in comparison to a pure Sèrsic fit in the

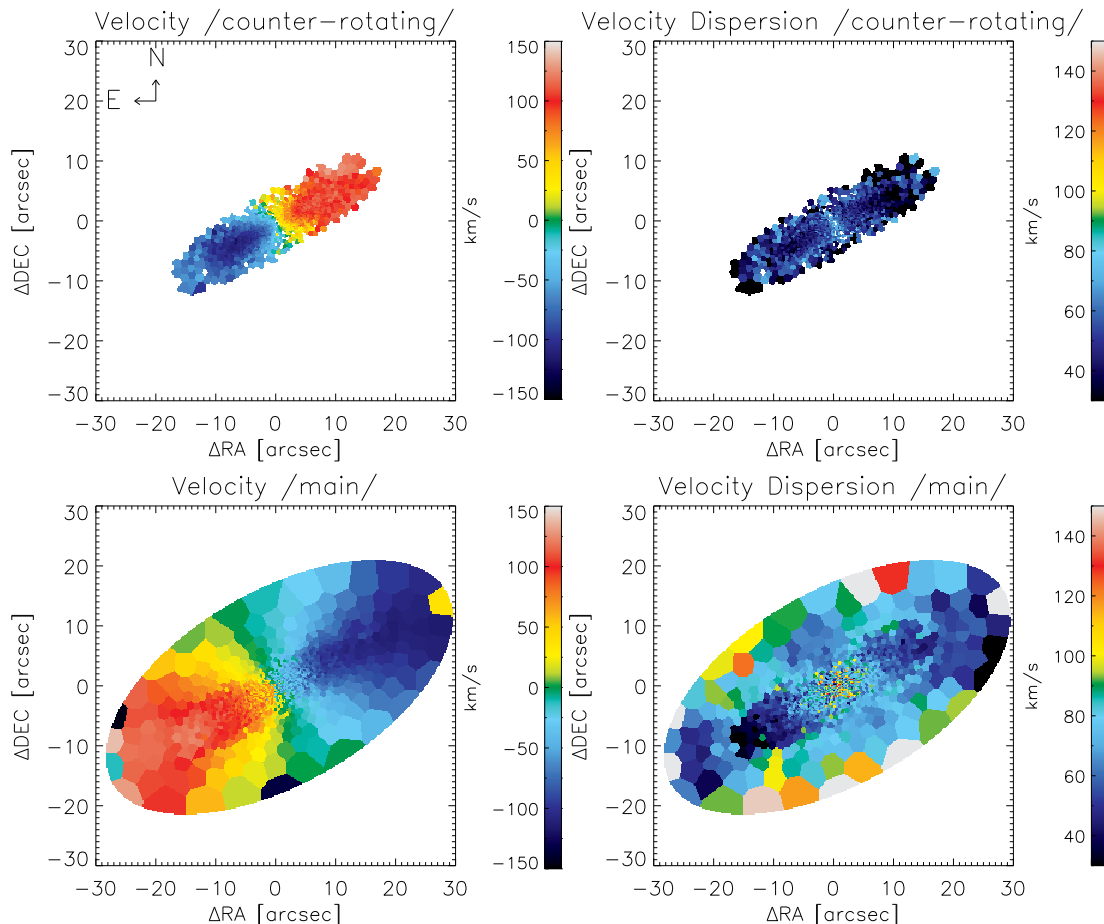


FIGURE 5.8: The extracted kinematic maps with the fractional light contribution fixed to correspond to the photometrically derived one for NGC 448. The bins are selected such that the fractional contribution of the counter-rotating component is greater than 15%. Top-left panel: The velocity field of the counter-rotating kinematic component. Top-right panel: The velocity dispersion map for the counter-rotating component. Bottom-left panel: The velocity field of the main kinematic component. Bottom-right panel: The velocity dispersion map for the main component.

central regions of the galaxy (Section 5.4). The presence of this exponential-like photometric component, however, is most likely due to the structures formed from the orbital families that can be found in galaxies of triaxial intrinsic shape, as previously found for some of the non-barred slow-rotator early-type galaxies with KDCs (Krajnović et al., 2013), and not those with a truly kinematically decoupled structure. Even though we obtain a somewhat satisfactory fit to the spectra for some of the Voronoi bins using our decomposition procedure, the velocity and velocity dispersion fields we recover for the two different components are highly irregular. The highly non-symmetric LOSVD profiles in the centres of some ellipticals, such as the one present in NGC 4365, have previously been shown to be well matched by a superposition of two Gaussian forms of different width (e.g. Franx and Illingworth, 1988; Bender, 1990; Rix and White, 1992b). Nevertheless, this finding alone, and especially without a matching photometric

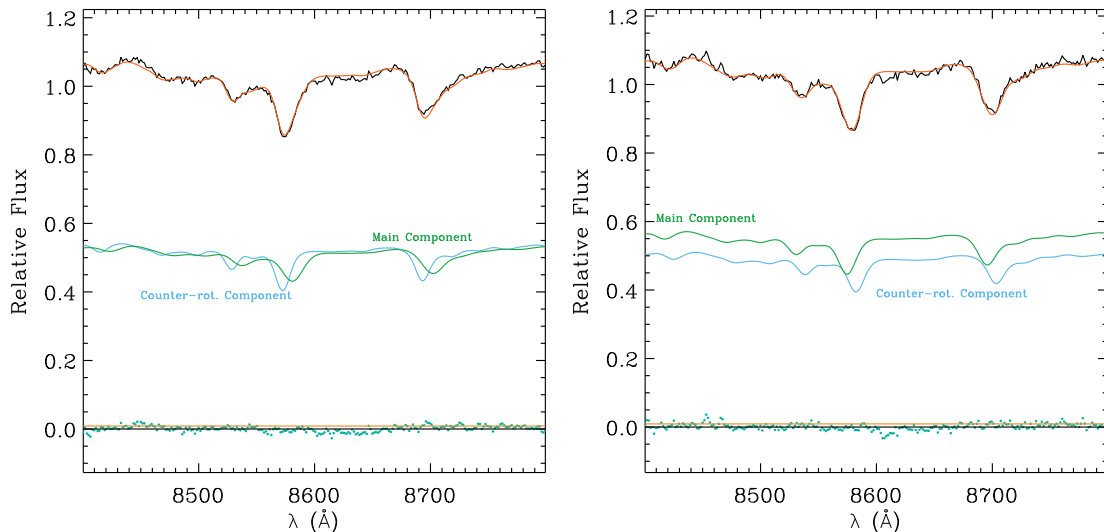


FIGURE 5.9: Fits to the CaT spectral region of NGC 4365 for bins approximately 10.5 arcsec away from the field center in the regions where we expect a large velocity difference between the two suspected kinematic components.

signature, is not sufficient to provide enough evidence for the presence of a physically decoupled kinematic component.

5.6 Line-strength indices and stellar population properties of NGC 448

In this section we present the line-strength maps and stellar population properties of the individual kinematic components (i.e. counter-rotating disk and main stellar body) of NGC 448 where our kinematic decomposition technique successfully recovered their presence.

5.6.1 Line-strength indices

Our initial choice to extract the kinematics only in the limited CaT spectral region for NGC 448 did not prevent us from obtaining the Lick absorption line-strength indices as defined by Worthey et al. (1994). We re-fitted the NGC 448 spectra in the 4700-6715 Å wavelength range, where one finds the strongest stellar absorption lines defining the $H\beta$, Mg b , Fe5270, Fe5335, Fe5406, Fe5709, Fe5782, NaD, TiO₁, and TiO₂, using the prior two-component kinematics as an initial guess for our kinematic decomposition. A small adjustment of ± 20 km s⁻¹ in velocity, ± 20 km s⁻¹ in velocity dispersion, and ± 0.05 for the light fraction in the counter-rotating component was allowed in order to accommodate any expected change in the extracted kinematics. Generally, the kinematics obtained in two sufficiently distant wavelength domains (e.g. 4800-5380

Å and 8480-8750 Å) could differ. In a varying mixture of stellar populations with different age, the fraction of young stars, outputting their light predominantly in the blue end of the spectrum, and older stars, dominant at the red end, could give rise to non-negligible $\sim 5 \text{ km s}^{-1}$ differences in velocity and velocity dispersion and variation as big as ~ 0.02 in the h3 and h4 Gauss-Hermite coefficients (Arnold et al., 2014). This is especially relevant when dealing with possibly kinematically decoupled structures such as those in our investigation and also observed by Mitzkus et al. (2017a). The kinematic decomposition we utilised in modelling the spectrum of our galaxies returns the best-fitting linear combination of library templates. We proceeded to extract the aforementioned line-strength indices on them. Coccato et al. (2011) carried out extensive verification by means of Monte Carlo simulations to test the ability of the best-fitting linear combination of templates to capture the underlying stellar population properties under different S/N levels and kinematic behaviours albeit with spectra obtained using VLT/VIMOS. The systematic error levels were found to be negligible with respect to the ones driven by the S/N. We have no reason to believe that the kinematic decomposition procedure would behave differently in our specific case of applying it to MUSE spectra. To crudely estimate the error on the measurements of the line-strength indices, we adopted a constant noise level equivalent to $\sqrt{2}$ of the resistant standard deviation (“robust sigma”) of the difference between the spectra and our best-fit model and the procedure outlined by Cardiel et al. (1998). Furthermore, we also evaluated the combined $[\text{MgFe}]' = \sqrt{\text{Mg } b(0.82 \cdot \text{Fe}5270 + 0.28 \cdot \text{Fe}5335)}$ and $\langle \text{Fe} \rangle = (\text{Fe}5270 + \text{Fe}5335)/2$ indices (Thomas et al., 2003; Gorgas et al., 1990). Both are considered to be good proxies for the total metallicity. In particular, $[\text{MgFe}]'$ has been demonstrated to be only weakly dependent on the alpha-element-to-iron abundance ratio, and the ratio of the Mg *b* to $\langle \text{Fe} \rangle$ for old stellar populations is found to correlate reliably with the total $[\alpha/\text{Fe}]$ enhancement (Thomas et al., 2003).

Figure 5.10 shows the strength of these indices for the bins where the relative light fraction of the counter-rotating component is higher than 15% and both components have velocity shifts relative to the galactic systemic one greater than 30 km s^{-1} with the corresponding Thomas et al. (2011) SSP model over-imposed. Within the mean errors the stellar population properties of both kinematic components show discernible differences. The strength of $\text{H}\beta$ for both components is comparable, however, the two kinematic components show a noteworthy difference in their $[\text{MgFe}]'$ strengths. The two components are also offset with respect to each other in $\langle \text{Fe} \rangle$ versus Mg *b* space with the counter-rotating component having higher values that cover as large a range as seen in the main stellar one, suggestive of a distinction between the $[\alpha/\text{Fe}]$ abundance ratios

of the two kinematic components.

These observations are further strengthened by inspecting the 2D maps presented in Fig. 5.11 for some selected line-strength indices of the counter-rotating and main components, respectively. In these maps, regions where the counter-rotating component is not reliably detected by our previously defined criteria (i.e. its light fraction < 0.15) are shown in the map for the main component, adopting their values measured on the outcome of our single-component fitting procedure. The fact that we observe a smooth transition even after such a combining procedure further validates the basis for our separation.

The right panels of Fig. 5.11 show the profiles of the median values obtained by considering the bins contained within an elliptical aperture defined by performing a fit with the `iraf` task `ellipse` to the reconstructed white image. The velocity amplitude of the kinematic components is taken to be $> 30 \text{ km s}^{-1}$ as a way to safeguard against any bins where the kinematic decomposition might not have fully converged. The error bars are evaluated by computing the resistant standard deviation within the apertures. At a first glance, both Figs. 5.10 and 5.11 show that the stellar-population properties of the two kinematic components are indeed different. Moreover, they both show evident radial gradients in $[\text{MgFe}]'$, $\text{Mg } b/\langle \text{Fe} \rangle$, and NaD. The counter-rotating component has a lower $\text{Mg } b/\langle \text{Fe} \rangle$ ratio indicating that its stellar population is less enriched in α -elements. Its metallicity as traced by $[\text{MgFe}]'$ is also systematically higher than that of the counter-rotating component. The bottom row in Fig. 5.11 presents the map and median radial profile for the $[\alpha/\text{Fe}]$ -insensitive NaD. We notice that this index behaves similarly to the $[\text{MgFe}]'$ one. However, due to its higher strength within the main component we could quite clearly separate the presence of a second disk and a halo component, as already suggested by the derived $[\text{MgFe}]'$ and expected ubiquitously in S0 galaxies (Guérou et al., 2016).

5.6.2 Stellar population properties

To translate our line-strength measurements into estimates for the stellar population age, metallicity and alpha-elements abundance for both the main and counter-rotating components, we applied the technique of Morelli et al. (2012) and Coccato et al. (2011) using the single-age models of Thomas et al. (2011) and the observed strength for the $\text{H}\beta$, $\text{Mg } b$, Fe5270, Fe5335, Fe5406, Fe5709, and Fe5782 absorption features. Figure 5.12 presents maps for the age, metallicity, and alpha-elements abundance of both stellar components in NGC 448 as well as radial

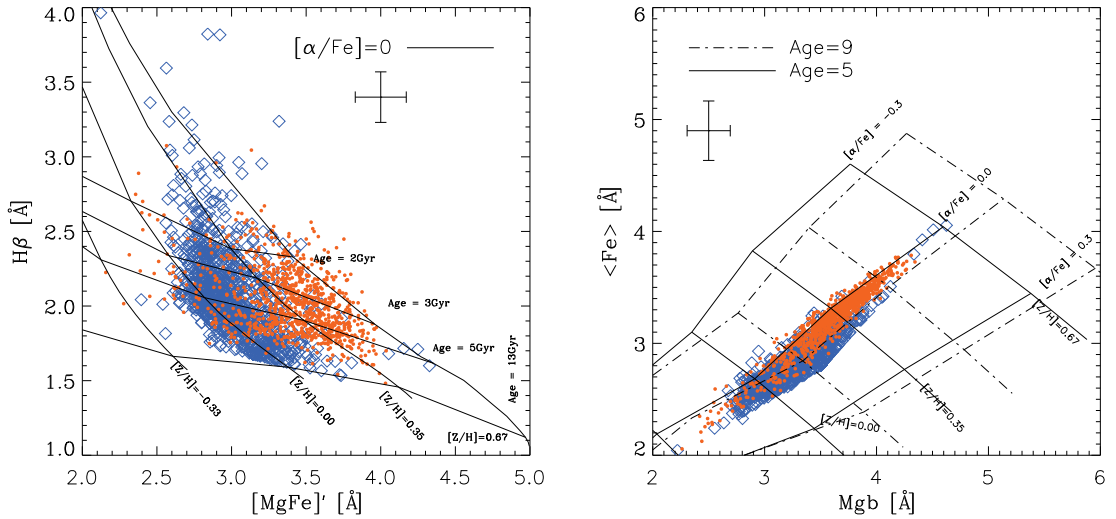


FIGURE 5.10: Equivalent widths of the composite Lick indices for NGC 448 for all bins where the two kinematic components have velocity amplitudes higher than 30 km s^{-1} . The Thomas et al. (2011) model prediction is over-imposed. The blue diamonds signify the main component and the red filled circles indicate the counter-rotating one. The crosses show the mean error.

profiles for the median value of these parameters evaluated in elliptical annuli. The main component is significantly older (median age of ~ 7.7 Gyr) in the very central region (up to $\sim 3''$ along the major axis) and more metal enriched ($[Z/H]$ of ~ 0.06) in comparison to other regions. With this distinction, the ages of the two kinematically distinct components are comparable to each other further away from the centre. The counter-rotating component is very metal rich (median $[Z/H] \sim 0.15$) and has a steeper gradient with values as large as ~ 0.4 , falling to as low as ~ 0 in its outer parts. On the other hand, over the extent of the counter-rotating component the main component has a median metallicity of ~ -0.05 . The alpha-enhancement of both components is observed to anti-correlate with metallicity; for the main component it ranges from ~ 0.05 in the central region to ~ 0.1 outwards. The counter-rotating component shows a hint of a reverse α -element abundance gradient. The values are very close to Solar in the centre and rise to match the ones observed for the main component further away.

Overall, our stellar-population measurements for the two kinematic components of NGC 448 do not compare very well with the results of Katkov et al. (2016). Along the major axis, the stellar metallicity and age derived by Katkov et al. (2016) are systematically lower and higher, respectively, than our own values, for both the main and counter-rotating components. It is difficult to comment on these differences, since the analysis of Katkov et al. (2016) is based on different stellar-population models and analysis techniques from ours, namely the NBURST spectral-fitting technique of Chilingarian et al. (2007a,b) with the PEGASE.HR SSP models

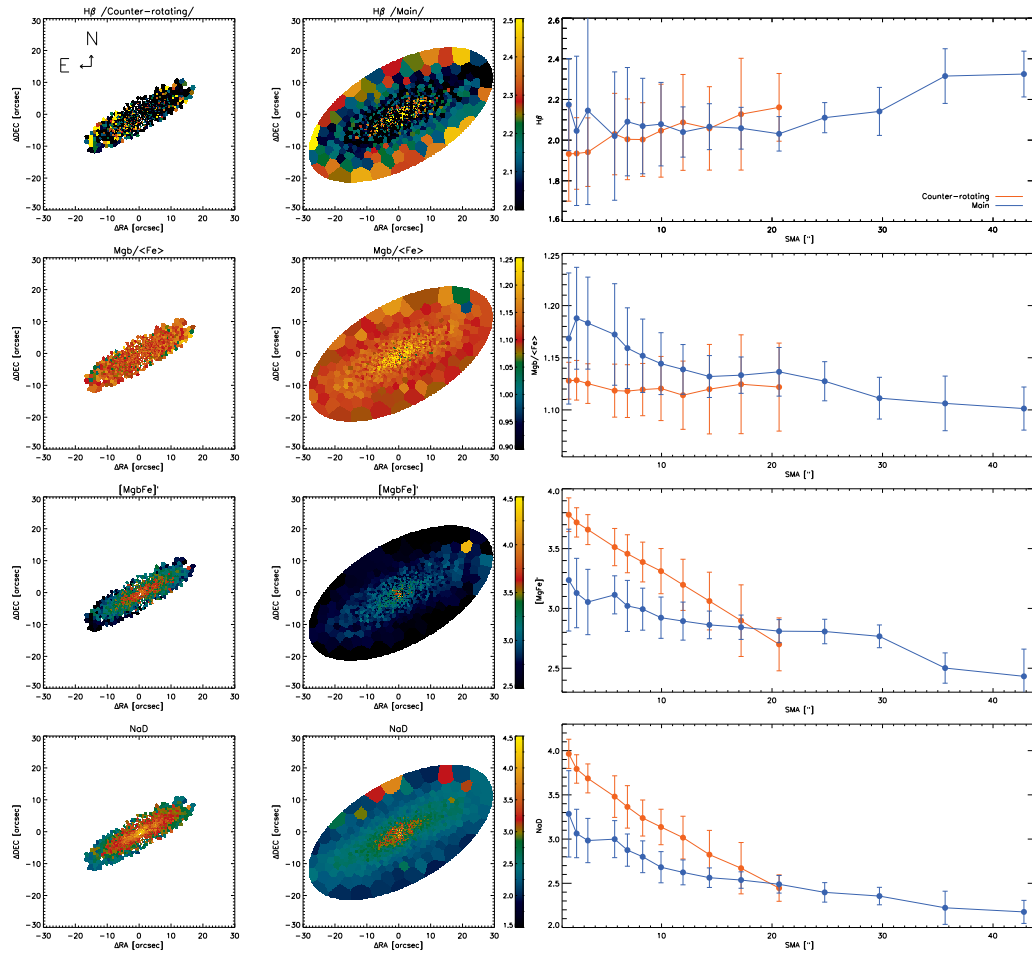


FIGURE 5.11: Line-strength index maps and radial profiles for NGC 448. Left panels: 2D maps of the index strengths of the counter-rotating component of $H\beta$, $Mg\ b/\langle Fe \rangle$, $[MgFe]'$, and NaD from top to bottom, respectively. Middle panels: Same 2D maps of the index strengths, but for the main component. Right panels: The index radial profiles taking elliptical annuli as for the counter-rotating (red) and main stellar (blue) kinematic components. The error bars represent the resistant standard deviation of the measurements within a given annulus.

of Le Borgne et al. (2004). Furthermore, Katkov et al. (2016) derive only stellar ages and metallicities whereas we further explore the role of alpha-element abundances.

On the other hand, McDermid et al. (2015) use a similar modelling approach to ours, based on line-strength measurements, but only consider the overall galaxy spectrum inside circular apertures without attempting to characterise the two stellar populations of NGC 448. Nonetheless, the McDermid et al. (2015) measurements and results can serve as a test for our modelling approach. Indeed, when applying our technique with the measured strength for the $H\beta$, $Mg\ b$, $Fe5270$, and $Fe5335$ indices that McDermid et al. (2015) measure inside one effective radius ($11''$) and using the Thomas et al. (2011) models, we find stellar age, metallicity, and alpha-element abundance values that are consistent with what we find in the same region with our own

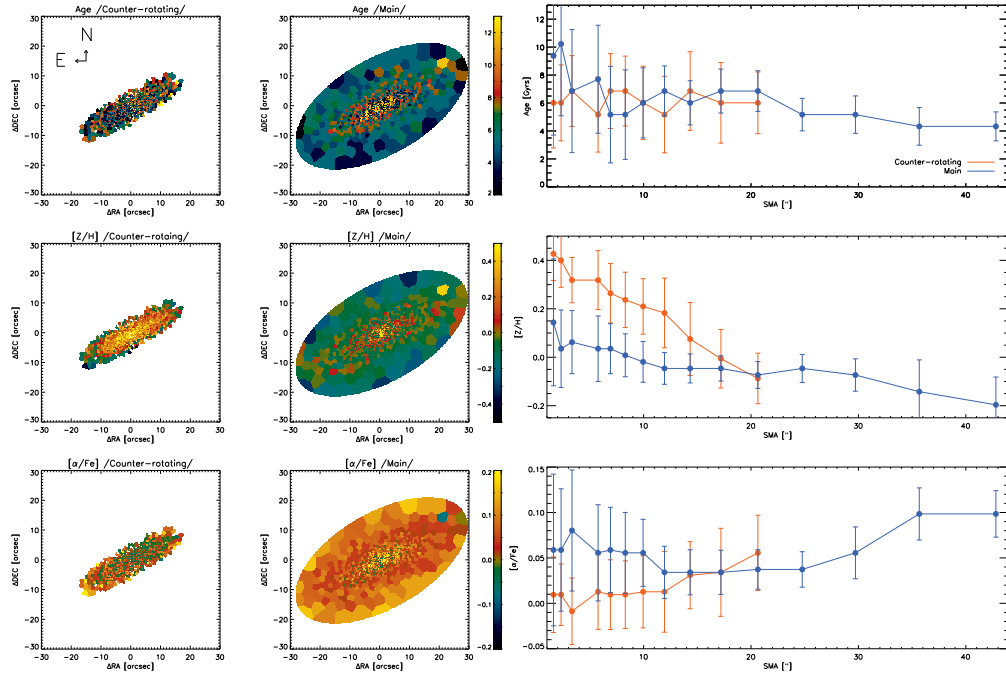


FIGURE 5.12: Single stellar population properties for NGC 448 recovered by fitting the Thomas et al. models. Left panel: 2D maps of the age, metallicity, and α -element-to-iron abundance ($[\alpha/\text{Fe}]$) for the counter-rotating component. Middle panel: Same age, metallicity, and $[\alpha/\text{Fe}]$ maps for the main stellar kinematic component. Right panel: Radial profiles of the best-fitting ages, $[Z/H]$, and $[\alpha/\text{Fe}]$ of the counter-rotating kinematic component (red) and the main one (blue). The error bars were evaluated by taking the resistant standard deviation of the values within a given annulus.

line-strength measurements. In the same region McDermid et al. (2015) finds older stellar ages when using the Schiavon (2007) models, suggesting that the choice of stellar-population models lies at the heart of this discrepancy.

In Fig. 5.13 we plot the $[Z/H]$ versus $[\alpha/Fe]$ for both kinematic components. We note that the retrieved values for $[Z/H]$ and $[\alpha/Fe]$ for both of our kinematic components are shifted towards higher metallicities and lower $[\alpha/Fe]$ in comparison to the trend observed in the solar neighbourhood (green dashed line McWilliam and Rich, 1994) implying a different chemical enrichment history than the Milky Way. No identifiable expected “knee”, carrying information for the star-formation efficiency (McWilliam, 1997) is present in the $[Z/H]$ against $[\alpha/Fe]$ diagrams, where we have plot the expected schematic model of (Tinsley, 1979) in accordance to other early-type galaxies (e.g. Walcher et al., 2015). Furthermore, we could not identify any bifurcation in the $[Z/H]$ against $[\alpha/Fe]$ trends of these kinematic components with respect to their $[\alpha/Fe]$ in analogy with the Milky Way disc (e.g. Nidever et al., 2014). Instead, both of our kinematic components resemble just their low- α sequence as we are observing a mix of stellar populations within our galaxy. We can also compare the $[Z/H]$ versus $[\alpha/Fe]$ patterns of our

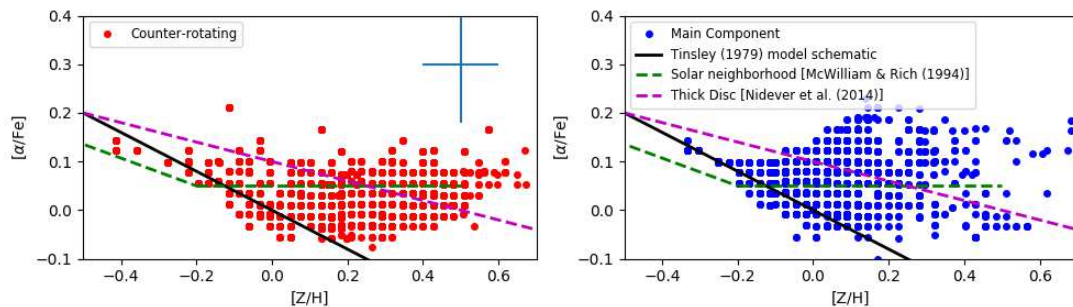


FIGURE 5.13: Left panel: The $[Z/H]$ vs. $[\alpha/Fe]$ relation for the counter-rotating disc. Right panel: The $[Z/H]$ vs. $[\alpha/Fe]$ relation for the main galactic component. Overplotted are the schematic of the Tinsley (1979) model (thick black line), the abundance relation for the solar neighborhood (dashed green line), and the abundance relation for the thick disc from Nidever et al. (2014) (dashed magenta line). Schematic for the Tinsley model and trend for the solar neighborhood adopted from Walcher et al. (2015) and McWilliam (1997), respectively. The blue error bar represents an estimate for the errors in our measurements.

kinematic components with the expected trend for the Milky Way thick disk using the fiducial line from (Nidever et al., 2014) to also speculatively assign the $[Z/H]$ against $[\alpha/Fe]$ patterns of our kinematic components to the two classes of early-type galaxies defined by Walcher et al. (2015) as both of our components should have non-negligible fraction of intermediate and old stellar populations. Due to the predominantly lower $[\alpha/Fe]$ (and according to the argument in Walcher et al. (2015) intermediate age stellar population) both kinematic components are more similar to their mergers/accretion (ACC-ETGs) early-type galaxy class. Finally, considering the large uncertainties associated with our measurements we warn that our comparison is mainly qualitative rather than quantitative and a more elaborate analysis can be performed with higher quality data that could potentially further elucidate the formation mechanisms in of our kinematic components.

5.7 Discussion and conclusions

The true nature of the kinematically distinct components, such as the ones observed in our two galaxies, is best studied using IFU spectroscopy, combining both photometric and kinematic information. Nevertheless, it is intrinsically difficult to reconstruct the formation mechanism for the retrograde stellar populations observed in these two early-type galaxies.

5.7.1 NGC 448

Counter-rotating kinematic components can generally originate from processes that are either external or internal to the host galaxy. The dominant formation channel for the assembly of stellar counter-rotating kinematic components is most often attributed to the accretion or reprocessing of gas and subsequent in situ star formation (Corsini, 2014).

On the one hand, fresh gas could be captured through a gas-rich minor merger. External gas can be acquired from the companion in a retrograde fashion and is of considerable quantity (i.e. more than what is already present within the more massive galaxy) it does not become completely dissipated and swept up by pre-existing gas within the more massive host galaxy and a subsequent star-formation episode results in a population of retrograde stars. This was recently illustrated through the aid of extensive merger numerical simulations by Bassett et al. (2017) and previously addressed by Thakar and Ryden (1996, 1998). They demonstrate how similar gas-rich minor mergers are likely to result in an S0 galaxy or did not change the morphological properties of an S0 progenitor. Usually, the resultant post-merger products of such simulations contain some appreciable gas reservoir. However, overall NGC 448 is surprisingly devoid of gas, contrary to other observed galaxies harbouring counter-rotating stellar disks. We confirm the absence of ionised-gas emission in our IFU spectra, as previously reported by Katkov et al. (2016) in their long-slit spectrum. This indicates that there is no ongoing substantial residual star formation. With these considerations, we cannot unambiguously use the coexistence of a gas reservoir and a counter-rotating disk as evidence that indeed gas accretion and subsequent in situ star-formation formed the truly kinematically decoupled structure. One possible way to reconcile such a formation scenario with our observations is to postulate that the gas has been fully consumed and processed to stars. As a consequence, the resulting recent star-formation episode should have left a sub-population of young stars predominately belonging to the counter-rotating disk. However, we do not detect any significant ($t < 0.1$ Gyr) difference in the ages of the stellar populations of either the main galaxy body or the decoupled kinematic subcomponent. In this case, the flat age radial profile and very sharp negative metallicity gradient could be the result of a rapid outside-in formation. Still, using the recovered alpha-element abundance and Eq.(4) from Thomas et al. (2005) implies that the counter-rotating disk stars formed through an extended period of star formation that lasted at least 10 Gyr. Therefore, the observed low $[\alpha/Fe]$ values in combination with the high metallicity similar to the main galactic stellar body age of the counter-rotating component are difficult to reconcile in a purely closed-box system. The low

$[\alpha/Fe]$ values could instead be present due to accreted gas material that had already been iron enriched to lower down the $[\alpha/Fe]$ ratio. Alternatively, star formation could have proceeded in both of the kinematic components (disk and main stellar body) generating a noticeably large ($\geq 1\%$ in mass) and young ($t \leq 2.5$ Gyr) stellar sub-population. This in turn would impact our line-strength luminosity-weighted age estimates and metallicities, shifting the age of the main stellar body towards smaller age estimates and the metallicity of the kinematically decoupled disk towards that of its oldest stellar sub-population (e.g. Serra and Trager, 2007; Sánchez-Blázquez et al., 2014). A more thorough analysis of the stellar population properties, allowing for multiple simple stellar populations instead of just one as in this work, and using higher-resolution spectra, could suffice to either confirm or rule out such a speculation. As an alternative to a gas-rich merger, Thakar and Ryden (1996, 1998) studied the possibility that the gas can fall in from the environment surrounding the galaxy through either a short or prolonged period of accretion. These numerical simulations produced counter-rotating disks, albeit most often resulting in profiles of a non-exponential nature, such as the one we recover for the counter-rotating component in NGC 448. Another possibility is that the galaxy was originally formed through filamentary gas accretion from two distinct cosmological filaments, in turn forming the two distinct kinematic structures under a special spatial configuration. Algorry et al. (2014) studied this process in a cosmological simulation of the formation of a disk galaxy. They concluded that a natural consequence of such a formation scenario would be a discriminable age difference in the two distinct kinematic components. As previously pointed out, this is not found to be the case for NGC 448.

A further puzzle results from the likely interaction with a suspected companion galaxy (LEDA 212690). A tidal stream was observed by Duc et al. (2015) and also pointed out by Katkov et al. (2016). They note that the galaxy is in tidal interaction with a morphologically disturbed companion. From the colour difference available as part of the Duc et al. (2015) survey, we can only speculate that the age of the stars constituting the tidal tail is similar to that of the stellar population of NGC 448. If the two galaxies are interacting, then the redshift of the suspected companion LEDA 212690 was possibly wrongfully inferred as ~ 0.074 as part of the CAIRNS survey (Rines et al., 2003). Another more exotic possibility is that the counter-rotating disk was assembled through the direct accretion of stars from a companion. It is however extremely unlikely that such a formation scenario would reproduce the observed metallicity gradient for the counter-rotating disk. There is no strong physical reason for the stars to be accreted preferentially in a spatial configuration that would produce a counter-rotating disk with higher metallicity

than that of the main galaxy body and with a strong gradient. Further observations of LEDA 212690 would unequivocally rule out some of the previously mentioned external-formation scenarios for the counter-rotating disk.

As opposed to the external acquisition of gas and a subsequent in situ star formation, the counter-rotating embedded stellar disk could be the product of an internal formation mechanism. The internal separatrix formation scenario (Evans and Collett, 1994) would be very unlikely in the case of NGC 448. Even though the two components have very similar stellar population ages, the counter-rotating disk is less extended than the main galaxy body, contrary to the predictions of such a formation mechanism. Furthermore, the chemical properties of the two stellar populations are quite different in opposition whereas the stars forming the counter-rotating disk should share the same star-formation history as the galaxy. Kantharia (2016) argued that counter-rotation in general could also stem from the exchange of angular momentum in close galaxy encounters. As pointed out previously we observe a “bridge” between the two galaxies. Nevertheless, we do not see any drastic misalignment in the kinematic rotation centres of the counter-rotating embedded disk and the main galactic body and we report a difference in the chemical properties of the stellar populations of the two kinematic components. Also, the two counter-rotating structures seem to share the same axis of rotation according to the accuracy of our velocity measurements (i.e. we do not observe an obvious offset between the heliocentric velocities of the two kinematic components). As the aforementioned angular momentum exchange due to a close fly-by scenario would largely result in the two components sharing different rotation axes we conclude that it is unlikely to be the origin of the separate stellar population kinematic components observed in NGC 448.

5.7.2 NGC 4365

Even though we retrieved a second photometric component through our photometric decomposition (see, Sect. 5.4) and also obtained a good spectral decomposition in some of our Voronoi bins (see, Sect. 5.5.3.2), we did not obtain adequate consistency in our photometric and kinematic decompositions to support the presence of two truly decoupled kinematic structures. It is well established by means of simulations that the KDCs in massive early-type ellipticals could be a product of a galaxy merger. To complement the finding of the ATLAS^{3D}, Bois et al. (2011) produced an extensive set of such merger simulations spanning a long range of possible mass ratios (1:1 to 6:1), initial conditions, and orbital parameters in order to discern the origins of the

two main classes of early-type galaxies on the basis of their resultant angular momentum. They report that the majority of the slow-rotator merger products in their simulations possess a distinct KDC. Additionally, a major merger of two disk galaxies even when initially both following prograde orbits (Tsatsi et al., 2015) could also produce a KDC in the resultant elliptical galaxy merger product. However, both these KDC-formation channels would result in a noticeable age difference compared to the main stellar body. As previously found by Davies et al. (2001) and reiterated by van den Bosch et al. (2008), the ages and properties of both the KDC and the rest of the galaxy have the same magnesium-to-iron abundance ratios and virtually the same ages implying that the KDC formed at least 12 Gyr ago or is indeed a projection effect. Furthermore, NGC 4365 does not even show symmetric velocity dispersion peaks and therefore does not resemble a typical 2σ galaxy considered to host truly decoupled counter-rotating structures. Even in the presence of such features, for the case of NGC 5813, Krajnović et al. (2015) did not infer that the KDC arises from two counter-rotating disks. Instead through detailed modelling, as also previously done for NGC 4365 by van den Bosch et al. (2008), Krajnović et al. (2015) found that also in NGC 5813 the KDC is likely not due to two dynamically decoupled components. It was found to most plausibly be the result of the complex nature of the orbits in such massive ellipticals.

To qualitatively verify these previous observations we have re-fitted our spectra taking advantage of the capabilities of the IFU-analysis pipeline of Bittner et al. (2019) in the broader wavelength range of 4800 to 6500 Å. We used the standard MILES SSP library (Vazdekis et al., 2010) and the routines of Kuntschner et al. (2006) and Martín-Navarro et al. (2018) that are already included to derive the strengths of the most common line indices and obtain the properties of the equivalent single stellar population. Similar to Sec. 5.6.1 in the upper panels of Fig. 5.14 we show our derived selected line-strength indices maps. In accordance to the previous study of Davies et al. (2001) using the SAURON spectrograph we find similar trends within our index maps and stellar population properties. The middle and rightmost panels show the spatial distributions of the previously discussed $[\text{MgFe}]'$ and $\langle \text{Fe} \rangle$ composite line-strength indices. The first panel shows the map of the $H\beta_0$ absorption strength index providing a good proxy for the stellar population age (Cervantes and Vazdekis, 2009). The strength of this index is roughly uniform throughout the previously investigated SAURON region. The very central region ($\lesssim 10''$), where we observe some of the higher values of the h_3 Gauss-Hermite coefficient (see Fig. 5.2) and part of the core of the “S-shape” velocity field twist, we report higher values of the composite $[\text{MgFe}]'$ index implying a peak in the stellar population metallicity in the very center with decreasing

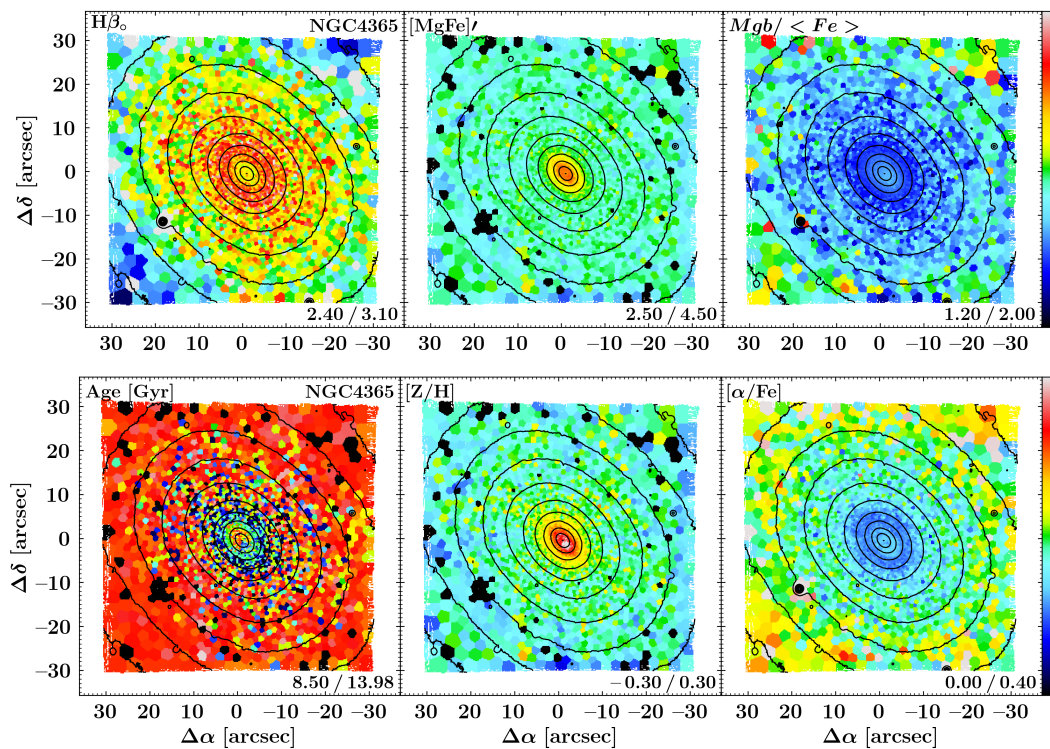


FIGURE 5.14: Top left panel: The strength of the $H\beta_0$ index. Top middle panel: The map of the strengths of the $[MgFe]'$ composite index. Top right panel: The measured composite index $Mg\ b/\langle Fe \rangle$ values. Bottom left panel: The retrieved stellar age. Bottom middle panel: The single stellar population metallicity $[Z/H]$. Bottom right panel: The retrieved $[\alpha/Fe]$.

values further outwards. On the other hand, in the central region we find lower values of the $Mg\ b/\langle Fe \rangle$ ratio hinting the presence of a α -element abundance gradient. These trends can be directly observed in the maps of the retrieved single stellar population properties (bottom panels of Fig. 5.14).

5.7.3 Conclusions

We investigated two early-type galaxies, NGC 448 and NGC 4365, that show central kinematically distinct cores. Using the kinematic decomposition technique by Coccato et al. (2011) we separated the individual contributions of two distinct kinematic components with the aid of integral-field observations of NGC 448. This latter galaxy hosts a counter-rotating stellar kinematic structure with an angular size of at least $42''$, which is considerably more extended (~ 1.5 times) than the regions with irregular stellar kinematics. Based on the observed nearly exponential photometric profile and the kinematic information we extracted, the distinct component is very kinematically cold ($V_\star/\sigma_\star \gg 1$), and therefore likely has a disk morphology.

The disk counter-rotates with similar velocity to that of the main stellar body. The stars of the counter-rotating disk and the main body have comparable age. However, the two distinct kinematic components have chemically different stellar populations. The stellar population of the counter-rotating disk displays a steeper metallicity gradient and is slightly less enriched in alpha-elements than the one constituting the bulk of the galaxy. In contrast to all other galaxies with embedded counter-rotating disks we do not observe evidence for any interstellar gas as traced by its ionized-gas emission. Although this prohibits us from unequivocally linking the formation of the counter-rotating disk to a past gas accretion event or a “wet” merger, our analysis points to two likely formation mechanisms for the counter-rotating stellar disk. Either it formed as result of a gas-rich merger after which the gas reservoir was exhausted in a period of outside-in star-formation, (provided that this gas reservoir was prior iron-enriched and just acquired in retrograde orbits) or it derived from two simultaneous star-formation bursts, one of which gave rise to the counter-rotating disk, whilst the other reshaped the chemical properties of the main disk.

We find no clear signature in the integral-field observations of NGC 4365 for a true kinematic decoupling. The KDC in this galaxy likely stems as previously suggested from a projection effect due to its triaxial nature.

Chapter 6

Further Steps with MaNGA

6.1 Overview and Motivation

Gas acquisition events in early-type galaxies are thought to be a common occurrence (Bertola et al., 1988, 1992). As the gas is externally acquired it can show some form of kinematic misalignment. It has been established using integral-field spectroscopy that up to $\sim 40\%$ of the galaxies with an ionized-gas component show such misalignment (e.g. Sarzi et al., 2006; Davis et al., 2011). One manifestation of misalignment is counter-rotation. It can occur either between the gaseous and stellar, stellar and stellar, or in some very rare cases gaseous-versus-gaseous galactic components (Corsini, 2014). Focusing, in particular, on S0 gaseous counter-rotation with respect to the galaxy stellar body has been measured in $\sim 32\%$ (Bertola et al., 1992; Kannappan and Fabricant, 2001; Pizzella et al., 2004). The fraction of galaxies with counter-rotating gas is quite high in isolated S0 galaxies with up to 71% of their 12 sample objects showed counter-rotating gas component that they deem to be of external origin (Katkov et al., 2014). Stellar counter-rotation, on the other hand, seems to be a much rarer phenomenon. S0 galaxies with more than $\sim 5\%$ of counter-rotating orbits occur in only $\lesssim 10\%$ of such systems (Kuijken et al., 1996). For late-type galaxies Pizzella et al. (2004) reported that $\lesssim 12\%$ and $\lesssim 8\%$ of their sample of different morphological type spirals had counter-rotating gaseous and stellar discs, respectively. In another sample of 38 galaxies, a limit of at most 8% of all spirals were shown to host gas-stellar counter rotating components (Kannappan and Fabricant, 2001). This picture is suggestive of the scenario where small amounts of externally acquired gas in some gas-poor S0 galaxies subsequently forms stars, whereas in more gas-rich spirals such newly acquired gas can be swept away by some pre-existing gas. Counter-rotating disks in

spiral galaxies can be formed only if the amount of externally acquired gas exceeds that of pre-existing gas (Pizzella et al., 2004). Testing whether this hypothesis is indeed true and putting constraints on the properties of galaxies with present counter-rotation can be informative of the overall process of galaxy assembly.

Capturing the process of gas accretion can be achieved using a myriad of absorption-line probes (e.g. Rubin, 2017, for a review). The ISM red-shifted NaD absorption lines have previously been reported to be indicative of inflowing gas in some star-forming and passive galaxies (Sato et al., 2009). The group reported nearly equal number of galaxies with blue- and red- shifted NaD line profiles with velocities greater than 50 km s^{-1} from the systemic velocity ($\sim 16\%$ and $\sim 15\%$ of their objects, respectively) which they deemed to be out- and in- flowing. Most of the inflowing objects were found to belong to the red sequence, whereas outflows were predominantly reported in objects in the blue cloud. The inflows were also often associated with either Seyfert or LINER activity as traced by some of their emission-lines. Moreover, Krug et al. (2010) reported the detection of inflows in a sample of AGN galaxies, with characteristic Seyfert emission lines and IR luminosities typically found in normal galaxies. A rather large fraction of these galaxies had interstellar NaD line-profile centres shifted by more than 50 km s^{-1} as high as 140 km s^{-1} . Such features were present in $\sim 37\%$ of their sample in comparison to only $\sim 11\%$ having blue-shifted lines indicative of outflows. Nevertheless, no strong dependence of the velocity of the inflowing gas with respect to galaxy properties, such as mass, IR luminosity, and inclination was deduced. The rather large inflows in these galaxies were interpreted to be suggestive of material located in the inner regions of the galaxies instead of being further outward. A big ($\sim 38\%$) fraction of their galaxies with inflows displayed some nuclear morphological features (e.g. dust spirals, bars, or rings) that can be creating torques strong enough to cause the gas to lose its angular momentum and fall inwards (e.g. Combes, 2008). Similar fraction of those galaxies were found to have a close companion and, therefore, possible interaction. The in-flow rate of these galaxies was also reported to be sufficient to power the strong AGN central engine.

The MaNGA survey (see, Sect. 3.1.6) presents several advantages for moving forwards with the investigations we addressed in the previous few chapters. In particular, the large number of galaxies surveyed by MaNGA offers a clear opportunity to explore the demographics of galaxies (see Appx. 8) that host a KDC and show a two peaks in their velocity dispersion fields. MaNGA data comes with somewhat inferior spectral quality and spatial sampling compared to MUSE. Therefore, we do not expect that the level of detail of our MUSE results would be surpassed for

single objects. Nevertheless, in some future work we would attempt to perform similar analysis as the one we have demonstrated in Chap. 5 on a few pre-selected MaNGA galaxies.

On the other hand, as regards to cold-gas outflows the spatial extent of the MaNGA data and their similarity to the SDSS spectra would allow us in the future to explore with a similar analysis to our Chap. 4, whether NaD outflows have an extended structure that is indeed biconical. We could also check if their occurrence is really connected to a central AGN or to a more extended nebular activity powered by star-formation formation. To that extent, we have explored the ability of MaNGA to resolve and trace the presence of cold ISM gas.

6.2 Samples

6.2.1 Seyfert 2 galaxies in MaNGA

We have cross-referenced our sample of Seyfert 2 SDSS galaxies with overly strong interstellar Sodium absorption (see chapter 4) to find whether these objects were observed as part of the ongoing IFS MaNGA survey. Within our sample of 9859 Seyfert 2 galaxies we found nine objects that were already observed with MaNGA as part of the SDSS DR15. We present these matches in Tab. 6.1. Unfortunately, none of our Seyfert 2s that showed signatures of cold-gas outflows fell within these galaxies. Our NaD analysis, on the contrary, was indicative of the presence of either relaxed cold gas (our $\Delta V \sim 0$) or inflow (our $\Delta V > 0$). In a few of those objects the amplitude-to-residual-noise A/rN of the excess NaD absorption-line profiles was more pronounced ($A/rN > 7$).

6.2.2 2-sigma and KDC MaNGA galaxies

To select galaxies displaying extraordinary stellar kinematics, reminiscent of embedded counter-rotating structures, we draw on the work of Graham et al. (2018). The group aimed to measure the stellar angular momentum of a large sample (~ 2300) of MaNGA galaxies. Through careful inspection and using kinemetry analysis (Krajnović et al., 2006) they highlighted potential galaxies with double-peaked stellar velocity dispersion and central kinematically distinct cores. We obtained the MaNGA DR15 cubes for their “ 2σ ” and KDC galaxy host candidates and re-examined them with the aim to pre-select a sample of galaxies for a future kinematic decomposition study. We refrained from directly performing the same procedure as outlined in Chap. 5

TABLE 6.1: The DR15 MaNGA galaxies part of our sample of Seyfert 2 DR7 sample.

DR7 SDSS ID	RA (dec.)	DEC (dec.)	plateIFU	mangaid	$A/N_{NaD, fiber}$	$\Delta V_{NaD, fiber}$	$\Delta\sigma_{NaD, fiber}$
588015507678887987	45.95462	-1.103742	9193-12701	1-37440	-9.33	42.98	54.16
588298662503579763	196.7551	46.30942	8318-1901	1-284321	-8.28	81.86	65.21
587731522818670711	137.8749	45.46832	8249-3704	1-137883	-4.68	12.50	45.83
588018253752565918	226.4317	44.40493	8552-12701	1-321739	-8.56	40.95	68.36
587729653422555416	249.5573	40.14681	8588-12704	1-135641	-6.22	53.745	76.91
587725993040740662	255.1015	38.3517	8612-12705	1-95842	-14.14	131.82	112.20
588018090547806501	248.1409	26.38073	9047-6104	1-270129	-4.40	-0.34	166.43
587738948284645503	156.4018	37.22144	8943-9101	1-392952	-7.34	77.76	163.79
587741490891587680	127.1708	17.5814	8241-9102	1-460812	-4.01	29.63	46.96

for this available data because of the presence of some sky emission and absorption lines in the CaT spectral regions among those cubes. We would aim to clean this sky contribution using the ZAP procedure, similar to what we have done for our MUSE data reduction, prior to any future analysis.

6.3 Methodology

To perform some preliminary analysis on our two MaNGA samples we adopted the Galaxy IFU Spectroscopy Tool¹ (Bittner et al., 2019, GIST). The GIST data-processing pipeline is a flexible and easily configurable framework for the analysis of integral-field data due to its modularity. It is capable of the fast extraction of both stellar and gaseous kinematics and stellar population properties using pPXF (see Chap. 2.2.2) and *GandALF* (see Chap. 2.2.3) with ongoing development to incorporate kinematic decomposition (see Chap. 2.2.6), owing to Python’s parallel computation capabilities. In addition, it provides a dedicated graphic user interface routine, facilitating the inspection of each fit, for the purpose of data analysis quality control. GIST also in addition to the pPXF build-in full spectral fitting method for obtaining stellar population properties is capable of retrieving the most widely adopted line-strength indices and their associated SSP properties using the methods of Kuntschner et al. (2006); Martín-Navarro et al. (2018). We have modified this data-processing pipeline to handle MaNGA datacubes. More specifically, we have implemented a new data-reading routine and have configured it following some of the prescriptions of Westfall et al. (2019) and recipes outlined by the SDSS team². We decided to adopt a signal-to-statistical noise of 7 per Voronoi bin and configured GIST to exclude bins that are below the isophote with $S/sN < 0.5$. The preliminary analysis of all of our galaxies was performed using the MILES SSP templates provided as part of the analysis pipeline. We have fitted the MaNGA spectra in the region between 3500 Å and 7000 Å adopting a 7th order multiplicative polynomial for the purpose of our pPXF fitting.

¹<https://abittner.gitlab.io/thegistpipeline/documentation/intro/introduction.html>

²<https://www.sdss.org/dr15/manga/manga-data/working-with-manga-data/>

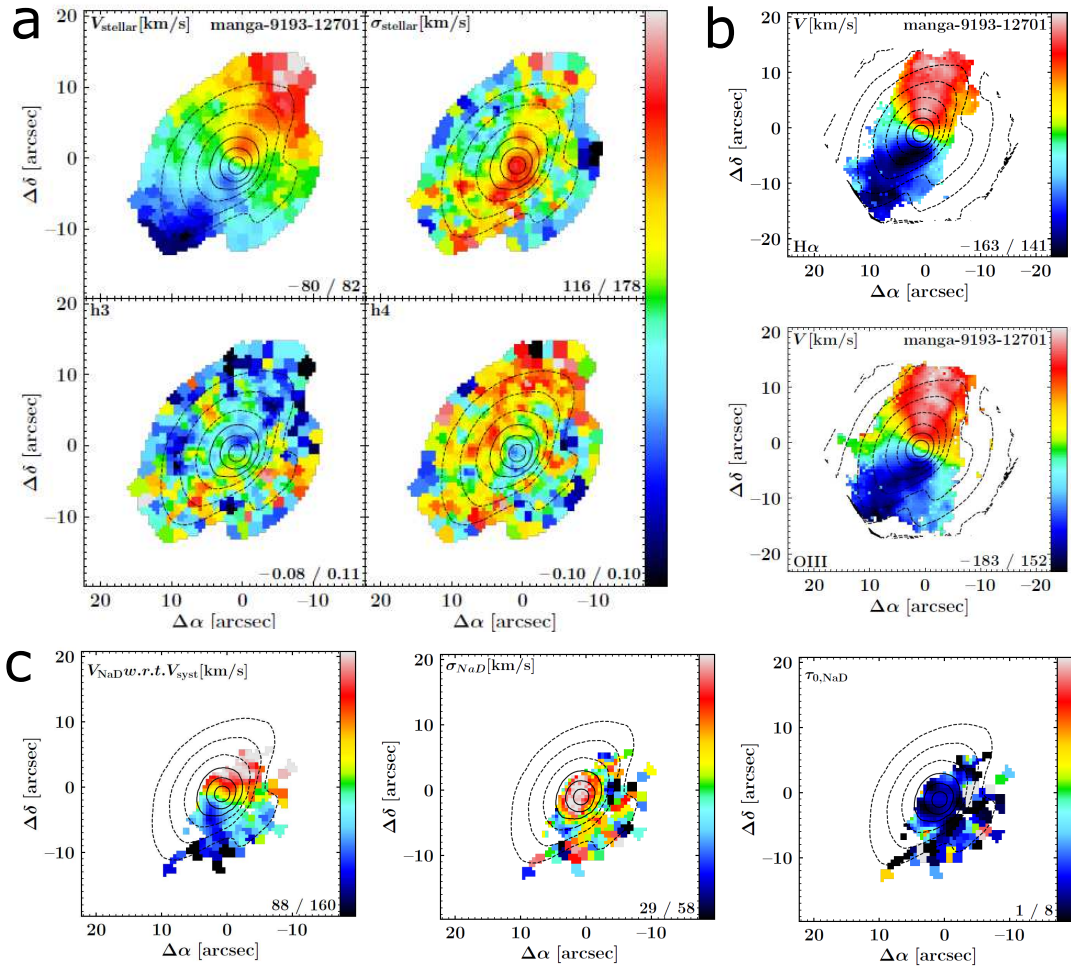


FIGURE 6.1: The stellar and gaseous kinematics of the Seyfert 2 *manga9193-12701* galaxy. Panel *a*: Stellar kinematics as indicated by the the label in the upper left corner of the panels. Panel *b*: Velocity fields for the ionized-gas of as traced by H α and [O III] (upper and lower panel, respectively). Panel *c*: The retrieved velocity, velocity dispersion, and optical depth of the interstellar NaD excess. The Overlaid contours show the reconstructed isophotes on the basis of the MaNGA cube in steps of 0.2 mag.

6.4 Preliminary Results

6.4.1 The Seyfert 2 galaxy

Here we outline some preliminary results in regards to our ability to trace cold gas by looking for the presence of interstellar NaD absorption. We would focus specifically on our results for one pre-selected by us as part of our Seyfert 2 sample and observed in MaNGA galaxy - “manga9193-12701”.

Figure 6.1 shows the outcome of our analysis for “manga9193-12701”. This galaxy hosts a prominent dust lane as visible in the composite SDSS images and by the bending of the isophotes

obtained from the reconstructed of the datacube surface brightness (shown with dashed lines). Its stellar kinematics show regular rotation with no distinct features in the higher Gauss-Hermite moments h_3 and h_4 (Fig. 6.1, panel a). It also possesses an extended gaseous disk as traced by the ionized-gas kinematics of the $H\alpha$ and [O III] emission lines (Fig. 6.1, panel b). In addition, we have also extracted the kinematics and optical depth of the excess NaD absorption profile previously adopted in this thesis (Fig. 6.1, panel c). Such NaD excess seems to be systematically red-shifted as indicated by our previous analysis on the basis of SDSS fiber spectra. Moreover, its spatial distribution, up to a high degree, coincide with the position of the host galaxy dust lane. Such behaviour is not surprising and has been previously demonstrated. For example, the equivalent widths of interstellar Sodium absorption towards stars in our Galaxy have been shown to follow a well defined empirical relation with respect to the inferred extinction due to dust (Poznanski et al., 2012). However, some recent works focusing on the dust contents of other galaxies, and in particular FCC 167 (Viaene et al., 2019), did not manage to detect substantial interstellar NaD excess absorption-line profiles. Instead, the presence of interstellar NaD absorption was clearly visible as a “bump” in the derived attenuation curves both in FCC 167 and in the dust lane of another galaxy (Viaene et al., 2017, NGC 5626). Perhaps more surprising is the systematic redshift, with respect to the galaxy stellar systemic velocity, of our ISM-attributed NaD profile. Such red-shifted absorption features have been previously utilised as proxies for in-flowing gas (e.g. Rubin, 2017, for a review). On the other hand, it is worthy noting that cold-gas, traced by interstellar NaD absorption, have already been shown not to in-fall, but counter-rotate with a large offset in velocity (Westmoquette et al., 2013). The unequivocal association of our observed red-shifted ISM NaD absorption profiles to an inflow of cold gas would be a step forwards in understanding the mechanisms that have been theorised to fuel an AGN (e.g. Combes, 2008, 2012, for a reviews).

6.4.2 2-sigma MANGA galaxies

We have performed a preliminary analysis of the available SDSS DR15 MaNGA galaxies, highlighted to have counter-rotating kinematic components, part of the Graham et al. (2018) sample. These included 24 “ 2σ ” candidates and 14 galaxies with a signature for a centralised KDC. We present our preliminary results with additional comments for each of those galaxies in Appx. 8. Out of the 14 KDC candidates we managed to confirm the true presence of a kinematically distinct cores in 8 objects. Moreover, we find that 3 galaxies have ionized-gas emission that

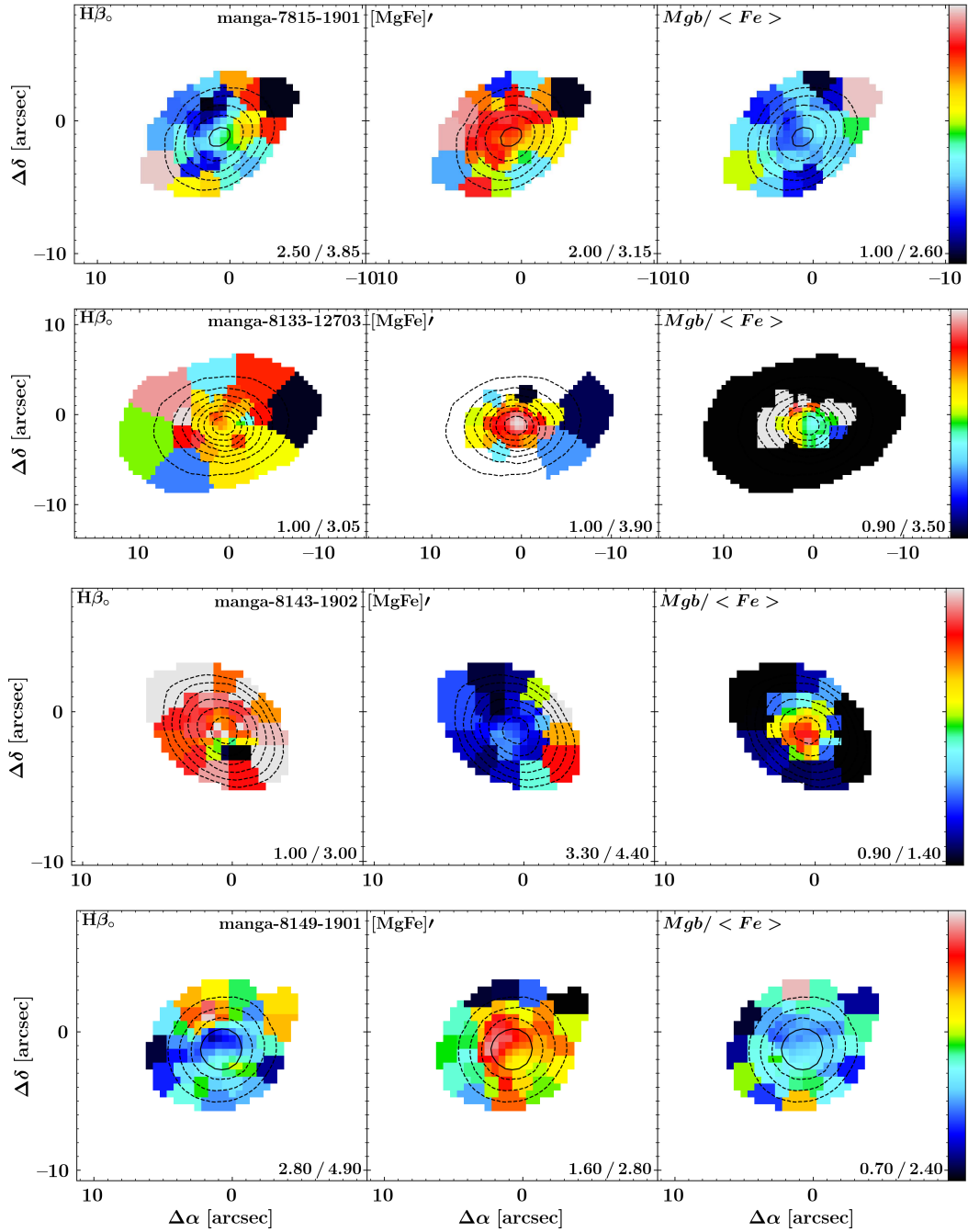


FIGURE 6.2: Each vertical panel shows the spatially resolved $H\beta$, $Mg\ b/\langle Fe \rangle$, $[MgFe]'$ line-strength indices for a 2-sigma or KDC MaNGA galaxy.

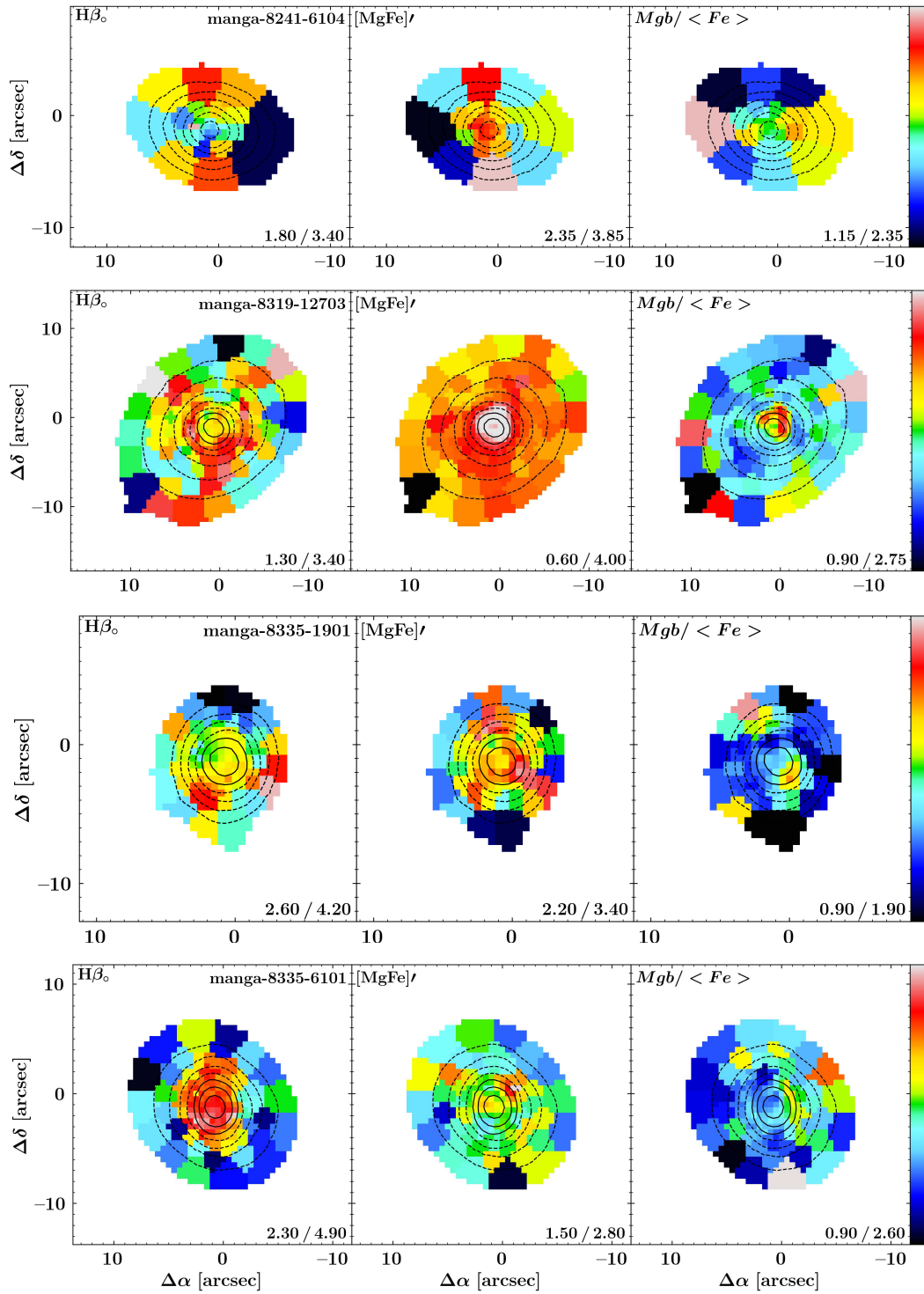


FIGURE 6.3: Same as Fig. 6.2

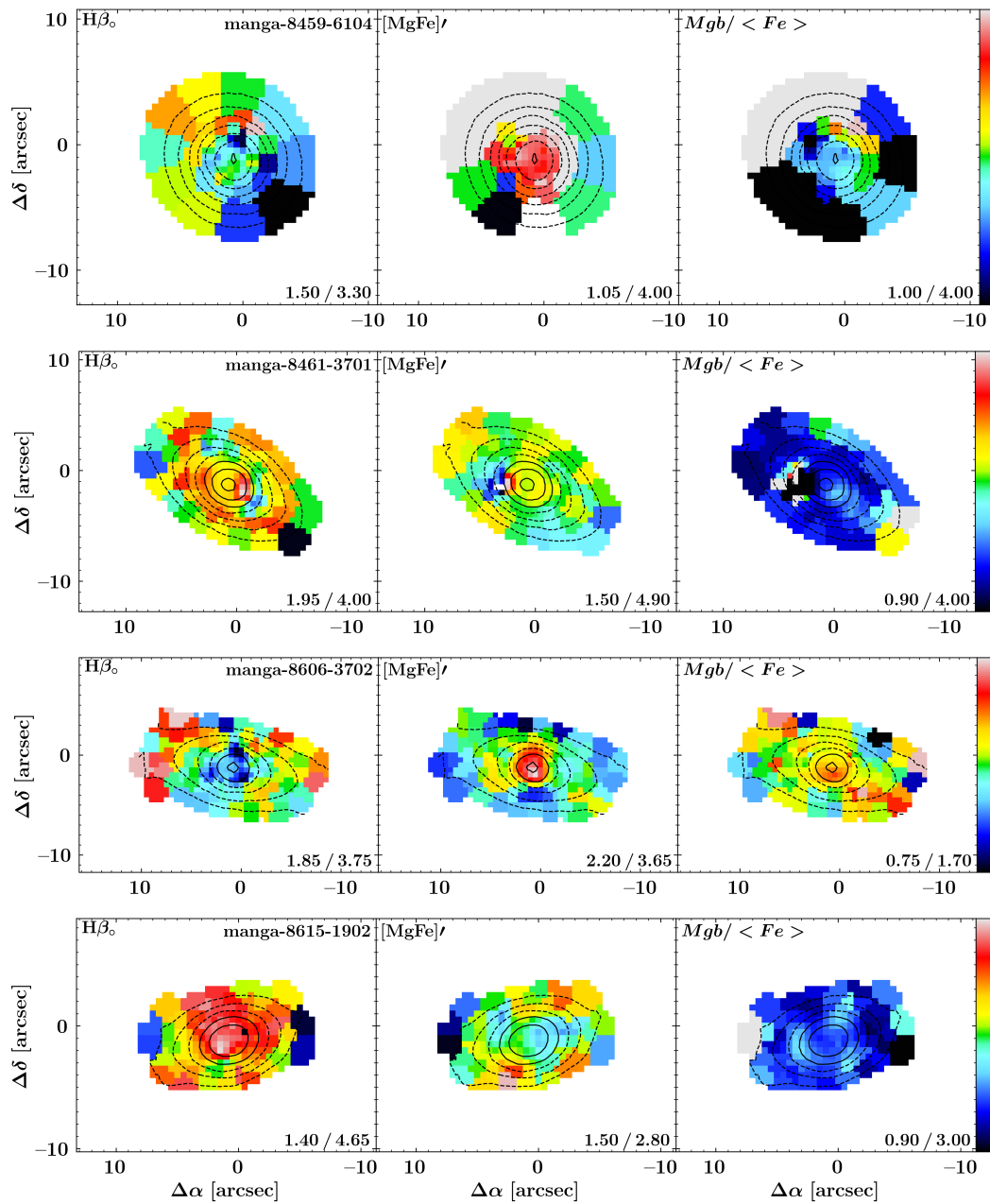


FIGURE 6.4: Same as Fig. 6.2

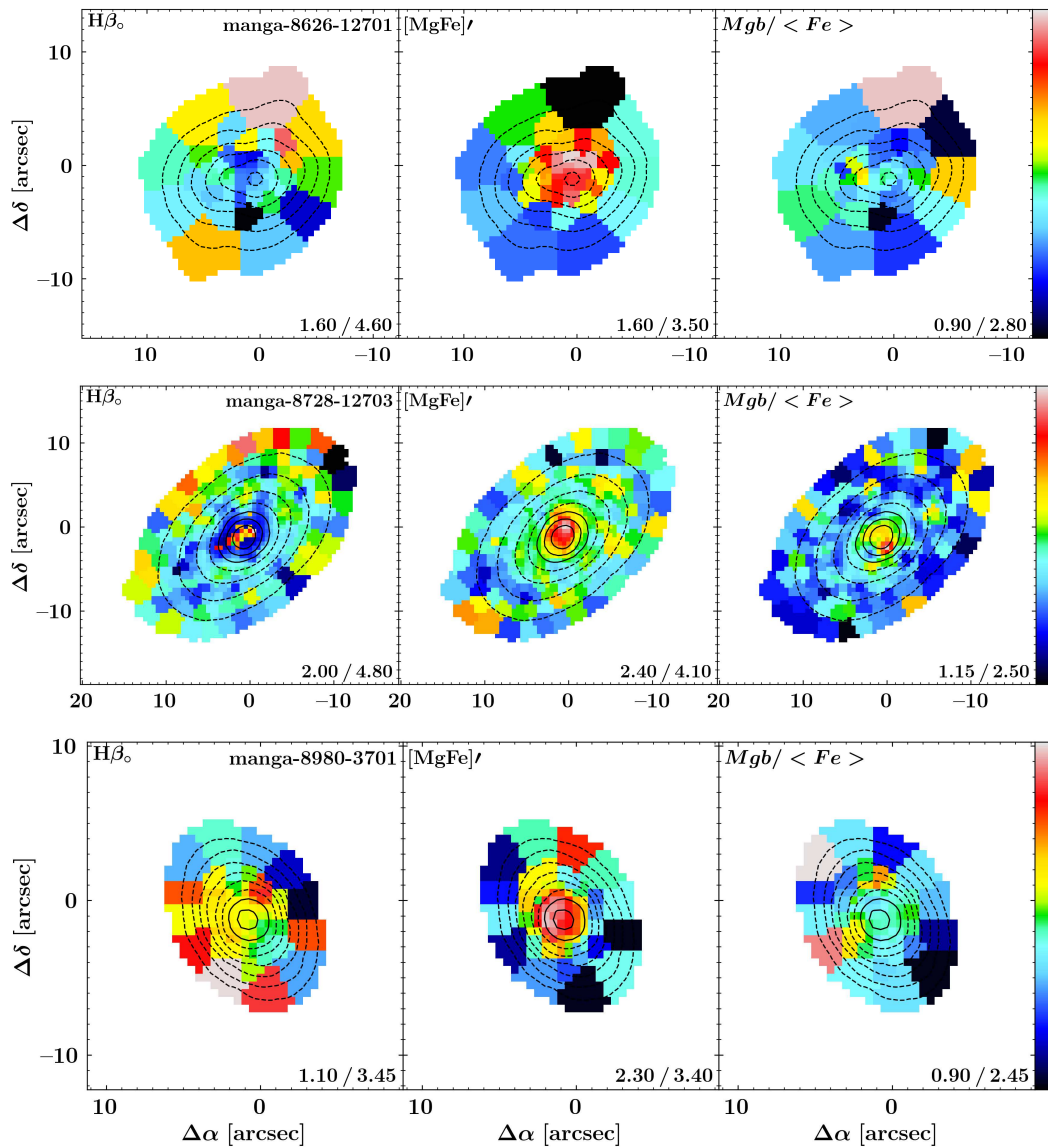


FIGURE 6.5: Same as Fig. 6.2

is either misaligned, concentrated in the same region as the KDC, or appears to rotate in a direction perpendicular to the kinematically distinct component. In regards to the “ 2σ ” galaxy candidates, we confirm the presence of counter-rotation in the velocity fields of 11 out of the total 24 objects. The velocity dispersion maps of 5 have a clear double peak signature. We also discerned a singular central velocity peak in 2 of the cases with visible counter rotation. Nebular emission is present in 5 of those 24 galaxies. The size of this sample allowed us to confirm some previous conclusions drawn on the demographics and properties of galaxies with present counter rotation, namely that such objects are probably even rarer than previously reported by Krajnović et al. (2011) on the basis of the ATLAS^{3D} survey. However, some recent work has highlighted the importance of obtaining high spatial resolution observations in order to properly

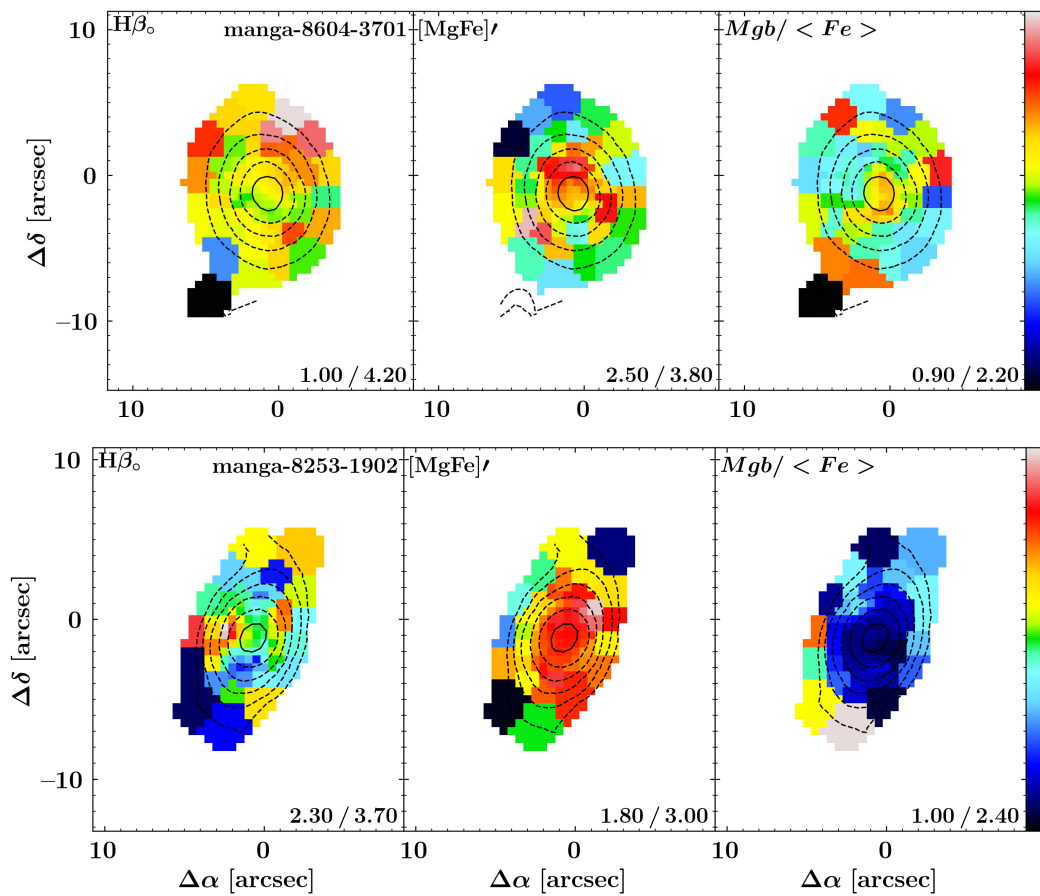


FIGURE 6.6: Same as Fig. 6.2

identify potential KDC or a central velocity twist (e.g. Viaene et al., 2018). Furthermore, we can qualitatively confirm the observed dichotomy in the stellar population properties of galaxies with counter rotation pointed out by McDermid et al. (2015).

Below, as illustrated in Figs. 6.2, 6.3, 6.4, 6.5, 6.6, 6.7), we qualitatively would focus on the line-strength maps of $H\beta_0$ and composite indices $Mg\ b/\langle Fe \rangle$ and $[MgFe]'$ that were found to be good proxies for the single stellar population equivalent ages, metallicity, and $[\alpha/Fe]$ abundance (see Sect 5.6.1) on each of the galaxies, where our analysis produced notable results.

manga-7815-1901

The region with decoupled component has higher metallicity than the one seen out of it. Some the region could also possibly have alpha-elemental abundance that is lower than the one of the rest of the galaxy. We could not distinguish any trend in the strength of $H\beta_0$.

manga-8133-12703

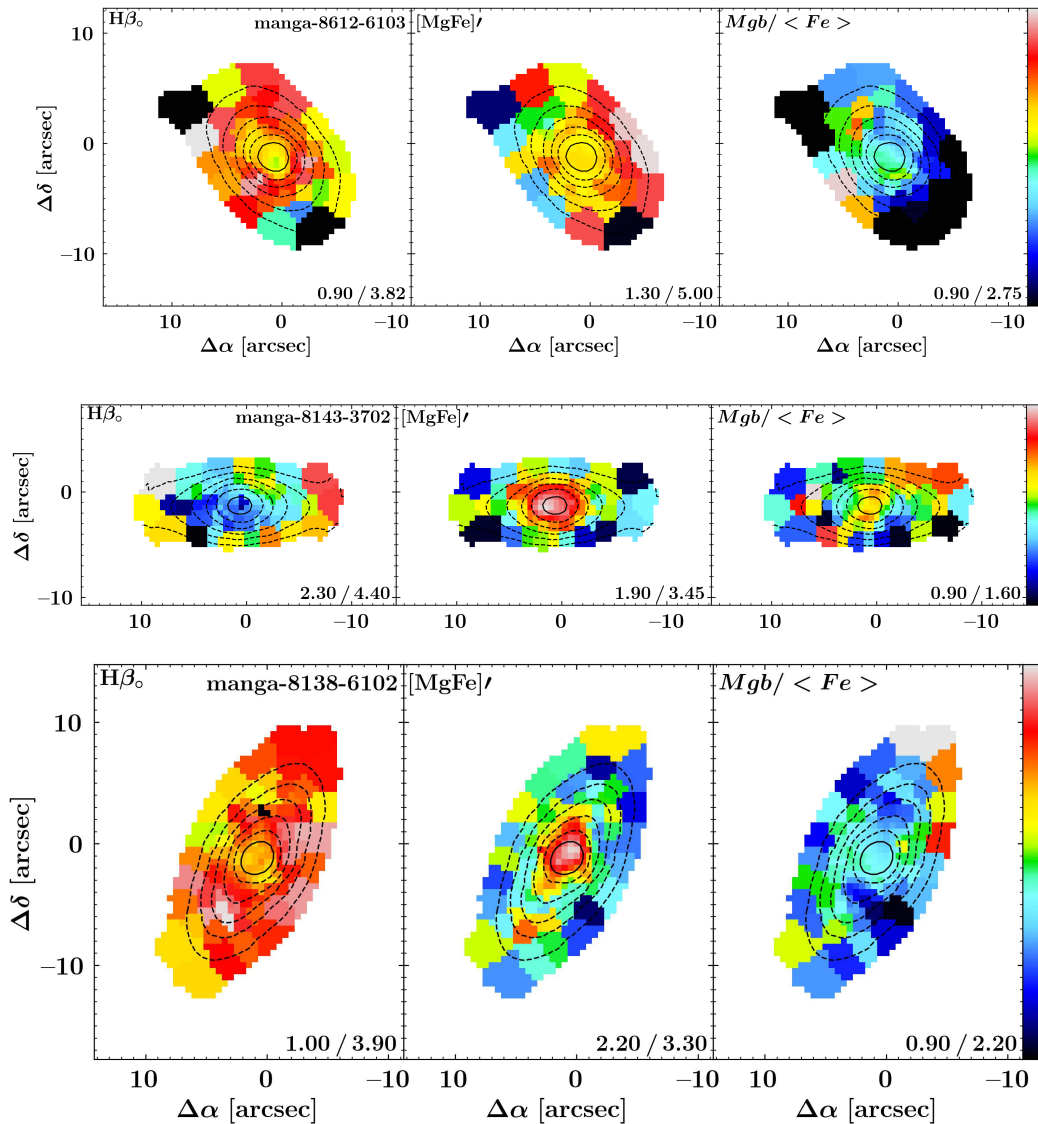


FIGURE 6.7: Same as Fig. 6.2

Higher metallicity is likely associated with the region of the kinematically decoupled component. No noticeable age or alpha- elemental abundance difference can be anticipated.

manga-8138-6102

We anticipate the SSP in the very centre associated with the kinematically decoupled component is younger than the rest of the galaxy that also possibly is of distinguishably higher metallicity. We cannot draw any reasonable expectations for the alpha-element abundance.

manga-8143-1902

The stellar population in the zone of the kinematic component is likely of higher alpha-element abundance. However, we could not put any reasonable assumption on any of the other stellar population parameters.

manga-8143-3702

We anticipate no difference in the ages of the stellar population in the zone of the kinematically distinct component and the host galaxy. The central region of the galaxy is likely characterised by a stellar population with high metallicity.

manga-8149-1901

We expect the stellar population of the galaxy where the kinematic component is present to have higher metallicity, older age, and lower alpha-elemental abundance in comparison to the main galaxy body.

manga-8241-6104

The quality of our data did not allow us to draw any predictions.

manga-8253-1902

The zone where kinematical decoupling is present is possibly of higher metallicity and has smaller alpha-element abundance than the rest of the galaxy.

manga-8319-12703

We predict the stellar population has similar age throughout the galaxy. However, we expect higher metallicity and alpha-element abundance in the stellar population for the zone where the kinematic component is present with respect to the rest of the host galaxy.

manga-8335-1901

We could not draw any predictions on the difference in the properties of the zone with and without kinematic decomposition.

manga-8335-6101

We anticipate younger stellar population in the region where the distinct kinematic component is present. However, the metallicity and alpha-element enhancement of the stellar population of the host seems to be uniform.

manga-8459-6104

We anticipate higher metallicity of the stellar population in the zone with the kinematically distinct component in comparison to the host galaxy.

manga-8461-3701

We could not draw any predictions for the different in the stellar population properties of the kinematically distinct component and the host galaxy.

manga-8604-3701

The stellar population in the zone, where we can notice the presence of the distinct kinematic component, is likely characterized with higher metallicity and alpha-element abundance in comparison to the host galaxy.

manga-8606-3702

We anticipate the central region of this galaxy consists of older stellar population with higher metallicity and alpha-element abundance in comparison to the rest of the galaxy.

manga-8612-6103

The region, where we can observe the kinematically distinct component we anticipate a stellar population of older age, lower metallicity, and lower alpha-abundance compared to the host galaxy.

manga-8615-1902

We expect the stellar population in the central region of this galaxy, where we can notice kinematically distinct component, to have younger age and lower metallicity stellar population with respect to its host galaxy.

manga-8626-12701

This system exhibits a very strange kinematic and photometric behaviour. We anticipate some problem with the data reduction.

manga-8728-12703

The stellar population in the central region of the galaxy, where a kinematically distinct component is present, likely has younger age, higher metallicity, and higher alpha-elemental abundance with respect to the rest of the system.

manga-8980-3701

We anticipate the stellar population in the center of the galaxy to have higher metallicity in comparison to the outskirts.

On the other hand, the absence of ionized-gas emission in a large fraction of these galaxies is puzzling and casts some doubts on the preferred scenario for the formation of counter-rotating structures (i.e. the acquisition of external gas in retrograde orbits as pointed out in the review of Corsini (2014)). Furthermore, we find that the ionized gas, when detected, more often co-rotates with the main galactic body (in 1 of the KDC galaxies and 3 of the “ 2σ ” objects) in comparison to co-rotation with respect to the kinematically distinct component (1 of the KDC host galaxies and 1 of the “ 2σ ” systems). Even more interesting is the occurrence of misaligned ionized gas distribution in one of the KDC hosts and the presence of nebular emission that shows rotation perpendicular to the kinematically distinct component in one of the KDC and “ 2σ ” systems.

6.5 Summary and Future Work

Using some preliminary analysis in this section we have confirmed some previous findings in regards to the demographics and properties of galaxies with observed counter rotation. Only more thorough analysis involving kinematic decomposition would further elucidate the nature of these objects and will be the scope of a future paper. Similarly, we have tentatively confirmed the presence of in-flowing cold gas in one of our Seyfert 2 galaxies already observed as part of the MaNGA survey. This confirms the validity of our analysis performed in Chap. 4 and allows us, as part of a future study, to focus on obtaining spatially resolved view of galactic in- and out-flows.

Chapter 7

Conclusions and Further Work

7.1 Conclusions

This thesis has attempted to probe the importance of two of the processes that can influence the population of galaxies and its individual members in the local Universe. In Chap. 4 we focused on the importance of Seyfert 2 AGN activity towards the driving of cold-gas large-scale galactic outflows, proposed as one manifestation of AGN feedback. We find that only a very small fraction of the galaxies with such optical AGN show absorption-line signatures of galactic winds. Moreover, in the cases with optical Seyfert 2 activity, suggestive of the presence of out-flowing cold gas, ancillary observations indicated that the primary driving mechanism was not the AGNs, but star formation. Such observations reinforce some recent suggestions in regards to nearby galaxies, that the somewhat long delay between the triggering of the central AGN and an associated episode of star formation leaves a significantly depleted gas reservoir for the AGN itself to couple to and directly influence. Instead, it largely just acts to remove or heat that residual gas and, therefore, not directly influence the process of star formation. Consequently, the quenching of local galaxies is very likely due to either the exhaustion of their star-forming gas reservoirs or winds driven by star-formation. On the other hand, in Chap. 5 we studied two galaxies that appear to host counter-rotating structures that are often linked to the acquisition of external gas or mergers. In one of these galaxies (NGC 448) we managed to separate the contribution of each counter-rotating component in our integral-field observations. Aided by this decomposition we could identify the embedded counter-rotating component is a disk. We showed that the stellar populations of each of the components have similar equivalent ages, but are chemically different, albeit this did not allow us to directly associate the origin of

this counter-rotating disk to either a past "wet" merger or a gas accretion event. We found no evidence for a distinct truly counter-rotating component in our second galaxy (NGC 4365). The observed counter-rotation in the velocity field of the stellar line-of-sight velocity distribution there is very likely simply a projection effect due to the complex orbital configuration of that galaxy. Finally, in Chap. 6 we have drawn on the large volume of a recent integral-field survey (MaNGA) to verify the analysis used in our study of the importance of AGN feedback and confirm some previously known observed demographics and properties of galaxies that display stellar counter-rotation. However, we report somewhat low fraction of galaxies that simultaneously have ionized-gas emission and counter rotation. These preliminary results conflict with previous studies that have more commonly identified counter rotation with the presence of a gas reservoir, detected through ionized-gas emission, and cast some doubt on the hypothesis that counter-rotating structures form predominantly by external gas acquisition.

7.2 Further Work

This thesis has probed the importance of AGN feedback and mergers in the formation and evolution of galaxies. Nevertheless, we could perform some complementary investigations to shed further light on the role of these two processes within the galaxy population and in its individual members, both locally and at higher redshifts. We propose the following future projects:

- To better understand the multi-phase nature of AGN-driven outflows in the local Universe we could apply the methods developed throughout this thesis drawing on the samples of AGN galaxies such as the WiFeS Siding Spring Southern Seyfert Spectroscopic Snapshot Survey (S7) AGN Survey (Scharwächter et al., 2016; Thomas et al., 2017), where the presence of deep NaD absorption such as the one investigated by us in Capt. 4 has been already noted (Dopita et al., 2015), and the Close AGN Reference Survey (Husemann et al., 2017, CARS). In particular, we would be very interested in deriving more stringent estimates for the mass-loading factors such winds have as we could potentially constrain the masses entrained in the cold and warm-to-hot ISM phase through the absorption and ionized-gas lines.
- Moreover, future surveys performed for higher redshift galaxies with multi-object spectrographs such as MOONS (Cirasuolo and MOONS Consortium, 2016) would open the possibility to perform similar analysis through stacking on the NaD absorption feature.

We could try to put a similar constraint on the ability of AGNs to drive large-scale cold-gas outflows as the one we have done in this thesis.

- The origin and evolution of the different kinematically distinct components such as the ones we have studied in Chap. 5 is still not well understood. Partially, this is due to fact that they are usually studies on an object-by-object basis. The wealth of information gathered by the new generation IFU surveys would be perfect for the identification and compilation of larger samples of such peculiar objects representing in some respects the extremes of the process of galaxy merging. Automatising the process of how such galaxies can be split in their distinctive components is therefore of great importance.

Chapter 8

Appendix A

In this appendix we give a brief overview of some important features that we were able to discern among the galaxies that display counter-rotation in the sample of Graham et al. (2018). Figures 8.1,8.2,8.3, 8.4, and 8.5 show some of our preliminary results for the sample of galaxies with suspected " 2σ " and KDC signatures. We have omitted the galaxies where we could not achieve a satisfactory fit or our Voronoi binning procedure produced bins with exceptionally large sizes. These figures consist of various panels. The separated panels display the ionized-gas kinematics of H α . The top left corner holds a label that shows the particular measurement label. The bottom right corner displays the corresponding scale of our adopted color-coding. In multiple places of the panels we have labeled the our adopted identification of the particular object displayed.

Below we provide some brief comments on the " 2σ " candidate galaxies:

manga-7815-1901: The stellar velocity map of this galaxy clearly shows a reverse in direction of rotation. We could also tentatively see the presence of two velocity dispersion peaks. The galaxy shows some ionized gas that appears to rotate perpendicular to the direction of rotation of the main galaxy body and the counter-rotating component.

manga-7962-9102: -

manga-8138-6102: We can clearly distinguish the presence of a distinct kinematic component in the velocity field of this galaxy. Moreover, it has a velocity dispersion map that is pronouncedly double-peaked. We also detect strong emission from ionized gas that counter-rotates with respect to the kinematically distinct component. The very central region of this galaxy shows enhanced strength of the Fe5015 index.

manga-8143-1902: This galaxy possess a clear " 2σ " signature in its velocity dispersion maps.

There is also some evidence for the presence of a distinct component in its velocity maps. The region overlapping with the kinematically distinct component appears to have higher Fe5015 index strength. We cannot discern any features in its $H\beta$ line-strength index map.

manga-8143-3702: We can clearly see two peaks in the velocity dispersion map of this galaxy. Moreover, there is a clear abrupt flip in the direction of rotation displayed by the velocity field. We have also detected the presence of ionized gas emission that appear to co-rotate with the main galaxy body. The central region of this galaxy shows very pronounced raise in the strength of the Mg b absorption-line index.

manga-8249-1901: –

manga-8253-1902: This galaxy shows some signature of two peaks in its velocity dispersion map. Its velocity field shows a non-abrupt change in the direction of rotation. The region occupied by the kinematically distinct component have lower $H\beta$ and higher Fe5015 line strength index measurements.

manga-8333-1902: –

manga-8335-1901: We could clearly identify an abrupt flip in the direction of rotation in the velocity field of this galaxy. We also see an increase in velocity dispersion indicative of two velocity dispersion peaks. In the region occupied by the kinematically distinct component we report higher $H\beta$ and Fe 5015 line-strength indices.

manga-8449-6101: –

manga-8453-3703: –

manga-8459-6104: We could not discern the presence of two peaks in the velocity dispersion map. We instead report a central peak. The line-strength indices are hard to interpret.

manga-8461-3701: We can clearly see the presence of a central counter-rotating region. The velocity dispersion seems to be more centrally peaked than double-peaked. We could not conclusively interpret the line-strength index measurements.

manga-8551-6101: –

manga-8604-3701: We can clearly see an abrupt change in the direction of rotation as displayed by the stellar velocity map. However, we cannot conclusively infer the presence of two peaks in the velocity dispersion field. The central region where the flip in the velocity occurs we measure lower $H\beta$ and higher Mg b line strength index.

manga-8551-6101: –

manga-8604-3701: We can clearly see an abrupt change in the direction of rotation in the central region of this galaxy. However our velocity dispersion measurements did not allow for its safe identification as “ 2σ ”. The region occupied by the kinematically distinct component shows

somewhat lower $H\beta$ and higher Mg b indices line-strength measurements.

manga-8606-3702: We could clearly identify both an abrupt flip in the direction of rotation and " 2σ " signature in the velocity and velocity dispersion maps. In addition we detect the presence of ionized gas that appears to counter-rotate with respect to the kinematically distinct region. Our line-strength measurements are indicative of the presence of older population that is more metal enriched and alpha-element abundant than the main galaxy body overlapping with the position of kinematically distinct component.

manga-8615-1902: This galaxy shows a velocity flip and a clear signature of " 2σ ". Moreover, it displays some ionized-gas emission that appears to counter-rotate with respect to the main galaxy body. The regions where the kinematically distinct component resides appear to have higher $H\beta$ and Fe5015 line-strength index values, whereas our maps show lower Mg b strengths.

manga-8618-1901: –

manga-8714-9102: –

manga-8980-3701: This galaxy shows a velocity flip in its central region. However, our analysis showed its velocity dispersion map is not reminiscent of " 2σ ", but is ordinarily peaked in the galaxy central region. Moreover, the higher Fe5015 index line-strength spatially overlap with the very central high velocity region. We cannot reliably interpret the $H\beta$ line-strength measurement.

manga-9026-1902: Our inspection and analysis of the datacube showed the presence of a second galaxy in the field of view. We were not able to conclusively establish two peaks in the velocity dispersion maps of this galaxy.

manga-8980-12703: We did not manage to identify this galaxy as " 2σ ".

We provide some brief comments on the galaxies that were highlighted to show a KDC below:

manga-8133-12703: The velocity map of this galaxy is indicative of a KDC. However, our results could not unequivocally interpret any of the line-strength measurements.

manga-8149-1901: This galaxy hosts a small KDC. We could also identify a co-spatial region with enhanced Mg b line-strength.

manga-8155-1902: –

manga-8241-6104: The velocity maps of this galaxy indicate the presence of a KDC. However, our fit to the outer regions of this galaxy were not satisfactory even despite our attempts to extract stellar kinematics with different Voronoi binning configurations.

manga-8259-12705: –

manga-8319-12703: This galaxy shows a clear signature of a KDC and has a centrally peaked velocity dispersion map. We were not able to discern any distinct features in our line-strength measurements.

manga-8335-6101: We detect the clear signature of a KDC in the velocity map of this galaxy. Moreover, we could identify the presence of ionized-gas emission that spatially overlaps with the KDC. The KDC appear to also have a younger stellar population as traced by the higher $H\beta$ line-strength in the regions where we detect ionized gas and the KDC itself.

manga-8592-12705: –

manga-8612-1901: –

manga-8612-6102: –

manga-8612-6103: This galaxy shows a clear velocity twist in its central region. It also has a clear central velocity dispersion peak. Moreover, at the region of the twist we see a dip in the strength of $H\beta$ indicating the presence of older stellar population.

manga-8626-12701: This galaxy shows very complex surface brightness profile as traced by the isophotes. It appears to have a twist in its central region. It also shows a dip in its velocity dispersion map at the position of highest surface brightness. The spacial region of the KDC is characterised by higher Fe5015 and Mg b line strengths and subtly lower $H\beta$. Perhaps more interesting is the distribution of the ionized gas. It shows clear rotation in the direction almost perpendicular to the one observed in for the KDC.

manga-8728-12703: This galaxy shows a clear signature of a central KDC. Its velocity dispersion field is centrally peaked. The region overlapping with the KDC shows lower $H\beta$ line strengths indicative of older stellar population. Moreover, the very central region of this galaxy shows an enhancement in the strengths of both Fe5015 and Mg b indices. This galaxy also possess ionize-gas that appears to be misaligned with respect to the semi-major photometric axis.

manga-8728-6104: –

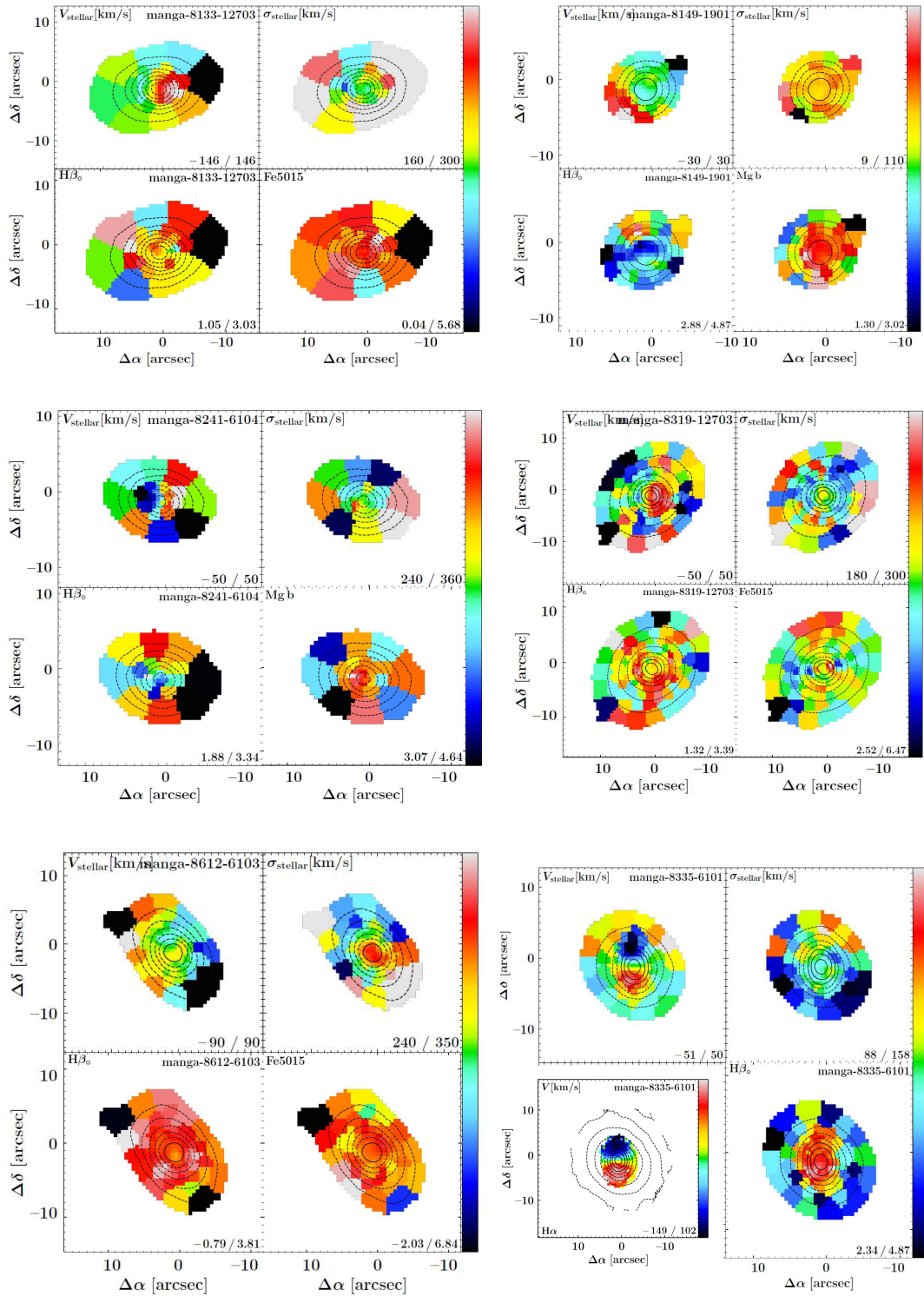


FIGURE 8.1: Various measurements on the kinematically distinct galaxies in MaNGA

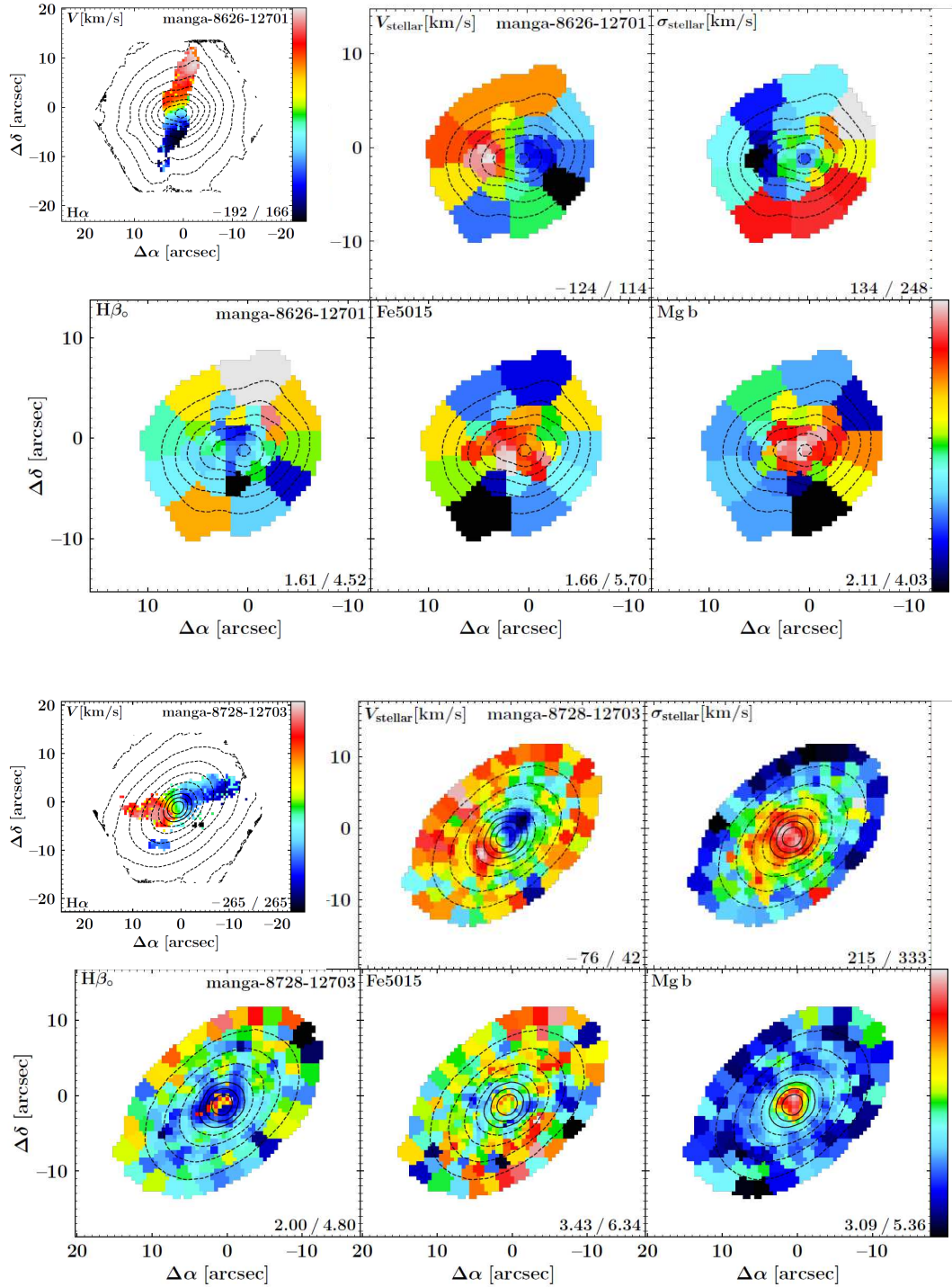


FIGURE 8.2: Same as Fig. A1

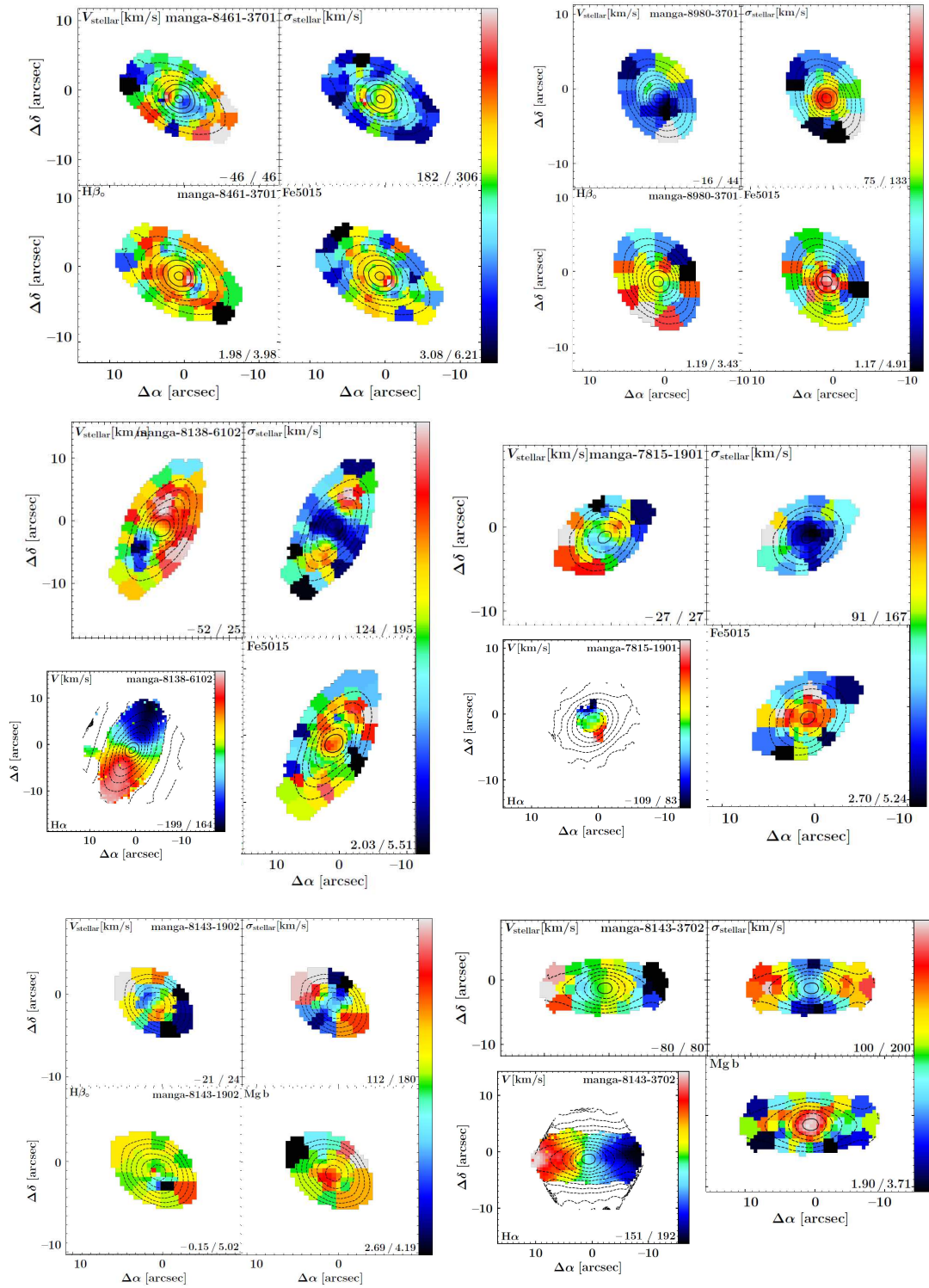


FIGURE 8.3: Same as Fig. A1

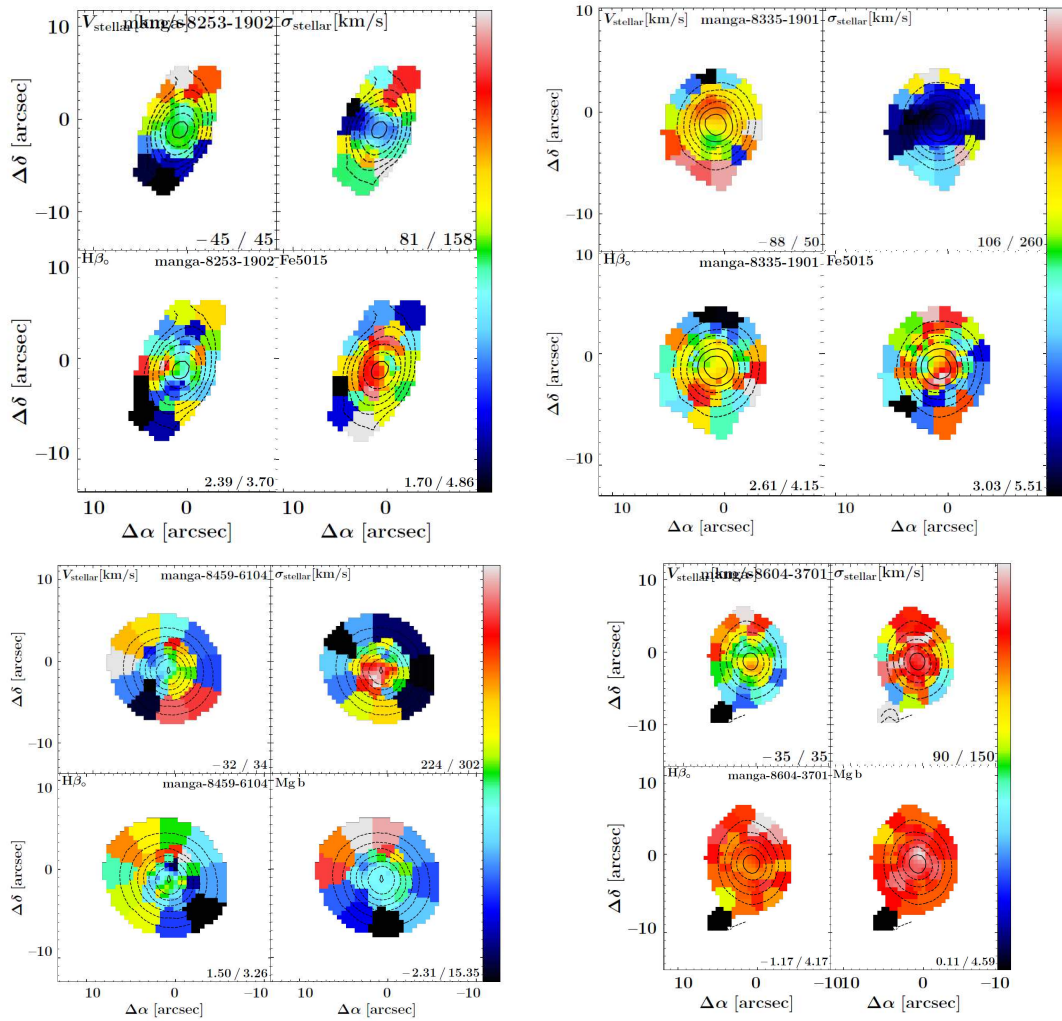


FIGURE 8.4: Same as Fig. A1

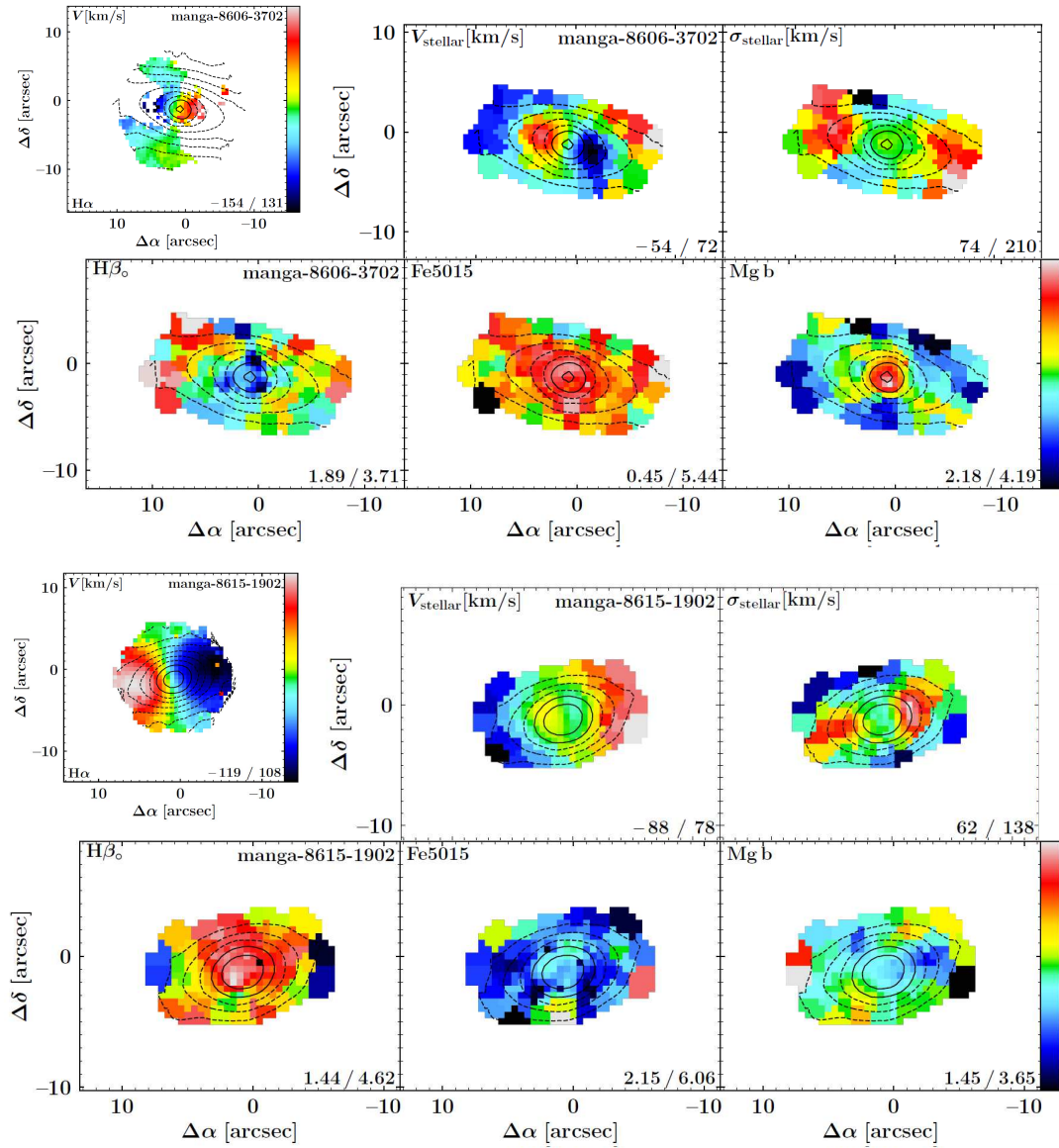


FIGURE 8.5: Same as Fig. A1

Bibliography

- Abazajian, K.N., Adelman-McCarthy, J.K., Agüeros, M.A., et al., 2009. The Seventh Data Release of the Sloan Digital Sky Survey. *ApJ*, 182:543-558.
- Abell, P.A., Allison, J., Anderson, S.F., et al., 2009. Lsst science book, version 2.0. *arXiv preprint arXiv:0912.0201*.
- Aguado, D.S., Ahumada, R., Almeida, A., et al., 2019. The Fifteenth Data Release of the Sloan Digital Sky Surveys: First Release of MaNGA-derived Quantities, Data Visualization Tools, and Stellar Library. *The Astrophysical Journal Supplement Series*, 240:23.
- Alatalo, K., Blitz, L., Young, L.M., et al., 2011. Discovery of an Active Galactic Nucleus Driven Molecular Outflow in the Local Early-type Galaxy NGC 1266. *ApJ*, 735(2):88.
- Alatalo, K., Cales, S.L., Rich, J.A., et al., 2016. Shocked POststarburst Galaxy Survey. I. Candidate Post-starburst Galaxies with Emission Line Ratios Consistent with Shocks. *ApJ*, 224:38.
- Algorry, D.G., Navarro, J.F., Abadi, M.G., et al., 2014. Counterrotating stars in simulated galaxy discs. *MNRAS*, 437:3596.
- Allen, M.G., Groves, B.A., Dopita, M.A., et al., 2008. The MAPPINGS III Library of Fast Radiative Shock Models. *ApJ*, 178(1):20.
- Alpher, R.A., Bethe, H., and Gamow, G., 1948. The Origin of Chemical Elements. *Physical Review*, 73(7):803.
- Andernach, H. and Zwicky, F., 2017. English and Spanish Translation of Zwicky's (1933) The Redshift of Extragalactic Nebulae. *arXiv e-prints*.
- Andrews, B.H. and Thompson, T.A., 2011. Assessing radiation pressure as a feedback mechanism in star-forming galaxies. *The Astrophysical Journal*, 727(2):97.

- Antonucci, R., 1993. Unified models for active galactic nuclei and quasars. *Annual Review of Astronomy and Astrophysics*, 31:473.
- Arav, N., Korista, K.T., de Kool, M., et al., 1999. Hubble Space Telescope Observations of the Broad Absorption Line Quasar PG 0946+301. *ApJ*, 516:27.
- Arnold, J.A., Romanowsky, A.J., Brodie, J.P., et al., 2014. The SLUGGS Survey: Wide-field Stellar Kinematics of Early-type Galaxies. *ApJ*, 791:80.
- Bacon, R., Accardo, M., Adjali, L., et al., 2010. The MUSE second-generation VLT instrument. In *Ground-based and Airborne Instrumentation for Astronomy III*, volume 7735 of *Proc. SPIE Conf. Ser.*, page 773508.
- Bacon, R., Bauer, S., Boehm, P., et al., 2006. Probing unexplored territories with MUSE: a second generation instrument for the VLT. In *ProSPIE*, volume 6269 of *Society of Photo-Optical Instrumentation Engineers (SPIE) Conference Series*, page 62690J.
- Bacon, R., Copin, Y., Monnet, G., et al., 2001. The SAURON project - I. The panoramic integral-field spectrograph. *MNRAS*, 326(1):23.
- Bae, H.J. and Woo, J.H., 2018. The Independence of Neutral and Ionized Gas Outflows in Low- z Galaxies. *ApJ*, 853(2):185.
- Balcells, M. and Quinn, P.J., 1990. The formation of counterrotating cores in elliptical galaxies. *ApJ*, 361:381.
- Baldry, I.K., Balogh, M.L., Bower, R., et al., 2004a. Color bimodality: Implications for galaxy evolution. In R.E. Allen, D.V. Nanopoulos, and C.N. Pope, editors, *The New Cosmology: Conference on Strings and Cosmology*, volume 743 of *American Institute of Physics Conference Series*, pages 106–119.
- Baldry, I.K., Glazebrook, K., Brinkmann, J., et al., 2004b. Quantifying the Bimodal Color-Magnitude Distribution of Galaxies. *ApJ*, 600(2):681.
- Baldwin, J.A., Phillips, M.M., and Terlevich, R., 1981. Classification parameters for the emission-line spectra of extragalactic objects. *PASP*, 93:5.
- Balogh, M.L., Morris, S.L., Yee, H.K.C., et al., 1999. Differential Galaxy Evolution in Cluster and Field Galaxies at $z \sim 0.3$. *ApJ*, 527:54.

- Bamford, S.P., Nichol, R.C., Baldry, I.K., et al., 2009. Galaxy Zoo: the dependence of morphology and colour on environment*. *MNRAS*, 393:1324.
- Bassett, R., Bekki, K., Cortese, L., et al., 2017. The formation of S0 galaxies with counter-rotating neutral and molecular hydrogen. *MNRAS*, 471:1892.
- Bastian, N., Covey, K.R., and Meyer, M.R., 2010. A Universal Stellar Initial Mass Function? A Critical Look at Variations. *Annual Review of Astronomy and Astrophysics*, 48:339.
- Beers, T.C., Flynn, K., and Gebhardt, K., 1990. Measures of location and scale for velocities in clusters of galaxies - A robust approach. *AJ*, 100:32.
- Belfiore, F., Maiolino, R., Maraston, C., et al., 2016. SDSS IV MaNGA - spatially resolved diagnostic diagrams: a proof that many galaxies are LIERs. *MNRAS*, 461:3111.
- Belfiore, F., Maiolino, R., Tremonti, C., et al., 2017. SDSS IV MaNGA - metallicity and nitrogen abundance gradients in local galaxies. *MNRAS*, 469(1):151.
- Bell, E.F., Wolf, C., Meisenheimer, K., et al., 2004. Nearly 5000 Distant Early-Type Galaxies in COMBO-17: A Red Sequence and Its Evolution since $z \sim 1$. *ApJ*, 608:752.
- Bellhouse, C., Jaffé, Y.L., Hau, G.K.T., et al., 2017. GASP. II. A MUSE View of Extreme Ram-Pressure Stripping along the Line of Sight: Kinematics of the Jellyfish Galaxy JO201. *ApJ*, 844(1):49.
- Bender, R., 1988. Rotating and counter-rotating cores in elliptical galaxies. *A&A*, 202:L5.
- Bender, R., 1990. Unraveling the kinematics of early-type galaxies - Presentation of a new method and its application to NGC4621. *A&A*, 229:441.
- Bender, R. and Surma, P., 1992. Mg2 line-strength profiles of elliptical galaxies with kinematically decoupled cores. *A&A*, 258:250.
- Bernardi, M., Meert, A., Sheth, R.K., et al., 2013. The massive end of the luminosity and stellar mass functions: dependence on the fit to the light profile. *MNRAS*, 436:697.
- Bertola, F., Buson, L.M., and Zeilinger, W.W., 1988. Counter-rotation in dust-lane ellipticals and the implications for accretion events in galaxies. *Nature*, 335(6192):705.
- Bertola, F., Buson, L.M., and Zeilinger, W.W., 1992. The External Origin of the Gas in S0 Galaxies. *ApJ*, 401:L79.

- Bertola, F., Cinzano, P., Corsini, E.M., et al., 1996. Counterrotating Stellar Disks in Early-Type Spirals: NGC 3593. *ApJ*, 458:L67.
- Best, P.N. and Heckman, T.M., 2012. On the fundamental dichotomy in the local radio-AGN population: accretion, evolution and host galaxy properties. *MNRAS*, 421:1569.
- Bettoni, D., Galletta, G., and Prada, F., 2001. The visible environment of galaxies with counter-rotation. *A&A*, 374:83.
- Binney, J., 2004. On the origin of the galaxy luminosity function. *MNRAS*, 347:1093.
- Binney, J., 2005. Rotation and anisotropy of galaxies revisited. *MNRAS*, 363(3):937.
- Binney, J. and Tabor, G., 1995. Evolving Cooling Flows. *MNRAS*, 276:663.
- Binney, J. and Tremaine, S., 2008. *Galactic Dynamics: Second Edition*. Princeton University Press.
- Birnboim, Y. and Dekel, A., 2003. Virial shocks in galactic haloes? *MNRAS*, 345:349.
- Bittner, A., Falcón-Barroso, J., Nedelchev, B., et al., 2019. The GIST pipeline: A multi-purpose tool for the analysis and visualisation of (integral-field) spectroscopic data. *A&A*, 628:A117.
- Blandford, R., Meier, D., and Readhead, A., 2019. Relativistic Jets from Active Galactic Nuclei. *Annual Review of Astronomy and Astrophysics*, 57:467.
- Blandford, R.D., 1990. Physical processes in active galactic nuclei. In R.D. Blandford, H. Netzer, L. Woltjer, T.J.L. Courvoisier, and M. Mayor, editors, *Active Galactic Nuclei*, pages 161–275.
- Blandford, R.D., Netzer, H., Woltjer, L., et al., editors, 1990. *Active Galactic Nuclei*.
- Blum, R.D., Burleigh, K., Dey, A., et al., 2016. The DECam Legacy Survey. In *American Astronomical Society Meeting Abstracts*, volume 228 of *American Astronomical Society Meeting Abstracts*, page 317.01.
- Bois, M., Emsellem, E., Bournaud, F., et al., 2011. The ATLAS^{3D} project - VI. Simulations of binary galaxy mergers and the link with fast rotators, slow rotators and kinematically distinct cores. *MNRAS*, 416:1654.
- Bolton, A.S., Schlegel, D.J., Aubourg, É., et al., 2012. Spectral Classification and Redshift Measurement for the SDSS-III Baryon Oscillation Spectroscopic Survey. *AJ*, 144:144.

- Boveia, A. and Doglioni, C., 2018. Dark Matter Searches at Colliders. *Annual Review of Nuclear and Particle Science*, 68:429.
- Bressan, A., Marigo, P., Girardi, L., et al., 2012. PARSEC: stellar tracks and isochrones with the PAdova and TRieste Stellar Evolution Code. *MNRAS*, 427(1):127.
- Brinchmann, J., Charlot, S., White, S.D.M., et al., 2004a. The physical properties of star-forming galaxies in the low-redshift Universe. *MNRAS*, 351:1151.
- Brinchmann, J., Charlot, S., White, S.D.M., et al., 2004b. The physical properties of star-forming galaxies in the low-redshift Universe. *MNRAS*, 351(4):1151.
- Brown, T., Catinella, B., Cortese, L., et al., 2017. Cold gas stripping in satellite galaxies: from pairs to clusters. *MNRAS*, 466(2):1275.
- Bruzual, G. and Charlot, S., 2003. Stellar population synthesis at the resolution of 2003. *MNRAS*, 344:1000.
- Bundy, K., Bershady, M.A., Law, D.R., et al., 2015. Overview of the SDSS-IV MaNGA Survey: Mapping nearby Galaxies at Apache Point Observatory. *ApJ*, 798:7.
- Calzetti, D., Armus, L., Bohlin, R.C., et al., 2000. The Dust Content and Opacity of Actively Star-forming Galaxies. *ApJ*, 533:682.
- Capaccioli, M., 1989. Photometry of early-type galaxies and the $r^{1/4}$ law. In J. Corwin Harold G. and L. Bottinelli, editors, *World of Galaxies (Le Monde des Galaxies)*, pages 208–227.
- Cappellari, M., 2016. Structure and Kinematics of Early-Type Galaxies from Integral Field Spectroscopy. *Annual Review of Astronomy and Astrophysics*, 54:597.
- Cappellari, M., 2017. Improving the full spectrum fitting method: accurate convolution with Gauss-Hermite functions. *MNRAS*, 466:798.
- Cappellari, M. and Copin, Y., 2003. Adaptive spatial binning of integral-field spectroscopic data using Voronoi tessellations. *MNRAS*, 342:345.
- Cappellari, M. and Emsellem, E., 2004. Parametric Recovery of Line-of-Sight Velocity Distributions from Absorption-Line Spectra of Galaxies via Penalized Likelihood. *PASP*, 116:138.
- Cappellari, M., Emsellem, E., Bacon, R., et al., 2007. The SAURON project - X. The orbital anisotropy of elliptical and lenticular galaxies: revisiting the $(V/\sigma, \epsilon)$ diagram with integral-field stellar kinematics. *MNRAS*, 379:418.

- Cappellari, M., Emsellem, E., Krajnović, D., et al., 2011. The ATLAS^{3D} project - I. A volume-limited sample of 260 nearby early-type galaxies: science goals and selection criteria. *MNRAS*, 413:813.
- Cappellari, M., Scott, N., Alatalo, K., et al., 2013. The ATLAS^{3D} project - XV. Benchmark for early-type galaxies scaling relations from 260 dynamical models: mass-to-light ratio, dark matter, Fundamental Plane and Mass Plane. *MNRAS*, 432(3):1709.
- Cardiel, N., Gorgas, J., Cenarro, J., et al., 1998. Reliable random error estimation in the measurement of line-strength indices. *A&A Supp.*, 127:597.
- Cardoso, L.S.M., Gomes, J.M., and Papaderos, P., 2017. Impact of an AGN featureless continuum on estimation of stellar population properties. *ArXiv e-prints*.
- Carlberg, R.G., 1984. Dissipative formation of an elliptical galaxy. *ApJ*, 286:403.
- Carollo, C.M., Franx, M., Illingworth, G.D., et al., 1997a. Ellipticals with Kinematically Distinct Cores: V - I Color Images with WFC2. *ApJ*, 481(2):710.
- Carollo, C.M., Franx, M., Illingworth, G.D., et al., 1997b. Ellipticals with Kinematically Distinct Cores: V - I Color Images with WFC2. *ApJ*, 481(2):710.
- Cazzoli, S., Arribas, S., Colina, L., et al., 2014. Spatially resolved kinematics, galactic wind, and quenching of star formation in the luminous infrared galaxy IRAS F11506-3851. *A&A*, 569:A14.
- Cazzoli, S., Arribas, S., Maiolino, R., et al., 2016. Neutral gas outflows in nearby [U]LIRGs via optical NaD feature. *A&A*, 590:A125.
- Cenarro, A.J., Cardiel, N., Gorgas, J., et al., 2001. Empirical calibration of the near-infrared Ca ii triplet - I. The stellar library and index definition. *MNRAS*, 326(3):959.
- Cervantes, J.L. and Vazdekis, A., 2009. An optimized H β index for disentangling stellar population ages. *MNRAS*, 392(2):691.
- Chabrier, G., 2003. Galactic Stellar and Substellar Initial Mass Function. *PASP*, 115:763.
- Chen, X.Y., Liang, Y.C., Hammer, F., et al., 2010a. Comparing six evolutionary population synthesis models by performing spectral synthesis for galaxies. *A&A*, 515:A101.
- Chen, Y.M., Tremonti, C.A., Heckman, T.M., et al., 2010b. Absorption-line Probes of the Prevalence and Properties of Outflows in Present-day Star-forming Galaxies. *AJ*, 140:445.

- Chevalier, R.A. and Clegg, A.W., 1985. Wind from a starburst galaxy nucleus. *Nature*, 317(6032):44.
- Chilingarian, I., Prugniel, P., Sil'Chenko, O., et al., 2007a. NBursts: Simultaneous Extraction of Internal Kinematics and Parametrized SFH from Integrated Light Spectra. In A. Vazdekis and R. Peletier, editors, *Stellar Populations as Building Blocks of Galaxies*, volume 241 of *IAU Symposium*, pages 175–176.
- Chilingarian, I.V., Prugniel, P., Sil'Chenko, O.K., et al., 2007b. Kinematics and stellar populations of the dwarf elliptical galaxy IC 3653. *MNRAS*, 376:1033.
- Choi, J., Dotter, A., Conroy, C., et al., 2016. Mesa Isochrones and Stellar Tracks (MIST). I. Solar-scaled Models. *ApJ*, 823:102.
- Cicone, C., Maiolino, R., and Marconi, A., 2016. Outflows and complex stellar kinematics in SDSS star-forming galaxies. *A&A*, 588:A41.
- Cicone, C., Maiolino, R., Sturm, E., et al., 2014. Massive molecular outflows and evidence for AGN feedback from CO observations. *A&A*, 562:A21.
- Cid Fernandes, R., González Delgado, R.M., Schmitt, H., et al., 2004. The Stellar Populations of Low-Luminosity Active Galactic Nuclei. I. Ground-based Observations. *ApJ*, 605:105.
- Cid Fernandes, R., Stasińska, G., Mateus, A., et al., 2011. A comprehensive classification of galaxies in the Sloan Digital Sky Survey: how to tell true from fake AGN? *MNRAS*, 413:1687.
- Cid Fernandes, R., Stasińska, G., Schlickmann, M.S., et al., 2010. Alternative diagnostic diagrams and the 'forgotten' population of weak line galaxies in the SDSS. *MNRAS*, 403:1036.
- Cirasuolo, M. and MOONS Consortium, 2016. MOONS: A New Powerful Multi-Object Spectrograph for the VLT. In I. Skillen, M. Balcells, and S. Trager, editors, *Multi-Object Spectroscopy in the Next Decade: Big Questions, Large Surveys, and Wide Fields*, volume 507 of *Astronomical Society of the Pacific Conference Series*, page 109.
- Coccatto, L., Fabricius, M., Morelli, L., et al., 2015. Properties and formation mechanism of the stellar counter-rotating components in NGC 4191. *A&A*, 581:A65.
- Coccatto, L., Iodice, E., and Arnaboldi, M., 2014. Spectral decomposition of the stellar kinematics in the polar disk galaxy NGC 4650A. *A&A*, 569:A83.

- Coccatto, L., Morelli, L., Corsini, E.M., et al., 2011. Dating the formation of the counter-rotating stellar disc in the spiral galaxy NGC 5719 by disentangling its stellar populations. *MNRAS*, 412:L113.
- Coccatto, L., Morelli, L., Pizzella, A., et al., 2013. Spectroscopic evidence of distinct stellar populations in the counter-rotating stellar disks of NGC 3593 and NGC 4550. *A&A*, 549:A3.
- Coenda, V., Martínez, H.J., and Muriel, H., 2018. Green valley galaxies as a transition population in different environments. *MNRAS*, 473(4):5617.
- Cole, S., Norberg, P., Baugh, C.M., et al., 2001. The 2dF galaxy redshift survey: near-infrared galaxy luminosity functions. *MNRAS*, 326:255.
- Combes, F., 2008. Gaseous flows in galaxies. In M. Bureau, E. Athanassoula, and B. Barbuy, editors, *Formation and Evolution of Galaxy Bulges*, volume 245 of *IAU Symposium*, pages 151–160.
- Combes, F., 2012. Dynamical processes in galaxy centers. In *Journal of Physics Conference Series*, volume 372 of *Journal of Physics Conference Series*, page 012041.
- Concas, A., Popesso, P., Brusa, M., et al., 2017. Light breeze in the local Universe. *A&A*, 606:A36.
- Concas, A., Popesso, P., Brusa, M., et al., 2019. Two-face(s): ionized and neutral gas winds in the local Universe. *A&A*, 622:A188.
- Conroy, C., 2013. Modeling the Panchromatic Spectral Energy Distributions of Galaxies. *Annual Review of Astronomy and Astrophysics*, 51(1):393.
- Conselice, C.J., 2014. The Evolution of Galaxy Structure Over Cosmic Time. *Annual Review of Astronomy and Astrophysics*, 52:291.
- Corsini, E.M., 2014. Counter-Rotation in Disk Galaxies. In E. Iodice and E.M. Corsini, editors, *Multi-Spin Galaxies*, volume 486 of *Astronomical Society of the Pacific Conference Series*, page 51.
- Cowie, L.L., Songaila, A., Hu, E.M., et al., 1996. New Insight on Galaxy Formation and Evolution From Keck Spectroscopy of the Hawaii Deep Fields. *AJ*, 112:839.
- Creasey, P., Theuns, T., and Bower, R.G., 2013. How supernova explosions power galactic winds. *MNRAS*, 429(3):1922.

- Cresci, G., Marconi, A., Zibetti, S., et al., 2015. The MAGNUM survey: positive feedback in the nuclear region of NGC 5643 suggested by MUSE. *A&A*, 582:A63.
- Crocker, A.F., Jeong, H., Komugi, S., et al., 2009. Molecular gas and star formation in the red-sequence counter-rotating disc galaxy NGC 4550. *MNRAS*, 393:1255.
- Croton, D.J., Springel, V., White, S.D.M., et al., 2006. The many lives of active galactic nuclei: cooling flows, black holes and the luminosities and colours of galaxies. *MNRAS*, 365:11.
- Cushing, M.C., Rayner, J.T., and Vacca, W.D., 2005. An Infrared Spectroscopic Sequence of M, L, and T Dwarfs. *ApJ*, 623:1115.
- Daddi, E., Cimatti, A., Renzini, A., et al., 2004. A New Photometric Technique for the Joint Selection of Star-forming and Passive Galaxies at $1.4 < z < 2.5$. *ApJ*, 617:746.
- Dale, J.E., 2015. The modelling of feedback in star formation simulations. *New Astronomy Reviews*, 68:1.
- Davé, R., Katz, N., Oppenheimer, B.D., et al., 2013. The neutral hydrogen content of galaxies in cosmological hydrodynamic simulations. *MNRAS*, 434(3):2645.
- Davé, R., Thompson, R., and Hopkins, P.F., 2016. MUFASA: galaxy formation simulations with meshless hydrodynamics. *MNRAS*, 462(3):3265.
- Davies, R.L., Kuntschner, H., Emsellem, E., et al., 2001. Galaxy Mapping with the SAURON Integral-Field Spectrograph: The Star Formation History of NGC 4365. *ApJ*, 548:L33.
- Davis, M., Guhathakurta, P., Konidaris, N.P., et al., 2007. The All-Wavelength Extended Groth Strip International Survey (AEGIS) Data Sets. *ApJ*, 660(1):L1.
- Davis, T.A., Alatalo, K., Sarzi, M., et al., 2011. The ATLAS^{3D} project - X. On the origin of the molecular and ionized gas in early-type galaxies. *MNRAS*, 417(2):882.
- Davis, T.A., Krajnović, D., McDermid, R.M., et al., 2012. Gemini GMOS and WHT SAURON integral-field spectrograph observations of the AGN-driven outflow in NGC 1266. *MNRAS*, 426(2):1574.
- Dawson, K.S., Kneib, J.P., Percival, W.J., et al., 2016. The SDSS-IV Extended Baryon Oscillation Spectroscopic Survey: Overview and Early Data. *AJ*, 151:44.
- Dawson, K.S., Schlegel, D.J., Ahn, C.P., et al., 2013. The Baryon Oscillation Spectroscopic Survey of SDSS-III. *AJ*, 145(1):10.

- De Lucia, G., Weinmann, S., Poggianti, B.M., et al., 2012. The environmental history of group and cluster galaxies in a Λ cold dark matter universe. *MNRAS*, 423(2):1277.
- de Vaucouleurs, G., 1948. Recherches sur les Nebuleuses Extragalactiques. *Annales d'Astrophysique*, 11:247.
- de Vaucouleurs, G., 1959. Classification and Morphology of External Galaxies. *Handbuch der Physik*, 53:275.
- de Vaucouleurs, G., 1961. Integrated Colors of Bright Galaxies in the u, b, V System. *ApJ*, 5:233.
- de Zeeuw, P.T., Bureau, M., Emsellem, E., et al., 2002. The SAURON project - II. Sample and early results. *MNRAS*, 329(3):513.
- de Zeeuw, T. and Franx, M., 1991. Structure and dynamics of elliptical galaxies. *Annual Review of Astronomy and Astrophysics*, 29:239.
- Dempster, A.P., Laird, N.M., and Rubin, D.B., 1977. Maximum likelihood from incomplete data via the em algorithm. *Journal of the Royal Statistical Society: Series B (Methodological)*, 39(1):1.
- D'Eugenio, F., Colless, M., Groves, B., et al., 2018. The gas-phase metallicities of star-forming galaxies in aperture-matched SDSS samples follow potential rather than mass or average surface density. *MNRAS*, 479(2):1807.
- Dicke, R.H., Peebles, P.J.E., Roll, P.G., et al., 1965. Cosmic Black-Body Radiation. *ApJ*, 142:414.
- Dopita, M.A. and Evans, I.N., 1986. Theoretical Models for H II Regions. II. The Extragalactic H II Region Abundance Sequence. *ApJ*, 307:431.
- Dopita, M.A., Shastri, P., Davies, R., et al., 2015. Probing the Physics of Narrow Line Regions in Active Galaxies. II. The Siding Spring Southern Seyfert Spectroscopic Snapshot Survey (S7). *ApJ*, 217(1):12.
- Dopita, M.A., Vogt, F.P.A., Sutherland, R.S., et al., 2018. Shocked Interstellar Clouds and Dust Grain Destruction in the LMC Supernova Remnant N132D. *ApJ*, 237(1):10.
- Drory, N., MacDonald, N., Bershady, M.A., et al., 2015. The MaNGA Integral Field Unit Fiber Feed System for the Sloan 2.5 m Telescope. *AJ*, 149(2):77.

- Dubois, Y., Pichon, C., Welker, C., et al., 2014. Dancing in the dark: galactic properties trace spin swings along the cosmic web. *MNRAS*, 444:1453.
- Duc, P.A., Cuillandre, J.C., Karabal, E., et al., 2015. The ATLAS^{3D} project - XXIX. The new look of early-type galaxies and surrounding fields disclosed by extremely deep optical images. *MNRAS*, 446:120.
- Ebeling, H., Stephenson, L.N., and Edge, A.C., 2014. Jellyfish: Evidence of Extreme Ram-pressure Stripping in Massive Galaxy Clusters. *ApJ*, 781(2):L40.
- Efstathiou, G., Ellis, R.S., and Carter, D., 1980. Spectroscopic observations of three elliptical galaxies. *MNRAS*, 193:931.
- Efstathiou, G., Ellis, R.S., and Carter, D., 1982. Further observations of the elliptical galaxy NGC 5813. *MNRAS*, 201:975.
- Eggen, O.J., Lynden-Bell, D., and Sandage, A.R., 1962. Evidence from the motions of old stars that the Galaxy collapsed. *ApJ*, 136:748.
- Eisenstein, D.J., Annis, J., Gunn, J.E., et al., 2001. Spectroscopic Target Selection for the Sloan Digital Sky Survey: The Luminous Red Galaxy Sample. *AJ*, 122:2267.
- Elbaz, D., Daddi, E., Le Borgne, D., et al., 2007. The reversal of the star formation-density relation in the distant universe. *A&A*, 468(1):33.
- Ellison, S.L., Teimoorinia, H., Rosario, D.J., et al., 2016. The infrared luminosities of 332 000 SDSS galaxies predicted from artificial neural networks and the Herschel Stripe 82 survey. *MNRAS*, 455:370.
- Emsellem, E., Cappellari, M., Krajnović, D., et al., 2007. The SAURON project - IX. A kinematic classification for early-type galaxies. *MNRAS*, 379(2):401.
- Emsellem, E., Cappellari, M., Krajnović, D., et al., 2011. The ATLAS^{3D} project - III. A census of the stellar angular momentum within the effective radius of early-type galaxies: unveiling the distribution of fast and slow rotators. *MNRAS*, 414:888.
- Emsellem, E., Cappellari, M., Peletier, R.F., et al., 2004. The SAURON project - III. Integral-field absorption-line kinematics of 48 elliptical and lenticular galaxies. *MNRAS*, 352(3):721.

- English, W., Hardcastle, M.J., and Krause, M.G.H., 2016. Numerical modelling of the lobes of radio galaxies in cluster environments - III. Powerful relativistic and non-relativistic jets. *MNRAS*, 461:2025.
- Evans, I.N. and Dopita, M.A., 1985. Theoretical models for H II regions. I. Diagnostic diagrams. *ApJ*, 58:125.
- Evans, N.W. and Collett, J.L., 1994. Separatrix crossing and the enigma of NGC 4550. *ApJ*, 420:L67.
- Fabian, A.C., 2012. Observational Evidence of Active Galactic Nuclei Feedback. *Annual Review of Astronomy and Astrophysics*, 50:455.
- Falcón-Barroso, J., Lyubenova, M., van de Ven, G., et al., 2017. Stellar kinematics across the Hubble sequence in the CALIFA survey: general properties and aperture corrections. *A&A*, 597:A48.
- Falcón-Barroso, J., Sánchez-Blázquez, P., Vazdekis, A., et al., 2011. An updated MILES stellar library and stellar population models. *A&A*, 532:A95.
- Fall, S.M., Krumholz, M.R., and Matzner, C.D., 2010. Stellar Feedback in Molecular Clouds and its Influence on the Mass Function of Young Star Clusters. *ApJ*, 710(2):L142.
- Farber, R., Ruszkowski, M., Yang, H.Y.K., et al., 2018. Impact of Cosmic-Ray Transport on Galactic Winds. *ApJ*, 856(2):112.
- Ferrarese, L., Côté, P., Jordán, A., et al., 2006. The ACS Virgo Cluster Survey. VI. Isophotal Analysis and the Structure of Early-Type Galaxies. *ApJ*, 164:334.
- Fielding, D., Quataert, E., and Martizzi, D., 2018. Clustered supernovae drive powerful galactic winds after superbubble breakout. *MNRAS*, 481(3):3325.
- Fluetsch, A., Maiolino, R., Carniani, S., et al., 2019. Cold molecular outflows in the local Universe and their feedback effect on galaxies. *MNRAS*, 483(4):4586.
- Fogarty, L.M.R., Scott, N., Owers, M.S., et al., 2015. The SAMI Pilot Survey: stellar kinematics of galaxies in Abell 85, 168 and 2399. *MNRAS*, 454:2050.
- Franx, M., Illingworth, G., and Heckman, T., 1989. Major and Minor Axis Kinematics of 22 Ellipticals. *ApJ*, 344:613.

- Franx, M. and Illingworth, G.D., 1988. A counterrotating core in IC 1459. *ApJ*, 327:L55.
- Freudling, W., Romaniello, M., Bramich, D.M., et al., 2013. Automated data reduction workflows for astronomy. The ESO Reflex environment. *A&A*, 559:A96.
- Fritz, J., Moretti, A., Gullieuszik, M., et al., 2017. GASP. III. JO36: A Case of Multiple Environmental Effects at Play? *ApJ*, 848(2):132.
- Fujita, A., Martin, C.L., Mac Low, M.M., et al., 2009. The Origin and Kinematics of Cold Gas in Galactic Winds: Insight from Numerical Simulations. *ApJ*, 698:693.
- Fukugita, M., Ichikawa, T., Gunn, J.E., et al., 1996. The Sloan Digital Sky Survey Photometric System. *AJ*, 111:1748.
- Gamow, G., 1946. Expanding Universe and the Origin of Elements. *Physical Review*, 70:572.
- Ge, J., Mao, S., Lu, Y., et al., 2019. Recovering stellar population parameters via different population models and stellar libraries. *MNRAS*, 485(2):1675.
- Gebhardt, K., Bender, R., Bower, G., et al., 2000. A Relationship between Nuclear Black Hole Mass and Galaxy Velocity Dispersion. *ApJ*, 539:L13.
- Gehrels, N., 1986. Confidence limits for small numbers of events in astrophysical data. *ApJ*, 303:336.
- Gentry, E.S., Krumholz, M.R., Dekel, A., et al., 2017. Enhanced momentum feedback from clustered supernovae. *MNRAS*, 465(2):2471.
- Girardi, L., Bressan, A., Bertelli, G., et al., 2000. Evolutionary tracks and isochrones for low- and intermediate-mass stars: From 0.15 to 7 M_{sun} , and from $Z=0.0004$ to 0.03. *A&A Supp.*, 141:371.
- Gitti, M., Brighenti, F., and McNamara, B.R., 2012. Evidence for AGN Feedback in Galaxy Clusters and Groups. *Advances in Astronomy*, 2012:950641.
- Gorgas, J., Efstathiou, G., and Aragon Salamanca, A., 1990. Line strengths in early-type galaxies. *MNRAS*, 245:217.
- Graham, M.T., Cappellari, M., Li, H., et al., 2018. SDSS-IV MaNGA: stellar angular momentum of about 2300 galaxies: unveiling the bimodality of massive galaxy properties. *MNRAS*, 477(4):4711.

- Gregg, M.D., Silva, D., Rayner, J., et al., 2006. The HST/STIS Next Generation Spectral Library. In A.M. Koekemoer, P. Goudfrooij, and L.L. Dressel, editors, *The 2005 HST Calibration Workshop: Hubble After the Transition to Two-Gyro Mode*, page 209.
- Groves, B., 2007. The Narrow-line Region: Current Models and Future Questions. In L.C. Ho and J.W. Wang, editors, *The Central Engine of Active Galactic Nuclei*, volume 373 of *Astronomical Society of the Pacific Conference Series*, page 511.
- Groves, B.A., Heckman, T.M., and Kauffmann, G., 2006. Emission-line diagnostics of low-metallicity active galactic nuclei. *MNRAS*, 371(4):1559.
- Guérou, A., Emsellem, E., Krajnović, D., et al., 2016. Exploring the mass assembly of the early-type disc galaxy NGC 3115 with MUSE. *A&A*, 591:A143.
- Gullieuszik, M., Poggianti, B.M., Moretti, A., et al., 2017. GASP. IV. A Muse View of Extreme Ram-pressure-stripping in the Plane of the Sky: The Case of Jellyfish Galaxy JO204. *ApJ*, 846(1):27.
- Gunn, J.E., Carr, M., Rockosi, C., et al., 1998. The Sloan Digital Sky Survey Photometric Camera. *AJ*, 116:3040.
- Gunn, J.E. and Gott, J. Richard, I., 1972. On the Infall of Matter Into Clusters of Galaxies and Some Effects on Their Evolution. *ApJ*, 176:1.
- Gunn, J.E., Siegmund, W.A., Mannery, E.J., et al., 2006. The 2.5 m Telescope of the Sloan Digital Sky Survey. *AJ*, 131:2332.
- Hamann, F. and Ferland, G., 1999. Elemental Abundances in Quasistellar Objects: Star Formation and Galactic Nuclear Evolution at High Redshifts. *Annual Review of Astronomy and Astrophysics*, 37:487.
- Hamilton, D., 1985. The spectral evolution of galaxies. I. an observational approach. *ApJ*, 297:371.
- Han, Y. and Han, Z., 2019. A Comprehensive Bayesian Discrimination of the Simple Stellar Population Model, Star Formation History, and Dust Attenuation Law in the Spectral Energy Distribution Modeling of Galaxies. *ApJ*, 240(1):3.
- Harrison, C., 2017. Impact of supermassive black hole growth on star formation. *ArXiv e-prints*.

- Harrison, C.M., Alexander, D.M., Mullaney, J.R., et al., 2014. Kiloparsec-scale outflows are prevalent among luminous AGN: outflows and feedback in the context of the overall AGN population. *MNRAS*, 441:3306.
- Harrison, C.M., Costa, T., Tadhunter, C.N., et al., 2018. AGN outflows and feedback twenty years on. *Nature Astronomy*, 2:198.
- Hartmann, D.H., 1999. Afterglows From the Largest Explosions in the Universe. *Proceedings of the National Academy of Science*, 96(9):4752.
- Heckman, T.M., 1980. An optical and radio survey of the nuclei of bright galaxies. Activity in normal galactic nuclei. *A&A*, 500:187.
- Heckman, T.M., Lehnert, M.D., Strickland, D.K., et al., 2000. Absorption-Line Probes of Gas and Dust in Galactic Superwinds. *ApJ*, 129:493.
- Heckman, T.M. and Thompson, T.A., 2017. A Brief Review of Galactic Winds. *arXiv e-prints*, arXiv:1701.09062.
- Heger, M.L., 1919. Stationary Sodium Lines in Spectroscopic Binaries. *PASP*, 31:304.
- Hernández-García, L., Masegosa, J., González-Martín, O., et al., 2016. Unveiling the Physics of Low-luminosity AGNs through X-Ray Variability: LINER versus Seyfert 2. *ApJ*, 824(1):7.
- Hidalgo, S.L., Pietrinferni, A., Cassisi, S., et al., 2018. The Updated BaSTI Stellar Evolution Models and Isochrones. I. Solar-scaled Calculations. *ApJ*, 856(2):125.
- Hirschmann, M., Dolag, K., Saro, A., et al., 2014. Cosmological simulations of black hole growth: AGN luminosities and downsizing. *MNRAS*, 442:2304.
- Ho, I.T., Kewley, L.J., Dopita, M.A., et al., 2014. The SAMI Galaxy Survey: shocks and outflows in a normal star-forming galaxy. *MNRAS*, 444:3894.
- Ho, L.C., 2008. Nuclear activity in nearby galaxies. *Annual Review of Astronomy and Astrophysics*, 46:475.
- Hoffman, L., Cox, T.J., Dutta, S., et al., 2010. Orbital Structure of Merger Remnants. I. Effect of Gas Fraction in Pure Disk Mergers. *ApJ*, 723:818.
- Hopkins, P.F., Quataert, E., and Murray, N., 2012. Stellar feedback in galaxies and the origin of galaxy-scale winds. *MNRAS*, 421(4):3522.

- Hubble, E., 1929. A Relation between Distance and Radial Velocity among Extra-Galactic Nebulae. *Proceedings of the National Academy of Science*, 15:168.
- Hubble, E.P., 1922. A general study of diffuse galactic nebulae. *ApJ*, 56:162.
- Hubble, E.P., 1925. Cepheids in spiral nebulae. *The Observatory*, 48:139.
- Hubble, E.P., 1926. Extragalactic nebulae. *ApJ*, 64.
- Hubble, E.P., 1936. *Realm of the Nebulae*.
- Hubeny, I., Blaes, O., Krolik, J.H., et al., 2001. Non-lte models and theoretical spectra of accretion disks in active galactic nuclei. iv. effects of compton scattering and metal opacities. *The Astrophysical Journal*, 559(2):680–702.
- Husemann, B., Tremblay, G., Davis, T., et al., 2017. The Close AGN Reference Survey (CARS). *The Messenger*, 169:42.
- Huterer, D. and Shafer, D.L., 2018. Dark energy two decades after: observables, probes, consistency tests. *Reports on Progress in Physics*, 81(1):016901.
- Iodice, E., Coccato, L., Combes, F., et al., 2015. Mapping the inner regions of the polar disk galaxy NGC 4650A with MUSE. *A&A*, 583:A48.
- Ishibashi, W. and Fabian, A.C., 2015. AGN feedback: galactic-scale outflows driven by radiation pressure on dust. *MNRAS*, 451(1):93.
- Ivezić, Ž., Connelly, A.J., VanderPlas, J.T., et al., 2014. *Statistics, Data Mining, and Machine Learning in Astronomy*.
- Ivezić, Ž., Lupton, R.H., Schlegel, D., et al., 2004. SDSS data management and photometric quality assessment. *Astronomische Nachrichten*, 325:583.
- Ivezic, Z., Tyson, J., Acosta, E., et al., 2008. Lsst: from science drivers to reference design and anticipated data products. *arXiv preprint arXiv:0805.2366*.
- Jedrzejewski, R. and Schechter, P.L., 1988. Evidence for Dynamical Subsystems in Elliptical Galaxies. *ApJ*, 330:L87.
- Jedrzejewski, R.I., 1987. CCD surface photometry of elliptical galaxies. I - Observations, reduction and results. *MNRAS*, 226:747.

- Jeong, H., Sukyoung, K.Y., Kyeong, J., et al., 2013. On the nature of sodium excess objects. i. data and observed trends. *The Astrophysical Journal Supplement Series*, 208(1).
- Johnston, E.J., Merrifield, M.R., Aragón-Salamanca, A., et al., 2013. Disentangling the stellar populations in the counter-rotating disc galaxy NGC 4550. *MNRAS*, 428:1296.
- Jones, T., Stark, D.P., and Ellis, R.S., 2018. Dust in the Wind: Composition and Kinematics of Galaxy Outflows at the Peak Epoch of Star Formation. *ApJ*, 863(2):191.
- Juneau, S., Glazebrook, K., Crampton, D., et al., 2005. Cosmic Star Formation History and Its Dependence on Galaxy Stellar Mass. *ApJ*, 619(2):L135.
- Kacprzak, G.G., 2017. Gas Accretion in Star-Forming Galaxies. In A. Fox and R. Davé, editors, *Gas Accretion onto Galaxies*, volume 430 of *Astrophysics and Space Science Library*, page 145.
- Kallman, T. and Bautista, M., 2001. Photoionization and High-Density Gas. *ApJ*, 133:221.
- Kannappan, S.J. and Fabricant, D.G., 2001. A broad search for counterrotating gas and stars: Evidence for mergers and accretion. *The Astronomical Journal*, 121(1):140–147.
- Kantharia, N.G., 2016. Torques and angular momentum: Counter-rotation in galaxies and ring galaxies. *ArXiv e-prints*.
- Karim, A., Schinnerer, E., Martínez-Sansigre, A., et al., 2011. The Star Formation History of Mass-selected Galaxies in the COSMOS Field. *ApJ*, 730:61.
- Katkov, I.Y., Sil'chenko, O.K., and Afanasiev, V.L., 2013. Lenticular Galaxy IC 719: Current Building of the Counterrotating Large-scale Stellar Disk. *ApJ*, 769:105.
- Katkov, I.Y., Sil'chenko, O.K., and Afanasiev, V.L., 2014. Decoupled gas kinematics in isolated S0 galaxies. *MNRAS*, 438(4):2798.
- Katkov, I.Y., Sil'chenko, O.K., Chilingarian, I.V., et al., 2016. Stellar counter-rotation in lenticular galaxy NGC 448. *MNRAS*, 461:2068.
- Kauffmann, G., Heckman, T.M., Tremonti, C., et al., 2003. The host galaxies of active galactic nuclei. *MNRAS*, 346:1055.
- Kaviraj, S., 2009. An ultraviolet study of nearby luminous infrared galaxies: star formation histories and the role of AGN. *MNRAS*, 394:1167.

- Kaviraj, S., 2014a. The importance of minor-merger-driven star formation and black hole growth in disc galaxies. *MNRAS*, 440:2944.
- Kaviraj, S., 2014b. The significant contribution of minor mergers to the cosmic star formation budget. *MNRAS*, 437:L41.
- Kaviraj, S., Devriendt, J., Dubois, Y., et al., 2015a. Galaxy merger histories and the role of merging in driving star formation at $z > 1$. *MNRAS*, 452:2845.
- Kaviraj, S., Laigle, C., Kimm, T., et al., 2017. The Horizon-AGN simulation: evolution of galaxy properties over cosmic time. *MNRAS*, 467:4739.
- Kaviraj, S., Schawinski, K., Silk, J., et al., 2011. A simple model for AGN feedback in nearby early-type galaxies. *MNRAS*, 415:3798.
- Kaviraj, S., Shabala, S.S., Deller, A.T., et al., 2015b. The triggering of local AGN and their role in regulating star formation. *MNRAS*, 452:774.
- Kennicutt, Robert C., J., 1998a. Star Formation in Galaxies Along the Hubble Sequence. *Annual Review of Astronomy and Astrophysics*, 36:189.
- Kennicutt, R.C. and Evans, N.J., 2012. Star Formation in the Milky Way and Nearby Galaxies. *Annual Review of Astronomy and Astrophysics*, 50:531.
- Kennicutt, Jr., R.C., 1998b. The Global Schmidt Law in Star-forming Galaxies. *ApJ*, 498:541.
- Kewley, L.J., Dopita, M.A., Sutherland, R.S., et al., 2001. Theoretical Modeling of Starburst Galaxies. *ApJ*, 556:121.
- Kewley, L.J., Maier, C., Yabe, K., et al., 2013. The Cosmic BPT Diagram: Confronting Theory with Observations. *ApJ*, 774:L10.
- Kewley, L.J., Nicholls, D.C., and Sutherland, R.S., 2019. Understanding galaxy evolution through emission lines. *Annual Review of Astronomy and Astrophysics*, 57(1):511.
- Khandai, N., Di Matteo, T., Croft, R., et al., 2015. The MassiveBlack-II simulation: the evolution of haloes and galaxies to $z = 0$. *MNRAS*, 450:1349.
- Kilerci Eser, E., Goto, T., and Doi, Y., 2014. Ultraluminous Infrared Galaxies in the AKARI All-sky Survey. *ApJ*, 797:54.

- Kim, C.G. and Ostriker, E.C., 2015. Momentum Injection by Supernovae in the Interstellar Medium. *ApJ*, 802(2):99.
- Kim, C.G. and Ostriker, E.C., 2018. Numerical Simulations of Multiphase Winds and Fountains from Star-forming Galactic Disks. I. Solar Neighborhood TIGRESS Model. *ApJ*, 853(2):173.
- King, A. and Pounds, K., 2015a. Powerful Outflows and Feedback from Active Galactic Nuclei. *Annual Review of Astronomy and Astrophysics*, 53:115.
- King, A. and Pounds, K., 2015b. Powerful outflows and feedback from Active Galactic Nuclei. *Annual Review of Astronomy and Astrophysics*, 53:115.
- King, A.R. and Pounds, K.A., 2003. Black hole winds. *MNRAS*, 345(2):657.
- Koratkar, A.P., 1999. The Ultraviolet and Optical Continuum Emission in Active Galactic Nuclei. In C.M. Gaskell, W.N. Brandt, M. Dietrich, D. Dultzin-Hacyan, and M. Eracleous, editors, *Structure and Kinematics of Quasar Broad Line Regions*, volume 175 of *Astronomical Society of the Pacific Conference Series*, page 131.
- Kormendy, J., 1984. Recognizing merger remnants among normal elliptical galaxies NGC 5813. *ApJ*, 287:577.
- Kormendy, J., 1989. Did Elliptical Galaxies Form by Mergers or by Dissipative Collapse? *ApJ*, 342:L63.
- Kormendy, J. and Ho, L.C., 2013. Coevolution (Or Not) of Supermassive Black Holes and Host Galaxies. *Annual Review of Astronomy and Astrophysics*, 51:511.
- Kraemer, S.B. and Crenshaw, D.M., 2000. Resolved Spectroscopy of the Narrow-Line Region in NGC 1068. III. Physical Conditions in the Emission-Line Gas. *ApJ*, 544(2):763.
- Kraemer, S.B., Trippe, M.L., Crenshaw, D.M., et al., 2009. Physical Conditions in the Inner Narrow-Line Region of the Seyfert 2 Galaxy Markarian 573. *ApJ*, 698(1):106.
- Krajnović, D., Emsellem, E., Cappellari, M., et al., 2011. The atlas3d project – ii. morphologies, kinematic features and alignment between photometric and kinematic axes of early-type galaxies. *MNRAS*, 414(4):2923.
- Krajnović, D., Alatalo, K., Blitz, L., et al., 2013. The ATLAS^{3D} project - XVII. Linking photometric and kinematic signatures of stellar discs in early-type galaxies. *MNRAS*, 432:1768.

- Krajnović, D., Bacon, R., Cappellari, M., et al., 2008. The SAURON project - XII. Kinematic substructures in early-type galaxies: evidence for discs in fast rotators. *MNRAS*, 390:93.
- Krajnović, D., Cappellari, M., de Zeeuw, P.T., et al., 2006. Kinemetry: a generalization of photometry to the higher moments of the line-of-sight velocity distribution. *MNRAS*, 366:787.
- Krajnović, D., Weilbacher, P.M., Urrutia, T., et al., 2015. Unveiling the counter-rotating nature of the kinematically distinct core in NGC 5813 with MUSE. *MNRAS*, 452:2.
- Kroupa, P., 2001. On the variation of the initial mass function. *MNRAS*, 322:231.
- Krug, H.B., Rupke, D.S.N., and Veilleux, S., 2010. Neutral Gas Outflows and Inflows in Infrared-faint Seyfert Galaxies. *ApJ*, 708:1145.
- Krumholz, M.R., Thompson, T.A., Ostriker, E.C., et al., 2017. The Observable Properties of Cool Winds from Galaxies, AGN, and Star Clusters. I. Theoretical Framework. *ArXiv e-prints*.
- Kuijken, K., Fisher, D., and Merrifield, M.R., 1996. A search for counter-rotating stars in s0 galaxies. *Monthly Notices of the Royal Astronomical Society*, 283(2):543–550.
- Kuntschner, H., Emsellem, E., Bacon, R., et al., 2006. The SAURON project - VI. Line strength maps of 48 elliptical and lenticular galaxies. *MNRAS*, 369(2):497.
- Kuntschner, H., Emsellem, E., Bacon, R., et al., 2010. The SAURON project - XVII. Stellar population analysis of the absorption line strength maps of 48 early-type galaxies. *MNRAS*, 408(1):97.
- LaMassa, S.M., Heckman, T.M., Ptak, A., et al., 2013. On the Star Formation-AGN Connection at $z < 0.3$. *ApJ*, 765:L33.
- Lamastra, A., Bianchi, S., Matt, G., et al., 2009. The bolometric luminosity of type 2 AGN from extinction-corrected [OIII]. No evidence of Eddington-limited sources. *A&A*, 504:73.
- Larson, R.B., 1975. Models for the formation of elliptical galaxies. *MNRAS*, 173:671.
- Law, D.R., Cherinka, B., Yan, R., et al., 2016. The Data Reduction Pipeline for the SDSS-IV MaNGA IFU Galaxy Survey. *AJ*, 152(4):83.
- Lawson, C.L. and Hanson, R.J., 1974. *Solving least squares problems*.

- Le Borgne, D., Rocca-Volmerange, B., Prugniel, P., et al., 2004. Evolutionary synthesis of galaxies at high spectral resolution with the code PEGASE-HR. Metallicity and age tracers. *A&A*, 425:881.
- Leitherer, C., Schaerer, D., Goldader, J.D., et al., 1999. Starburst99: Synthesis Models for Galaxies with Active Star Formation. *ApJ*, 123(1):3.
- Leja, J., Johnson, B.D., Conroy, C., et al., 2017. Deriving Physical Properties from Broadband Photometry with Prospector: Description of the Model and a Demonstration of its Accuracy Using 129 Galaxies in the Local Universe. *ApJ*, 837(2):170.
- Lemaitre, G., 1925. Note on de sitter's universe. *Journal of Mathematics and Physics*, 4(1-4):188.
- Leroy, A.K., Walter, F., Martini, P., et al., 2015. The Multi-phase Cold Fountain in M82 Revealed by a Wide, Sensitive Map of the Molecular Interstellar Medium. *ApJ*, 814(2):83.
- L'Huillier, B., Combes, F., and Semelin, B., 2012. Mass assembly of galaxies. Smooth accretion versus mergers. *A&A*, 544:A68.
- Li, C. and White, S.D.M., 2009. The distribution of stellar mass in the low-redshift Universe. *MNRAS*, 398:2177.
- Li, H., Mao, S., Cappellari, M., et al., 2018. SDSS-IV MaNGA: The Intrinsic Shape of Slow Rotator Early-type Galaxies. *ApJ*, 863(2):L19.
- Li, Y., Bryan, G.L., Ruszkowski, M., et al., 2015. Cooling, AGN Feedback, and Star Formation in Simulated Cool-core Galaxy Clusters. *ApJ*, 811:73.
- Lintott, C., Schawinski, K., Bamford, S., et al., 2011. Galaxy Zoo 1: data release of morphological classifications for nearly 900 000 galaxies. *MNRAS*, 410:166.
- Lintott, C.J., Schawinski, K., Slosar, A., et al., 2008. Galaxy Zoo: morphologies derived from visual inspection of galaxies from the Sloan Digital Sky Survey. *MNRAS*, 389:1179.
- Liu, G., Arav, N., and Rupke, D.S.N., 2015. Integral Field Spectroscopy of AGN Absorption Outflows: Mrk 509 and IRAS F04250-5718. *ApJ*, 221:9.
- Lofthouse, E.K., Kaviraj, S., Conselice, C.J., et al., 2017. Major mergers are not significant drivers of star formation or morphological transformation around the epoch of peak cosmic star formation. *MNRAS*, 465(3):2895.

- Lonsdale, C.J., Farrah, D., and Smith, H.E., 2006. *Ultraluminous Infrared Galaxies*, page 285.
- López-Corredoira, M., 2017. Tests and Problems of the Standard Model in Cosmology. *Foundations of Physics*, 47(6):711.
- Lupton, R., Blanton, M.R., Fekete, G., et al., 2004. Preparing Red-Green-Blue Images from CCD Data. *PASP*, 116:133.
- Lupton, R., Gunn, J.E., Ivezić, Z., et al., 2001. The SDSS Imaging Pipelines. In F.R. Harnden Jr., F.A. Primini, and H.E. Payne, editors, *Astronomical Data Analysis Software and Systems X*, volume 238 of *Astronomical Society of the Pacific Conference Series*, page 269.
- Lyubenova, M., Martín-Navarro, I., van de Ven, G., et al., 2016. IMF shape constraints from stellar populations and dynamics from CALIFA. *Monthly Notices of the Royal Astronomical Society*, 463(3):3220.
- Madau, P. and Dickinson, M., 2014. Cosmic Star-Formation History. *Annual Review of Astronomy and Astrophysics*, 52:415.
- Magorrian, J., Tremaine, S., Richstone, D., et al., 1998. The Demography of Massive Dark Objects in Galaxy Centers. *AJ*, 115(6):2285.
- Maier, C., Kuchner, U., Ziegler, B.L., et al., 2016. CLASH-VLT: Strangulation of cluster galaxies in MACS J0416.1-2403 as seen from their chemical enrichment. *A&A*, 590:A108.
- Maiolino, R. and Mannucci, F., 2019. De re metallica: the cosmic chemical evolution of galaxies. *The Astronomy and Astrophysics Review*, 27(1):3.
- Maiolino, R., Ruiz, M., Rieke, G.H., et al., 1997. Molecular Gas, Morphology, and Seyfert Galaxy Activity. *ApJ*, 485:552.
- Maraston, C., 2005. Evolutionary population synthesis: models, analysis of the ingredients and application to high-z galaxies. *MNRAS*, 362:799.
- Markwardt, C.B., 2009a. Non-linear Least-squares Fitting in IDL with MPFIT. In D.A. Bohlander, D. Durand, and P. Dowler, editors, *Astronomical Data Analysis Software and Systems XVIII*, volume 411 of *Astronomical Society of the Pacific Conference Series*, page 251.
- Markwardt, C.B., 2009b. Non-linear Least-squares Fitting in IDL with MPFIT. In D.A. Bohlander, D. Durand, and P. Dowler, editors, *Astronomical Data Analysis Software and Systems XVIII*, volume 411 of *Astronomical Society of the Pacific Conference Series*, page 251.

- Marleau, F.R., Clancy, D., and Bianconi, M., 2013. The ubiquity of supermassive black holes in the Hubble sequence. *MNRAS*, 435(4):3085.
- Martin, C.L., 1999. Properties of Galactic Outflows: Measurements of the Feedback from Star Formation. *ApJ*, 513:156.
- Martin, C.L., 2005. Mapping Large-Scale Gaseous Outflows in Ultraluminous Galaxies with Keck II ESI Spectra: Variations in Outflow Velocity with Galactic Mass. *ApJ*, 621:227.
- Martin, C.L., 2006. Mapping Large-Scale Gaseous Outflows in Ultraluminous Infrared Galaxies with Keck II ESI Spectra: Spatial Extent of the Outflow. *ApJ*, 647(1):222.
- Martin, G., Kaviraj, S., Devriendt, J.E.G., et al., 2017. The limited role of galaxy mergers in driving stellar mass growth over cosmic time. *MNRAS*, 472(1):L50.
- Martín-Fernández, P., Jiménez-Vicente, J., Zurita, A., et al., 2016. The multiphase starburst-driven galactic wind in NGC 5394. *MNRAS*, 461(1):6.
- Martín-Navarro, I., Lyubenova, M., van de Ven, G., et al., 2019. Fornax 3D project: a two-dimensional view of the stellar initial mass function in the massive lenticular galaxy FCC 167. *Astronomy and Astrophysics*, 626:A124.
- Martín-Navarro, I., Vazdekis, A., Falcón-Barroso, J., et al., 2018. Timing the formation and assembly of early-type galaxies via spatially resolved stellar populations analysis. *MNRAS*, 475(3):3700.
- Martizzi, D., Faucher-Giguère, C.A., and Quataert, E., 2015. Supernova feedback in an inhomogeneous interstellar medium. *MNRAS*, 450(1):504.
- Masters, K.L., Mosleh, M., Romer, A.K., et al., 2010a. Galaxy Zoo: passive red spirals. *MNRAS*, 405:783.
- Masters, K.L., Nichol, R., Bamford, S., et al., 2010b. Galaxy Zoo: dust in spiral galaxies. *MNRAS*, 404:792.
- McDermid, R.M., Alatalo, K., Blitz, L., et al., 2015. The ATLAS^{3D} Project - XXX. Star formation histories and stellar population scaling relations of early-type galaxies. *MNRAS*, 448:3484.

- McDermid, R.M., Emsellem, E., Shapiro, K.L., et al., 2006. The SAURON project - VIII. OASIS/CFHT integral-field spectroscopy of elliptical and lenticular galaxy centres. *MNRAS*, 373(3):906.
- McKee, C.F. and Ostriker, E.C., 2007. Theory of Star Formation. *Annual Review of Astronomy and Astrophysics*, 45(1):565.
- McWilliam, A., 1997. Abundance Ratios and Galactic Chemical Evolution. *Annual Review of Astronomy and Astrophysics*, 35:503.
- McWilliam, A. and Rich, R.M., 1994. The First Detailed Abundance Analysis of Galactic Bulge K Giants in Baade's Window. *ApJ*, 91:749.
- Mehlert, D., Saglia, R.P., Bender, R., et al., 1998. The kinematically peculiar cores of the Coma cluster early-type galaxies NGC 4816 and IC 4051. *A&A*, 332:33.
- Mehlert, D., Thomas, D., Saglia, R.P., et al., 2003. Spatially resolved spectroscopy of Coma cluster early-type galaxies. III. The stellar population gradients. *A&A*, 407:423.
- Milliard, B., Grange, R., Martin, C., et al., 2017. GALEX: a UV telescope to map the star formation history of the universe. In *ProSPIE*, volume 10569 of *Society of Photo-Optical Instrumentation Engineers (SPIE) Conference Series*, page 1056912.
- Mitzkus, M., Cappellari, M., and Walcher, C.J., 2017a. Dominant dark matter and a counter-rotating disc: MUSE view of the low-luminosity S0 galaxy NGC 5102. *MNRAS*, 464:4789.
- Mitzkus, M., Cappellari, M., and Walcher, C.J., 2017b. Dominant dark matter and a counter-rotating disc: MUSE view of the low-luminosity S0 galaxy NGC 5102. *MNRAS*, 464(4):4789.
- Mo, H., van den Bosch, F.C., and White, S., 2010. *Galaxy Formation and Evolution*.
- Morelli, L., Corsini, E.M., Pizzella, A., et al., 2012. Structure and dynamics of galaxies with a low surface-brightness disc - II. Stellar populations of bulges. *MNRAS*, 423:962.
- Morelli, L., Pizzella, A., Coccato, L., et al., 2017. Kinematic and stellar population properties of the counter-rotating components in the S0 galaxy NGC 1366. *A&A*, 600:A76.
- Morelli, L., Pompei, E., Pizzella, A., et al., 2008. Stellar populations of bulges in 14 cluster disc galaxies. *MNRAS*, 389(1):341.
- Moretti, A., Paladino, R., Poggianti, B.M., et al., 2018. GASP - X. APEX observations of molecular gas in the discs and in the tails of ram-pressure stripped galaxies. *MNRAS*, 480(2):2508.

- Morton, D.C., 2003. Atomic Data for Resonance Absorption Lines. III. Wavelengths Longward of the Lyman Limit for the Elements Hydrogen to Gallium. *ApJ*, 149:205.
- Munari, U., Sordo, R., Castelli, F., et al., 2005. An extensive library of 2500 10 500 Å synthetic spectra. *A&A*, 442(3):1127.
- Murray, N., Ménard, B., and Thompson, T.A., 2011. Radiation Pressure from Massive Star Clusters as a Launching Mechanism for Super-galactic Winds. *ApJ*, 735(1):66.
- Murray, N., Quataert, E., and Thompson, T.A., 2005. On the Maximum Luminosity of Galaxies and Their Central Black Holes: Feedback from Momentum-driven Winds. *ApJ*, 618(2):569.
- Naab, T. and Burkert, A., 2003. Statistical Properties of Collisionless Equal- and Unequal-Mass Merger Remnants of Disk Galaxies. *ApJ*, 597(2):893.
- Naab, T. and Ostriker, J.P., 2017. Theoretical Challenges in Galaxy Formation. *Annual Review of Astronomy and Astrophysics*, 55(1):59.
- Nardini, E., Risaliti, G., Watabe, Y., et al., 2010. The role of nuclear activity as the power source of ultraluminous infrared galaxies. *MNRAS*, 405:2505.
- Narlikar, J.V. and Padmanabhan, T., 2001. Standard cosmology and alternatives: A critical appraisal. *Annual Review of Astronomy and Astrophysics*, 39(1):211.
- Nelder, J.A. and Mead, R., 1965. A simplex method for function minimization. *The Computer Journal*, 7(4):308.
- Netzer, H., 2013. *The Physics and Evolution of Active Galactic Nuclei*.
- Nidever, D.L., Bovy, J., Bird, J.C., et al., 2014. Tracing chemical evolution over the extent of the milky way's disk with apogee red clump stars. *The Astrophysical Journal*, 796(1):38.
- Nidever, D.L., Bovy, J., Bird, J.C., et al., 2014. Tracing Chemical Evolution over the Extent of the Milky Way's Disk with APOGEE Red Clump Stars. *ApJ*, 796(1):38.
- Nieto-Santisteban, M.A., Szalay, A.S., and Gray, J., 2004. ImgCutout, an Engine of Instantaneous Astronomical Discovery. In F. Ochsenbein, M.G. Allen, and D. Egret, editors, *Astronomical Data Analysis Software and Systems (ADASS) XIII*, volume 314 of *Astronomical Society of the Pacific Conference Series*, page 666.

- Noeske, K.G., Weiner, B.J., Faber, S.M., et al., 2007. Star Formation in AEGIS Field Galaxies since $z=1.1$: The Dominance of Gradually Declining Star Formation, and the Main Sequence of Star-forming Galaxies. *ApJ*, 660:L43.
- Nyland, K., Alatalo, K., Wrobel, J.M., et al., 2013. Detection of a High Brightness Temperature Radio Core in the Active-galactic-nucleus-driven Molecular Outflow Candidate NGC 1266. *ApJ*, 779:173.
- Nyland, K., Young, L.M., Wrobel, J.M., et al., 2017. Star formation in nearby early-type galaxies: the radio continuum perspective. *MNRAS*, 464:1029.
- Ocvirk, P., Pichon, C., Lançon, A., et al., 2006. STECKMAP: STEllar Content and Kinematics from high resolution galactic spectra via Maximum A Posteriori. *MNRAS*, 365:74.
- Oh, K., Sarzi, M., Schawinski, K., et al., 2011. Improved and Quality-assessed Emission and Absorption Line Measurements in Sloan Digital Sky Survey Galaxies. *ApJ*, 195(2):13.
- Oh, K., Yi, S.K., Schawinski, K., et al., 2015. A New Catalog of Type 1 AGNs and its Implications on the AGN Unified Model. *ApJ*, 219:1.
- O'Mill, A.L., Duplancic, F., García Lambas, D., et al., 2011. Photometric redshifts and k-corrections for the Sloan Digital Sky Survey Data Release 7. *MNRAS*, 413:1395.
- Oort, J.H., 1932. The force exerted by the stellar system in the direction perpendicular to the galactic plane and some related problems. *Bulletin of the Astronomical Institutes of the Netherlands*, 6:249.
- Oser, L., Naab, T., Ostriker, J.P., et al., 2012. The Cosmological Size and Velocity Dispersion Evolution of Massive Early-type Galaxies. *ApJ*, 744(1):63.
- Oser, L., Ostriker, J.P., Naab, T., et al., 2010. The Two Phases of Galaxy Formation. *ApJ*, 725:2312.
- Osterbrock, D.E. and Ferland, G.J., 2006. *Astrophysics of gaseous nebulae and active galactic nuclei*.
- Ostriker, J.P. and McKee, C.F., 1988. Astrophysical blastwaves. *Reviews of Modern Physics*, 60(1):1.
- Ostriker, J.P. and Peebles, P.J.E., 1973. A Numerical Study of the Stability of Flattened Galaxies: or, can Cold Galaxies Survive? *ApJ*, 186:467.

- Padmanabhan, N., Schlegel, D.J., Finkbeiner, D.P., et al., 2008. An Improved Photometric Calibration of the Sloan Digital Sky Survey Imaging Data. *ApJ*, 674:1217.
- Park, J., Jeong, H., and Yi, S.K., 2015. Outflows in Sodium Excess Objects. *ApJ*, 809:91.
- Pedregosa, F., Varoquaux, G., Gramfort, A., et al., 2011. Scikit-learn: Machine learning in Python. *Journal of Machine Learning Research*, 12:2825.
- Peebles, P.J. and Ratra, B., 2003. The cosmological constant and dark energy. *Reviews of Modern Physics*, 75:559.
- Peng, C.Y., Ho, L.C., Impey, C.D., et al., 2002. Detailed Structural Decomposition of Galaxy Images. *AJ*, 124:266.
- Peng, Y., Maiolino, R., and Cochrane, R., 2015. Strangulation as the primary mechanism for shutting down star formation in galaxies. *Nature*, 521(7551):192.
- Peng, Y.j., Lilly, S.J., Kovač, K., et al., 2010. Mass and Environment as Drivers of Galaxy Evolution in SDSS and zCOSMOS and the Origin of the Schechter Function. *ApJ*, 721:193.
- Penoyre, Z., Moster, B.P., Sijacki, D., et al., 2017. The origin and evolution of fast and slow rotators in the Illustris simulation. *MNRAS*, 468(4):3883.
- Penzias, A.A. and Wilson, R.W., 1965. A Measurement of Excess Antenna Temperature at 4080 Mc/s. *ApJ*, 142:419.
- Perlmutter, S., Aldering, G., Goldhaber, G., et al., 1999. Measurements of Ω and Λ from 42 High-Redshift Supernovae. *ApJ*, 517(2):565.
- Perna, M., Lanzuisi, G., Brusa, M., et al., 2017. An X-ray/SDSS sample (I): multi-phase outflow incidence and dependence on AGN luminosity. *ArXiv e-prints*.
- Peter, A.H.G., 2012. Dark Matter: A Brief Review. *arXiv e-prints*, arXiv:1201.3942.
- Petrosian, V., 1976. Surface brightness and evolution of galaxies. *ApJ*, 209:L1.
- Pier, J.R., Munn, J.A., Hindsley, R.B., et al., 2003. Astrometric Calibration of the Sloan Digital Sky Survey. *AJ*, 125(3):1559.
- Pizzella, A., Corsini, E.M., Vega Beltrán, J.C., et al., 2004. Ionized gas and stellar kinematics of seventeen nearby spiral galaxies. *A&A*, 424:447.

- Pizzella, A., Morelli, L., Corsini, E.M., et al., 2014a. The difference in age of the two counter-rotating stellar disks of the spiral galaxy NGC 4138. *A&A*, 570:A79.
- Pizzella, A., Morelli, L., Corsini, E.M., et al., 2014b. The difference in age of the two counter-rotating stellar disks of the spiral galaxy NGC 4138. *A&A*, 570:A79.
- Planck Collaboration, Aghanim, N., Akrami, Y., et al., 2018. Planck 2018 results. VI. Cosmological parameters. *arXiv e-prints*, arXiv:1807.06209.
- Poggianti, B.M., Moretti, A., Gullieuszik, M., et al., 2017. GASP. I. Gas Stripping Phenomena in Galaxies with MUSE. *ApJ*, 844(1):48.
- Poznanski, D., Prochaska, J.X., and Bloom, J.S., 2012. An empirical relation between sodium absorption and dust extinction. *MNRAS*, 426(2):1465.
- Prochaska, J.X., Kasen, D., and Rubin, K., 2011. Simple Models of Metal-line Absorption and Emission from Cool Gas Outflows. *ApJ*, 734(1):24.
- Prugniel, P. and Soubiran, C., 2001. A database of high and medium-resolution stellar spectra. *A&A*, 369:1048.
- Puchwein, E. and Springel, V., 2013. Shaping the galaxy stellar mass function with supernova- and AGN-driven winds. *MNRAS*, 428:2966.
- Puerari, I. and Pfenniger, D., 2001. Formation of Massive Counter-Rotating Discs: An Alternative Scenario. *APSS*, 276:909.
- Putman, M.E., 2017. *An Introduction to Gas Accretion onto Galaxies*, volume 430 of *Astrophysics and Space Science Library*, page 1.
- Radovich, M., Poggianti, B., Jaffé, Y.L., et al., 2019. GASP - XIX. AGN and their outflows at the centre of jellyfish galaxies. *MNRAS*, 486(1):486.
- Rayner, J.T., Cushing, M.C., and Vacca, W.D., 2009. The Infrared Telescope Facility (IRTF) Spectral Library: Cool Stars. *ApJ*, 185:289.
- Renzini, A. and Peng, Y.j., 2015. An Objective Definition for the Main Sequence of Star-forming Galaxies. *ApJ*, 801(2):L29.
- Rich, J.A., Kewley, L.J., and Dopita, M.A., 2014. Composite Spectra in Merging U/LIRGs Caused by Shocks. *ApJ*, 781:L12.

- Rich, J.A., Kewley, L.J., and Dopita, M.A., 2015. Galaxy Mergers Drive Shocks: An Integral Field Study of GOALS Galaxies. *ApJ*, 221:28.
- Richards, G.T., Fan, X., Newberg, H.J., et al., 2002. Spectroscopic Target Selection in the Sloan Digital Sky Survey: The Quasar Sample. *AJ*, 123:2945.
- Riess, A.G., Filippenko, A.V., Challis, P., et al., 1998. Observational Evidence from Supernovae for an Accelerating Universe and a Cosmological Constant. *AJ*, 116(3):1009.
- Rines, K., Geller, M.J., Kurtz, M.J., et al., 2003. CAIRNS: The Cluster and Infall Region Nearby Survey. I. Redshifts and Mass Profiles. *AJ*, 126:2152.
- Rix, H.W., Franx, M., Fisher, D., et al., 1992. NGC 4550 - A laboratory for testing galaxy formation. *ApJ*, 400:L5.
- Rix, H.W. and White, S.D.M., 1992a. Optimal estimates of line-of-sight velocity distributions from absorption line spectra of galaxies - Nuclear discs in elliptical galaxies. *MNRAS*, 254:389.
- Rix, H.W. and White, S.D.M., 1992b. Optimal estimates of line-of-sight velocity distributions from absorption line spectra of galaxies - Nuclear discs in elliptical galaxies. *MNRAS*, 254:389.
- Robaina, A.R., Hoyle, B., Gallazzi, A., et al., 2012. The similar stellar populations of quiescent spiral and elliptical galaxies. *MNRAS*, 427(4):3006.
- Roberts, M.S. and Haynes, M.P., 1994. Physical Parameters along the Hubble Sequence. *Annual Review of Astronomy and Astrophysics*, 32:115.
- Roberts-Borsani, G.W. and Saintonge, A., 2019. The prevalence and properties of cold gas inflows and outflows around galaxies in the local Universe. *MNRAS*, 482(3):4111.
- Robotham, A.S.G., Taranu, D.S., Tobar, R., et al., 2017. PROFIT: Bayesian profile fitting of galaxy images. *MNRAS*, 466(2):1513.
- Röck, B., Vazdekis, A., Ricciardelli, E., et al., 2016. MILES extended: Stellar population synthesis models from the optical to the infrared. *A&A*, 589:A73.
- Rosario, D.J., Burtscher, L., Davies, R.I., et al., 2018. LLAMA: normal star formation efficiencies of molecular gas in the centres of luminous Seyfert galaxies. *MNRAS*, 473:5658.

- Rose, J.A., 1985. Constraints on stellar populations in elliptical galaxies. *AJ*, 90:1927.
- Rubin, K.H.R., 2017. Gas Accretion Traced in Absorption in Galaxy Spectroscopy. In A. Fox and R. Davé, editors, *Gas Accretion onto Galaxies*, volume 430 of *Astrophysics and Space Science Library*, page 95.
- Rubin, K.H.R., Prochaska, J.X., Koo, D.C., et al., 2014. Evidence for Ubiquitous Collimated Galactic-scale Outflows along the Star-forming Sequence at $z \sim 0.5$. *ApJ*, 794(2):156.
- Rubin, V.C., 1994. Multi-spin galaxies. *AJ*, 108:456.
- Rubin, V.C., Burstein, D., Ford, Jr., W.K., et al., 1985. Rotation velocities of 16 SA galaxies and a comparison of Sa, Sb, and SC rotation properties. *ApJ*, 289:81.
- Rubin, V.C. and Ford, W. Kent, J., 1970. Rotation of the Andromeda Nebula from a Spectroscopic Survey of Emission Regions. *ApJ*, 159:379.
- Rubin, V.C., Graham, J.A., and Kenney, J.D.P., 1992. Cospatial counterrotating stellar disks in the Virgo E7/S0 galaxy NGC 4550. *ApJ*, 394:L9.
- Rupke, D., 2018. A Review of Recent Observations of Galactic Winds Driven by Star Formation. *Galaxies*, 6(4):138.
- Rupke, D.S., Veilleux, S., and Sanders, D.B., 2002. Keck Absorption-Line Spectroscopy of Galactic Winds in Ultraluminous Infrared Galaxies. *ApJ*, 570:588.
- Rupke, D.S., Veilleux, S., and Sanders, D.B., 2005a. Outflows in Infrared-Luminous Starbursts at $z < 0.5$. I. Sample, Na I D Spectra, and Profile Fitting. *ApJ*, 160:87.
- Rupke, D.S., Veilleux, S., and Sanders, D.B., 2005b. Outflows in Infrared-Luminous Starbursts at $z < 0.5$. II. Analysis and Discussion. *ApJ*, 160:115.
- Rupke, D.S.N., Gültekin, K., and Veilleux, S., 2017. Quasar-mode Feedback in Nearby Type 1 Quasars: Ubiquitous Kiloparsec-scale Outflows and Correlations with Black Hole Properties. *ApJ*, 850(1):40.
- Rupke, D.S.N. and Veilleux, S., 2011. Integral Field Spectroscopy of Massive, Kiloparsec-scale Outflows in the Infrared-luminous QSO Mrk 231. *ApJ*, 729:L27.
- Rupke, D.S.N. and Veilleux, S., 2013. The Multiphase Structure and Power Sources of Galactic Winds in Major Mergers. *ApJ*, 768:75.

- Rupke, D.S.N. and Veilleux, S., 2015. Spatially Extended Na I D Resonant Emission and Absorption in the Galactic Wind of the Nearby Infrared-Luminous Quasar F05189-2524. *ApJ*, 801:126.
- Saintonge, A., Catinella, B., Cortese, L., et al., 2016. Molecular and atomic gas along and across the main sequence of star-forming galaxies. *MNRAS*, 462:1749.
- Saintonge, A., Kauffmann, G., Kramer, C., et al., 2011. COLD GASS, an IRAM legacy survey of molecular gas in massive galaxies - I. Relations between H₂, H I, stellar content and structural properties. *MNRAS*, 415:32.
- Saintonge, A., Tacconi, L.J., Fabello, S., et al., 2012. The Impact of Interactions, Bars, Bulges, and Active Galactic Nuclei on Star Formation Efficiency in Local Massive Galaxies. *ApJ*, 758:73.
- Salim, S., 2014. Green Valley Galaxies. *Serbian Astronomical Journal*, 189:1.
- Salim, S., Rich, R.M., Charlot, S., et al., 2007. UV Star Formation Rates in the Local Universe. *ApJ*, 173:267.
- Salpeter, E.E., 1955. The Luminosity Function and Stellar Evolution. *ApJ*, 121:161.
- Sánchez, S.F., Kennicutt, R.C., Gil de Paz, A., et al., 2012. CALIFA, the Calar Alto Legacy Integral Field Area survey. I. Survey presentation. *A&A*, 538:A8.
- Sánchez-Blázquez, P., Peletier, R.F., Jiménez-Vicente, J., et al., 2006. Medium-resolution Isaac Newton Telescope library of empirical spectra. *MNRAS*, 371:703.
- Sánchez-Blázquez, P., Rosales-Ortega, F.F., Méndez-Abreu, J., et al., 2014. Stellar population gradients in galaxy discs from the CALIFA survey. The influence of bars. *A&A*, 570:A6.
- Sanders, D.B., 1997. Luminous Infrared Galaxies. In J. Franco, R. Terlevich, and A. Serrano, editors, *Revista Mexicana de Astronomía y Astrofísica Conference Series*, volume 6, page 42.
- Sarzi, M., Falcón-Barroso, J., Davies, R.L., et al., 2006. The SAURON project - V. Integral-field emission-line kinematics of 48 elliptical and lenticular galaxies. *MNRAS*, 366:1151.
- Sarzi, M., Iodice, E., Coccato, L., et al., 2018a. The Fornax3D project: overall goals, galaxy sample, MUSE data analysis and initial results. *ArXiv e-prints*.
- Sarzi, M., Kaviraj, S., Nedelchev, B., et al., 2016. Cold-gas outflows in typical low-redshift galaxies are driven by star formation, not AGN. *MNRAS*, 456:L25.

- Sarzi, M., Shields, J.C., Schawinski, K., et al., 2010. The SAURON project - XVI. On the sources of ionization for the gas in elliptical and lenticular galaxies. *MNRAS*, 402:2187.
- Sarzi, M., Spiniello, C., La Barbera, F., et al., 2018b. MUSE observations of M87: radial gradients for the stellar initial-mass function and the abundance of sodium. *Monthly Notices of the Royal Astronomical Society*, 478(3):4084.
- Sato, T., Martin, C.L., Noeske, K.G., et al., 2009. AEGIS: The Nature of the Host Galaxies of Low-Ionization Outflows at $z < 0.6$. *ApJ*, 696:214.
- Scannapieco, C., Wadepuhl, M., Parry, O.H., et al., 2012. The Aquila comparison project: the effects of feedback and numerical methods on simulations of galaxy formation. *MNRAS*, 423:1726.
- Scannapieco, E., Silk, J., and Bouwens, R., 2005. AGN Feedback Causes Downsizing. *ApJ*, 635:L13.
- Scarlata, C. and Panagia, N., 2015. A Semi-analytical Line Transfer Model to Interpret the Spectra of Galaxy Outflows. *ApJ*, 801(1):43.
- Scharwächter, J., Dopita, M.A., Shastri, P., et al., 2016. The WiFeS S7 AGN Survey: Current Status and Recent Results on NGC 6300. In N.R. Napolitano, G. Longo, M. Marconi, M. Paolillo, and E. Iodice, editors, *The Universe of Digital Sky Surveys*, volume 42, page 263.
- Schawinski, K., 2012. Black Hole – Galaxy Co-evolution. *ArXiv e-prints*.
- Schawinski, K., Lintott, C., Thomas, D., et al., 2009. Galaxy Zoo: a sample of blue early-type galaxies at low redshift*. *MNRAS*, 396(2):818.
- Schawinski, K., Thomas, D., Sarzi, M., et al., 2007. Observational evidence for AGN feedback in early-type galaxies. *MNRAS*, 382:1415.
- Schawinski, K., Urry, C.M., Simmons, B.D., et al., 2014. The green valley is a red herring: Galaxy Zoo reveals two evolutionary pathways towards quenching of star formation in early- and late-type galaxies. *MNRAS*, 440:889.
- Schaye, J., Crain, R.A., Bower, R.G., et al., 2015. The EAGLE project: simulating the evolution and assembly of galaxies and their environments. *MNRAS*, 446(1):521.
- Schechter, P., 1976. An analytic expression for the luminosity function for galaxies. *ApJ*, 203:297.

- Schiavon, R.P., 2007. Population Synthesis in the Blue. IV. Accurate Model Predictions for Lick Indices and UBV Colors in Single Stellar Populations. *ApJ*, 171:146.
- Schlegel, D.J., Blum, R.D., Castander, F.J., et al., 2015. The Dark Energy Spectroscopic Instrument (DESI): The NOAO DECam Legacy Imaging Survey and DESI Target Selection. In *American Astronomical Society Meeting Abstracts*, volume 225 of *American Astronomical Society Meeting Abstracts*, page 336.07.
- Schmidt, B.P., Suntzeff, N.B., Phillips, M.M., et al., 1998. The High-Z Supernova Search: Measuring Cosmic Deceleration and Global Curvature of the Universe Using Type IA Supernovae. *ApJ*, 507:46.
- Schmidt, M., 1959. The Rate of Star Formation. *ApJ*, 129:243.
- Schulze, F., Remus, R.S., and Dolag, K., 2017. On the Kinematics, Stability and Lifetime of Kinematically Distinct Cores: A Case Study. *Galaxies*, 5:41.
- Schwarzschild, M., 1979. A numerical model for a triaxial stellar system in dynamical equilibrium. *ApJ*, 232:236.
- Scoville, N., Aussel, H., Brusa, M., et al., 2007. The Cosmic Evolution Survey (COSMOS): Overview. *ApJ*, 172(1):1.
- Searle, L., Sargent, W.L.W., and Bagnuolo, W.G., 1973. The History of Star Formation and the Colors of Late-Type Galaxies. *ApJ*, 179:427.
- Sell, P.H., Tremonti, C.A., Hickox, R.C., et al., 2014. Massive compact galaxies with high-velocity outflows: morphological analysis and constraints on AGN activity. *MNRAS*, 441(4):3417.
- Serra, P. and Trager, S.C., 2007. On the interpretation of the age and chemical composition of composite stellar populations determined with line-strength indices. *MNRAS*, 374:769.
- Sérsic, J.L., 1968. *Atlas de Galaxias Australes*.
- Shabala, S.S., Deller, A., Kaviraj, S., et al., 2017. Delayed triggering of radio active galactic nuclei in gas-rich minor mergers in the local Universe. *MNRAS*, 464:4706.
- Shapley, H. and Curtis, H.D., 1921. The Scale of the Universe. *Bulletin of the National Research Council*, 2(11):171.

- Shimasaku, K., Fukugita, M., Doi, M., et al., 2001. Statistical Properties of Bright Galaxies in the Sloan Digital Sky Survey Photometric System. *AJ*, 122:1238.
- Sijacki, D., Springel, V., Di Matteo, T., et al., 2007. A unified model for AGN feedback in cosmological simulations of structure formation. *MNRAS*, 380:877.
- Silk, J. and Rees, M.J., 1998. Quasars and galaxy formation. *A&A*, 331:L1.
- Simien, F. and de Vaucouleurs, G., 1986. Systematics of bulge-to-disk ratios. *ApJ*, 302:564.
- Simkin, S.M., 1974. Measurements of Velocity Dispersions and Doppler Shifts from Digitized Optical Spectra. *A&A*, 31:129.
- Singh, R., van de Ven, G., Jahnke, K., et al., 2013. The nature of LINER galaxies: Ubiquitous hot old stars and rare accreting black holes. *A&A*, 558:A43.
- Slipher, V.M., 1914. The detection of nebular rotation. *Lowell Observatory Bulletin*, 2:66.
- Smee, S.A., Gunn, J.E., Uomoto, A., et al., 2013. The Multi-object, Fiber-fed Spectrographs for the Sloan Digital Sky Survey and the Baryon Oscillation Spectroscopic Survey. *AJ*, 146:32.
- Smith, J.A., Tucker, D.L., Kent, S., et al., 2002a. The u'g'r'i'z' Standard-Star System. *AJ*, 123:2121.
- Smith, L.J., Norris, R.P.F., and Crowther, P.A., 2002b. Realistic ionizing fluxes for young stellar populations from 0.05 to 2 Z_{solar} . *MNRAS*, 337:1309.
- Smith, R.J., Lucey, J.R., Hammer, D., et al., 2010. Ultraviolet tails and trails in cluster galaxies: a sample of candidate gaseous stripping events in Coma. *MNRAS*, 408:1417.
- Somerville, R.S. and Davé, R., 2015. Physical Models of Galaxy Formation in a Cosmological Framework. *Annual Review of Astronomy and Astrophysics*, 53:51.
- Soto, K.T., Lilly, S.J., Bacon, R., et al., 2016. ZAP - enhanced PCA sky subtraction for integral field spectroscopy. *MNRAS*, 458:3210.
- Sparke, L.S. and Gallagher, John S., I., 2007. *Galaxies in the Universe: An Introduction*.
- Spilker, J.S., Aravena, M., Béthermin, M., et al., 2018. Fast molecular outflow from a dusty star-forming galaxy in the early Universe. *Science*, 361(6406):1016.
- Stasińska, G., Costa-Duarte, M.V., Vale Asari, N., et al., 2015. Retired galaxies: not to be forgotten in the quest of the star formation - AGN connection. *MNRAS*, 449(1):559.

- Statler, T.S., 1991. On the velocity fields of elliptical galaxies. *AJ*, 102:882.
- Stoughton, C., Lupton, R.H., Bernardi, M., et al., 2002. Sloan Digital Sky Survey: Early Data Release. *AJ*, 123:485.
- Strateva, I., Ivezić, Ž., Knapp, G.R., et al., 2001. Color Separation of Galaxy Types in the Sloan Digital Sky Survey Imaging Data. *AJ*, 122:1861.
- Strauss, M.A., Weinberg, D.H., Lupton, R.H., et al., 2002. Spectroscopic Target Selection in the Sloan Digital Sky Survey: The Main Galaxy Sample. *AJ*, 124:1810.
- Tabor, M., Merrifield, M., Aragón-Salamanca, A., et al., 2017. Untangling galaxy components: full spectral bulge-disc decomposition. *MNRAS*, 466:2024.
- Taghizadeh-Popp, M., 2010. CfunBASE: A Cosmological Functions Library for Astronomical Databases. *PASP*, 122:976.
- Thakar, A.R. and Ryden, B.S., 1996. Formation of Massive Counterrotating Disks in Spiral Galaxies. *ApJ*, 461:55.
- Thakar, A.R. and Ryden, B.S., 1998. Smoothed Particle Hydrodynamics Simulations of Counterrotating Disk Formation in Spiral Galaxies. *ApJ*, 506:93.
- Thomas, A.D., Dopita, M.A., Shastri, P., et al., 2017. Probing the Physics of Narrow-line Regions in Active Galaxies. IV. Full Data Release of the Siding Spring Southern Seyfert Spectroscopic Snapshot Survey (S7). *ApJ*, 232(1):11.
- Thomas, D., Maraston, C., and Bender, R., 2003. Stellar population models of Lick indices with variable element abundance ratios. *MNRAS*, 339:897.
- Thomas, D., Maraston, C., Bender, R., et al., 2005. The Epochs of Early-Type Galaxy Formation as a Function of Environment. *ApJ*, 621:673.
- Thomas, D., Maraston, C., and Johansson, J., 2011. Flux-calibrated stellar population models of Lick absorption-line indices with variable element abundance ratios. *MNRAS*, 412:2183.
- Thompson, T.A., Fabian, A.C., Quataert, E., et al., 2015a. Dynamics of dusty radiation-pressure-driven shells and clouds: fast outflows from galaxies, star clusters, massive stars, and agn. *Monthly Notices of the Royal Astronomical Society*, 449(1):147–161.
- Thompson, T.A., Quataert, E., Zhang, D., et al., 2015b. An origin for multiphase gas in galactic winds and haloes. *Monthly Notices of the Royal Astronomical Society*, 455(2):1830–1844.

- Tinsley, B.M., 1979. Stellar lifetimes and abundance ratios in chemical evolution. *ApJ*, 229:1046.
- Tombesi, F., Cappi, M., Reeves, J.N., et al., 2011. Evidence for Ultra-fast Outflows in Radio-quiet Active Galactic Nuclei. II. Detailed Photoionization Modeling of Fe K-shell Absorption Lines. *ApJ*, 742(1):44.
- Tonry, J. and Davis, M., 1979. A survey of galaxy redshifts. I. Data reduction techniques. *AJ*, 84:1511.
- Tonry, J.L. and Davis, M., 1981. Velocity dispersions of elliptical and S0 galaxies. I - Data and mass-to-light ratios. II - Infall of the local group to Virgo. *ApJ*, 246:666.
- Toomre, A., 1977. Mergers and Some Consequences. In B.M. Tinsley and D.C. Larson Richard B. Gehret, editors, *Evolution of Galaxies and Stellar Populations*, page 401.
- Toomre, A. and Toomre, J., 1972. Galactic Bridges and Tails. *ApJ*, 178:623.
- Tremonti, C.A., Heckman, T.M., Kauffmann, G., et al., 2004. The Origin of the Mass-Metallicity Relation: Insights from 53,000 Star-forming Galaxies in the Sloan Digital Sky Survey. *ApJ*, 613:898.
- Tsatsi, A., Macciò, A.V., van de Ven, G., et al., 2015. A New Channel for the Formation of Kinematically Decoupled Cores in Early-type Galaxies. *ApJ*, 802:L3.
- Tumlinson, J., Peebles, M.S., and Werk, J.K., 2017. The Circumgalactic Medium. *Annual Review of Astronomy and Astrophysics*, 55(1):389.
- Unterborn, C.T. and Ryden, B.S., 2008. Inclination-Dependent Extinction Effects in Disk Galaxies in the Sloan Digital Sky Survey. *ApJ*, 687:976-985.
- Valdes, F., Gupta, R., Rose, J.A., et al., 2004. The Indo-US Library of Coude Feed Stellar Spectra. *ApJ*, 152(2):251.
- van den Bosch, R.C.E., van de Ven, G., Verolme, E.K., et al., 2008. Triaxial orbit based galaxy models with an application to the (apparent) decoupled core galaxy NGC 4365. *MNRAS*, 385:647.
- van der Marel, R.P. and Franx, M., 1993. A new method for the identification of non-Gaussian line profiles in elliptical galaxies. *ApJ*, 407:525.

- Vazdekis, A., Coelho, P., Cassisi, S., et al., 2015. Evolutionary stellar population synthesis with MILES - II. Scaled-solar and α -enhanced models. *MNRAS*, 449:1177.
- Vazdekis, A., Koleva, M., Ricciardelli, E., et al., 2016. UV-extended E-MILES stellar population models: young components in massive early-type galaxies. *MNRAS*, 463:3409.
- Vazdekis, A., Ricciardelli, E., Cenarro, A.J., et al., 2012. MIUSCAT: extended MILES spectral coverage - I. Stellar population synthesis models. *MNRAS*, 424:157.
- Vazdekis, A., Sánchez-Blázquez, P., Falcón-Barroso, J., et al., 2010. Evolutionary stellar population synthesis with MILES - I. The base models and a new line index system. *MNRAS*, 404:1639.
- Veilleux, S., Cecil, G., and Bland-Hawthorn, J., 2005. Galactic Winds. *Annual Review of Astronomy and Astrophysics*, 43:769.
- Veilleux, S. and Osterbrock, D.E., 1987. Spectral classification of emission-line galaxies. *ApJ*, 63:295.
- Vergani, D., Pizzella, A., Corsini, E.M., et al., 2007. NGC 5719/13: interacting spirals forming a counter-rotating stellar disc. *A&A*, 463:883.
- Viaene, S., Sarzi, M., Baes, M., et al., 2017. MUSE stares into the shadows: the high-resolution dust attenuation curve of NGC 5626. *MNRAS*, 472(2):1286.
- Viaene, S., Sarzi, M., Baes, M., et al., 2018. NGC 5626: a massive fast rotator with a twist. *MNRAS*, 474(1):L47.
- Viaene, S., Sarzi, M., Zabel, N., et al., 2019. The Fornax 3D project: dust mix and gas properties in the centre of early-type galaxy FCC 167. *A&A*, 622:A89.
- Villar Martín, M., Emonts, B., Humphrey, A., et al., 2014. The triggering mechanism and properties of ionized outflows in the nearest obscured quasars. *MNRAS*, 440:3202.
- Vito, F., Maiolino, R., Santini, P., et al., 2014. Black hole accretion preferentially occurs in gas-rich galaxies*. *MNRAS*, 441:1059.
- Vogelsberger, M., Genel, S., Springel, V., et al., 2014. Introducing the Illustris Project: simulating the coevolution of dark and visible matter in the Universe. *MNRAS*, 444:1518.
- Vulcani, B., Poggianti, B.M., Jaffé, Y.L., et al., 2018a. GASP - XII. The variety of physical processes occurring in a single galaxy group in formation. *MNRAS*, 480(3):3152.

- Vulcani, B., Poggianti, B.M., Moretti, A., et al., 2018b. GASP. VII. Signs of Gas Inflow onto a Lopsided Galaxy. *ApJ*, 852(2):94.
- Vulcani, B., Poggianti, B.M., Moretti, A., et al., 2019. GASP - XVI. Does cosmic web enhancement turn on star formation in galaxies? *MNRAS*, 487(2):2278.
- Walch, S. and Naab, T., 2015. The energy and momentum input of supernova explosions in structured and ionized molecular clouds. *MNRAS*, 451(3):2757.
- Walcher, C.J., Coelho, P.R.T., Gallazzi, A., et al., 2015. Abundance patterns in early-type galaxies: is there a “knee” in the [Fe/H] vs. [α /Fe] relation? *A&A*, 582:A46.
- Walcher, J., Groves, B., Budavári, T., et al., 2011. Fitting the integrated spectral energy distributions of galaxies. *APSS*, 331:1.
- Weigel, A.K., Schawinski, K., Caplar, N., et al., 2017. Galaxy Zoo: Major Galaxy Mergers Are Not a Significant Quenching Pathway. *ApJ*, 845(2):145.
- Weijmans, A.M., de Zeeuw, P.T., Emsellem, E., et al., 2014. The ATLAS ^{3D} project - XXIV. The intrinsic shape distribution of early-type galaxies. *MNRAS*, 444(4):3340.
- Weilbacher, P.M., Streicher, O., Urrutia, T., et al., 2012. Design and capabilities of the MUSE data reduction software and pipeline. In *Software and Cyberinfrastructure for Astronomy II*, volume 8451 of *ProcSPIE*, page 84510B.
- Weinberg, S., 1993. *The first three minutes : a modern view of the origin of the universe*.
- Weiner, B.J., Coil, A.L., Prochaska, J.X., et al., 2009. Ubiquitous Outflows in DEEP2 Spectra of Star-Forming Galaxies at $z = 1.4$. *ApJ*, 692(1):187.
- Westera, P., Lejeune, T., Buser, R., et al., 2002. A standard stellar library for evolutionary synthesis. III. Metallicity calibration. *A&A*, 381:524.
- Westfall, K.B., Cappellari, M., Bershadsky, M.A., et al., 2019. The Data Analysis Pipeline for the SDSS-IV MaNGA IFU Galaxy Survey: Overview. *arXiv e-prints*, arXiv:1901.00856.
- Westmoquette, M.S., Smith, L.J., Gallagher, J.S., et al., 2013. Spatially resolved kinematics of the multi-phase interstellar medium in the inner disc of M82. *MNRAS*, 428(2):1743.
- Westoby, P.B., Mundell, C.G., and Baldry, I.K., 2007. Are galaxies with active galactic nuclei a transition population? *MNRAS*, 382:1541.

- White, S.D.M. and Frenk, C.S., 1991. Galaxy formation through hierarchical clustering. *ApJ*, 379:52.
- White, S.D.M. and Rees, M.J., 1978. Core condensation in heavy halos - A two-stage theory for galaxy formation and clustering. *MNRAS*, 183:341.
- Wiener, J., Pfrommer, C., and Oh, S.P., 2017. Cosmic ray-driven galactic winds: streaming or diffusion? *MNRAS*, 467(1):906.
- Wild, V., Heckman, T., and Charlot, S., 2010. Timing the starburst-AGN connection. *MNRAS*, 405:933.
- Wilkinson, D.M., Maraston, C., Goddard, D., et al., 2017. FIREFLY (Fitting Iteratively For Likelihood analysis): a full spectral fitting code. *MNRAS*, 472:4297.
- Williams, C.C., Giavalisco, M., Cassata, P., et al., 2014. The Progenitors of the Compact Early-type Galaxies at High Redshift. *ApJ*, 780(1):1.
- Worthey, G., Faber, S.M., Gonzalez, J.J., et al., 1994. Old stellar populations. 5: Absorption feature indices for the complete LICK/IDS sample of stars. *ApJ*, 94:687.
- Wright, E.L., Eisenhardt, P.R.M., Mainzer, A.K., et al., 2010. The Wide-field Infrared Survey Explorer (WISE): Mission Description and Initial On-orbit Performance. *AJ*, 140(6):1868.
- Wylezalek, D., Zakamska, N.L., Greene, J.E., et al., 2018. SDSS-IV MaNGA: identification of active galactic nuclei in optical integral field unit surveys. *MNRAS*, 474:1499.
- Yan, R. and Blanton, M.R., 2012. The Nature of LINER-like Emission in Red Galaxies. *ApJ*, 747:61.
- Yan, R., Bundy, K., Law, D.R., et al., 2016. SDSS-IV MaNGA IFS Galaxy Survey—Survey Design, Execution, and Initial Data Quality. *AJ*, 152(6):197.
- Yi, S., Demarque, P., Kim, Y.C., et al., 2001. Toward Better Age Estimates for Stellar Populations: The Y^2 Isochrones for Solar Mixture. *ApJ*, 136:417.
- York, D.G., Adelman, J., Anderson, Jr., J.E., et al., 2000a. The Sloan Digital Sky Survey: Technical Summary. *AJ*, 120:1579.
- York, D.G., Adelman, J., Anderson, Jr., J.E., et al., 2000b. The Sloan Digital Sky Survey: Technical Summary. *AJ*, 120:1579.

- Young, L.M., Bureau, M., Davis, T.A., et al., 2011. The ATLAS^{3D} project - IV. The molecular gas content of early-type galaxies. *MNRAS*, 414:940.
- Zhang, D., 2018. A Review of the Theory of Galactic Winds Driven by Stellar Feedback. *Galaxies*, 6(4):114.
- Zheng, X.Z., Bell, E.F., Papovich, C., et al., 2007. The Dependence of Star Formation on Galaxy Stellar Mass. *ApJ*, 661(1):L41.
- Zhu, G.B., Comparat, J., Kneib, J.P., et al., 2015. Near-ultraviolet Spectroscopy of Star-forming Galaxies from eBOSS: Signatures of Ubiquitous Galactic-scale Outflows. *ApJ*, 815(1):48.
- Zubovas, K. and King, A., 2012. Clearing Out a Galaxy. *ApJ*, 745(2):L34.
- Zwicky, F., 1933. Die Rotverschiebung von extragalaktischen Nebeln. *Helvetica Physica Acta*, 6:110.